University of Padua

ICEA Department

PhD School of Civil and Environmental Sciences

- Flow Dynamics Field -

PhD Thesis

Development of a Laboratory for Cardiovascular Fluid Dynamics Studies

PhD Candidate: *Riccardo Toninato*

Supervisor: Ing. *Francesca Maria Susin*

PhD School Director: Prof. *Stefano Lanzoni*

ICEA

Scuola di Dottorato
Scienze dell'Ingegneria Civile ed Ambientale
Dipartimento IMAGE - DCT - DMMMSA
Università degli Studi di Padova

Nelle mie scoperte scientifiche ho appreso più col concorso della divina grazia che con i telescopi.

(Galileo Galilei, prof. of geometry, mechanics, and astronomy at University of Padua from 1592 until 1610)

Preface

This PhD thesis described the realization and development of a new experimental laboratory for cardiovascular studies. Three years later, the Healing Research Laboratory (HeR Lab) is an approved reality, located within the ICEA Dept. of the University of Padua. The present paper explores the different aspects that have been involved on its development, and the principal research fields that have been touched along the doctorate program.

It is subdivided in four parts: a first overview of the aortic district linked to the insertion of prosthetic devices, from physiological and engineering points of views. After this, the experimental activities are widely discussed. The experimental research was focused on the design, realization, trial-tests and first optimization of a mechanical-hydraulic closed circuit (called pulse duplicator), for the study of fluid dynamics in the systemic circulation after the implantation of prosthetic devices. Innovative feature of the workbench is the presence of a compliant silicone phantom replica of a healthy aorta, that permits investigations of mechanics and flow dynamics characteristics of the district via an experimental approach. A third section is depicted to external experimental projects, developed within the division of Cardiac Surgery, dept. of cardiac, thoracic and vascular sciences, University of Padua Medical School, to investigate the haemodynamic performances of a total artificial heart (CardioWest TAH-t); and within the UCL Cardiovascular Engineering Laboratory (University College London, UK), to perform *in vitro* assessment of prosthetic cardiovascular devices performances (biological aortic valves). The last part focuses on a numerical study based on the design of a 2D mechanical model for a red blood cell, and the computation of deformation-damage effects on the shield, due to the shear stresses induced downstream of mechanical aortic valves.

The possibility to made up an experimental laboratory, and the development of a new-born research group, give the chance to obtain strong expertise along these three years in the R&D field, giving the possibility to actually touch all the different faces of the research, from the funding recruitment to the physical workbench realization or prototype testing.

Nota riassuntiva

Nella presente tesi di Dottorato è descritta la realizzazione e lo sviluppo di un nuovo laboratorio sperimentale per studi di fluidodinamica cardiovascolare. Il laboratorio, denominato Healing Research Laboratory (HeR Lab), a tre anni dalla sua creazione, è una realtà di Dipartimento consolidata; presente nel dip. ICEA dell'Università degli Studi di Padova. Nel proseguo dell'elaborato vengono indagati gli aspetti che hanno partecipato allo sviluppo del laboratorio, ed i principali campi di ricerca che sono stati toccati lungo il percorso di dottorato.

La tesi è strutturata in quattro parti principali: la prima fornisce una panoramica del distretto aortico, in relazione all'inserimento di device protesici, sia dal punto di vista fisiologico che ingegneristico. La seconda parte è incentrata nella descrizione approfondita della ricerca sperimentale. Si focalizza nella progettazione, realizzazione e messa punto di un circuito meccanico-idraulico (chiamato *pulse duplicator*), per lo studio della fluido dinamica nella circolazione sistemica, a seguito dell'impianto di dispositivi protesici. Parte innovativa è costituta dalla presenza di un prototipo siliconico compliante di radice aortica ottenuta da CT-scan di paziente, per lo studio delle caratteristiche meccaniche del vaso e dei campi fluidodinamici locali. La terza sezione è costituita da progetti sperimentali sviluppati in strutture esterne all'HeR Lab. Il primo presso la Cardiochirurgia, dipartimento di Scienze Cardiache, Toraciche e Vascolari della Università degli Studi di Padova, allo scopo di investigare le performance emodinamiche di un cuore artificiale totale (CardioWest TAH-t); la seconda come membro dell'UCL Cardiovascular Engineering Laboratory (University College London), con l'obiettivo di indagare le performance di valvole aortiche biologiche per via sperimentale. La quarta sezione descrive uno studio numerico basato sul design di un modello meccanico 2D del globulo rosso, e sul calcolo di deformazioni e danni subiti dalla membrana, dovuti agli sforzi tangenziali indotti dal flusso effluente da valvole aortiche meccaniche.

Lo sviluppo del laboratorio e del nuovo gruppo di ricerca cardiovascolare ha permesso di incamerare ottime competenze nell'ambito della ricerca e progettazione, dando la possibilità di toccare diversi aspetti dello sviluppo, dalla ricerca fondi alla realizzazione fisica di prototipi o banchi sperimentali.

Contents

Chapter 3

Chapter 4

Chapter 5

Chapter 6

Chapter 7

Chapter 8

Introduction

The aim of this doctorate in hydraulic and fluid dynamic engineer was focused on the realization of an experimental laboratory for cardiovascular studies. The established Healing Research (HeR) laboratory sets itself as an innovative service for a productive exchange between engineering and clinical-medicine entities, as well as other enterprises. In order to develop products, this gives expert advice services, and initiates a mechanism based on the technological transfer of knowledge that doesn't seem to be sufficiently developed in the Italian environment. The HeR research group born four years ago under the direction of Ing. Francesca Maria Susin, who introduced myself to this project, with the means to start after securing a PRAT funding of 45.000 Euro in 2012.

In this context, the first results after these three years are certain to have obtained a growing interest and curiosity, in a clinical-medical working environment, both at a regional and national scale. Three years later, the laboratory is a department approved reality, located at ICEA Dept. of the University of Padua, and consists of two engineer researchers, one post-doc, two PhD students, several master's students in thesis, alongside the important help of two lab technicians, working on its development. The Lab has two aspects: experimental and numerical, working in different projects. During this period, three important clinical collaborations were started: with the worldwide known division of Cardiac Surgery, dept. of cardiac, thoracic and vascular sciences, University of Padua Medical School, led by Prof. Dr. Gino Gerosa; with the paediatric cardiac surgery unit, University of Padua Medical School, through Prof. Dr. Giovanni Stellin and Dr. Massimo Padalino; and also with the dept. of vascular surgery, University of Padua Medical School, through Dr. Stefano Bonvini and Dr. Mirko Menegolo. In particular, Dr. Stefano Bonvini is the one that has been beloved in the Lab since its first steps and, with his great help, a self-funding charity sail race in Venice in June 2015 raised 10.000 Euro, all intended for HeR Lab. Moreover, in the engineering research field, three fruitful collaborations started in two years: with UCL Cardiovascular Engineering Laboratory (University College London, UK), leaded by Prof. Gaetano Burriesci, for studies about *in vitro* assessment of prosthetic cardiovascular devices performances; with the Research Unit of Biomechanics & Imaging in Cardiology group (University of Montreal, Canada), coordinate by

Damien Garcia, for studies of numerical models of aortic transvalvular pressure drop; and also with the Te.Si. Laboratory group (University of Padua), leaded by prof. Paolo F. Bariani, for the realization of silicone anatomic parts for *in vitro* tests. The idea for the near future is to also start collaborations with industries, trying to develop a technology transfer upon the industrial needs. Although these projects are in an initial phase, they highlight the growing relevance of the HeR Lab mission.

The doctorate conducted activities have involved various aspects, both planning and organizational, but also management and communicative. The expertise obtained along these three years leads the development of the laboratory and the new-born research group, and gives the possibility to actually touch all the different faces of the research, from the funding recruitment to the physical workbench testing. In detail, the experimental research was focused on the design, realization, trial-tests and first optimization of a mechanical-hydraulic closed circuit (called a pulse duplicator), for the study of fluid dynamics in the systemic circulation after the implantation of prosthetic devices. A brief introduction to the fluid dynamics in the systemic district and to the connected engineering solution able to mimic the physiology will be found in *Chapter 1*. Particular attention was depicted to the aortic district, composed of aortic valve, root and arch. The design and development of the workbench was the main part of the doctorate and will be described in *Chapters 2*, *3*, and *4*. *Chapter 2* examines in depth the design technique and the 1D numerical model developed for an initial sizing of the workbench. In *Chapter 3,* the actual pulse duplicator characteristic are provided, with a detailed description of mechanical and software parts, as well as an innovative manufacturing technique to realize a silicone aortic arch prototype. The detailed results about hydrodynamic performances of the system, obtained for different prosthesis and several heart rate and stroke volume variations, are described in *Chapter 4*. A section is depicted to an *in vitro* comparison, for a similar experimental set up, against the most used commercial mock loop system. The experimental activities were also conducted not only in the Dept. ICEA, but also in two different sites, as an external project, referenced to the development of the HeR Lab. They should not be seen as unconnected works, because they place themselves in the prosthesis assessment through experimental tests, following the leitmotiv of this thesis.

The first external collaboration was focused on *in vitro* tests developed using a patient simulator machine, to assess the hydrodynamic performances of an artificial heart prosthetic devices for patients waiting for transplant: the CardioWest TAH-t and Freedom drive pumping system. The study gave the chance to work in close contact with the Centro V. Gallucci, within the Cardiovascular Surgery Operative Unit, Central State Hospital of Padova, allowing for fast growth in terms of expertise and the ability to work in a

heterogeneous team. This activity was carried out during the first year of the PhD, and it's described in *Chapter 5*.

A second "external" research study was developed at Cardiovascular Engineering Laboratory, Mechanical Engineer Dept. at UCL – University College London, under the supervision of Gaetano Burriesci (director of the lab and reader in Biomedical Engineering) and Andrea Ducci (lecturer in fluid mechanics), for a period of six months during the third year of the PhD. This research was hinged on the estimation of the hemodynamic performances expressed by different aortic valves and roots coupled systems. These *in vitro* tests were conducted using a commercial pulse duplicator system (ViVitro SuperPump System), bio-prosthetic aortic valves, and self-made silicone aortic roots with different shape characteristics. The detailed description and results of this research, that also give interesting ideas for a system capability comparison with regard to the hydraulic system developed in the HeR Lab, are described in *Chapter 6*. *Chapter 7* keeps distance from the previous sections because it describes a numerical study carried out during the first and second year of the PhD. This *in silico* modelling parenthesis was based on the design of a 2D mechanical model for a red blood cell, and the computation of deformation-damage effects on the shield, due to the shear stress induced by the fluid downstream of the aortic valve. In particular, the total haemolysis index of a cloud of red blood cells in multiple passages through a prosthetic mechanical aortic valve was computed. To obtain this quantity, a new definition of incremental damage on the corpuscolate part of blood was developed.
As the conclusion, *Chapter 8* shows a brief resume of the different tasks and the results obtained during the PhD period, also giving some ideas on new possibilities for the HeR Lab, both in terms of experimental and numerical studies.

Chapter 1

Fluid dynamics in the systemic circulation, and engineering solutions to mimic physiology

1.1 Introduction

I decided to start this chapter with the words of Lee R. Waite, professor of mechanical and biomedical engineering, at the Rose Hulman Institute (Indiana, USA). In my opinion, these are the best to introduce the argument:

"One may question why it is important for a biomedical engineer to study physiology. To answer this question, we could begin by recognizing that cardiovascular disorders are now the leading cause of death in developed nations. Furthermore, to understand the pathologies or dysfunctions of the cardiovascular system, engineers must first begin to understand the physiology or proper functioning of that system. If an engineer would then like to design devices and procedures to remedy those cardiovascular pathologies, then she/he must be well acquainted with physiology." (Waite, 2005).

I am really convinced that this idea reflects the reality, and a multi-disciplinary figure, such as a biomedical engineer, should have the intelligence to build up an open and curious mind, ever ready to understand the physics and the physiology of the problem.

The next paragraphs are meant to be an engineering centred digression about the cardiovascular system, with a particular focus on the aortic area, seen as a physiologic district, but also as a possible implant site, such as for a prosthetic valve, an aortic stent, a ventricular assistive device, etc.

1.2 The cardiovascular system

The cardiovascular system is normally subdivided into heart, arteries, veins, capillaries, and lymphatic vessels. The main role of the cardiovascular system is to deliver oxygen, but it also plays other important functions such as temperature regulation, the delivering of nutrients, and waste removal. The engine of this complex system is the heart, a muscle that acts as a double pump: the left and the right heart. The outflow blood discharge coming to the

aorta (cardiac output) is dependent upon arterial pressure generated by the body tissues, and the heart itself. So, via the correct pressure, this double pump is able to generate, modify, and adjust the correct amount of blood that flows along the different vessels to feed all the organs. Just to have an idea of the work supported by the heart, it is possible to make a rough count: it beats 70 times per minute in a rest situation, so it will beat ~100,000 times per day, ~35 million times per year. A typical cardiac output is 70 mL of blood each beat, so a medium heart pumps over 7000 L, or the equivalent of 1800 gal, per day. Moreover, is made by a muscle with a mass of approximate 300 g (for an average adult man) (Waite, 2005; Ganong, 2007).

The cardiovascular system can be further divided into three subsystems: the systemic, the pulmonary, and the coronary circulation. The first one is the subsystem that is supplied by the aorta and feeds the systemic capillaries, and is the one that will be most analysed by this PhD thesis, for two main reasons. First, it is the most stressed system in terms of flow discharge and pressure peak values and, as a consequence of that, the different parts (valves, flow tracts, etc.) tend to be the first that need a substitution. The global market plays an important role to direct the development of device solutions and the benchmarks able to test the new models in this area. In this scenario, the simulation systems have to fulfil international regulations that change quite frequently to follow the engineer -and clinical- solutions. A direct consequence of this is the important role played by the aortic valve and aortic arch prosthetic devices, and the ability to assess the real *in vitro* haemodynamic performance before the commercialization.

1.2.1 Systemic circulation as a hydraulic loop

After these preliminary considerations, let's have a look at the systemic circulation physiology and its hydraulic loop parallelism. It is the principal blood circuit that allows the constant supply of oxygen to all organs and tissues. The heart acts as exchange element between two circulation systems, and it is subdivided in two double parts, for a total of four chambers and four mono-direction passive valves (*fig.1.1*). This division helps the heart to provide a two stage cardiac cycle, that reflects the duality of the blood system circuit. The chambers are: left atrium and left ventricle, right atrium and right ventricle. The former two control the oxygenated blood loop, the latter two coordinate the cycle for the blood coming back through the inferior and superior *vena cava*. The mitral (bicuspid) and the aortic (tricuspid) valves separate the left atrium and the aorta from the ventricle. The tricuspid and the pulmonary valves act as a septum for the inflow and outflow of the right ventricle. So, using the left heart as a starting point for the systemic hydraulic loop, the left ventricle can be imagined as an in-pressure mobile chamber, with an inflow tract and an outflow tract. A tank and a valve make the inflow tract: the left atrium and the mitral valve. The aortic valve and the aortic root constitute the outflow part. The oxygenated blood is supplied to the left atrium from the lungs, via the

pulmonary vein. The cardiac cycle and the relative pressure fields (*fig.1.2*) can be explained as starting from here. The blood stored in the atrium passes through the mitral valve into the ventricle during the diastolic phase (about 60% of the time of the cardiac cycle), where the aortic valve is closed. The mitral valve is a bileaflet valve, with an ellipsoid shape. Its size changes a lot among subjects but it is normally bigger than the aortic one, and a medium man's diameter could be 27-32 mm. Once the ventricle is filled, the pressure difference closes the mitral valve, but -for a few instants- the aortic also remains closed and a relevant force is imposed by the pericardium, increasing the pressure inside the ventricle. This short interval (about 7% of the entire cycle) is called iso-volumetric contraction. When the pressure inside the left ventricle is high enough to ensure the correct perfusion pressure to the organs, the blood flows through the aorta and performs the ejection (or systolic phase). Normally this part is about 33% of the cardiac cycle. The stroke volume generated from the heart can vary from 50 ml/beat up to 120 ml/beat in response to the function of the tissue oxygen allowing a cardiac output from 4 l/min up to 20 l/min. The aortic valve is a trileaflet valve, with a normal size of about 27±4 mm for men and 24±4 mm for woman. The aorta provides the supply to the femoral, brachiocephalic, carotid arteries, coronaries, up to the capillaries; closing the circuit of oxygenated blood (and the systemic circulation). At the end of the systole, another diastolic phase starts and the aortic valve, due to a negative pressure difference between ventricle and aortic root, closes the leaflets allowing for the filling of the ventricle.

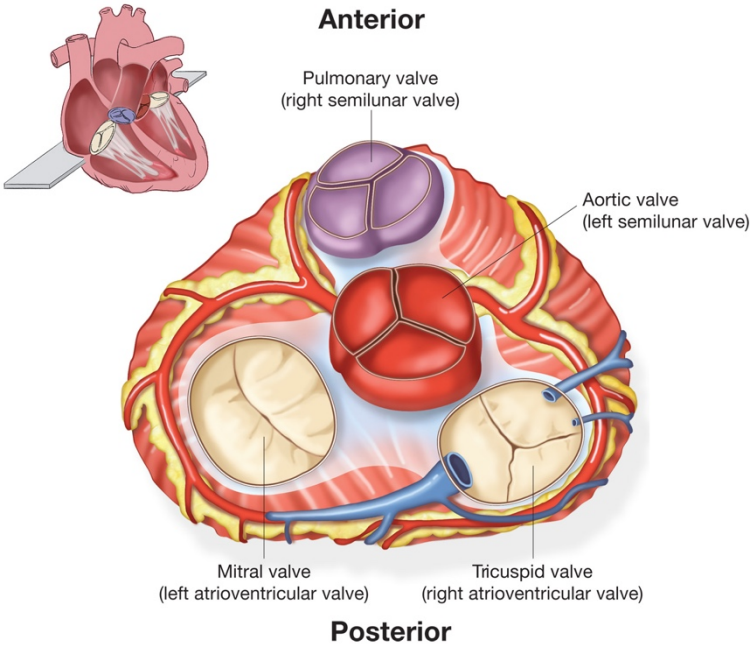

Fig.1.1 Cross-section of the heart showing the four valves in a closed position.

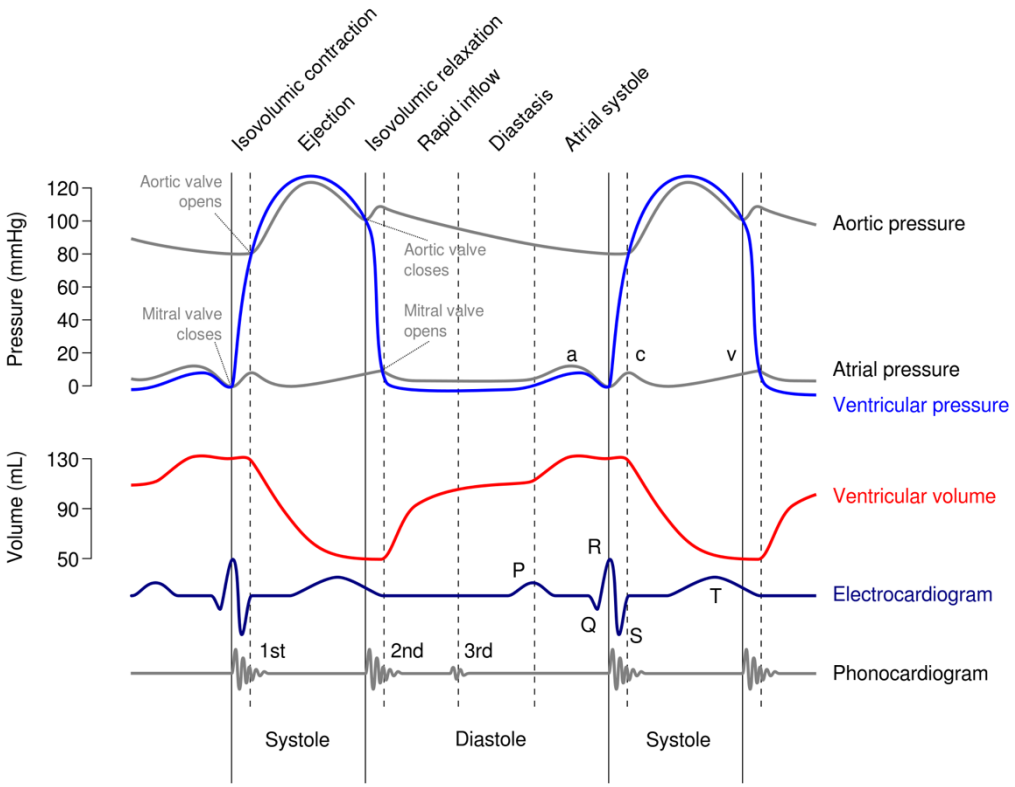

Fig.1.2 A typical cardiac cycle, showing pressures waves with values for the main points, ventricular volume trend, electrocardiogram curve and the phonocardiogram measurement.

1.2.2 Aortic district: valve, root and arch. Physiology and fluid mechanics

The native aortic valve is anatomically identified using the physiologic name of tricuspid semilunar valve (*fig.1.3*) (Ganong, 2009). Indeed, it is composed of three leaflets made from connective, less vascularized tissue, with the addition of a variable amount of protein, and their shape remains a half-moon profile. The cusps are connected to a fibrous tissue ring, or valve ring, that acts as a physical separation between the ventricular chamber and the sinuses of Valsalva. A functional description of its geometry and operating principles was developed by Thubrikar, (Thubrikar, 1990), and, before this, a dissertation on the leaflets motion was written by Swanson & Clark (Swanson & Clark, 1973). The dynamic behaviour of the valve is quite difficult to analyse, for two reasons. The challenging task of observing the *in vivo* movement with high spatial resolution detail, and the complexity to replicate -*in vitro*- geometry and flow conditions.

In spite of these issues, since the ‘60s various researchers started to study dynamics of the valve leaflets and the flow patterns across the valve (Bellhouse, 1969; B & Talbot, 1968; Yoganathan, 2000). Of course the typology of the flow field (pulsatile, with non-constant profile), the characteristics of the fluid (non Newtonian), and the elasticity of the site, underline that the problem can’t be trivialized. But, using a very simple hydraulic parallelism, the problem could be described as a jet that passes through a movable orifice flowing from a cylinder to a smaller tube. In particular, *in vivo* experiments (Giddens & Yoganathan, 1998) showed that the valve aperture is not immediate, and expresses a specific dynamic that changes in function of the patient condition. Moreover, the instantaneous variation of the geometric area of the orifice is called GOA (Geometric Orifice Area), that should not be confused with EOA (Effective Orifice Area), which indicates the blood area (the vena contracta) that forms downstream of the valve. The difference between the areas and a typical EOA trend for healthy and pathologic conditions, are illustrated in *fig.1.4* (Beauchesne et al., 2003; Garcia et al., 2004). Looking at the physiological trend, the opening phase is fast but not immediate, following different slopes since the maximum value. This difference is due to a common valve disease, leaflet stenosis, which stiffens the leaflets and hinders correct valve movement. For the healthy subject, it is possible to see the fluttering of the leaflets when the valve is open, a phenomenon due to the fast little movements that are a consequence of a complex geometry (the aortic root) and flow field. The complete open phase takes 60-70% of the cardiac cycle. The closing phase is fast, about 4% of the cycle, and is ruled by a high velocity gradient and vortices inside the Valsalva sinuses plus a physiological backflow that helps valve closure.

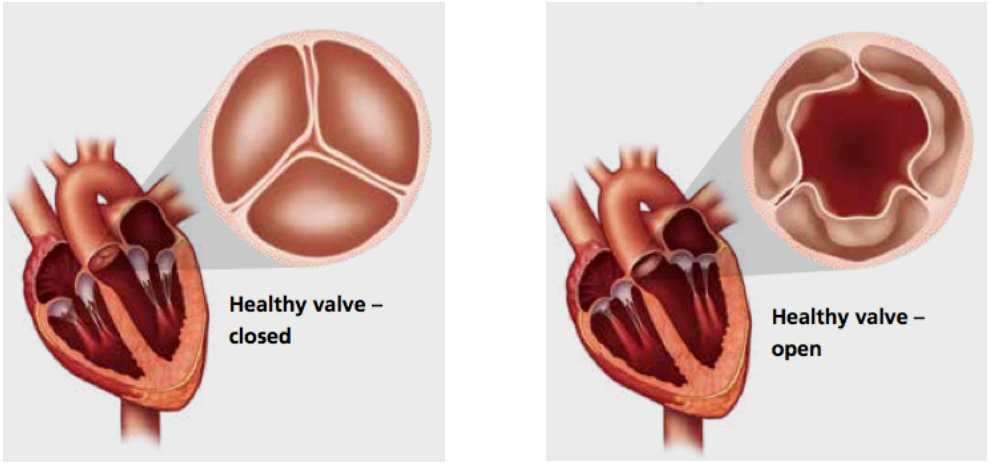

Fig.1.3 Open and closed healthy aortic valve profile from the cross-section plane.

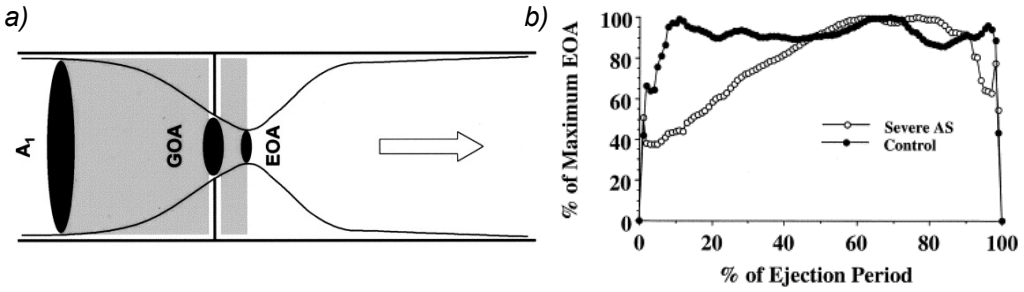

Fig.1.4 *a)* Schematic representation of flow through a rigid orifice plate. A_1, Inlet cross-sectional area; *EOA*, effective orifice area; *GOA*, geometric orifice area (Garcia et al., 2004). *b)* Instantaneous effective orifice area (EOA) during 1 ejection period for patient with severe aortic stenosis (AS) and age-/sex-matched control patient (Beauchesne et al., 2003).

The detailed flow patterns visible downstream of an aortic valve will be studied in *Chapter 6*. Some general information is summarized here, to clarify the physics of the problem. The aortic valve opens when the ventricular pressure exceeds that of the aorta (with a pressure difference across the valve, Δp, of about 2-3 mm Hg), and the blood is accelerated into the artery. In healthy individuals, it is possible to reach a velocity peak value of the jet of approximately 1.25 m/s just downstream of the valve. This value is slightly higher in children, about 1.5 m/s. For the pulmonic valve, peak velocities are smaller, about 0.75 m/s in adults and 0.9 m/s in children (Kilner et al., 1993; Weyman, 1994). The blood velocity peak is reached in the first third of systole (11% of the cardiac cycle). The jet shape can not be perfectly cylindrical because the ventricle translates and rotates (and, in accordance, the base of the aortic valve also varies in size, and moves), during the systole. For an aortic pressure range between 120 and 80 mmHg, the perimeter varies approximately 22%(Waite et al., 2007). Indeed, roentgenographic studies in patients with normal aortic valves have shown that, under resting conditions, the valve opens only to 40% of its maximum opening area and even during exercise, it only opens to about 70% (Stein et al., 1971). These studies suggest that the valve opens with a triangular orifice under resting conditions and moves toward a circular orifice under exercise conditions (Reul et al., 1979). Numerous experimental and mathematical analyses were performed to replicate and measure these velocities and characteristics. The first were Bellhouse and Talbot (Bellhouse & Talbot, 1969), which described steady and pulsatile flow studies in a model aortic flow chamber including the sinuses.

Past the valve, the blood flows into the aortic root, and onto the aorta. The human aorta is the largest blood vessel and has a complex, three-dimensional curved geometry with multiplanar curvature (Jacob & Francone, 1974; Enderson, 1978). The root of the aorta is composed by three bulges (sinuses

of Valsalva) and a small straight tract (from the sinotubular junction to the ascending aorta) (*fig.1.5*). Two of the three sinuses provide blood supply to the heart muscles by means of the coronary arteries. Numerous studies have focused on the geometry and function of the aortic root, since Da Vinci (Keele, 1952). In particular, the epitrocoidal top view profile was defined by Reul (Reul, 1990), the attachment profile angles of the leaflets from Thubrikar (Thubrikar et al., 1981), and the sagittal plane of the sinuses profile from Grigioni (Grigioni et al., 2005). The fundamental role of the Valsalva sinuses will be described in detail in *Chapter 6*, but for now it seems enough to say that they provide less flow energy dispersion through the aortic root, maximizing the vena contracta, and also helping in the dynamics of leaflet closure.

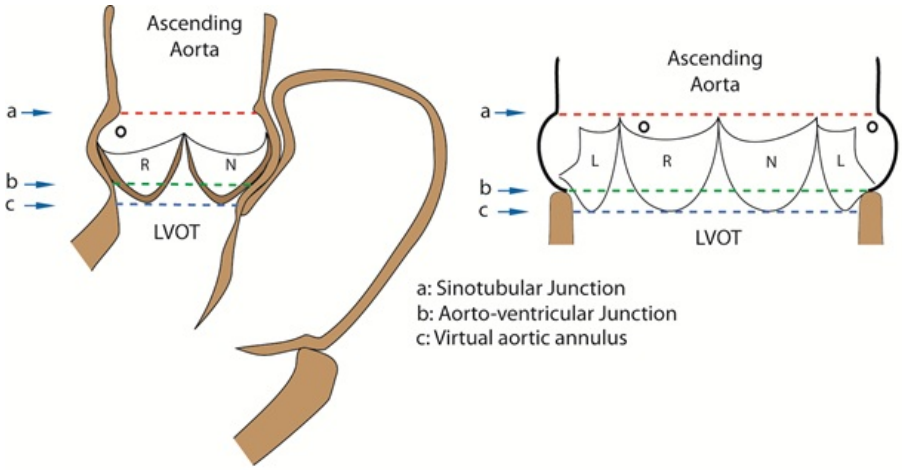

Fig.1.5 Aortic valve sketch with virtual and anatomical rings (Zalkind et al., 2013).

Past the valve and the Valsalva sinuses, the vessel starts to be called ascending aorta (and then aortic arch). Its primary plane of curvature allows the aorta to arch over the left pulmonary vessels and the left fork. Then, the aorta curves around the esophagus and the trachea in the mid-arch region, creating a shallow secondary curvature. In the ascending aorta a third plane of curvature is present, when the aorta curves around the left atrium as it rises from the aortic root. These curvatures express a radius-to-radius ratio of the about 3.8, 7.25, and 7.5, respectively (Yearwood, 1979; Yearwood & Chandran, 1980). In the region of the mid-arch of the aorta, three major arterial branches originate. A typical drawing of the arch, from a physiology book, is shown in *fig.1.6*, where it is possible to appreciate the complexity of the geometry. To have a rough idea of the total dimensions, the aorta from the aortic root to the diaphragm stays inside an A4 paper (about 210 x 300 mm). The descending aorta, lying close to the vertebral bodies and passing through the diaphragm, gives rise to more major branches that feed blood to the visceral organs. The descending aorta is divided into the thoracic (above the

diaphragm) and the abdominal segments (below the diaphragm). The abdominal aorta bifurcates into the two common iliac arteries at the level of the fourth lumbar vertebra (Anderson, 1978; Yearwood & Chandran, 1982; Chandran, 1993; Shipkowitz, 1995). To better optimize the flow dynamics, the aorta cross-section expresses an elliptical shape, with the lumen diameter being slightly larger in the anterior–posterior plane compared to that in the lateral plane, and it shrinks about 50% from the root to the descending aorta. In particular, Li (Li, 1987) has expressed the cross-sectional area changes in the aorta in an exponential form given by the relationship

$$A(z) = A_0 e^{-kz/r}$$

where, k is the taper factor, r is the radius, z is the axial distance of the vessel from the aortic root, and A_0 is the area at the aortic root.

Furthermore, the aorta vessel wall movements are complex; it distends during the systole and contracts during the diastole. So, the flow development into the aorta is unsteady, passing through a vessel with an elliptical cross-section that tapers, with a moving arterial wall boundary, curvature in multiple planes, and major branches in the mid-arch region as well as in the descending aorta. The subject of complicated flow development in the aortic arch and the descending aorta has attracted the attention of numerous medical scientists and engineers.

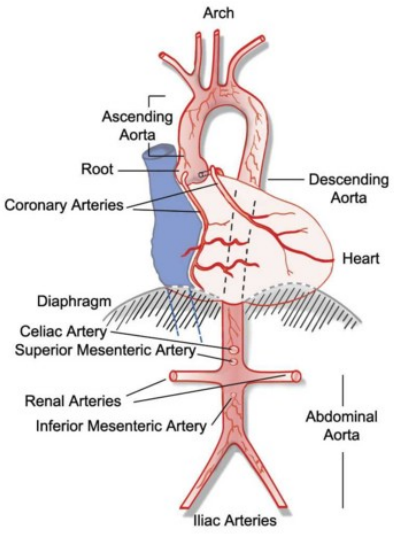

Fig.1.6 A schematic drawing of the aortic arch from the frontal plane.

One of the first studies was conducted by Rodkiewicz (Rodkiewicz, 1975) that studied a pulsatile flow in a 2D channel, that simulated the aortic arch with the three major arterial branches in the mid-arch region. The results of this model suggested the presence of five regions of flow stagnation and four regions of

boundary layer separation. Wright and Temple (Wright & Temple, 1977) developed research on a three-dimensional model of the human aorta, to visualize the flow and analyse the effect of prosthetic valves in the aortic root. Also Roach (Roach, 1977) used an *in vitro* approach to study the steady flow through a three dimensional model of the human aorta using flow visualization of dye filaments.

In particular, Chandran (Chandran et al., 1983; Chandran et al., 1984; Khalighi et al., 1983; Chandran et al., 1985; Chandran, 1985) specifically focused on the interpretation of the flow inside the aortic root in variations of valve prostheses housed in the aortic annulus. They employed a three-dimensional non-compliant model of the human aorta including the major branch vessels in the aortic arch. Using quantitative laser Doppler anemometer, they studied steady and pulsatile flow development downstream of different valves. The results showed that the flow development in the ascending aorta expresses a high dependence upon the valve design as well as on the orientation of the valve with respect to the root. Even in the mid-arch region, the velocity profiles exhibited variations depending on the valve at the root of the aorta. Representative flow patterns of these very informative studies, during the peak forward-flow phase with a tissue valve at the root of the aorta as well as a tilting disc valve in two different orientations, show a helicoidally shaped structure that forms and develops inside the vessel. An image extracted from Chandran (*fig.1.7*) shows the velocity measurements obtained using laser Doppler anemometry techniques at various planes in the aortic arch with a tilting disc mechanical valve and a porcine tissue valve.

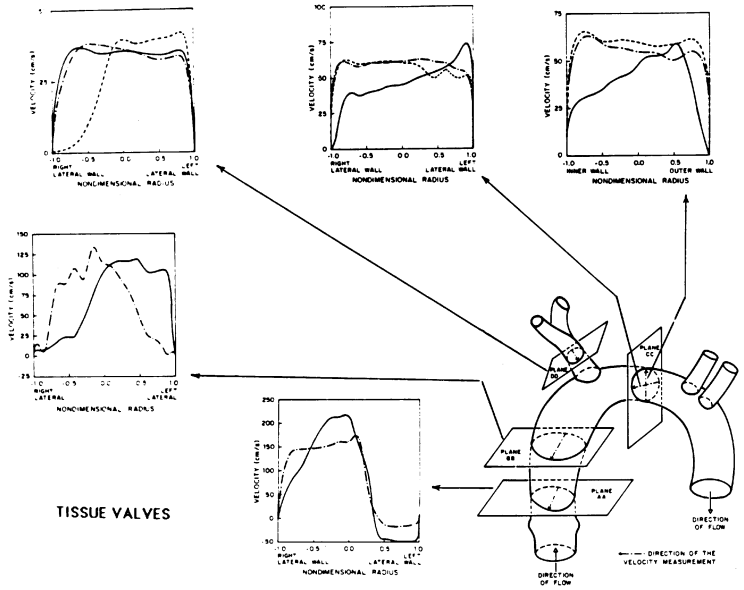

Fig.1.7 Velocity profiles measured in the various cross-sections in the model of the human aortic arch by laser Doppler anemometry technique with a porcine tissue valve (Roach, 1977; Chandran et al., 1984).

This thesis presents the case of ascending aorta and aortic arch replica, a project settled in collaboration with the dept. of vascular surgery of the Padua Hospital and the University Padua Hospital (see Chapter 3). In particular, the clinical need was the research of the reasons that cause a migration (or a malfunctioning) of the endovascular stent prosthesis placed to reduce aortic aneurisms. To better understand that problem, some information about the aortic arch aneurysms and the problems connected to the endovascular insertion are now provided.

A dissertation concerning the properties of the first mechanical aorta was given by Dal Borgo (Dal Borgo, 1952). One of the most relevant diseases from the clinical perspective is the aneurism of the ascending and descending aorta. This local vessel expansion could cause a rupture of the aorta or a dissection event, both of which are very dangerous for the patient. Garcia (Garcia et al., 2012) evaluated the aneurism severity via *in vitro* mechanical tests on biological tissues, trying to give some geometrical parameters to discriminate the disease level. The systemic pressure and hypertension condition are fundamental factors in the development of high radial forces that act on the aortic walls, and participate to a reshaping of the geometry of the aortic arch (Isnard et al. 1989; Gao et al., 2006). The wide geometric variation in terms of arch and aneurisms has become a problem, leading to the impossibility of developing a patient specific prosthesis in treating of an acute event.

The endovascular stent is the most widely used prosthesis for the aneurisms treatment (*fig.1.8* shows some abdominal stents). The insertion takes place from the femoral artery and the catheter is guided through the circulation towards the right position inside the aorta. Here the delivery system provides correct placement, and the Nitinol stent rings expand along the Teflon conduit, adapting to the aorta geometry (*fig.1.9* shows some aortic arch stents). The prosthesis oversizing and correct anchoring of the necks provide a stable solution for aneurisms bypass (Lumsden et al., 2012). The complications encountered post-surgery (long-term) are normally:

- Endoleaks (inadequate seal, sac filling, leaking through the stent, porous graft, endotension).
- Migration of the necks.
- Tightening of the nitinol structure for high curvature.
- Rupture of the graft.

In particular, developing an adequate replica of the anatomic district could provide some answers to these complications, studying the hydrodynamic performances in terms of pressure, velocity and stress fields. *In vitro* literature study about this topic is not so wide, for the difficulties to provide a correct anatomic replica or the precious physiological flow conditions for *in vitro* testing (Markl et al., 2005; Doyle et al.,2008; Sulaiman et al.,2008; Canstein et al., 2008; Biglino et al., 2012; Biglino et al., 2013).

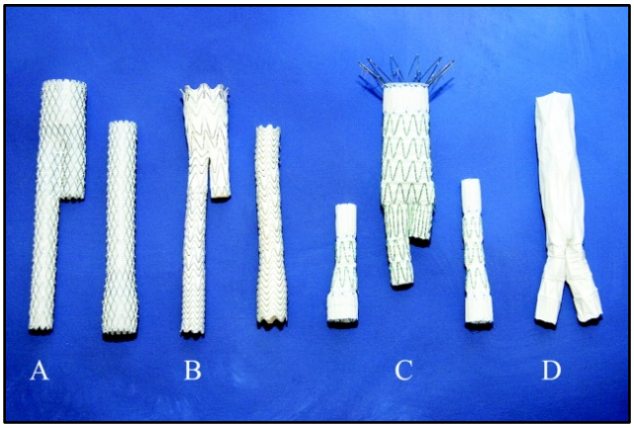

Fig.1.8 Examples of FDA-approved and currently marketed stent graft devices: (A) Medtronic, (B) Gore, (C) Cook Medical, and (D) Endologix.

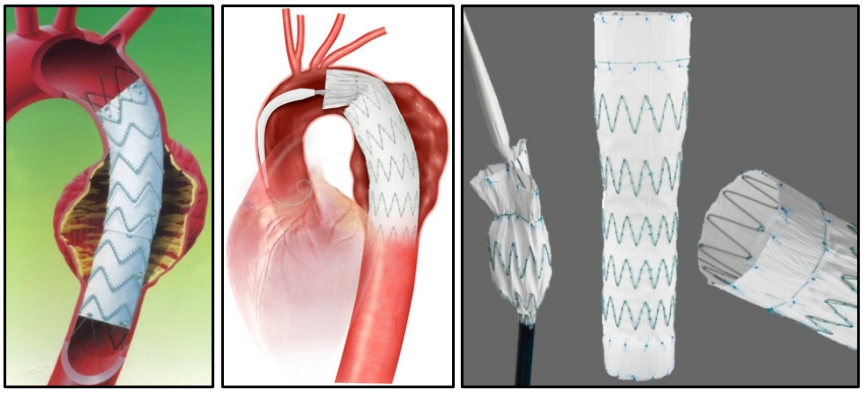

Fig.1.10 Ascending aorta endovascular stents for treatment of aneurysms. Left: Medtronic Talent, right: Gore Tag model.

1.2.3 Prosthetic devices inserted in the aortic region

The physiological overview, and the conducted studies on the flow dynamics, show how the variation of the aortic valve or the insertion of a prosthetic device into the aortic district could easily affect the flow pattern and the velocity profiles. A market device impact rank will probably put the aortic valve replacement in first place. Due to several societal and life factors, aortic valve diseases have become quite common in the north of the world, pushing the valve market into a constant rise from the ‘70s up to now. Moving from the mechanical Bjork-Shiley to the several bileaflet mechanical solutions, the prosthetic devices now tends to become more and more close to the native one, to overcome the problem of a strong anticoagulant therapy and other contraindications. So, since the late ‘90s, the companies have increased the study and the development on bioprosthetic solutions, able to guarantee an adequate durability, and provide an excellent flow dynamic across the valve. A detailed *in vitro* analysis of the flow patterns downstream of a porcine valve, in

couple with different aortic roots, can be found in *Chapter 6*. From 2005, new mini-invasive surgical solutions started to be developed: the trans-apical and trans-femoral accesses. These techniques use a catheter in which a valve is collapsed, and released *in situ* from the surgeons, via an expandable balloon system. An example of these very different prosthetic solutions is reported in *fig.1.10*.

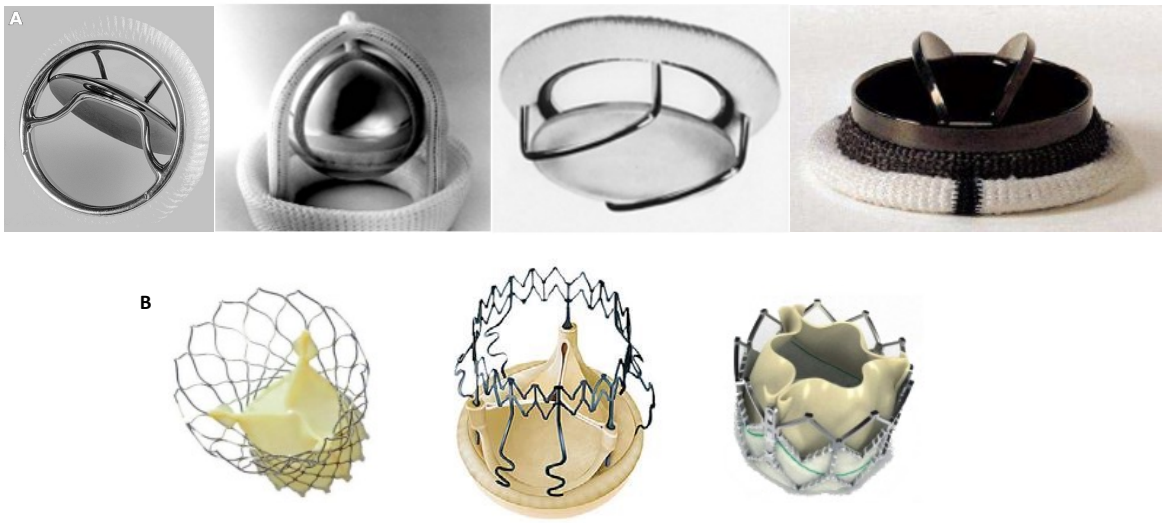

Fig.1.10 *A)* Mechanical valves. From left to right: Bjork-Shiley tilting disk, Starr-Edward caged ball, Kay-Shiley disc valve, Sorin Allcarbon bileaflet. *B)* Bioprosthetic valve. From left to right: Medtronic TAVI CoreValve, Sorin Perceval suterless, Edwards TAVI Sapien XT.

Talking about the aortic root, the most interesting device is certainly the composite valve graft prosthesis. This replacement is currently the treatment of choice for a wide variety of lesions of the aortic root and the ascending aorta. It is normally made from biomaterial tissues like Dacron® or Teflon® fibres, and is composed of the bulges, the sinotubular junction, and a part of the ascending aorta. In most cases, the substitution of the aortic root is due to aneurismatic cavities that grow around the sinotubular region. If the first solution was replacement of the part, surgeons and engineers have tried to bypass this problem in recent years, overcoming the great issues of an open thoracic surgery and using an endovascular strategy. The research in this field is oriented to find the best geometrical pattern, for example deciding if the Valsalva sinuses are fundamental, in accordance with the adopted aortic valve. One of the last company solutions is the Mitroflow Valsalva Conduit developed by Sorin in 2013, that coupled the Sorin's Mitroflow aortic pericardial heart valve with a Mitroflow graft (*fig.1.11*).

Fig.1.11 Mitroflow Valsalva Conduit with mitroflow aortic valve, developed and commercialized by Sorin Spa. Introduced in the USA at the end of 2012 following FDA approval, the Mitroflow Valsalva Conduit has received CE mark and is commercially available in Europe from November 2013.

The aortic arch, plus the descending aorta, is prone to aneurysms and dissections more than other vessel tracts. These diseases are caused by the remarkable stresses at the wall, and the complex flow patterns that characterize the double curvature part of the aorta. In particular, an aneurysm forms as a bulge in a section of the aorta, mainly caused by an underlying weakness in the aortic wall. Indeed, a dissection is classified using two different systems (see *fig.1.12*) but could be described as a tear between two vessel layers, which both continue to carry blood. The American College of Cardiology has supported and supervised several studies about aortic aneurysms and dissections, and a brief overview of these phenomena, the risk factors and the management is illustrated in *fig.1.10*. Moreover, the dissection and the aneurysm could be linked together in a more complex disease, increasing the risk even more for the patient. In the last decades the surgeons found two main operative options to treat these anomalies. The surgical options are the endovascular and the open repair ways. The first is based upon a minimally invasive insertion of a stent graft inside the vessel, released using a proper catheter, and expanded *in situ* via high pressure balloon.

This solution is preferable in terms of impact on the body, but is not lacking in disadvantages, as reported in *Chapter 4*. The second alternative is based on a traditional open surgery with the replacement of the injured tract with a tube graft. The median sternotomy is a well know surgical procedure but presents some disadvantages, as it is highly invasive, and requires an external-body blood support machine. A sketch comparison of these techniques is shown in *fig.1.13* (Isselbacher, 2005).

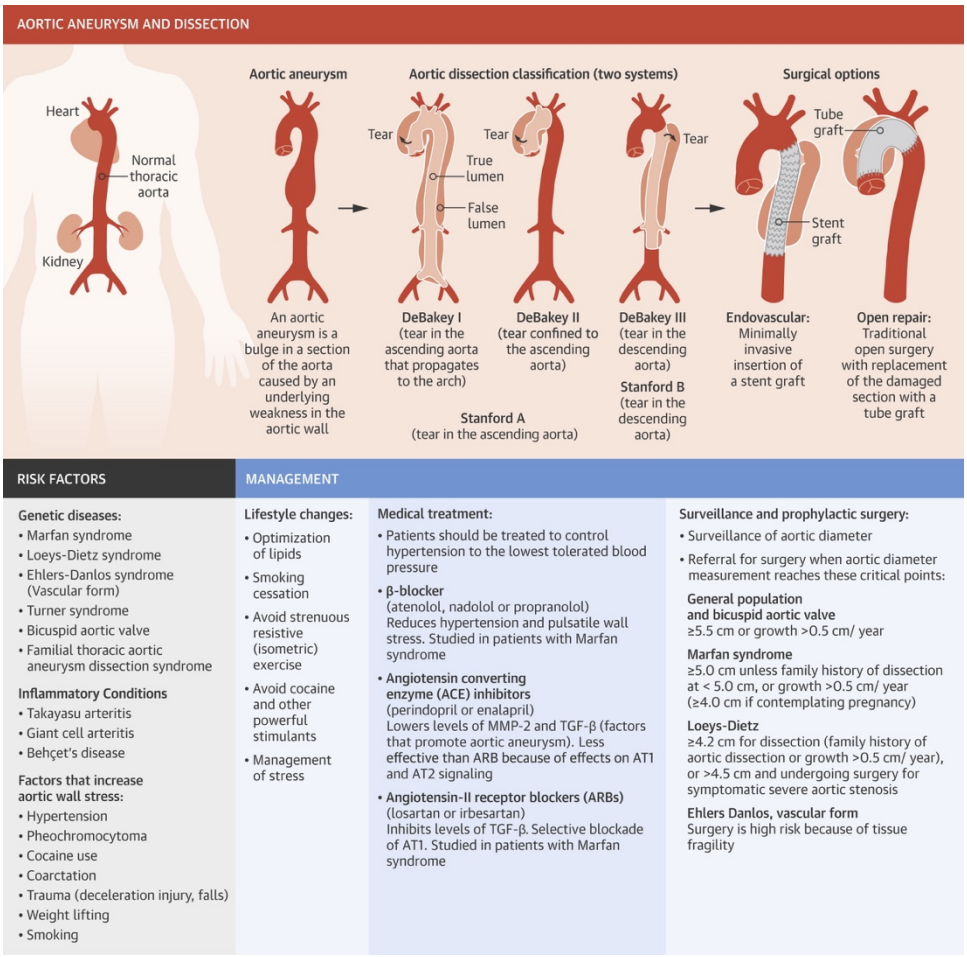

Fig.1.12 American College of Cardiology guidance for aortic and aneurysms classification.

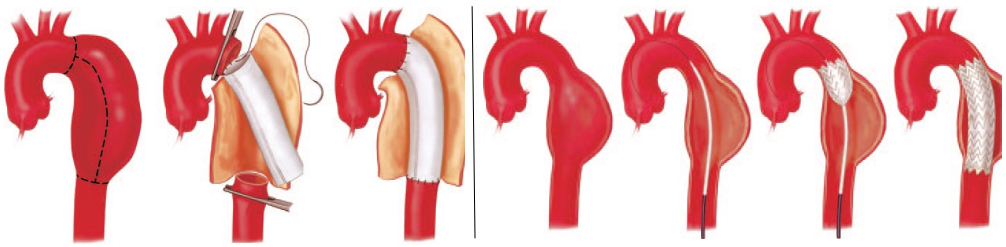

Fig.1.13 *Left*: repair sequence of a descending thoracic aortic aneurysm. *Right*: minimally invasive repair sequence of a descending thoracic aortic aneurysm using a transluminally placed endovascular stent-graft (Isselbacher, 2005).

1.3 Pulse duplicators: a simulation of the nature

The previous sections explained the characteristics of the aortic district and gave some ideas about the prosthetic solutions developed in the last few years to cure the diseases of the valve, root and aortic arch. The design, development, test and commercialization of all these prosthetic devices is impossible without continued research in optimization of materials, geometry and flow dynamics of the devices. To do that, different workbenches were built and commercialized. These devices are named mock loops (ML) or pulse duplicators (PD), starting from the idea of replicating the human circulation in terms of pressure and velocity fields through a hydro-mechanical machine. The main features have to be the pulsatile nature of the flow, following the physiological pressure trends in different areas, and a correct stroke volume and cardiac output, allowing the variation of the main hemodynamic parameters. These workbenches are normally made up with rigid and elastic tubes, chambers, air tanks, taps and silicone parts. From the '80s, the international regulations for the commercialization of these devices (UNI EN ISO 5840, last update in 2009, and FDA Draft Guidance for Industry and FDA Staff Heart Valves - Investigational Device Exemption (IDE) and Premarket Approval (PMA) Applications, last update in 2010) started to insert specific sections about *in vitro* tests and minimum performance requirements.

1.3.1 First mock loops

Cornhill designed one of the first examples of mock loops in the late seventies (Cornhill et al., 1977). The system used a deformable silicone sack in a pressurised chamber, acting as a left ventricle. The power driver was an air pump, able to reproduce the physiological conditions to test artificial prosthetic valves. The system was unable to correctly simulate the atrial systole.

Reul provided a second example in 1974, and realized a flexible tubes system to simulate the flow in the aorta and inside its branches. In particular, he developed a specific chamber to host the tubes system, in which it was possible to control the compliance of the aorta and derivations.

Scotten, in 1979, was the first that designed a PD able to evaluate both the mitral and the aortic valve performance. The ventricle was put in a sealed chamber, into which the fluid was injected by a pump. The circuit had several chambers and compliance systems, a deformable tract that simulated the aorta, and taps to replicate the vessels' resistances. Scotten also understood the importance allowing optical access to the system and so he realized the ML with transparent polymeric materials.

Rosenborg, in 1981, designed a specific hydraulic system able to connect and test the ventricular assist devices (VAD).

Verdonck, in 1992, developed a complex system to specifically test the right heart valves, with two pulmonary veins and a tank to simulate the lungs.

There are two independent systems to regulate the internal and external pressure of the ML tubes.

Probably one of the most used and known “research-made” PD was designed, developed and also commercialized by the University of Sheffield, during the ‘90s. It is known as Sheffield Pulse Duplicator (SPD), and it is composed of a hydraulic loop, made with plexiglass chambers, a glass aortic root and a servo-motor to control the flow and pressure fields inside the ML (*fig.1.12*) (AA.VV., 1989). In particular, the SPD was able to test all models of mechanical or stented tissue heart valves. It provides two test positions: aortic and mitral. A choice of aortic test sections, in four different sizes, enables the full range of valves to be accommodated in an appropriate model aorta. Various blood analogues can be used as the working fluid: saline solution or a saline and glycerol mix. Valve action may be photographed or filmed during a test, and access is provided for Laser Doppler anemometry and flow visualisation studies. The system is designed to perform pulsatile hydrodynamic testing of prosthetic heart valves following the requirements of ISO 5840:1989 (E) ‘Cardiovascular Implants - Cardiac Valve Prostheses’ and also to draft standards ISO/WD 5840 ‘Cardiac Valves’, and CEN 285 WG3 ‘Non-active Surgical Implants. Part 1: Cardiac Valves’ (March 1994).

Looking at the mechanical parts (*fig.1.12*), a positive-displacement pump simulates left ventricular flow at a heart rate and cardiac output specified by the user. During simulated diastole fluid enters the mitral section from the mitral reservoir flowing through the mitral valve that is mounted in a chamber-to-chamber configuration. Pressure transducers are situated upstream and downstream of the valve, and a flow transducer monitors forward flow and regurgitation. Fluid leaving the mitral section enters the model ventricle from where, during simulated systole, flow is directed through the aortic valve. Pressure transducers are mounted upstream and downstream of the aortic valve. A model aorta with sinuses is situated downstream of the valve. In order to obtain a close match between this and the test valve over the full range of valve sizes available, four aortae of various sizes are provided. After the passage through a flow probe, the flow reaches the compliance chamber, and then the fixed and variable system resistance, to finally flow into the mitral reservoir, in which the mitral valve is housed.

1.3.2 ViVitro mock loop

This session is focused on a specific mock loop, the ViVitro PD, that is probably the most world-wide used heart model. Indeed, all the factories that produce and test cardiovascular prosthetic device use this system to assess the hydrodynamic performance of the valve. It seems important to give some details (but a specific application with it will be found in *Chapter 6*), because the HeR Lab Pulse Duplicator, that will be described in the next chapters (3-4), is intended to be a starting point for a first alternative to this system. The ViVitro Systems company was founded by David Walker, and Larry Scotten, in

the mid-1970s. Their initial challenge was to build test equipment to evaluate a heart valve developed in the Cardiac Development Lab at Victoria's Royal Jubilee Hospital. David and Larry's prototype was soon able to simulate valve positioning and physiological compliances accurately and repeatably. Further development resulted in the first commercial Pulse Duplicator in 1984. The actual system is composed of the ViVitro model of the left heart, the SuperPump, that allows the correct motion at the work solution, a flow measuring system with two electromagnetic flow meters, and several pressure transducers, all controlled and adjustable by the ViViTest data acquisition system (*fig. 1.13*). As with other mock loops, the ViVitro system simulates the function of the heart by generating pulsatile flow through prosthetic heart valves placed in the Model Left Heart. The Pulse Duplicator simulates physiological or other complex flow variations while allowing the user to vary the peripheral resistance and compliance of the system. Pressure ports and flow measuring locations allow for data to be collected from aortic or mitral sites. Transparent viewpoints allow multiple viewing angles of the valve including inflow and outflow. The work solution is moved by a linear motor with high precision (controlled by software via LVDT). The pulsatile system can provide a cardiac output from 2 to 12 l/min, with heart beats from 30 to 140 bpm, and a stroke volume up to 180 mL. The flow is injected in the ventricular chamber in which is hosted a silicone mock (that simulates the ventricle). Between the motor and the ventricle, a viscoelastic impedance adapter is inserted, which has the role of limiting the impulsivity of the fluid motion. Both the valve chambers can host prosthetic valve from 18 to 30 mm, and they have a dedicated compliance. Upstream from the valves, two probes of the electromagnetic flowmeters (Carolina Medical) are positioned. The ViViTest software control system allows the replication of physiological flow and pressure waves, which can be modified, collected, and analyzed. The software also allows the user to easily modify and customize the waveforms the pump follows. The ViVitro Pulse Duplicator System is used by the US Food and Drug Administration and is recognized by a number of other regulatory bodies worldwide including TÜV, BSI and the Chinese SFDA.

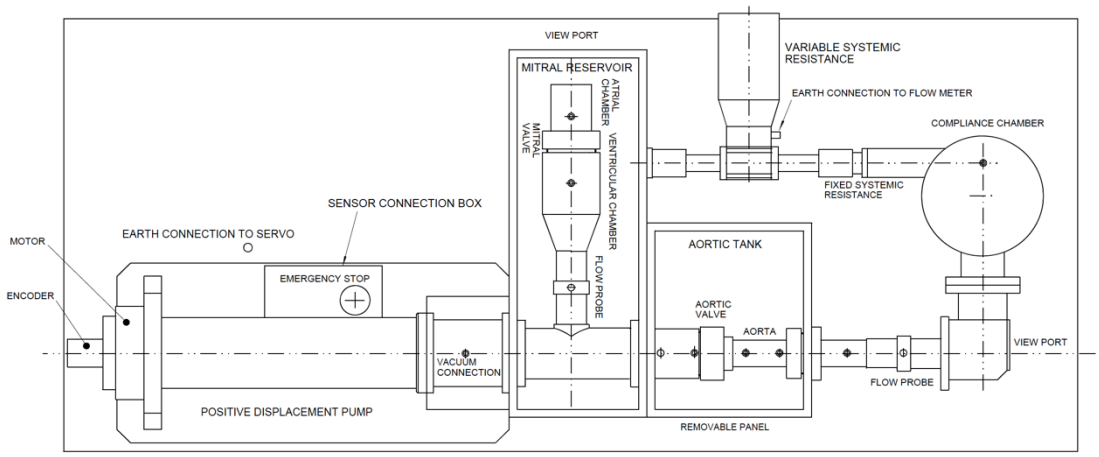

Fig.1.12 Sheffield mock loop engineer drawing (from SPD user manual).

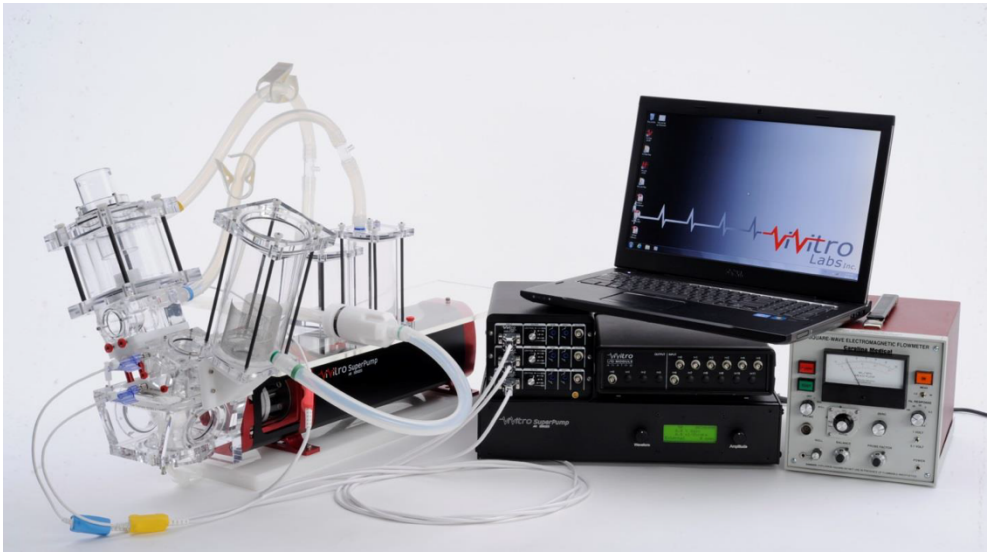

Fig.1.13 ViVitro pulse duplicator system, acquisition and control dock station and laptop, and the Carolina Medical Inc. electromagnetic flowmeter.

1.4 Chapter Bibliography

[1]. AA.VV. Heart valve hydrodynamic test apparatus. Service instruction manual, Dept. of Medical Physics and Clinical Engineering, Royal Halmshire Hospital, Sheffield, 1989.

[2]. J. E. Anderson, Grant's Atlas of Anatomy, (Williams and Wilkins, Baltimore), Seventh Edition, 1978.

[3]. B. J. Bellhouse, L. Talbot, J. Fluid Mech. 35 (1969): 721

[4]. Bellhouse, B. J. & Bellhouse, F. H. Mechanismn of Closure of the Aortic Valve. Nature 217, 86–87 (1968).

[5]. K. B. Chandran, B. Khalighi, C. J. Chen, H. L. Falsetti, T. L. Yearwood, L. Hiratzka, J. Thorac. Cardiovasc. Surg., 85(1983): 893.

[6]. K. B. Chandran, G. N. Cabell, B. Khalighi, C. J. Chen, J. Biomech., 17(1984): 609.

[7]. K. B. Chandran, J. Biomech. Eng. 115(1993): 611.

[8]. K. B. Chandran, B. Khalighi, C. J. Chen, J. Biomech., 18(1985): 763.

[9]. K. B. Chandran, B. Khalighi, C. J. Chen, J. Biomech., 18(1985): 773.

[10]. K. B. Chandran, J. Thorac. Cardiovasc. Surg., 89(1985): 743.

[11]. W. Ganong, “Fisiologia Medica”, Editore ’75, Roma, 2009.

[12]. F.S. Giddens, A.P. Yoganathan, Prosthetic cardiac valves, Cardiovascular Pathology, 1998.

[13]. Isselbacher Eric M. Thoracic and Abdominal Aortic Aneurysms. Circulation. 2005; 111:816-828.

[14]. S. W. Jacob, C. A. Francone, Structure and Function in Man, (W. B. Saunders Co., Third Edition, Philadelphia), 1974.

[15]. Kilner PJ, Yang GZ, Mohiaddin RH, et al. Helical and retrograde secondary flow patterns in the aortic arch studied by three-directional magnetic resonance velocity mapping,Circulation. 993;88(part I):2235.

[16]. B. Khalighi, K. B. Chandran, C.J. Chen, J. Biomech., 16(1983): 1003.

[17]. B. Khalighi, K. B. Chandran, C. J. Chen, J. Biomech., 16(1983): 1013.

[18]. K. J. Li, Arterial systems dynamics, New York University Press, New York, 1987.

[19]. H. Reul, N. Talukder, in Quantitative Cardiovascular Studies. Clinical and Research Applications of Engineering Principles, (N. H. C. Hwang, D. R. Gross, D. J. Patel (Eds), University Park Press), 1979, Chap. 12, pp. 527-564.

[20]. M. R. Roach, in Cardiovascular Flow Dynamics and Measurements, N. H. C. Hwang, N. A. Normann (Eds), University Park Press, Baltimore, (1977) Ch. 14.

[21]. C. M. Rodkiewicz, J. Biomech. 8(1975): 149.

[22]. A. T. Shipkowitz, Effects of secondary flow in the descending aorta on shear stress in downstream arteries, Ph.D. Dissertation, University of Iowa, 1995.

[23]. P. D. Stein, W. A. Munter, Circulation 44 (1971): 101.

[24]. T. L. Yearwood, Steady and pulsatile flow analysis in a model of the human aortic arch, Ph. D. Dissertation, Tulane University, 1979.

[25]. T. L. Yearwood, K. B. Chandran, J. Biomech. 13(1980): 1075.

[26]. L. Yearwood, K. B. Chandran, J. Biomech. 15(1982): 683.

[27]. Yoganathan AP, Hopmeyer J, Heinrich R S, Biomedical Engineering Handbook, Joseph D. Bronzino, ed. Boca Raton, FL. CRC Press; 1995.

[28]. L. Waite, J. Fine, Applied Biofluid Mechanics, McGraw-Hill, 2007, DOI: 10.1036/0071472177.

[29]. Weyman AE. Principles and Practices of Echocardiography. Philadelphia, PA. Lea & Febiger; 1994.

[30]. J. T. M. Wright, L. J. Temple, I. Mech. E., 6(1977): 31.

Chapter 2

The 1D numerical model for workbench preliminarily design

2.1 Introduction

The thought at the base of the pulse duplicator realization was the production of a new experimental research reference for clinicians and industries, useful for start a profitable technologies transfer upon these different organisations. In this prospective the mock loop is the first step of the new born HeR Lab. One of the problems observed at the beginning of the project was the absence of engineer drawings, or a pre-sizing, of already developed mock loop systems in literature, except for the Sheffield mock loop (Barbaro et al., 1991). The starting idea was to not make a precise copy of an existent pulse duplicator, but realise a system that simulate the left part of the heart and the human circulation, that could be easily modified following the research needs. For example, to study the changes due to the introduction of a compliant silicone vessel part instead of a rigid aortic root or creating bifurcations to investigate also the coronaries circulation.

Studying this kind of hydraulic circuits, we were aware that there are some “fixed points” in the project, as a linear pump with a bellow for the fluid handling, taps as local resistance, elastic tubes or air tanks for mimic the compliance. But the problem was: how big have to be the different chambers, which is the best diameter of the pipes to have the desired pressure fields, or the volume of the compliance chamber and the fluid-gas ratio? To provide a preliminary answer these questions a numerical strategy was adopted. In this chapter the mathematical approach chosen for a mechanical design and calculation of the pulse duplicator sizing is described. The decision of study the problem from a fluid dynamic point of view starts from the idea that the Windkessel models, already developed in literature, are not sufficient physically based and use an electric parallelism that sometimes is trivial (Westerhof et al., 1971).

The mathematical strategy follows the development of a 1D model with concentrate parameters, able to provide pressure waves and flow behaviour for

a specific hydraulic system, in which the boundary flow conditions are fixed and the solution is computed using an equations integration scheme (Defina, 2010). Implementation of the code was performed using MatLab (MathWorks®). The discharge of the fluid is considered unsteady and periodic, with a fixed period, and the flow in pipes is in pressure, to have a closer condition to the physiological one.

The 1D is clearly a strong simplification of the reality but, at this stage, the description of the flow behaviour won't to be detailed, but provides only a global design guidance. To do that the model should not be too complex due to mathematical heavy treatise and computational cost.

2.1.1 Unsteady flow in pipes

The fluid motion for in-pressure conduits is normally studied using the monodimensional equations system (Ghetti):

$$\frac{\partial E}{\partial s} = -\beta \frac{1}{g} \frac{\partial v}{\partial t} - j$$

$$\frac{\partial (\rho Q)}{\partial s} + \frac{\partial (\rho A)}{\partial t} = 0$$

in witch *E* is the energy for fluid weight unit, *j* is the dissipation energy for length unit along the path *s*, *v* is the velocity, *Q* is the discharge, *A* the transversal area section, ρ the fluid density, *g* the acceleration gravity, *s* the curvilinear abscissa, β the Coriolis coefficient (assumption equal to 1) and *t* the time. This system contains itself already a hypothesis: inside the *E* term, the effects of the spatial variation of the fluid density are neglected. In the general case the variables are: *p*, *v*, the density and the area of the transversal section. These quantities are general function of space and time. So the system is not close and some constitutive equations must to be used. In particular, a barotropic motion, that is $\rho = \rho(p)$, and an elastic deformation of pipes, $A = A(p)$, could be imposed, following an "elastic treatise". Usually is possible to adopt, with good approximation, the fluid density as constant in time and space, and also the transverse area section constant in time, adopting an "inelastic treatise". Following the inelastic view the unknown variables become the pressure and the velocity (time and space functions), and the up-script second equation could be rewrite as:

$$\frac{\partial Q}{\partial s} = 0$$

2.2 Theoretical Scheme

2.1.1 1D Geometrical model

To better understand the adopted theoretical scheme is necessary to define a simplified geometrical model that comprises the main physical characteristics that have to be reproduced mathematically. *Fig.2.1* illustrates a sketch of the hydraulic loop. Following the arrows is possible to easy catch the fluid motion and the different circuit parts: the pump (P), the ventricular chamber (VC), the aortic valve (AV) –through it passes the ejection discharge Q_e–, compliance chamber (CC), concentrate resistances (R), atrial tank (AC) –that collect and released the outflow Q_o–, and mitral valve (MV).

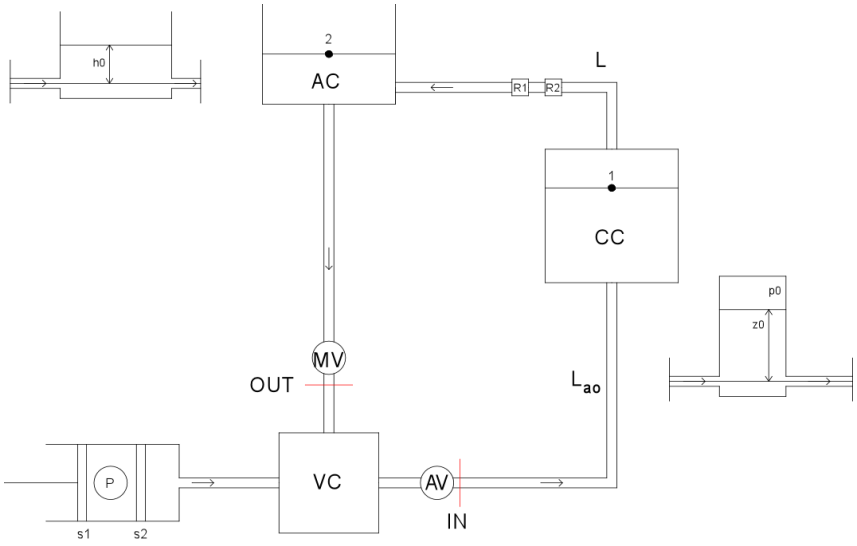

Fig.2.1 Hydraulic circuit plant: *P*) pump, *VC*) ventricular chamber, *AV*) aortic valve, *CC*) compliance chamber, *AC*) atrial chamber, *MV*) mitral valve, *IN* &) section of model flow inlet and outlet, respectively.

Using this sketch, and the linearization of the part from CC and OUT, is possible to easily set up the adopted mathematical scheme. In particular, *fig.2.2*, concentrates on the behaviour from Q_e (ejection flow) and Q_o (outflow in diastole), reporting the same nomenclature as before. A spatial integration of the motion equation between sections *1* and *2*, neglecting the inertia and dissipative terms in the airt tank and in the atrial chamber, gives:

$$E_2 - E_1 = -\beta \frac{L}{g} \frac{\partial v}{\partial t} - jL - \Delta E_c$$

where, *L* is the pipes length between CC and SA, *v* the fluid velocity, *j* the energy dissipation for each space unit, and ΔE_c the generic concentrated

dissipation inserted into the system. The *jL* term depends on the flow discharge, following:

$$jL = \alpha v|v|$$

where, α normally is a function of the geometry and roughness of the pipe, of the viscosity, and velocity. The most common formula adopted in practice to expresses the parameter is:

$$\alpha = \frac{fL}{d}\frac{1}{2g}$$

with *d* the tube diameter, where the drop is computed. The energy drops, due by concentrated resistance (measured in terms of hydraulic height), are normally expressed by:

$$\Delta E_c = r\frac{V^2}{2g}$$

where, *V* is the mean velocity in a reference section and *r* a parameter that is a function of the geometry.

Take as reference the initial section in *fig.2.2*, and neglected the kinetic load in the air tank: $E_1 = z(t) + \frac{p(t)}{\gamma}$, with *p* the pressure inside the air tank and $E_2 = h(t)$. In these hypothesis is possible to rewrite the equation as:

$$h(t) - \left(z(t) + \frac{p(t)}{\gamma}\right) = -\beta\frac{L}{g}\frac{\partial v}{\partial t} - jL - \Delta E_c$$

this, has to be associated with the continuity equation at the node between the CC and the AC.

$$Q_e = vA + v_cA_c \qquad\qquad Q_o = vA + v_sA_s$$

Here, *A* is the section area of the pipe, A_c the section area of the compliance, A_s the section area of the tank, v_c the velocity of the fluid inside the air tank, v_s the velocity inside the tank, Q_e the ejection flow and Q_o the outgoing flow from the tank (SA). Using $v_c = dz/dt$ and $v_s = dh/dt$ we have:

$$Q_e = vA + \frac{dz}{dt}A_c \qquad\qquad Q_o = vA - \frac{dh}{dt}A_s$$

To close the problem another equation is needed. Is possible to include a relation that describes the thermodynamic transformation undergo to the gas inside the compliance. In general it will be a politropic transformation as:

$$P_0^*U_0^k = P^*U^k$$

where, P^* and U are the absolute pressure and the air volume in the compliance at a generic instant, instead P_0^* e U_0^* are referred to the initial instant. K for air varies from 1 to 1.4. Using z_m as the highest quota of the compliance:

$$(P_0 + P_{atm})A_c(z_m - z_0)^k = (P + P_{atm})A_c(z_m - z)^k$$

where, p_{atm} is the atmospheric pressure and z_0 the initial fluid level inside the compliance.

Known the flow discharge in time (Q_e and Q_o), the system composed by the up-script equations could be solved, giving the pressures and levels of the work solution in function of time. It also provides the flow discharge along the pipe between the chambers. Before compute the solution of the problem is better to add other information and expand the system, including the aortic valve behavior.

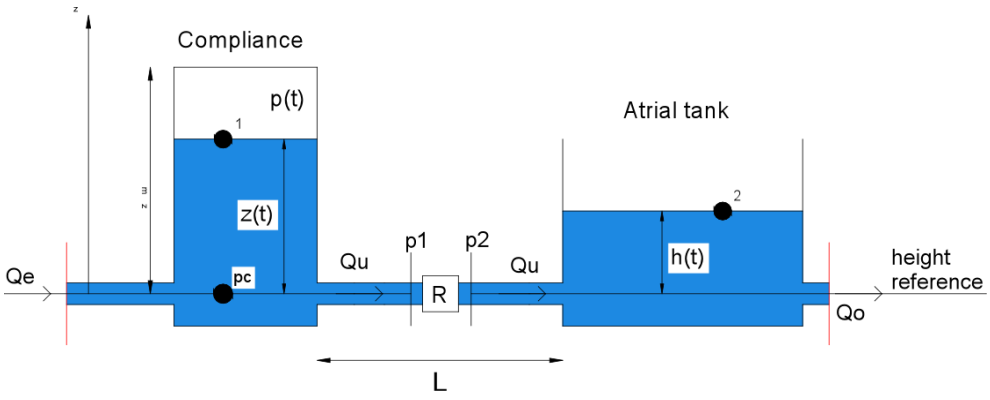

Fig.2.2 Linearized scheme with quotes of the system, from the compliance chamber to the outlet section after the atrial tank.

2.2.2 Transvalvular pressure drop

The importance of introduce the valve dynamic in the mathematical description is relevant, so a model of the pressure drop across the valve was developed, using the literature studies (Garcia et al., 2000, Fiore et al., 2002; Garcia et al., 2005) and adding some information. To focus the valve behaviour is necessary to refer to a simplified geometrical model. In *fig.2.3* is illustrated the adopted scheme, in which the ventricular chamber is identified as a portion of pipe at the left side of the orifice. The aortic valve is designed as a rigid circle orifice with a specific geometrical area that can varying in time, and the aortic root as rigid straight portion of pipe that connects the valve to the compliance chamber. From the fluid dynamic point of view, the valve imposed a contraction of the jet, a *vena contracta* (*vc*) section located just downstream the orifice, where the velocity is highest. After that, the jet reattaches the wall,

and the decreased velocity (re)become equal to V_1. In the outlet region a recirculation flow is present, so a dispersion of energy has to be computed, following the rules of submerged jets. In particular, *fig.2.3* shows a theoretical comportment of the jet from the left ventricle outflow tract (*LVOT*, section 1), to the separation region and vortices formation (*vc* to 2), and the reattach of the jet to the walls. *Fig.2.4* illustrates the same behavior for a schematic situation, in which is possible to assume the jet profile as linear, and the two angles: α_u (upstream) and α_d (downstream) describe the main jet behavior.

The presence of the restricted orifice section acts on the flow cinematic following the continuity equation:

$$\frac{\partial(\rho Q)}{\partial s} + \frac{\partial(\rho A)}{\partial t} = 0$$

Where, *r* is the fluid density (kg/m^3), *Q* the flow discharge (m^3/s), *A* the transversal area of the jet (m^2), *s* the coordinate along the flow (m), and *t* the time (s). In the hypothesis of uncompressible flow and un-deformable pipe the equation reduces to:

$$Q = Cost(s)$$

The velocity and pressure behaviour along the jet path could be obtained from the generic equation of the energy balance between section *1* and the generic section *s*:

$$E_1 - E_s = \left(\frac{p_1}{\gamma} + h_1 + \alpha\frac{V_1^2}{2g}\right) - \left(\frac{p_s}{\gamma} + h_s + \alpha\frac{V_s^2}{2g}\right) = \frac{\beta}{g}\int_s^1 \frac{\partial V}{\partial t}\,ds + \Delta E_{1\to s}$$

Under the condition of a non-stationary flow, and using the hypothesis of uniform velocity profiles ($a = b = 1$), $h_1 = h_2$ (because the height difference is negligible), and $V_1 = V_2$ (because there are not branches in the considered pipe portion), the energy drop across the valve corresponds with the transvalvular pressure drop. In formula:

$$\left(\frac{\Delta P}{\gamma}\right)_{net} = \frac{1}{g}\int_2^1 \frac{\partial V}{\partial t}\,ds + \Delta E_{1\to 2}$$

The accelerated flow from *1* to *vc* allows to neglect the local energy losses phenomena. Instead, from *vc* to *2* the deceleration causes a vorticity region after the valve, so the energy lost from *1* to *2* is equal to the one lost from *vc* to *2*:

$$\Delta E_{1\to 2} = \Delta E_{vc\to 2} = \frac{p_{vc} - p_2}{\gamma} + \frac{V_{vc}^2 - V_2^2}{2g} - \frac{1}{g}\int_2^{vc} \frac{\partial V}{\partial t}\,ds$$

Appling the conservation of momentum along the axis *s*, at a specific volume of fluid (the rectangle *1* to *2*), and after easy mathematical passages result:

$$\Delta E_{vc\to 2} = \frac{(V_{vc} - V_2)^2}{2g}$$

This term can be substitutes in the expression of the pressure drop. With the hypothesis of *dA/dt ≠ 0* (and a jet geometry of a snub cone), using EAO = V_{vc} (effective orifice area) and A_1=A_2=A, considering the flow *Q* not function of *s* (*Q* = *Q(t)*), *L* the total length of the pipe -in particular, using the expression derived by Garcia for $\mathrm{L} = 2\pi\sqrt{A_s - EOA}$ (Garcia et al., 2005)-, is possible to obtain the complete expression of the transvalvular pressure drop across the valve:

$$\left(\frac{\Delta p}{\gamma}\right)_{net} = \frac{Q^2}{2gEOA^2}\left(1 - \frac{EOA}{A}\right)^2 + \frac{1}{g}\frac{dQ}{dt}\frac{2\pi}{\sqrt{EOA}}\sqrt{1 - \frac{EOA}{A}} - \frac{Q}{g}\frac{\pi}{EOA^{1.5}}\frac{1 - \sqrt{\frac{EOA}{A}}}{\sqrt{1 - \frac{EOA}{A}}}\frac{dEOA}{dt}$$

where, the first part is called *pure dissipative* term, the second is linked to the *temporal flow inertia* and the third to the *jet inertia*.

Now, there are all the theoretical ingredients to build up the model implementing a numerical scheme. Later will be analysed the model results to understand if a simplified 1D tool could provide a useful solution for a first sizing of the different mock loop parts.

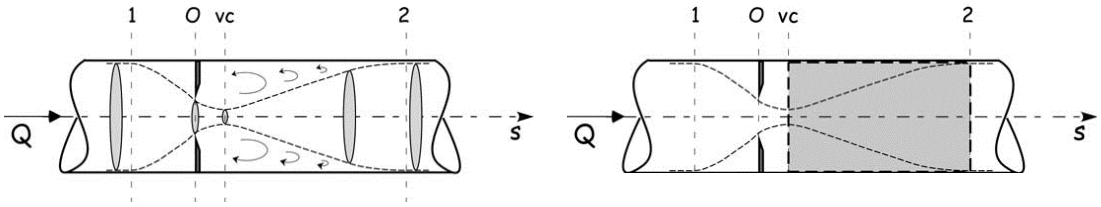

Fig.2.3 Left: sketch of the localised orifice along the conduit plus the recirculation regions. The grey box on the right identifies the area in which the conservation of momentum is applied.

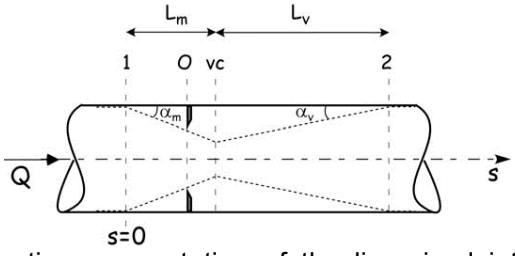

Fig.2.4 Schematic representation of the linearized jet, with the different angles for the cones.

2.3 Build up the numerical model

Following the theoretical description, the model will be divided in two parts that are also physically separated: the first goes from the compliance to the atrial chamber, the second goes from the ventricular chamber to the air tank. This last will be analysed using a reverse strategy, for mathematical reasons that will be explain later.

2.3.1 Compliance – Atrial chamber tract

Referring to *fig.2.2*, and to the expressions for pressure, velocity, flow discharge, and amount of fluid in tanks, these equations could be rewrite using an explicit integration method (Defina, 2010). Basically the time and the derivate has to be discretized, using incremental steps ($t = i\Delta t$, with $i = 1, 2, 3, \ldots n$). This strategy gave:

$$\frac{v^{i+1} - v^i}{\Delta t} = \frac{g}{L}\left[z + \frac{p}{\gamma} - h - jL - \Delta E_c\right]^i$$

$$\frac{z^{i+1} - z^i}{\Delta t} = \frac{Q_e^i - v^i A}{\Delta c}$$

$$\frac{h^{i+1} - h^i}{\Delta t} = \frac{v^i A - Q_r^i}{A_s}$$

and, computed z_i, is possible to obtain the pressure p from the formula:

$$p = (P_0 + P_{atm})(z_m - z_0)^k \frac{1}{(z_m - z)^k}$$

The system is then completely defined adding the initial conditions for the specific problem. The first is the discharge, which in systole passes through the initial section *in*, and in diastole through the final section, *out*. The flow shape derives from Grigioni (Barbaro et al., 1991; AA.VV., 1989), and is a typical volume in time curve for a physiologic case (*fig.2.5a*). The proposed model has a linear scheme (*fig.2.2*), so the flow is pumped at *in* and extract from *out*, as having two positive physical hydraulic pumps, following the imposed curve in *fig.2.5b*. In particular, the ratio between systole and diastole is fixed (33/100), but the entire cycle is variable, as the flow peak.

The pressure, tanks fluid levels and flow velocity in a quiet condition, were chosen as initial conditions for the model. They are: z_0 in compliance, p_0 in compliance, v_0 inside the pipe. The scheme needs also the definition of geometrical quantities as L and d, length and diameter of the pipes, and z_m, the tank height. To complete the model the continuous (jL) and concentrate (ΔE_c)

dissipation parameters has to be computed. The local dissipation is described by a tap -*R*- in *fig.2.2* and the mathematical relation (*r*) was already present in the previous paragraph. The iterative scheme tries to describe the obstruction via an incremental step definition. The initial condition is the quiet of the fluid, so the value of resistance has to be the one that guarantee other initial conditions, as for example levels of fluid in the tanks and pressure in compliance. The dissipation provide non zero values only if there is a flow through the tap, so a first step discharge Q_{res0} is imposed. At initial instant the relation becomes:

$$r_0 = \frac{\left(\frac{P_0}{\gamma} + z_0 - h_0\right) 2gA^2}{Q_{res0}^2}$$

where, all quantities have been already described (*A* is the area of the pipe). The flow through the resistance is updated at each step following the relation:

$$Q_{res}^{i+1} = v_{mean}^{i} A$$

Where, v_{mean} is the mean velocity in the period, computed using the velocity vector at the previous iteration. Using these quantities is possible to update the resistance coefficient, keeping constant the pressure drop across the tap.

$$r^{i+1} = \frac{\left(\frac{P_0}{\gamma} + z_0 - h_0\right) 2gA^2}{\left(Q_{res}^{i+1}\right)^2}$$

To obtain a convergence of the model is fundamental the presence of this dissipation coefficient. Indeed, the mathematical model becomes easily unstable in dependence of little variations of the parameters. To avoid divergence behaviour of the solution is important to introduce this dissipation factor, that helps to reach a stable condition after an initial transient phase.

2.3.2 Ventricular chamber – Compliance tract

The circuit part going from the ventricular chamber to the compliance (*fig.2.1*) could be linearized following the strategy already adopted before (*fig.2.6*). In this case the main fluid dynamic issue is the presence of a restriction along the pipe (aortic valve), that changes its behaviour in time. To describe the transvalvular pressure drop the non-stationary complete model described in 2.2.1 was adopted.

In particular, given the numerical solution for the pressure trend at the base of the air tank (p_c), through the integration implemented in 2.3.1, and applying the energy balance equation, is possible to obtain the pressure downstream

the aortic valve. Following this thought, the pressure upstream the valve is achievable using the non-stationary model, obtaining the flow in the outflow tract of the ventricular chamber. The idea is to take advantage of the pressure computed at a middle point in the circuit, to calculate the numerical solution using a different scheme in the two directions. So, backwards from compliance, the pressure in aortic root area could be obtained as:

$$\frac{pAO}{\gamma} = \frac{p_1}{\gamma} + h_1 + \frac{\beta}{g}\frac{\partial v}{\partial t}L + jL - \frac{Q^2}{2gA^2}$$

Implementing this formula using a iterative scheme, and imposed a specific behaviour for terms *Q(t)* and *EOA(t)*, the pressure upstream the valve (p_{LV}) is immediately available:

$$\frac{pLV}{\gamma} = \frac{pAO}{\gamma} + \left(\frac{\Delta p}{\gamma}\right)_{net}$$

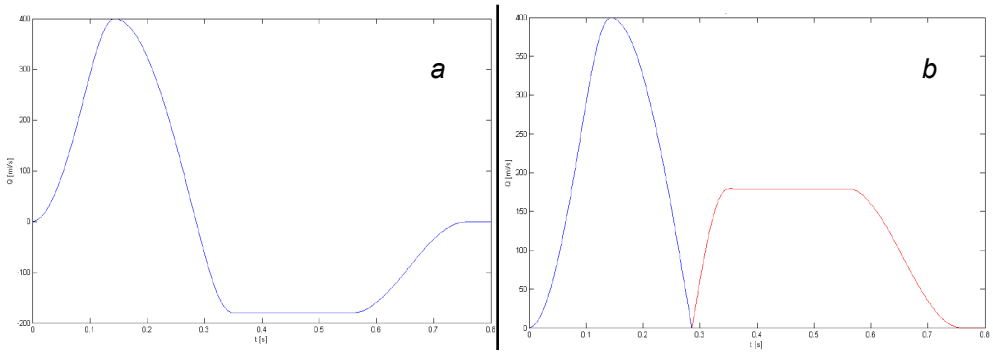

Fig.2.5 *a)* Typical physiological flow in the left ventricle, *b)* Adopted Q_e (blue) and Q_o (red) in the mathematical model.

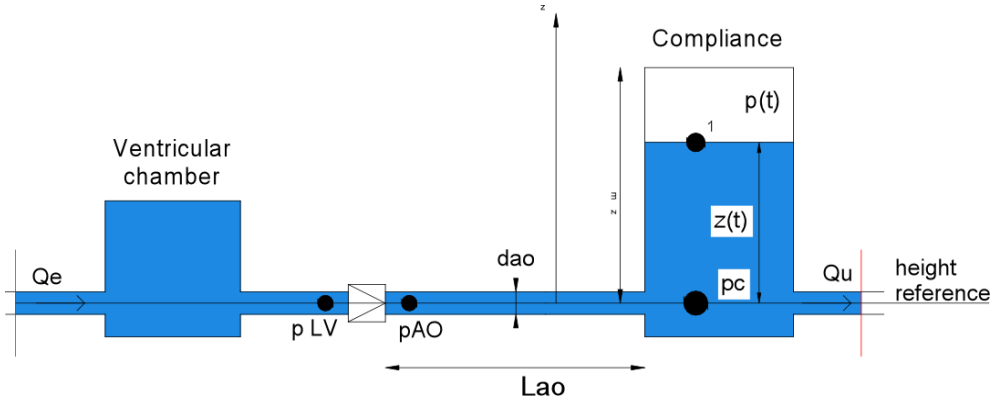

Fig.2.6 Linearized part from the ventricular chamber to the compliance chamber.

2.4 Preliminary sizing of the pulse duplicator

This paragraph describes a sensitivity analysis performed using the 1D numerical model. The idea is to take advantage on the different output obtaining with different geometric input configurations, and decide which is better for a physic realization and implementation of the workbench. The best configuration is the one that provides the closer solution, in terms of pressure and flow, with respect to a physiological behaviour.

2.4.1 Compliance and atrial chamber design

The compliance chamber was designed as a rectangular air tank (*fig.2.7*), and the geometric variations imposed on it in the different tests are:

Test	**(a)**	**(b)**	**(c)**
Side base: ***b*** [cm]	20	20	20
Compliance height: ***a*** [cm]	35	45	25
Initial level: z_0 [cm]	32.8	42.8	22.8
Air pressure: p_0 [mmHg]	75	68	82.5

Table 2.1: Geometric variation for compliance chamber.

Here the idea is to maintain constant the air volume inside the tank. The air pressure is determined using a energy relation, suffered by the current flowing through the resistance

$$p_0 = \gamma \Delta p_{res} - \gamma z_0 + \gamma h_0$$

where, Δp_{res} is the pressure drop across the tap, keep constant during the cycles. So, greater is the level of fluid in the compliance, lesser has to be the gas pressure in the initial condition. As is shown in *fig.2.8a*, the geometry variation has no effect on the pressure registered inside the tank, instead of a variation on the air volume entrapped inside the compliance (*fig.2.8b*). The values of the showed behavior were obtained for little variation of the gas volume (with a fixed geometry):

Test	**(a)**	**(b)**	**(c)**
Side base: ***b*** [cm]	20	20	20
Compliance height: ***a*** [cm]	35	35	35
Initial level: z_0 [cm]	32.8	31	33.5
Air pressure: p_0 [mmHg]	75	76.3	74.4

Table 2.2: Pressure variation for compliance chamber using a specific geometric configuration (b).

Fig.2.8b shows a higher impulsive output, generated when the system come closer to a rigid configuration (i.e. the volume inside the compliance is smaller). Instead, more elastic solution is provided when a higher volume is available, and also the pressure range is reduced.

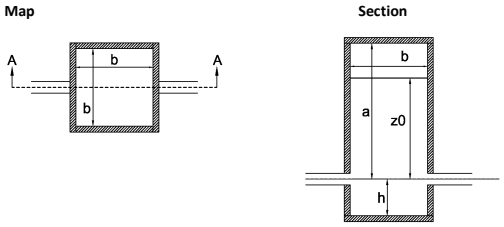

Fig.2.7 Example of the typical engineer drawing with references, in particular related to compliance chamber.

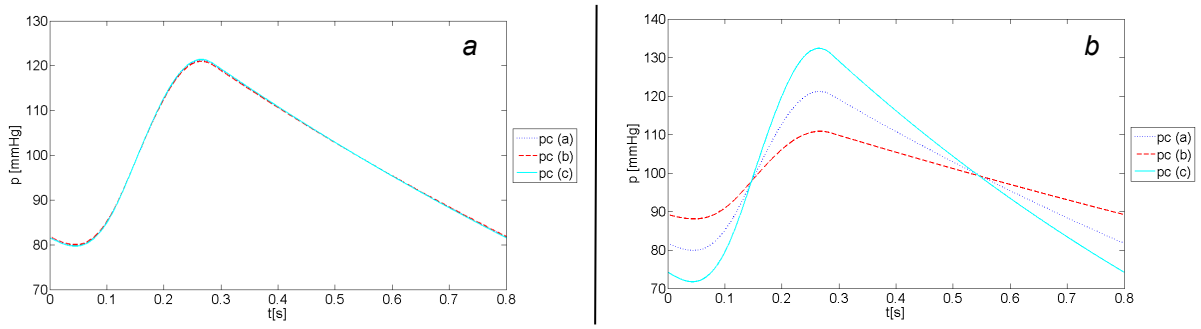

Fig.2.8 *a)* Compliance fluid pressure curves for a geometric configuration (see Table 2.1) and *b)* compliance fluid pressure curves in variation of the gas pressure (following Table 2.2).

The different geometric quantities described were changed since the achievement of a comfortable set up of the model. The related optimal parameters are here reported, and adopted as first sizing for the pulse duplicator realization.

Optimal geometric parameters:

- L_{ao} = 0.5 m (length of the pipe before the compliance)
- D_{ao} = 0.03 m (diameter of the pipe)
- d_c = 0.2 m (base side of the square compliance)
- z_0 = 0.328 m (liquid level in the compliance at time = 0 s)
- d_s = 0.4 m (base side of the square atrial chamber)
- h_0 = 0.086 m (liquid level, from the reference)
- L = 1 m (conduit from compliance to atrial chamber)
- d_L = 0.03 m (diameter of L)

In the initial step of the linear pump displacement, the conditions are:

- $z = z_0$
- $v = 0$ m/s
- $p_0 = 75$ mmHg

The boundary values are related to flow discharge values:

- $Q_p = 65*10^{-6}$ m^3/s (mean stroke volume)
- $Q_{res0} = \max(Q_e)/3$
- $T = 0.8$ s

The flow shape was already showed in *fig.2.5*. Other references are: g = 9810 N/m^3, p_{atm} = 101325 Pa, f = 0.026 (resistance function for the continuous losses from Moody diagram), g = 9.81 m/s^2. The pressure curves and velocity trend remain close in terms of shape with the presented above.

As last observation, the concentrate resistance coefficient trend is reported, in *fig.2.9*. Could be interesting to observe how the system, after an initial phase, become stable and the value of the resistance converge after $n \approx 50$ cycles. This information provides an idea of the system inertia because, also in a realistic case, using this settings a stable solution will probably reached after an adequate number of iterations, and not instantaneously.

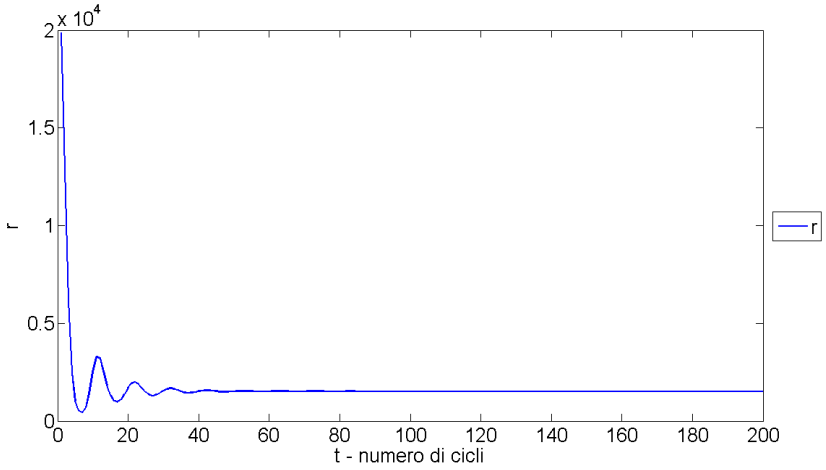

Fig.2.9 Behaviour of the resistance coefficient *r* along the cycles.

2.4.2 Pressure upstream and downstream the valve

The analysis in this case considers the variation of the length and diameter of the aortic tract. These are the distance between the aortic valve and the compliance, and the diameter of the pipe. As shows in *fig.2.10*, fixed the diameter of the conduit, the extension of the tract determines an increase in the pressure peaks, both positive and negative. Instead, keeping constant the

length, a bigger diameter has an opposite effect on the pressure behaviour. These possibilities are illustrated in *fig.2.10a-b*.

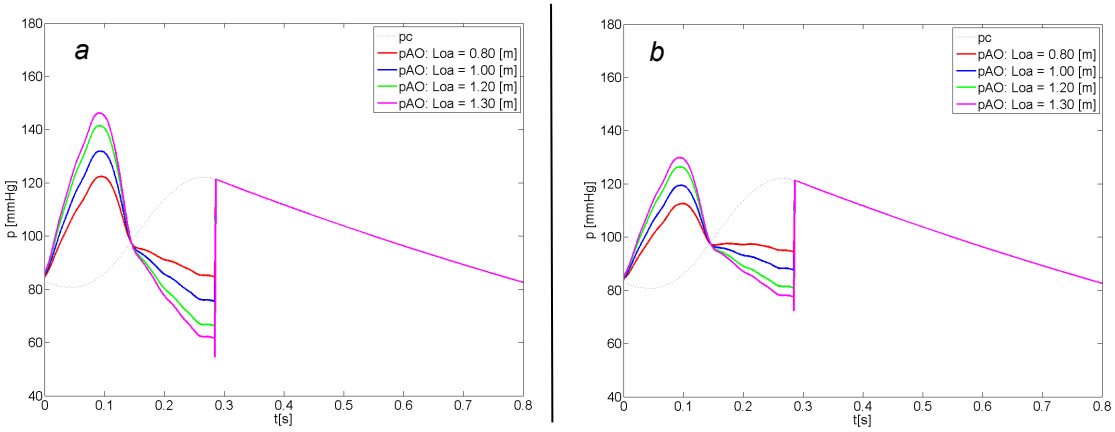

Fig.2.10 Compliance and aortic pressure curves for different pipe lengths and pipe diameter of 30 mm *(a)* and 35 mm *(b)*.

Computed the pressure downstream the valve, the upstream behaviour is obtained via integration scheme. Here the transvalvular pressure drop model plays an important role, with the diameter of the orifice and the value of the jet area in time. The maximum value of the jet area was computed using a typical fluid dynamic approach (Ghetti), in which different contraction coefficient (C_c) are adopted to determine the area of a jet passing through a rigid orifice. For example using a orifice diameter of 27 mm the C_c is 0.861, where 1 is the whole jet (vc_{area} = GOA·C_c). Using the obtained area as the maximum EOA achievable, a specific shape of *EOA(t)* was developed, following literature observation (Arsenault et al., 1998; Handke et al., 2003) (*fig.2.11*).

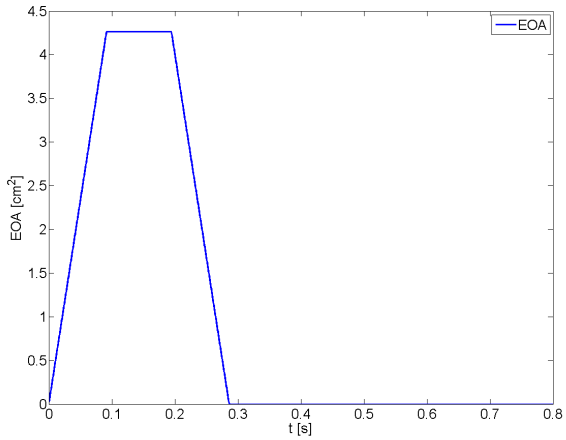

Fig.2.11 *EOA(t)* along the entire cardiac cycle computed using a 27 mm aortic valve.

Now there are all the ingredients (p_{AO}, *Q(t), EOA(t)*) to compute the pressure upstream the aortic valve. *Fig.2.12* illustrates the variation experienced by p_{LV} for a variation of the valve diameter. As expected, a smaller valve introduces a higher dispersion of energy in the flow, and a bigger pressure drop.

All these information are provided for the positive part of the flow discharge, for the ejection phase. When the valve close the ventricular pressure goes directly to the initial value around zero, and the aortic pressure become close to pressure inside the compliance chamber.

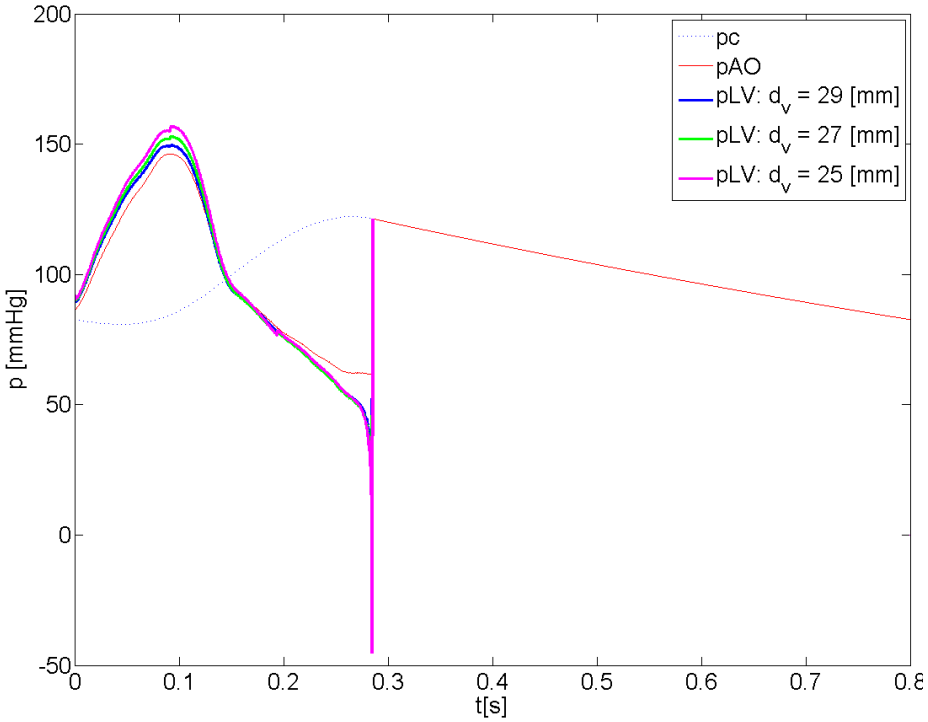

Fig.2.11 Detailed p_{LV} for different aortic valve sizes.

2.4.3 Introduction of the closing volume

A perfect and instantaneously closure of the aortic valve was an adopted condition, until now. In the reality, the last part of the ejection phase expresses a backward volume, due to the physical and geometric characteristics of the aortic valve and root. We tried to simulate this closing volume using in-vitro test data and extracting typical values for the closing period and for the maximum peak of backward flow. The adopted values were: 4% of *T* (*T* = total cycle) for the duration of the phenomena and 10% of Q_{max} for the maximum negative flow peak (*fig.2.13*).

The parameters kept as optimal for this tract were:

- L_3 = 1.3 m (distance between valve and compliance)
- d_3 = 0.03 m (pipe diameter in L_3)

- d_v = 0.027 m (aortic valve diameter)

In these conditions *fig.2.14* illustrates the impact of this new flow shape on the pressure trends (p_{AO} and p_{LV}). Seems that now the behaviour of the pressure is closer to the physiological one especially near the closure, where the dicrotic notch is observed. This characteristic pressure recovery comportment is probably due to the obstacle encountered by the backflow in pass the semi-closed valve.

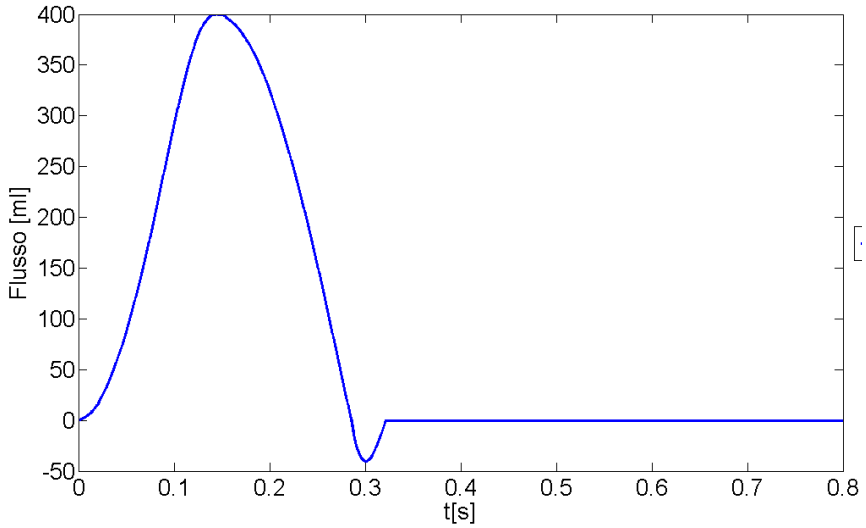

Fig.2.13 Example of the implemented discharge curve with backflow.

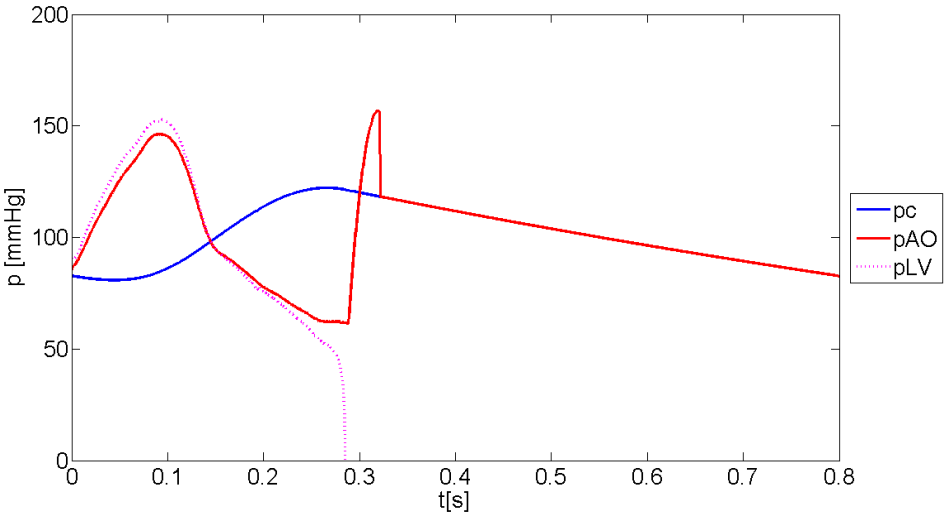

Fig.2.14 Pressure behaviour for aortic, ventricular and compliance districts, with the adoption of a backflow in the discharge curve.

2.5 Study abstract

In this chapter the adopted mathematical model for a first sizing of the pulse duplicator was described. A new 1D strategy, in the cardiovascular fluid dynamic scenario, was developed to study the pressure and velocity behaviour inside a hydraulic circuit that simulates a Sheffield mock loop. A first characterization of the fluid dynamic equations for the different parts was described, and a translation into an iterative scheme was performed.

In particular, the circuit was divided in two segments starting from the inflow section of the compliance chamber. One develops downstream, since the outflow section of the atrial chamber, and one upstream to the ventricular chamber passing through the aortic valve. For both these schemes, the velocity, pressure trends and liquid levels were computed. A comparative criterion was adopted to find the optimal parameters and a sensitivity analysis was performed varying the geometric characteristics of the model and the initial conditions of the flow, the pressure and the liquid levels (around physiological conditions).

In general, both for the part downstream and upstream the compliance chamber, the mathematical model was able to provide interesting and useful results that could help to better understand different phenomena of this particular kind of hydraulic circuit, that works in a cyclic non-stationary flow conditions.

The performance provided by the mathematical model allows also a first sizing of the main geometric parts of the pulse duplicator, that will used as a “base” for the consecutive physical development of the workbench.

2.6 Chapter bibliography

[1]. AA.VV. Heart valve hydrodynamic test apparatus. Service instruction manual, Dept. of Medical Physics and Clinical Engineering, Royal Halmshire Hospital, Sheffield, 1989.

[2]. Arsenault M., Masani N., Magni G., Yao J., Deras L., and Pandian N., Variation of Anatomic Valve Area During Ejection in Patients With Valvular Aortic Stenosis Evaluated by Two-dimensional Echocardiographic Planimetry: Comparison With Traditional Doppler Data. Journal of the American College of Cardiology, vol. 32, no. 7 (1998):1931–7.

[3]. Barbaro V., Daniele C., Grigioni M., Descrizione di un sistema a flusso pulsatile per la valutazione delle protesi cardiache valvolari. ISTISAN 91/7 (ISSN-0391-1675), Roma, 1991.

[4]. Defina A., Moto Vario Nelle Condotte, Alcuni Appunti. Università degli Studi di Padova, Dipartimento di Ingegneria Idraulica, Marittima, Ambientale e Geotecnica, (2010).

[5]. Dumesnil JG, Yoganathan AP. Theoretical and practical differences between the Gorlin formula and the continuity equation for calculating aortic and mitral valve areas. Am J Cardiol 1991;67:1268–72. 23.

[6]. Fiore G.B., Grigioni M., Daniele C., D'Avenio G., Barbaro V., and Fumero R., Hydraulic functional characterization of aortic mechanical heart valve prostheses through lumped-parameter modelling. Journal of Biomechanics 32, (2002), 1427-1432.

[7]. Garcia D., Pibarot P., Dumesnil J.G., Sakr F., and Durand L.G., Assessment of aortic valve stenosis severity: a new index based on the energy loss concept. Circulation, 22, (2000), pp. 765-771.

[8]. Garcia D., Pibarot P., Durand L.G., Analytical modeling of the instantaneous pressure gradient across the aortic valve. Journal of Biomechanics 38 (2005), 1303–1311.

[9]. Ghetti A., Idraulica. Edizioni Libreria Progetto, 1995, Padova, Italy.

[10]. Handke M., Jahnke C., Heinrichs G., Schlegel J., Vos C., Schmitt D., Bode C., and Geibel A., New Three-Dimensional Echocardiographic System Using Digital Radiofrequency Data—Visualization and Quantitative Analysis of Aortic Valve Dynamics With High Resolution: Methods, Feasibility, and Initial Clinical Experience. Circulation, 2003;(107):2876- 2879.

[11]. Susin F.M., Fluidodinamica per la Bioingegneria – Raccolta di Appunti delle Lezioni, Padova, (2010).

[12]. F. M. Susin, R. Toninato, Effects of aortic valve aperture dynamics on mathematical formulation of the instantaneous transvalvular pressure drop. *In preparation*.

[13]. P. D. Stein & W. A. Munter, New Functional Concept of Valvular Mechanics in Normal and Diseased Aortic Valves Circulation, 44, (1971): 101-108.

[14]. Westerhof N., Elzinga G., Sipkema P., An artificial arterial system for pumping hearts, J. Applied Physiology, n.31, 1971, pp. 776-781.

Chapter 3

HeR Lab Pulse Duplicator

3.1 First step for the HeR Lab

The PhD project has been based on the development of a mock loop device, from the first idea to the final implementation. This means not only design and project drawing but also the research of all the different components, correctly sized in function of their aim. The pulse duplicator is the first experimental tool implemented in the Healing Research Laboratory for Cardiovascular Studies (HeR Lab).

The chapter organization includes: a brief overview of the literature about pulse duplicator examples, then move to the HeR mock loop hardware parts, in which are described in detail all the adopted solution on the physical realization of the workbench. Here it is also insert a session with the incoming updates. The third part deals extensively on the software programs, developed ad hoc for the piston fluid handling, data acquisition, and post processing. Instead, the next chapter will be a first comparison in terms of global performances between HeR device, ViVitro Superpump and typical physiologic pressure and flow curves.

3.1.1 Brief literature overview and state of art

Seems important to recall the literature works that helped to guide the development of the workbench. Some were already cited in *Chapter 1,* are here reported the most influent for precision. In particular, the Sheffield pulse duplicator (AA.VV., 1989) is the adopted “base” for the HeR mock loop development. A detailed description of hydrodynamic measures performed with this workbench was given by Barbaro (Barbaro et al., 1991). Before, other interesting systems were developed, in particular Scotten and Reul derived the first functional examples of hydraulic circuit to test prosthetic devices in a non-stationary flow conditions (Scotten et al., 1979; Reul et al., 1974).

Innovative solutions in terms of hardware and software components were introduced by ViVitro, and Grigioni (Grigioni et al., 2003) performed several *in vitro* tests, enhancing the important benefits of some technical solutions. In this

sense the state of the art is represent by the ViVitro Superpump with viscoelastic impedance and other design solutions (double comlpiance), that allows great flexibility of measure but with high costs (about 120.000 Euro). The last literature works concentrates the attention on various issues: Hildebrand and Schleicher focused on bioreactor design (Hildebrand et al., 2003; Schleicher et al., 2010), Mouret and Tannè –Piebarot's research group– developed an atrio-ventricular system similar to the ViVitro (Mouret et al., 2000; Tannè et al., 2010), Timms –Fraser's research group–, Reddy and Yokoyama designed pulse duplicators able to test different kind of prosthetic cardiovascular devices (Timms et al., 2010; Reddy et al., 2010; Bazan et al., 2011; Yokoyama et al., 2010). A vertical mock loop was also developed to perform studies on the aortic district via an integrated approach (Toninato: http://tesi.cab.unipd.it/39527/; Querzoli et al., 2014; Fortini et al., 2015).

The here presented pulse duplicator falls into the category of systemic circulation simulation devices, with horizontal extension, as the Sheffield mock loop. It catches some solutions from the ViVitro, especially for the aortic section. But it also includes new solutions as the possibility to introduce a physiologic replica of the entire aortic root and arch. A constant attention has been placed on the realization of the system in according to the requirements requested by ISO5840:2009 and FDA guidance (ISO 5840, last update in 2009, and FDA Draft Guidance for Industry and FDA Staff Heart Valves – Investigational Device Exemption (IDE) and Premarket Approval (PMA) Applications, last update in 2010). Of course, also the derived mathematical model described in *Chapter 2* helped to better understand which parameters in the hydraulic circuit play important roles in the achievement of physiological curves, providing a first sizing of the parts. For example, thickness of ventricular chamber walls, and its dimension; best diameter and length of the tubes upstream and downstream the aortic valve, thickness of compliance chamber wall in relation to highest probably pressures, level of tap closure to ensure a correct medium aortic pressure, and extension of calm tank to interrupt the pulsatile of the flow.

3.1.2 A pulse duplicator view

The next disclosed system is a result of a step improvement strategy that had characterized the project along the three years. Intermediate configurations are reported in Di Micco and Bellio MS thesis (Di Micco: http://tesi.cab.unipd.it/46857/, Bellio: http://tesi.cab.unipd.it/47983/). Only the actual experimental configuration, that produces the best results in terms of hydrodynamic performances -in comparison with physiology curves and literature results- is here reported, to avoid confusion.

Fig.3.1 illustrates a bird's eye intuitive functional scheme of the workbench. The arrows describe the fluid direction, and the different parts are labelled to easily understand the subsystems functions. The work solution is handled by an electromagnetic linear motor, controlled via software by the operator.

Control and condition units provide the signals management to the system, also from the pulse duplicator sensors. The imposed position curve is transferred to the fluid via a metallic bellow, that pumps the fluid in both directions. An in-pressure ventricular chamber supplies the fluid in ejection and diastole, and it is connect with the aortic valve –passing through a flowmeter probe- and with the mitral district on the other side. The aortic district is characterised by a flowmeter chamber, a valve housing, the aortic compliance chamber and the aortic root. All these components are located inside the aortic chamber, that contains several pressure sensors. Following the scheme, the fluid flows through the compliance chamber, the systemic resistance and emerges into the atrial tank. After the calm tank, a pipe connects to the ventricular chamber via the atrial valve, closing the circuit.

The whole described apparatus is illustrated in *fig.3.2* and *fig.3.3* with a lateral and bird's eye view.

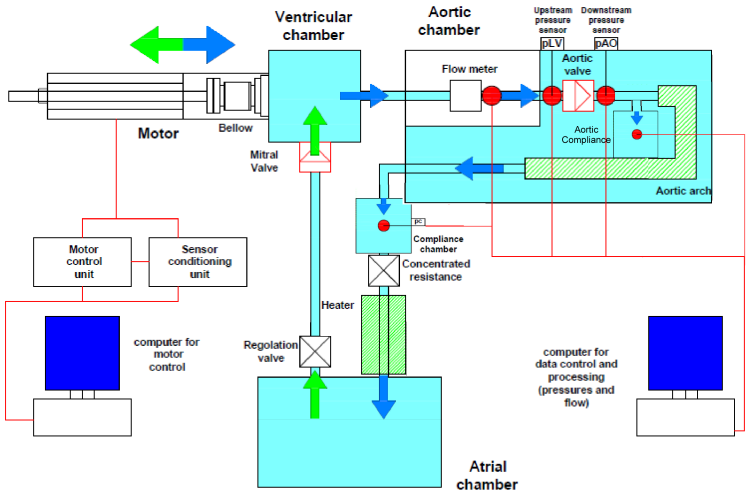

Fig.3.1 Functional scheme of the pulse duplicator.

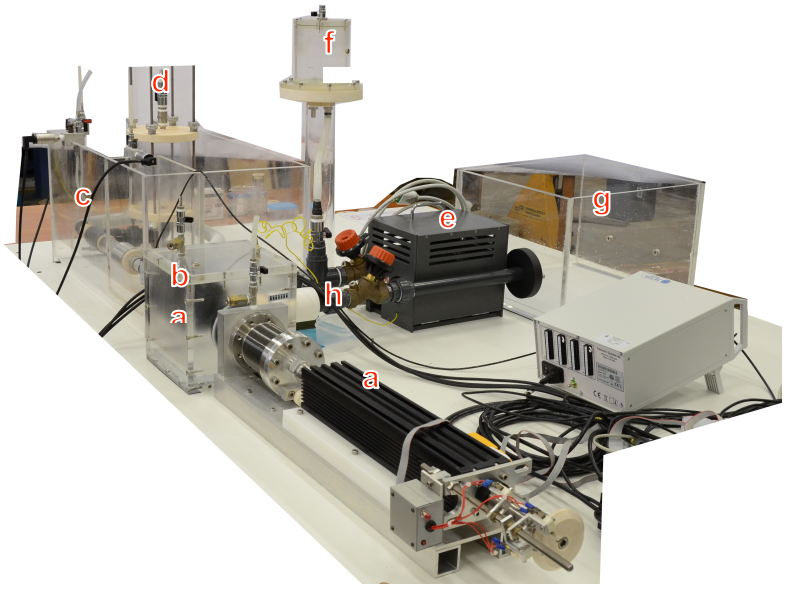

Fig.3.2 Her pulse duplicator lateral view: a) electromagnetic motor, b) ventricle chamber, c) aortic chamber, d) aortic compliance, e) heater, f) systemic compliance, g) atrial tank, h) resistance and mitral valve.

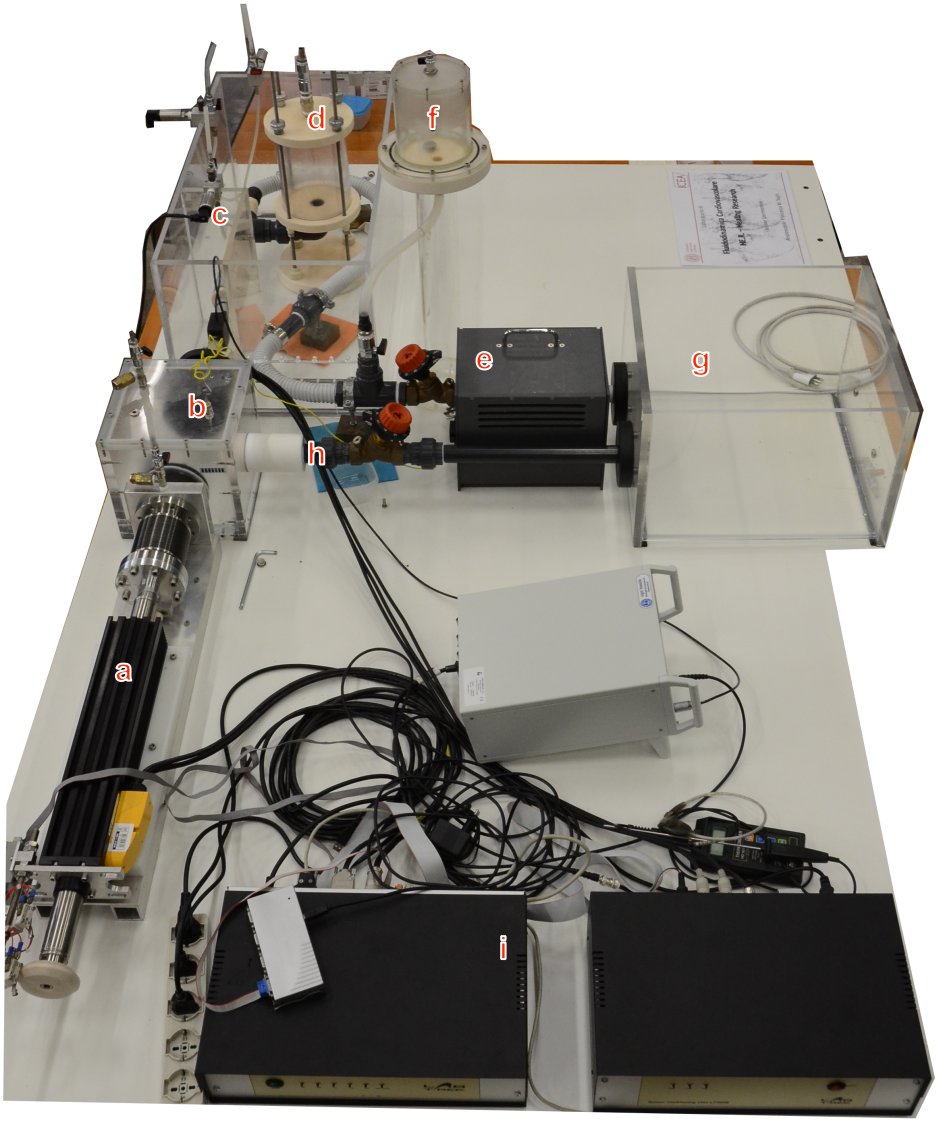

Fig.3.3 Pulse duplicator bird's eye view: a) electromagnetic motor, b) ventricle chamber, c) aortic chamber, d) aortic compliance, e) heater, f) systemic compliance, g) atrial tank, h) resistance and mitral valve.

3.2 Mechanical parts

3.2.1 Electromagnetic linear motor and bellow

The linear motor moves the fluid solution using a metallic bellow. The whole system works as a double direction pump, reproducing the left heart

contractile function. This device was chosen for the constructive characteristics: high thermic efficiency under load conditions, absence of gearwheels or parts subjected to wear and tear, ability to provide a constant force to the fluid inside a wide range of velocities.

The chosen electromagnetic engine is a Parker PRA3810S, illustrated in *fig.3.4*, and the current position is given by a variable tension imposed to the stator via software. The motor stator is fixed to an aluminium and Teflon frame, to avoid high vibrations and to reach the correct height of the movement axis. An engineer drawing is reported in *fig.3.5*, where the principal dimensions are showed. The main part is connected to the control unit via flexible cables, one for the energy supply and another for the position data transfer. A variable tension is transferred to the metallic bar that moves in both directions with a variable controllable velocity. Values of voltage, motion curve, and period of the cycle are imposed via software by the operator using a graphic interface. A LVDT sensor constantly monitors the current position. The PRA3810S provides, in absence of load and in environment temperature of 25°C, a peak force of 1860 N for 1 s, an absorbed current peak of 14.1 A for 1 s, a maximum velocity of 2.6 m/s. To hold the actuator in a fixed position 1.94 A are requested. For our porpoises, a continuous work condition is requested and the expressed force of 200 N for an operating velocity of 2 – 2.5 m/s is enough. In *fig.3.6* the force against velocity curves are illustrated.

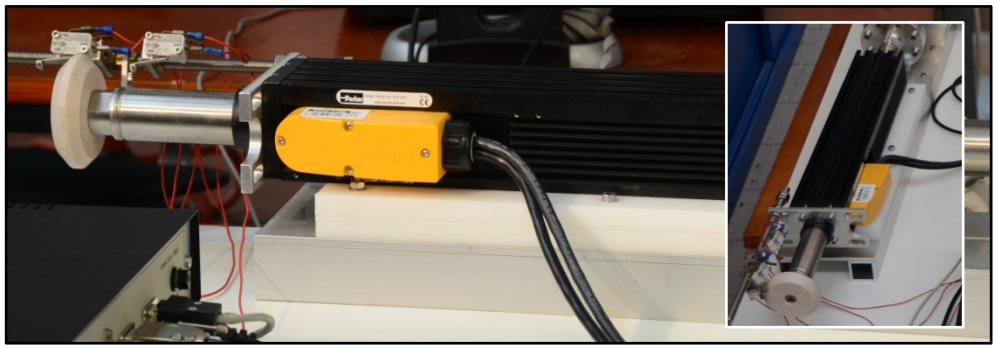

Fig.3.4 Detail of the Parker linear electromagnetic motor, where are visible the supply and control cables and the end stroke relays.

A metallic movable flange connects the linear motor to the bellow (a beam with ball bearing connection preserve from wear), and a second -frame fixed-flange joints the bellow with the ventricular chamber (*fig.3.7*). The bellows expresses an internal diameter of 65.0 mm, external diameter of 90.0 mm, length in compression of 16.5 mm and 66.5 mm in extension. So, the useful stroke is about 50 mm, that corresponds to a movable fluid volume for beat of 200 ml. Comvat Inc produces this component and an engineer drawing is visible in *fig.3.8*.

In couple with the LVDT sensor, for the metallic bean position monitoring, three microswitch relays were installed. These Cherry D45X have the task to control the two stroke limits and the zero position, allowing a constant signal reference that can be handle by the operator. The two limits are installed for security and, if the bar surpasses them, the motor is instantaneously stopped. The zero-position relay ensures a precise and reliable initial condition for different tests. In *fig.3.9* the adopted relays configuration is showed.

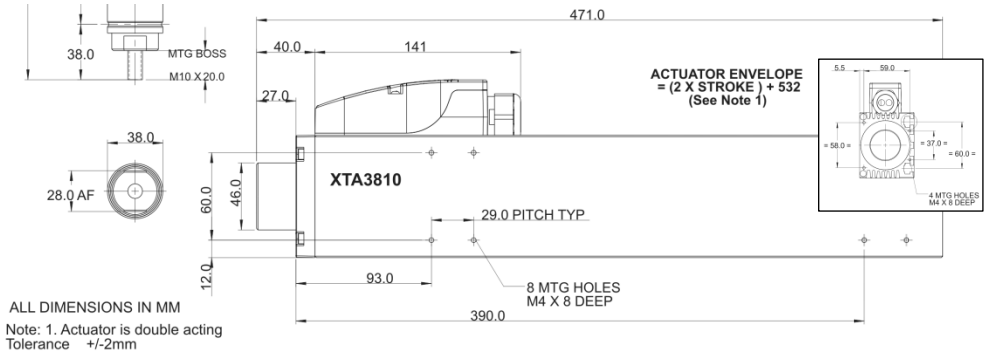

Fig.3.5 Engineer drawing of the adopted motor, from the company data sheet.

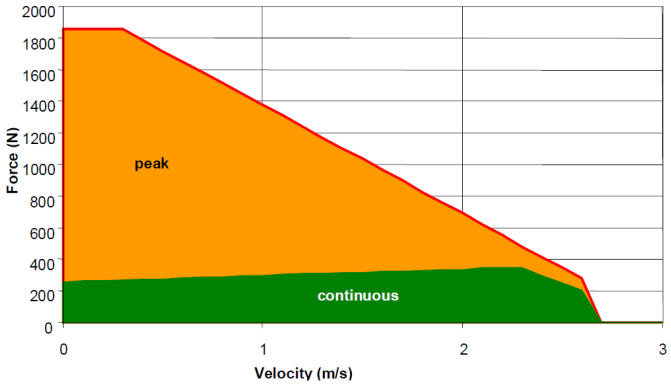

Fig.3.6 Parker PRA3810s force/velocity specifications.

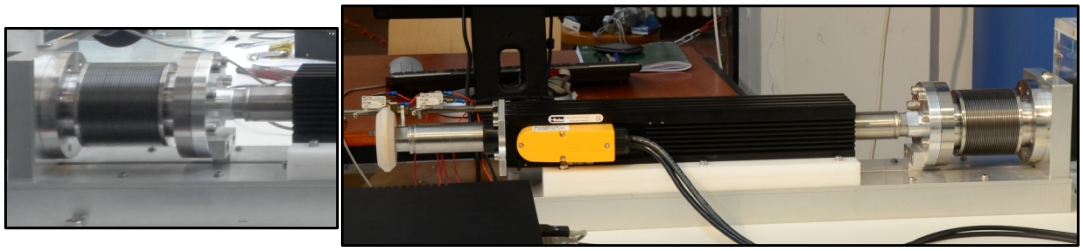

Fig.3.7 Linear motor and bellow connection. On the left side is easy to see the rail for the ball bearing and the bean connected to the bellow.

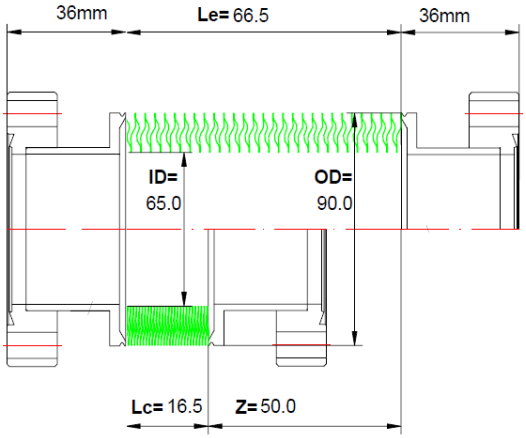

Fig.3.8 Engineer drawing of the bellow, from the company technical sheet.

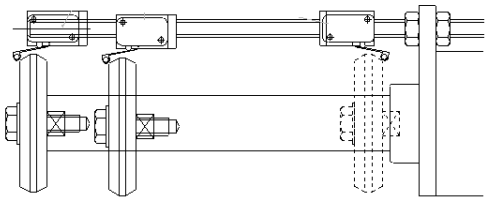

Fig.3.9 Detail of the end-stroke switches.

A global vision of the linear motor, bellow, and relays system is provided in *fig.3.10*.

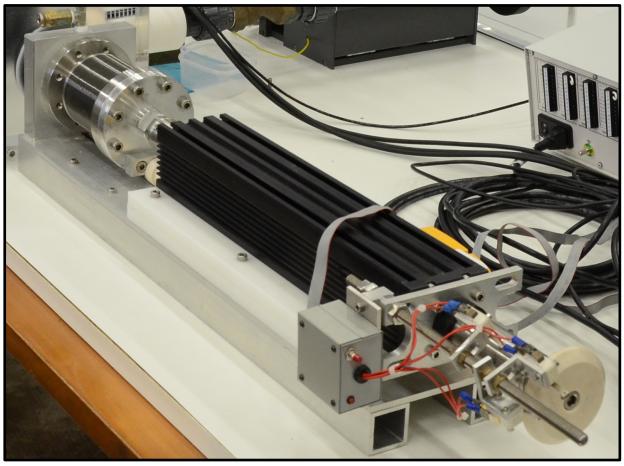

Fig.3.10 Detail of the 0-position and emergency switches, with the OK status led.

3.2.2 Control unit

To governor the motor via remote software, the control unit LT0510 developed by LabTrek S.r.l., represents a fundamental element for the pulse duplicator efficiency (*3.11*). Looking at the front panel, is possible to monitoring the correct status of the communication between the driver and the pc, via some red leds (power On, status Ok, Position Mode, Error, etc.). The outputs are cables for the motor control, for the relays monitoring, and a bus connection to the master-pc.

This board manages the different signals to and from the engine, and guarantees a correct translation of the commands via the servo-drive system developed by Parker. Three principal parts characterised the control unit: the power supply circuit (that ensures a correct energy to all different parts), the *on board* pc and the linear motor drive (*fig.3.11*). The Parker SLVDN5N is a digital-analogue converter that provides the correct strings to the motor (converts a data in a specific voltage). The communication is ruled by the *on board* pc Rabbit BL2120, that received commands from LabView and traduces them, based on a Dynamic C language installed in a programmable flash memory.

3.2.3 Conditioning unit

The sensor-conditioning unit LS0609, developed by LabTrek S.r.l., is a device that acquires, amplifies and filters the signals coming from the sensors along the hydraulic circuit and adapt them for the pc elaboration (*fig.3.12*). The hardware module is composed by a supply voltage unit for the different integrated-circuits, and by a filtering and amplifying board (*fig.3.12*). The front panel provides information via led about the correct power supplying of the different circuits. The inputs are 11, divided in amplified (*In0* to *In5*) and general purpose (*In6* to *In10*).

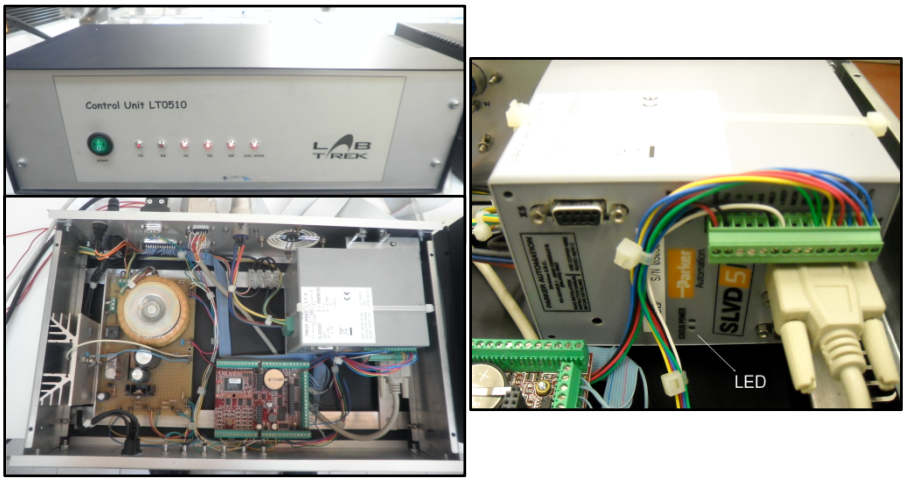

Fig.3.11 Control unit box, and inside parts (left up and bottom). On the right: detail of the SLVD drive of the linear motor.

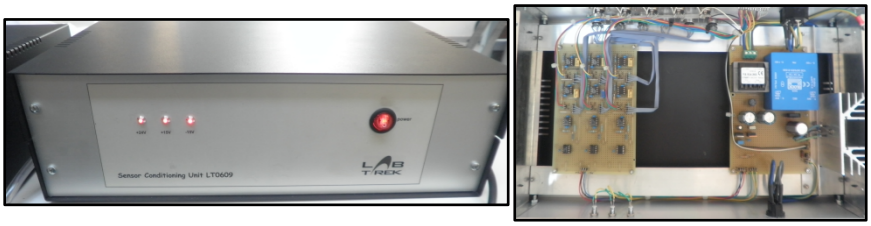

Fig.3.12 Signals conditioning unit, box and inside circuits for filtering and amplification.

3.2.4 Ventricular chamber

Directly connected to the bellow takes place the ventricular chamber, showed in *fig.3.13*. Represents the node of the circuit, and has two entrance holes, one for the bellow and one for the incoming mitral flow, and one output, to the aortic chamber. The chamber is made with Plexiglas panels, the base is a square of 0.23 m, the height is 0.23 m and the wall thickness is 15 mm. M3 metallic screws guarantee the parts join and the cover watertight seal is ensured by specific silicon material. Panels engineer drawings are illustrate in *fig.3.14*.

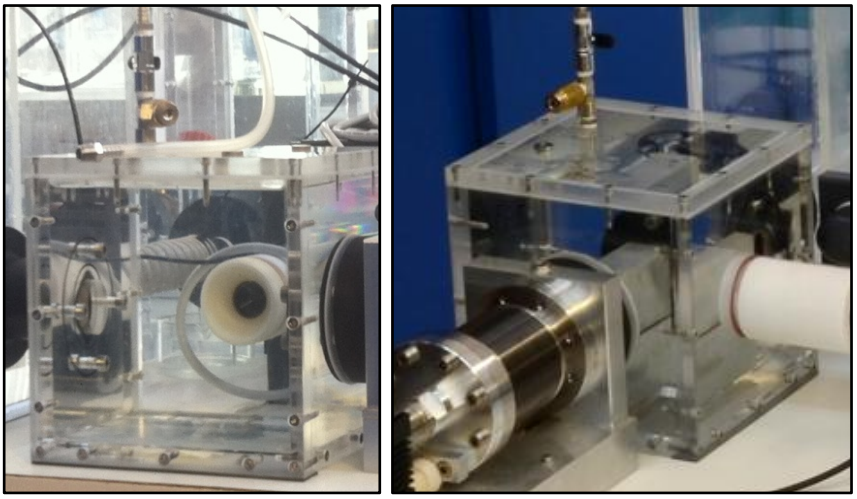

Fig.3.13 Ventricular chamber from a side view.

The three chamber connections are illustrated in *fig.3.15-16*. The bellow is linked via a Teflon disk (3 cm thick, 65 mm diameter) to the ventricular chamber, using two aluminium multi screwed flange disks and a double silicone O-ring to ensure the seal. PVC double T-shape part, with an internal variable diameter, connects the ventricular to the aortic chamber. The output internal diameter is 25.4 mm, for a best adaption of the flowmeter module. Two

pierced PVC flanges with pass through aluminium screws and silicone O-rings guarantee the seal. The third connection is with the mitral part, that contains the mitral valve: a mechanical bileaflet Sorin Allcarbon (27 mm annulus diameter). The mitral valve guarantees a flow to the ventricular chamber in diastole and a complete seal in systole. It is housed in a removable Teflon structure (140 mm length, 70 mm width) with a variable internal diameter (to house different valve sizes), made by two pieces: one internal and one external to the chamber, that screw one on each other ensuring a perfect watertight stop (fig.3.16).

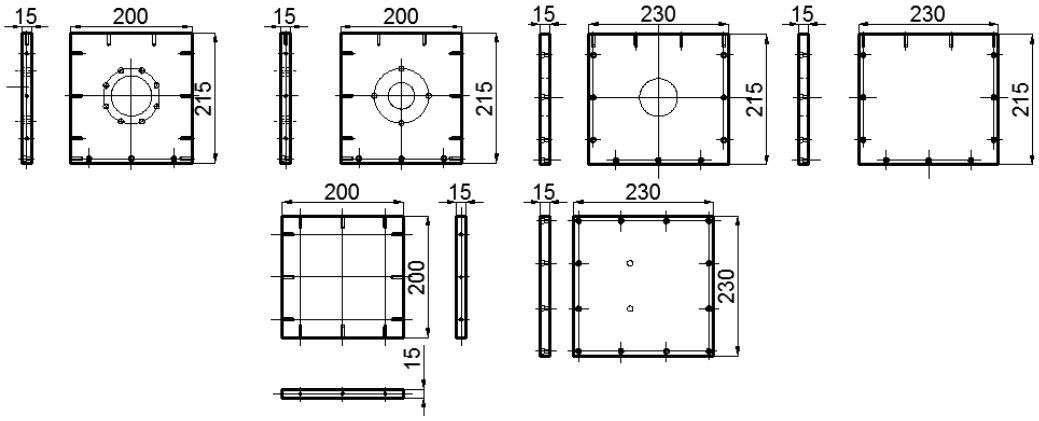

Fig.3.14 Engineer drawing of the ventricular chamber. In a clockwise orientation: chamber side to the aortic part, side from the bellow, side from the mitral valve, and the three last sides.

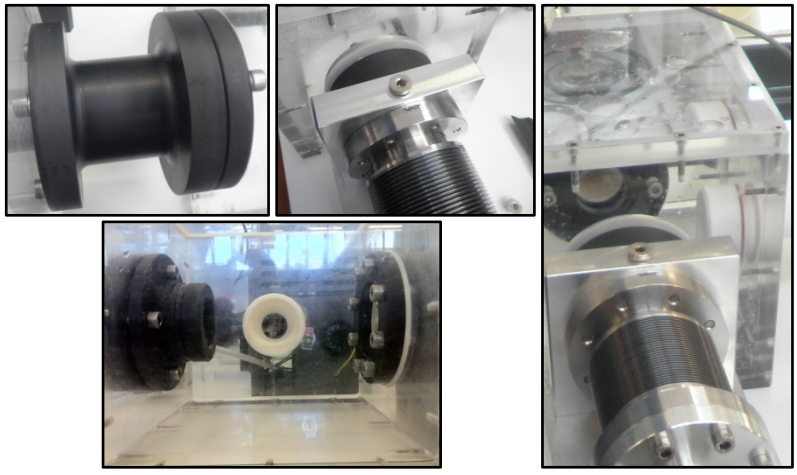

Fig.3.15 In clockwise orientation: connection from the ventricle chamber to the aortic chamber, from bellow to ventricle chamber and the three connection from a top and side view.

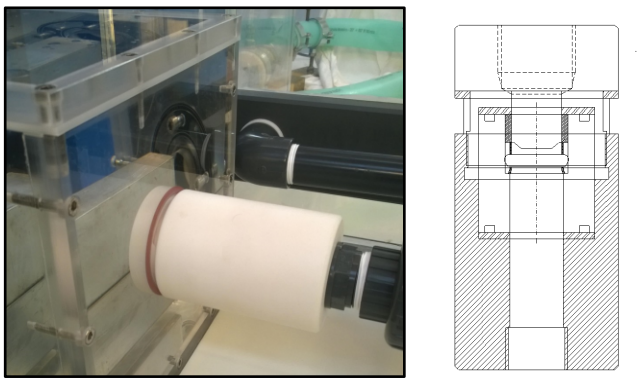

Fig.3.16 Detail of the mitral connection, picture and technical scheme.

3.2.5 Aortic chamber

The aortic chamber includes the most interesting and innovative parts of the system. It contains a small box for the flow meter sensor, a straight part with several pressure taps, in which the aortic valve housing and the prosthetic valve are placed, a dedicated compliance chamber, and in the next future a deformable silicone physiologic aortic arch, with the ascending arch derivations (*fig.3.17*). All these parts are housed in a rectangular 1.10 x 0.7 x 0.36 m (b x b x h) Plexiglas box, with wall thickness of 15 mm.

In a operative condition the tank will be filled with fluid to replicate a correct transmural pressure on the aortic arch walls. A Transonic System Inc. ultrasonic probe model ME19PXN is positioned inside a sealed box. A shielded cable connects it to the control module TS410, and the signal is transferred to the conditioning unit. The module was programmed to work with temperature of 20±3°C or 37±3°C. *Figure 3.18* contains the flowmeter module, the probe and the relevant datasheet information.

The aortic valve housing was obtained from a Plexiglas straight tube with internal diameter of 30 mm. The housing engineer drawing and a picture of used valve (OnX mechanical valve) are illustrated in *fig.3.19*. Valve exchange structure is simple and based on a double rings system (metallic and teflon) with multiple screws (M2.5, nylon) that acts as a sandwich, immobilizing the valve. This connection provides a valve housing range from 19 to 27 mm (at the annulus, with different adaptors). Upstream and downstream the valve are located several pressure taps, to allocate sensors, and measure the transvalvular pressure drop. The adopted transducer are PCB Piezotronics series 1500, with pre-amplification, double shielded cable and compensated in temperature. Thanks to the high sensibility (9.67 mV/mmHg), range (-20 to 500 mmHg) and acquisition frequency (>1000 Hz), is possible to measure and see in *live-view* (via LabView software) multiple high resolution pressure curves. A cable connects each sensor to the conditioning unit. An engineer drawing, and a picture of the piezometer are reported in *fig.3.20*.

Passed the aortic valve, a T-derivation is inserted. In one direction the fluid flow to the aortic arch and in the other goes to the aortic compliance. That is a mono-directional solution that provides the correct amount of compliance at the aortic arch tract (that is -now- rigid). The chamber is the one that was identified in *Chapter 2* as compliance chamber (CC), in the numerical model. The aortic compliance is made with a cylinder Plexiglas structure with a single in-outflow way at its base. Two ABS plates with O-rings guarantee the seal, and a pressure taps and a valve on the cover provide the adjustment and the monitoring of the internal gas pressure (overview of the device in *fig.3.21*). The sizing of the chamber was done following the specification given by FDA guidelines. In particular, the tract to make compliant was L* = 350 mm (about the length of the aortic arch), the choice was to reproduce a “high compliant chamber”. As initial conditions were used: D_c = 140 mm (compliance chamber diameter), Pao_{min} = 60 mmHg, Pao_{max} = 150 mmHg (min and max pressure range to reach). Using the formulas given by guidance, the final design gave a d_h = 24.4 mm, and an exchange volume of 364 ml. The relative dimensions that has been implemented in the realized compliance are H = 210 mm, D = 140 mm. After the aortic compliance, the aortic arch is inserted. In this thesis was not possible to include data of the fluid-dynamic performances with the new silicone arch, for process schedule reasons. Actually, a non-permanent plastic tube (30 mm inner diameter) is placed instead of it. At the end of this session a paragraph is dedicated to a deep description of the silicone physiological aortic arch design and development is provided.

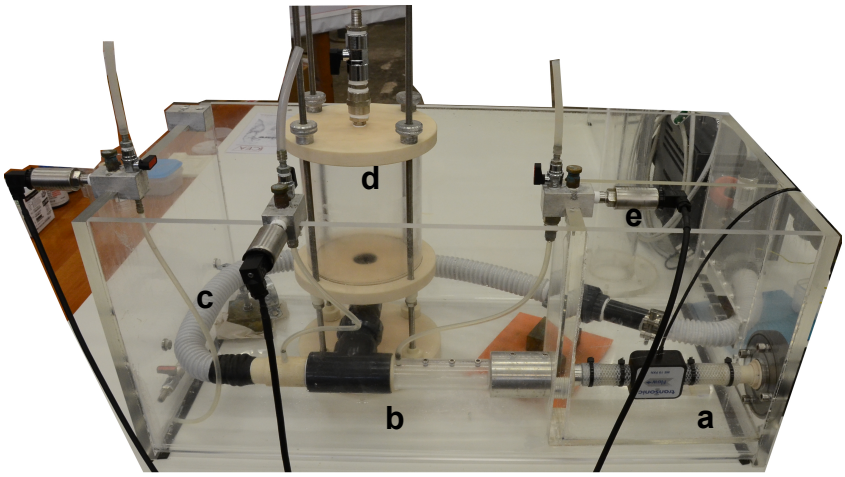

Fig.3.17 Global vision of aortic chamber: a) flowmeter box, b) valve housing, c) aortic arch, d) aortic compliance, e) pressure sensor.

INLINE SENSOR	Physical Specifications						Accuracy Specifications							
	Tubing ID		Barb OD[1]		Dimensions[2]		Bidirectional Flow				Accuracy			Ultra-sound
Catalog #	inches	mm	inches	mm	Total Length w/ tube ends mm	Case Length w/out ends mm	Resolution at 10 Hz ml/min	Low Flow 1 Volt = ml/min	Standard Range 1 Volt = ml/min	Max Flow in Standard Range ml/min	Maximum Zero Offset[3] ml/min	Absolute Accuracy %	Non-Linearity[4] %	Frequency MHz
ME19PXN	3/4	19.1	0.86	21.9	101.1	64	± 5	2.5 L	10 L	50 L	± 100	± 4	± 2	0.9
ME25PXN	1	25.4	1.14	29.0	128	79.8	± 10	5 L	20 L	100L	± 200	± 4	± 2	0.6

[1]Subject to minor modification
[2]Standard cable length: 1.85 meters.
[3] Zero offset can be eliminated by Zero Adjustment prior to measurement.
[4] Within specified calibration range.

Fig.3.18 Flowmeter unit, probe, positioning and technical data sheet.

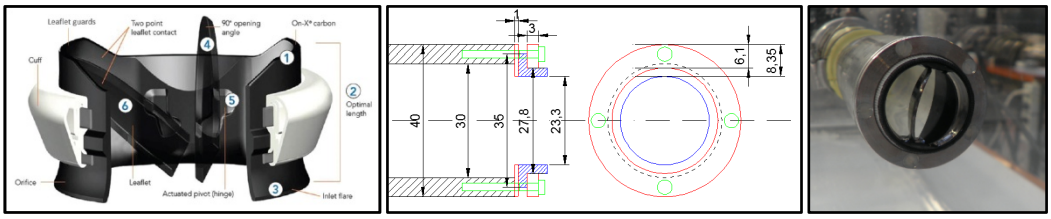

Fig.3.19 OnX bileafleat mechanical aortic prosthetic valve, valve housing scheme and picture (with this system, also bioprosthetic valves has been tested).

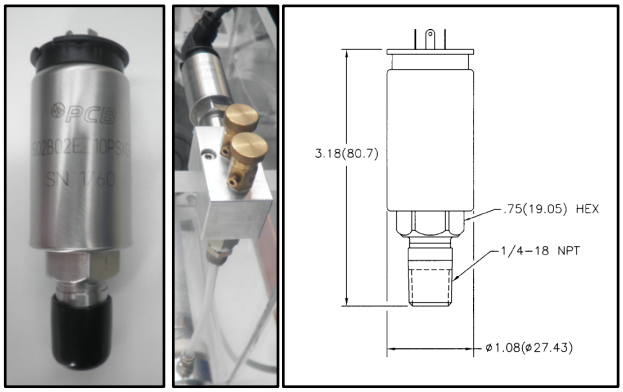

Fig.3.20 Pressure sensor picture, positioning, technical scheme, and performance data.

3.2.6 Additional compliance chamber

An additional compliance was inserted after the arch, outside of aortic chamber, just before the systemic resistance. This chamber provides two tasks: adding an elastic component if necessary, partitionable using a tap, and gives a pressure reference in a static condition, been positioned 50 cm high from the bench.

Compliance sizing was performed following the FDA specification. The maximum compliant tract to simulate was L* = 500 mm (about the length of the descending aorta plus major derivation), the choice was to reproduce a “mid compliant chamber”. As initial conditions were used: D_c = 120 mm (compliance chamber diameter), Pc_{min} = 50 mmHg, Pc_{max} = 120 mmHg. Using the formulas given by guidance, the final design gave a max fluid increment in the chamber of d_h = 9.8 mm, and an exchange volume of 110 ml. The realized compliance expresses dimensions H_2 = 210 mm, D_2 = 120 mm.

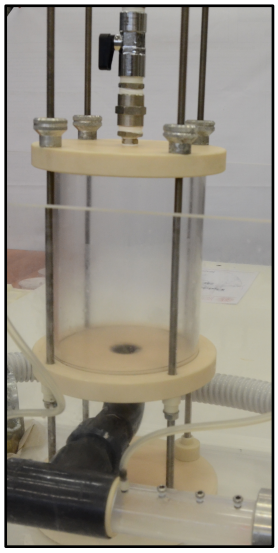

Fig.3.21 Aortic compliance chamber

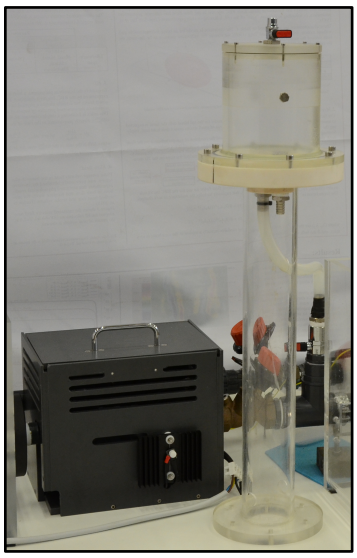

Fig.3.22 Additional systemic compliance

3.2.7 Concentrated resistances

At the outflow tract of the compliance chamber a taps is inserted. It provides a fundamental pressure drop that helps to obtain the desired aortic pressure trend, in the cardiac cycle. The adjustment made by the operator has to be very fine, for this porpoise the chosen taps are BOA-control SAR regulation valve with smooth seal, developed by KSB (*fig.3.23*). These metallic devices provide an incremental number, from 0 to 48 that expresses the degree of aperture of the gate.

Another tap with the same characteristics is inserted just upstream of the mitral section. In this case a current flows through the tap only in diastole

(moving back of the motor). An overview picture of them is observable in *fig.3.24*.

Fig.3.23 KSB multi-rotations BOA-control SAR valve.

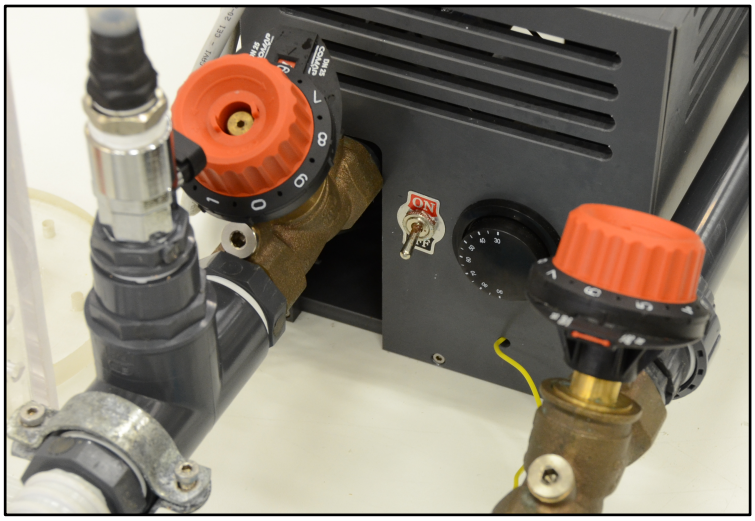

Fig.3.24 Systemic resistances overview.

3.2.8 Fluid heater

After the resistance, a rectangular PVC isolated box is inserted (*fig.3.22-3.24*). Inside of it, a metallic heater with an electronic control circuit is placed. The metallic tube acts as a resistance and heat up the working fluid, thanks to a high current across two poles positioned at its extremes. A switch, connected to a thermostat and a temperature sensor, creates a closed loop that permit a good control of the temperature of the work solution. The electric circuit is also composed by a diode that allows a splitting of the power. Two control steps are provided: 1 KW or 2 KW, to regulate the time of heating up. The electronic scheme of the developed circuit is showed in *fig.3.25*, right. The device is

independent from the other electronic part of the pulse duplicator and uses a 220 V energy plug supply.

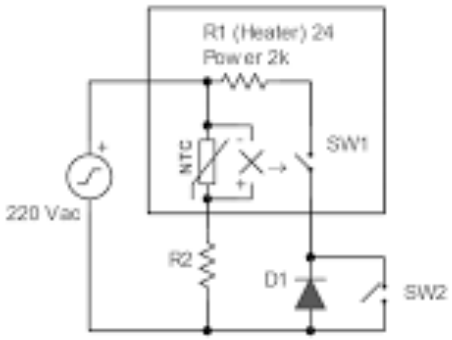

Fig.3.25 Fluid heater electronic scheme.

The presence of this device is important to carry the temperature up to 37 °C, that is the physiological blood temperature, and a typical request made by the international regulations. Hysteresis and performance tests on temperature in different sections of the pulse duplicator were performed, a difference of 2-3 °C on the far parts was obtained, with a total time to rise the temperature from 19 to 37 °C of 90 mins.

3.2.9 Atrial chamber

The last circuit component is the atrial chamber, that is a calm tank, in which the fluid oscillatory behaviour is softened. This mechanism is guaranteed by the wide horizontal size of the tank, that is a square Plexiglas box of 0.4 x 0.4 x 0.36 mm (b x b x h), with a wall thickness about 15 mm. It presents two holes for inflow and outflow, positioned on the same side, at identical height of all the other conduits in the circuit (about 10 cm from zero reference). A constant fluid level is present in the chamber, to mimic the systemic distal pressure reference, of about 6-7 mmHg. Picture and engineer drawing of the atrial chamber and are showed in *fig.3.26*.

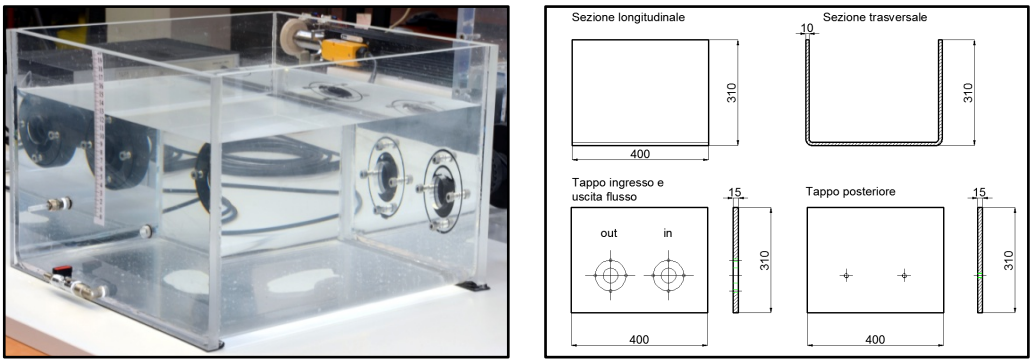

Fig.3.26 Atrial chamber picture and its technical drawing.

3.2.10 A new component: the deformable arch

The real innovation of the pulse duplicator developed inside the HeR Lab is the possibility of test several different aortic prosthetic devices, in a physiological replica of the anatomic district. This is possible by making different customized parts, and measuring the fluid dynamic performances - global and local parameters of the flow- via advanced experimental tools. Of course, a reproducible moulding technique was developed, so is possible to adapt it in relation of the research.

The technique that permits the creation of the final silicone product, in the specific case of the aortic arch is explained. It is opinion of the author that this procedure, that given very good results, could be generalized for different kind of anatomic vessel parts.

CT scan images and aorta segmentation

CT scan images of an average adult healthy patient were used to extract the aortic arch. An adequate number of slices n = 1000 (for a spatial resolution of 0.2 mm) allows the fine reconstruction of the ascending part of the aorta, from the aortic root, since the abdominal bifurcation. The DICOM files segmentation was performed using OsiriX and a single layer geometry definition file format was exported (wavefront .obj file). An example of these passages is illustrated in *fig.3.27*.

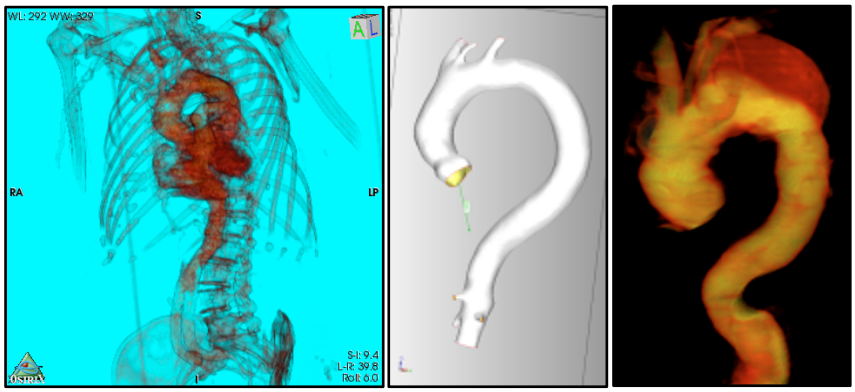

Fig.3.27 Osirix segmentation process: isolation of the region of interest via tissue thresholding and cutting tool, obtainment of a single layer healthy aortic arch, and a single layer –still not exported- of a aneurysmatic arch.

Creation of a mesh model

Rhinoceros and Geomegic software were used to modify and refine the arch geometry, to create a mesh and a surface model with specific characteristics. In particular, inflow and outflow customized conduits were inserted to perform a good adaptation on the workbench. A local remeshing of high curvature regions was performed and a specific smoothness of the surfaces was performed, obtaining a *m* = 20.000 rectangles mesh file (with vessel thickness of 0.1 mm), and a multi-surface file. To fit on a fast prototyping

machine, the aortic arch has been reduced to a height of 0.28 mm (the width was left univariate). A third stereolithographic file with all the dimensions increased by a specific factor, to obtain a shell of the native of 2.5 mm, was product. The final files are showed in *fig.3.28*.

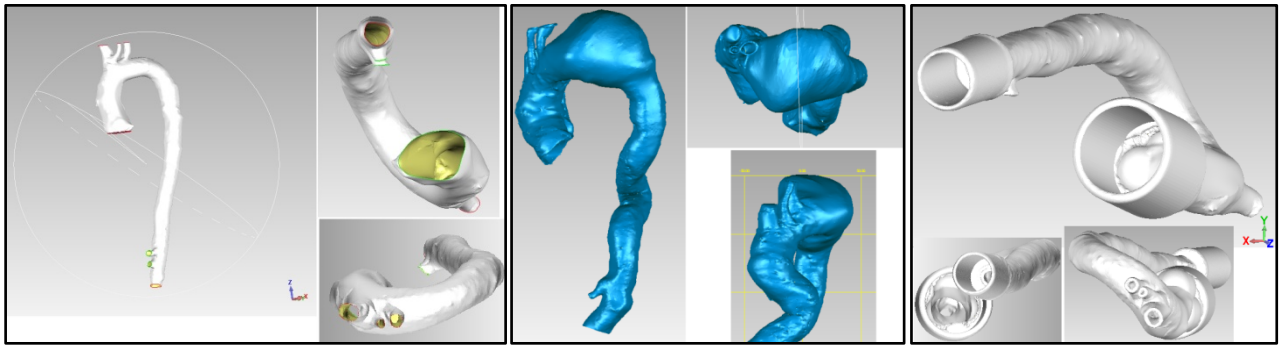

Fig.3.28 Geomagic healthy aortic arch mesh file, aneurysmatic mesh aortic root and healthy aortic root with inflow and outflow tract for pulse duplicator connection.

Monoaxial tests on pig's aorta

At the same time, axial stress-strain tests on fresh pig's aorta tissue were performed. No chemical components were added at the samples, and only the deepest tonaca layer of the vessel was cut off to obtain the two pure connective – muscular layers. In particular, 7 tests were performed using a Bose ElectroForce® Planar Biaxial TestBench Test Instrument (*fig.3.29*).

The experimental set-up was:

- 7 tests, 3 on axial direction traction, 4 on radial direction traction
- v = 0.5 mm/s (constant velocity of deformation)
- T = 2 s (maximum test traction time)

Characteristics of the samples:

- L_i = 5 mm (undeformed width)
- w = 5 mm (width)
- h = 2.5±0.09 mm (thickness)

Observing the obtained σ–ε curves (*fig.3.30*), the first observation is that the medium elastic modulus of axial and radial orientation is quite similar. Typical hyperelastic behaviour is expressed by both curves, with maximum deformations of about 160%.

Silicone choice

The rubber that we need has to respect some restrictions: has to be transparent (to allow marker tracking tests and particle image velocimetry induction -see Chapter 8-), with the same elastic modulus and shore of the aortic tissue, fusion temperature has to be higher than the ABS softening

threshold. A low viscosity is needed for the molding process, and no interference with acetone, Teflon spray, and detach wax spray are fundamental. Now all the information to match the silicone material for the aortic arch are provided. Prochima Inc. C-Rubber is a commercial product that respects most of these characteristics. At this time are in developing accurate mechanical tests on silicone samples made with different thickness. This bi-component liquid silicone was chosen as the material for the aortic arch replica, and expresses:

- S = 30 (Shore, in points after 6 hours of reticulation, with sample depth h=6 mm)
- D = 1.5 MPa (damage limit, h=2 mm)
- σ_{max}=200% (elongation limit, h=2 mm)
- L = 5 KN/m (limit before laceration, h=2 mm)
- r_l < 0.1% (linear shrink after 7 days at 23°C)
- t > 160°C (thermic seal)

To make the silicone a ratio of 1:10 for the catalyser has to be used. The reaction starts immediately and in an environment temperature (about 23°C) it takes 24 h. If posed in freezer (2-4 °C) the reticulation stopped.

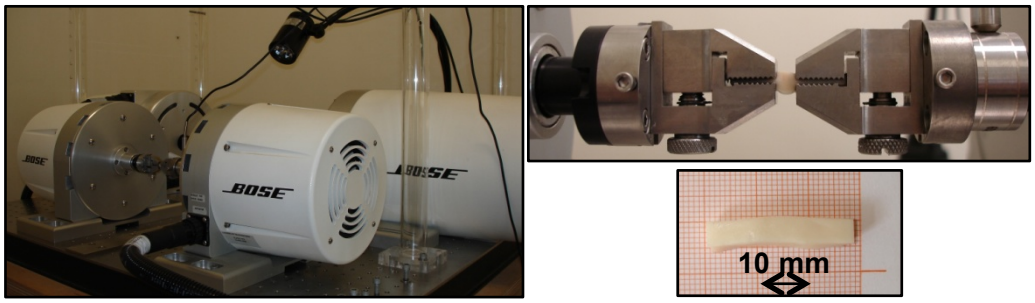

Fig.3.29 Bose ElectroForce® Planar Biaxial Test Bench, mono-axial test image and pig's aorta sample example.

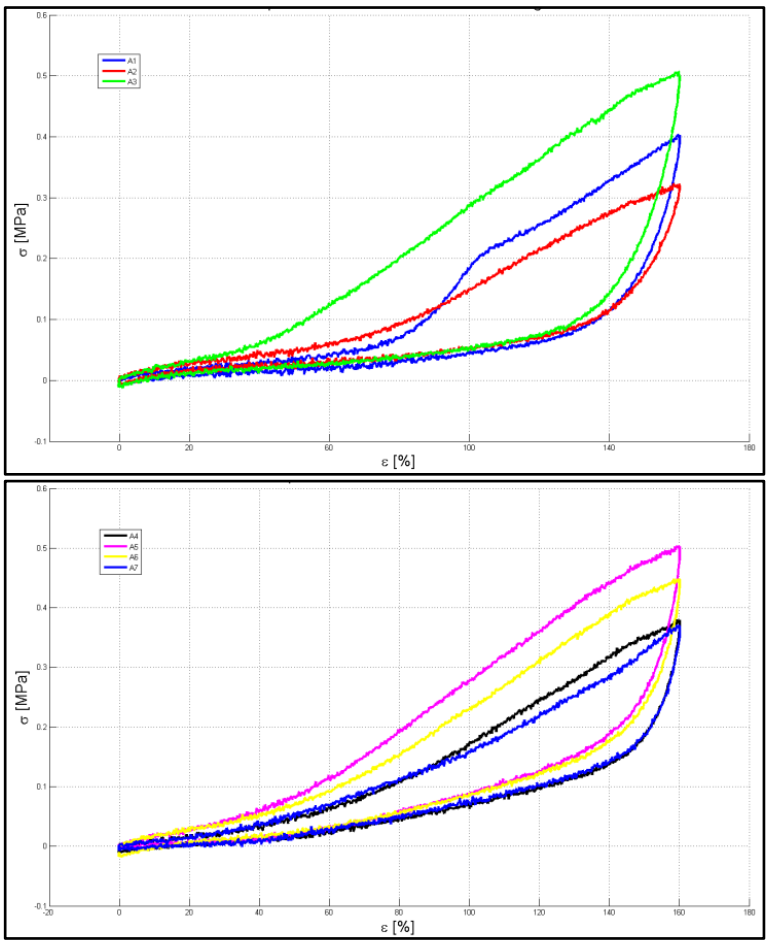

Fig.3.30 Longitudinal (above) and radial (below) graph for a mono-axial stress-strain test on aorta pig's tissue.

Surfaces separation tests

For the obtainment of a perfect separation between the silicone rubber and ABS samples, several products were tested beforehand. The surface treatments were compared via electronic microscopy induction. In *fig.3.31* are showed different tests: polished ABS, polished ABS with Teflon spray, polished ABS with wax spray, and polished ABS with acrylic varnish spray. The differences are evident: the last solution provides a uniform thin layer of product that acts as a separator between silicone and the plate. This solution, with an additional layer of wax spray, permits an easy detach without damaging after 24 h of contact between the ABS and a thick layer of silicone. The silicone was not contaminated by wax and no remains on the surface were founded.

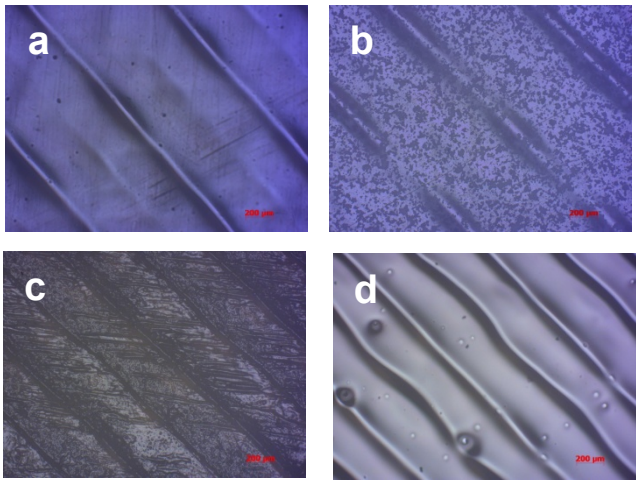

Fig.3.31 polished ABS, polished ABS with teflon spray, polished ABS with wax spray, and polished ABS with acrylic varnish spray.

External and internal ABS moulds and final product

The adopted procedure to create the final prototype is a casting on multiple moulds. First, with the Geomagic surface file of the artic arch (+2.5 mm uniform shell compared to the patient aorta), a female ABS mold was designed with SolidWorks software and realized with fast prototyping technique. This part acts as a "sarcophagus" of the real aorta. This mould has been designed in 4 different parts to follow the double curvature of the arch, and to help the opening phase (*fig.3.32*). In *fig.3.32* is also possible to see some chimneys used to cast the silicone, or to allow the exit of entrapped air.

A second plate was made from the physiological .stl aorta file, via fast prototype technique, with an internal wall thickness of 0.1 mm, in ABS (*fig.3.33*). This is then polished, smoothed and sprayed with acrylic paint and wax spray. After, it is posed inside the first mould (sprayed with detach wax), and fixed following specific adaptors. The external 4 parts are then closed with screws, the junctions were sealed with Motorsil red paste, and sprayed with sealing silicone (fig.3.34).

The liquid silicone was then prepared adding the components and casted, filling the gap between the internal thin ABS aorta and the external full ABS plate. Completed the fill up, all the structure was put in freezer for 24 h, to help a complete degasification of the entrapped air bubbles. The complete reticulation takes then 36 h in hoven with controlled humidity and temperature (40 °C).

The final silicone aorta is showed in *fig.3.34*, where is possible to appreciate the fine internal resolution of the mold, and the physiological geometry obtained.

For the fast prototype stamps creation a Stratasys Dimension 1200es printer was used, the adopted material was a custom ABS developed by

Stratasys Inc.. All the casting procedure and the production of the plates were developed with the collaboration of the Te.Si. Laboratory of the University of Padua.

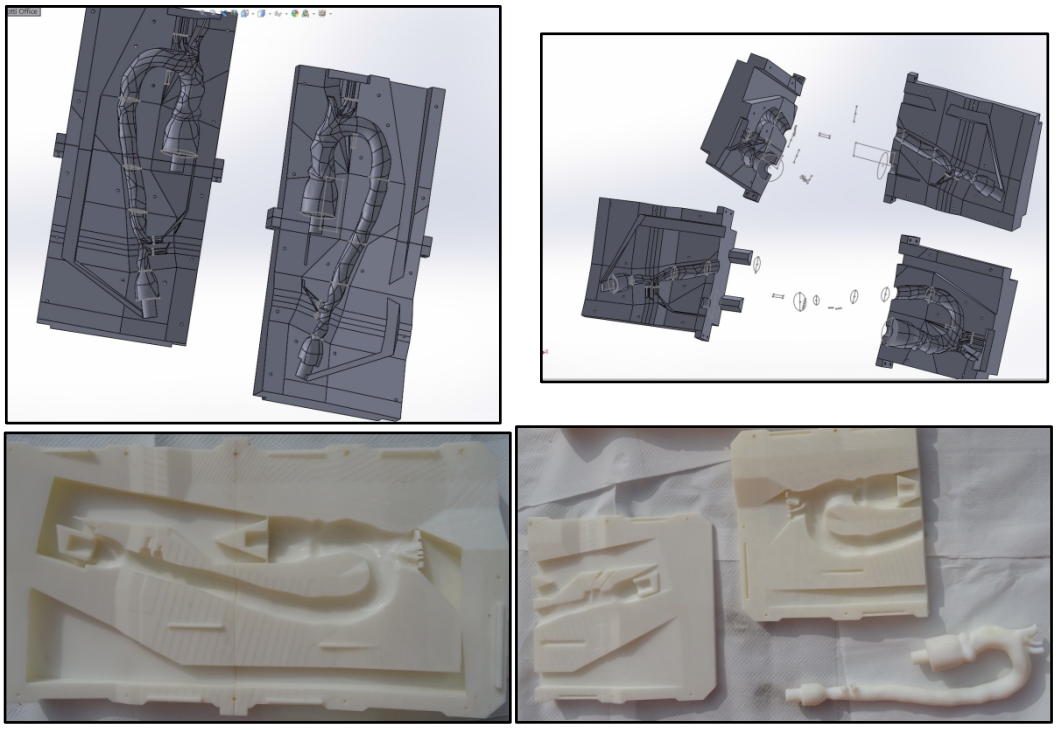

Fig.3.32 SolidWorks four parts mould file (above) and ABS forms plus aorta from fast prototype printer (below).

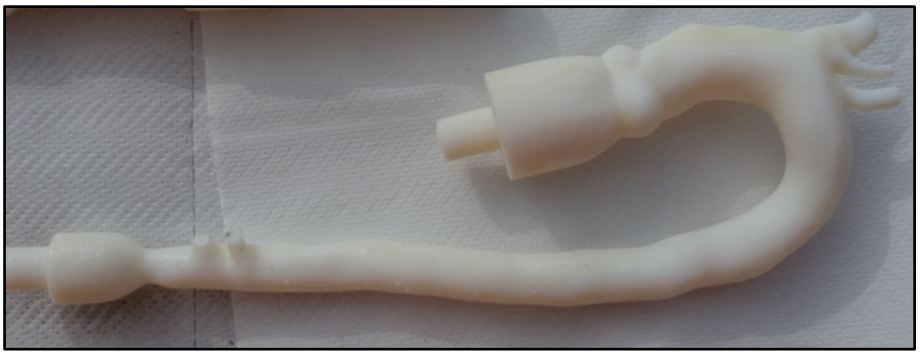

Fig.3.33 ABS mold of the internal aortic arch core.

Fig.3.34 Sealed close mould in which the silicone has been casted, and the final silicone aortic arch.

As last, seems important to report an observation about the aortic arch creation that had influenced the choice of this technique. Indeed, the first idea was to realize the aortic arch directly using a fast prototype printing, with rubber like materials. Unfortunately these materials (Stratasys Tango FLX series) are still not enough advanced to satisfied our requirements (especially in terms of biaxial resistance and transparency). This way will probably be the fastest (and best), when the materials will became enough resistant and similar to the real rubbers.

3.3 Software parts

The pulse duplicator control is realized through three main steps, each one is characterized by specific software. The low level data acquisition buffering from all the measure devices, pre-processing and communication between the linear motor and the control pc, is due using a Dynamic C program. This is implemented on the flash memory of the board pc, inside the control unit and the signals conditioning part. Live-view visualization of the measured data (motor displacement, pressures, flow), adjustment of the hydraulic test parameter (stroke volume, heart rate, motor motion curve, etc.), and the control of the motor, are possible through a specific LabView program, that represents the intermediate level. Post processing of the obtained global flow fields following the ISO and FDA regulations is due through a developed MatLab

program. The next paragraph will shortly describe these three software levels from a functional point of view.

3.3.1 Data acquisition and transfer

To permit a communication between the linear motor drive and the pc control system, an intermediary is needed. The developed Dynamic-C program and the Rabbit *on board*-pc conduct this role, governing the strings and commands via a serial port communication from and to the Parker PRA3810s. This program was developed offline, and then transferred to the control unit where it works in stand-alone mode. The program reads the data sent by LabView, and answers with the correct command to the motor drive (i.e. the right voltage for the displacement). It also regulates: the command timing and trigger from and to the linear motor, the end-stroke sensors signals and the velocity of the buffer transmission. As last, it manages the different data packages that arrive from the motor drive and all the other sensors (pressure, flow, etc.), subdividing in terms of importance (i.e. information from the motor have the priority, to preserve a fast communication) and sending them through another flat cable to the LabView control program, when a specific signal asks for the download.

The signal-conditioning unit acts as a bridge between the measure instruments and the on-board pc. It picks-up all the data, filters and amplifies them, in order to have the same type of data (sample frequency, same start acquisition instant) for all the measures. After the collection, it sends the data packages to the control unit at each acquisition cycle.

3.3.2 LabView

The developed LabView program is a key part for the good behaviour of the workbench. It is a temporized time-machine structure with different communication drivers that dialogs with the peripheral devices, allowing a fast correct downloading of the data sent by the control unit. It provides a translation in visual signals or numeric indicators of the data, and also the possibility to impose several work parameters via a user-friendly control panel to the pulse-duplicator (overview of it in *fig.3.35*).

Different controls have been implemented in the program:

a) Initializing panels that allow a correct set up of the system and start the signals and motor commands acquisition.
b) Curve displacement: is possible to upload a custom curve for the pump displacement. It has to be normalized at “1”, in period and amplitude, for n_c=100 samples. At the moment FDA (ViVitro used) displacement curve is implemented. This parameter gives the possibility of high-customized studies, for example to investigate pressure and flow behaviour in case of non-healthy situation that reflect on a different volume curve.

c) Motor parameters control: direction, offset (from the position reference), heart rate (beats per minute, from 15 to 125), and amplitude (in cm, directly correlated to the ejected volume) that can vary from 0.1 to 3 cm for a corresponding maximum stroke volume of about 120 ml. These controls allow the modification of the hydrodynamic parameter of the test in a wide range of options (ISO and FDA requirements range are covered).

d) Pressures and flow acquisition tool that, via different buttons and led, provides the downloading of the data package for the requested quantities. The signals are showed together at each pressing of the "acquisition" button.

e) Re-zero sensor tool, that allows a re-calibration of the different sensors (both pressure and flow) during the initialization phase, for each experimental test.

f) Saving quantities tool, that permits the saving in a user defined folder, of the visualized curves in a .txt file, subdivided in columns for the different signals. Multiple test saving could be done and the last data block is placed in queue, extending the .txt file.

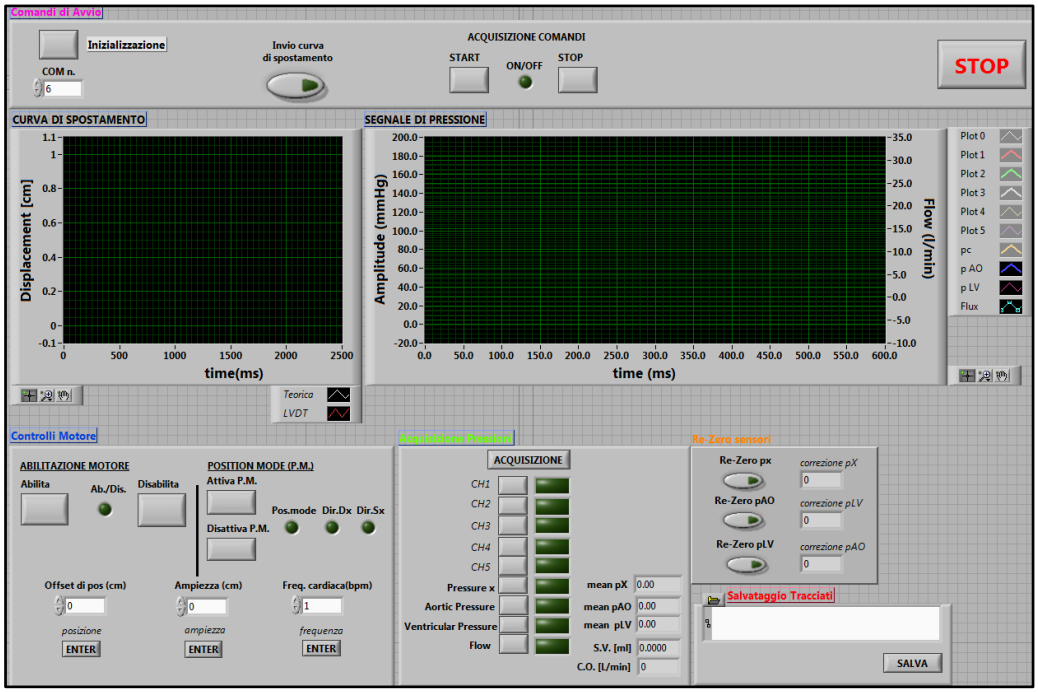

Fig.3.35 LabView pulse duplicator front panel control. The purple box highlight the initializing controls, the blue one the motor controls and indicators, the green is depicted to pressure acquisition and data measurements, the orange is for re-zero of sensors.

Several indicators were implemented (*fig.3.36-37*):

a) The graph shows both the imposed curve to the linear motor, also called theoretical displacement (white line) and measure data from LVDT sensor, called real displacement (red line). From here is possible to easy detach errors in the motion repeatability, in terms of shape, phase and peak value.

b) The data box illustrates the different measured data, chosen for the visualization by the acquisition box and with a colour legend. The plot includes pressure and flow data, showed with two different scales, for a better visualization. The acquired and visualized data could be saved as described before; if the data is not saved it will be lost at a new data refresh.

c) Some numeric indicators give back useful information for a correct aortic valve testing, as for example the stroke volume or the mean aortic pressure in the cycle.

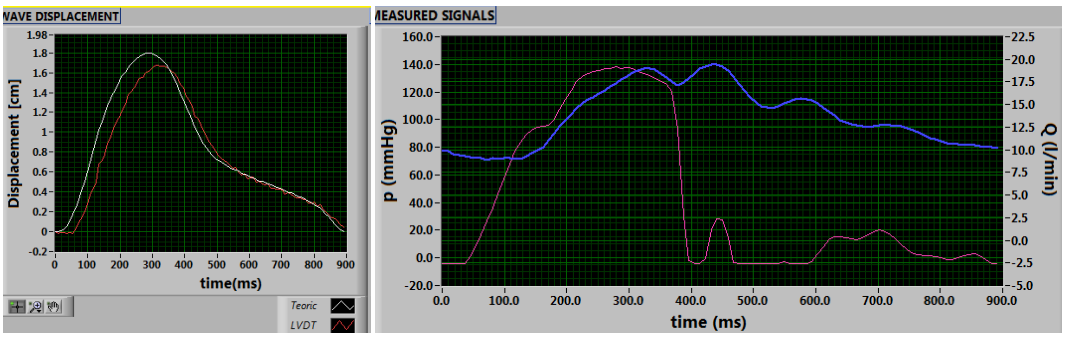

Fig.3.36 Examples of FDA curve and LVDT measured displacement (left), and typical real-time measured pressure curves for a porcine aortic valve are showed on the right side.

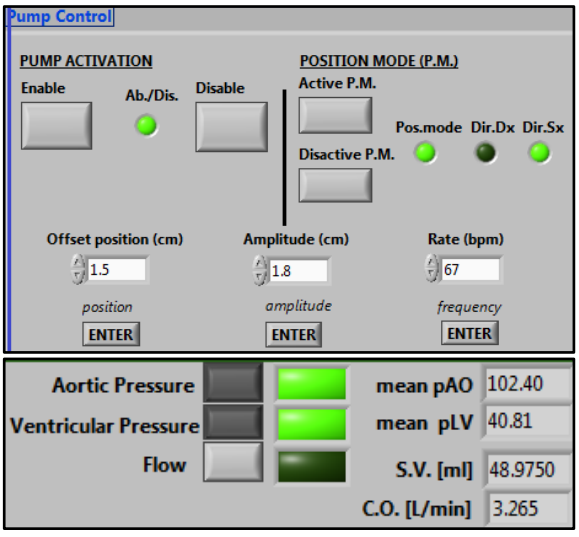

Fig.3.37 Example of typical pump control indicators during an experiment (above): bellow position offset amplitude of the displacement and heart rate. Below, pressure indicator as: mean aortic and ventricular pressures, pumped stroke volume and cardiac output.

3.3.3 MatLab

The post-processing data analysis has been carry out developing a MatLab program that allows the automatic calculation of all the main global flow parameters in according to the ISO 5840:2009. The script read the data collected in the test file and compute the flow parameters. Moreover, taking advantage of the ViVitro used test software, also the ViVitest parameters were computed, to help for a fast performance comparison, in case of same fluid dynamic tests performed with both workbenches.

Computed parameters divided by area of performance are now listed and described, and after a validation of the program through a comparison with ViVitro data is provided. The generic physical quantities used in the calculation are: *T*, period of the cycle, in *s*; *HR*, heart rate, in *bpm*; *dt*, time interval between two consecutive samples; *EA*, bellow area. The crossover points are defined as follows: P_1, Beginning of Systole Positive Pressure Drop; P_2, End of Systole Positive Pressure Drop; P_3, Beginning of Diastole Positive Pressure Drop; P_4, End of Diastole Positive Pressure Drop. I_1, Beginning of systole Forward Flow; I_2, End of systole forward flow; I_3, Outflow Valve Closing, leakage begins; I_4, End of Leakage/Cycle. All the next discussed formulas are computed among the mean curve of 10 acquired cycles. *Fig.3.38* includes all these peculiar test points.

Flow parameters:

- Aortic Forward Flow Time (AFFT): this parameter indicates the positive flow interval, in time.

$$AFFT(s) = I_2 - I_1$$

- Aortic Forward Flow Time Percent (AFFTP): percentage value of the positive flow duration, on the total period.

$$AFFT(\%) = \frac{AFFT}{T}100$$

- Aortic Forward Flow (AFV): expresses, in ml, the area of the positive flow curve. Q_i is measured in l/min.

$$AFV(ml) = \sum_{I_1}^{I_2} \left(Q_i \cdot \frac{10^3}{60} \right) \cdot dt_i$$

- Cardiac Output (CO): ejected amount of fluid (net) from the left ventricle, for unit of time.

$$CO\left(\frac{L}{min}\right) = HR \cdot AFV - HR \cdot (CV + LV)$$

- Pumped Stroke Volume (PSV): based on the motor displacement, allows the obtainment of the volume ejected for each cycle. *S* is the displacement variable, in mm.

$$PSV\ (ml) = (S_{max} - S_{min}) \cdot EA$$

- Closing Volume (CV): aortic backflow volume, in ml, computed using the ISO specification (flow area from I_2 to the intersection between the x-axis and the bend point of the negative flow).

$$CV(ml) = \sum_{I_2}^{I_3} \left(Q_i \cdot \frac{10^3}{60}\right) \cdot dt_i$$

- Regurgitant Volume (RV): flow integration between I_2 and I_4. It includes the total backflow, both closing and leakage.

$$RV(ml) = \sum_{I_2}^{I_4} \left(Q_i \cdot \frac{10^3}{60}\right) \cdot dt_i$$

- Leakage Volume (LV): flow area includes between the bend point in the backflow and the starting point of a new cycle.

$$LV(ml) = RV - CV$$

- Regurgitant Fraction (RF): indicates the percentage of backflow related to the whole cycle.

$$RF(\%) = \left(\frac{CV + LV}{AFV}\right) \cdot 100$$

- Systolic Time (ST): duration in seconds of the ejection, obtained through the difference between I_1 and I_3.

$$ST(s) = I_3 - I_1$$

- Systolic Time Percent (STP): percentage value of the systolic time, on the total period.

$$STP(\%) = \frac{ST}{T}100$$

Most of the mentioned quantities are labelled and showed in *fig.3.39*.

Pressure parameters (all expressed in mmHg):

- Aortic Mean Pressure (AMP): aortic pressure over the whole cycle.
- Aortic Max/Min Pressure (AMaP/AMiP): max/min aortic pressure.
- Ventricular Mean Pressure (VMP): mean ventricular pressure.
- Ventricular Max/Min Pressure (VMaP/VMiP): max/min ventricular pressure.
- Gradient Pressure (GP): vector that contains the transvalvular aortic pressure drop computed as:

$$GP(mmHg) = P_{LV} - P_{AO}$$

  From this equation is possible to compute different drops, in relation to positive crossing points (CP) or with positive and negative contributions (CT). The main crossing points are the pressure First/Last Crossing (PCT_F/L): first/last pressure crossing between ventricular and aortic pressure. Using an implemented graphic interface the MatLab user could decide the two points on the averaged pressure curves and the respective pressure values used to compute the GP_P.

Mixed parameters:

- Effective Orifice Area (EOA): important global parameter that takes in account both flow and pressure values. It is derived from Gorlin's formula and is a fundamental performance value requested by the ISO and FDA guidance. If the flow *Q* is expressed in ml/s, the *GP* in mmHg and *r* in g/cm^3, the computed area will be in cm^2.

$$EOA(cm^2) = \frac{Q_{rms}}{51.6 \cdot \sqrt{\frac{GP}{\rho}}}$$

The automatic MatLab script, that contains these quantities, was validated using as control a typical ViVitro *in vitro* test on aortic valve.

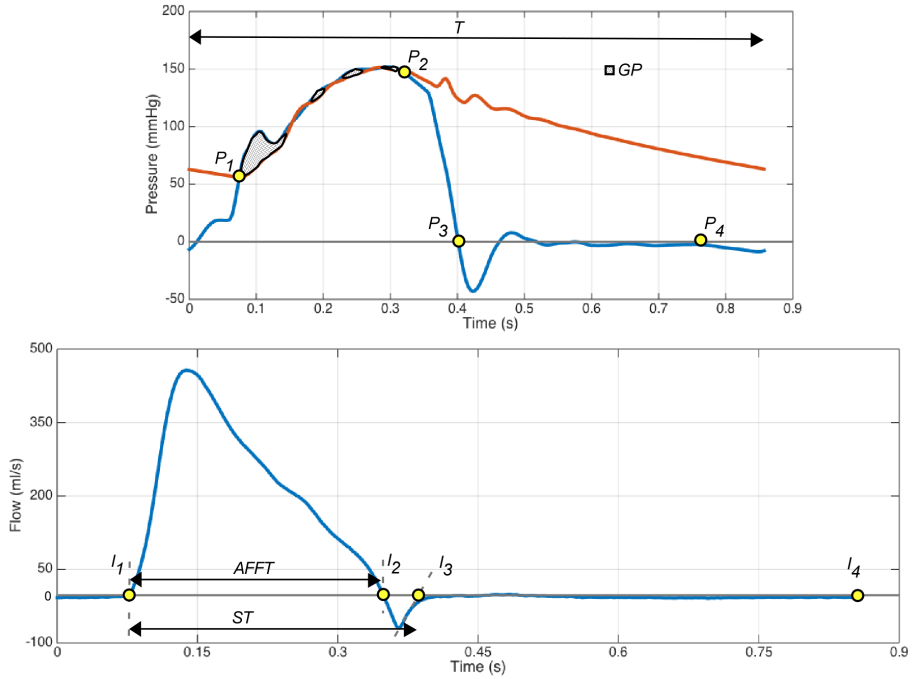

Fig.3.38 Pressure and flow remarkable points during the cardiac cycle.

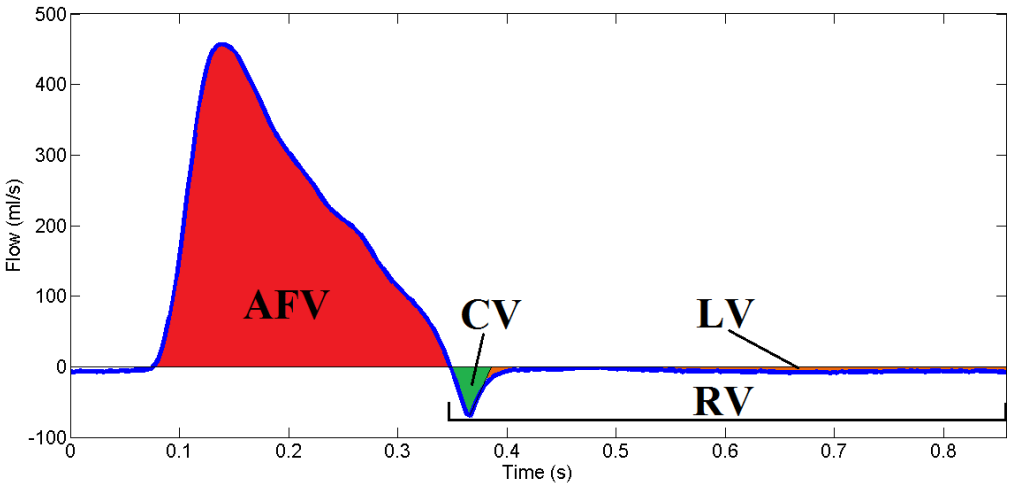

Fig.3.39 Flow calculated areas, in according to ISO5840 regulation.

Validation of the MatLab program:

Taking as gold reference an output sheet from ViVitro test, carried out on an experimental test on a mechanical aortic prosthetic valve Sorin Bicarbon 25 mm with a Sorin Allcarbon 27 mm in the mitral position, a validation of the implemented MatLab program was conduit. The investigation shows how, for

the same input data, the difference obtained between the software is extremely small (*table 3.1*), strengthen the goodness of the implemented script for the HeR pulse duplicator data analysis.

In particular, the reported table shows a trial on an aortic bioprosthetic valve in couple with a physiological healthy three leaflets root. The boundary flow characteristics of the test were: 70 bpm, 37°C for the fluid temperature, 4.0 l/min for cardiac output. The accuracy in the global performances evaluation is high: the min/max pressures values, flow characteristics, pumped SV, aortic forward flow, cardiac output are very close. The little differences concentrates where the value are directly dependent by the operator, as for aortic valve time of closure or the positive/negative crossing points, those have to be pointed by the user on the mean pressure curves showed on screen. This implies little variation especially in the volume-flow quantities as aortic RMS, or closing and leakeage volume data. Lots of considerations could be done (i.e. the choice to differentiate between what is closing and what is leakage) but seems that the implemented MatLab tool computes a correct algebraic sum of these quantities and the deviation depends on the chosen computation strategy (using different area integration for example). In general, the errors are behind the 3% so the MatLab program validation is satisfied.

Data Description	MatLab	ViVitro
TRANSVALVE PRESSURES		
TransAortic mean pressure [P]	10.343	10.343
TransAortic max pressure	42.641	42.646
TransAortic pressure at peak flow	14.025	14.112
PRESSURES (gage)		
Aortic mean pressure	101.166	101.166
Aortic RMS pressure	103.852	103.853
Aortic minimum pressure	65.563	65.555
Aortic maximum pressure	140.284	140.320
Ventricular mean pressure	42.042	41.959
Ventricular RMS pressure	74.679	74.668
Ventricular minimum pressure	-51.089	-51.089
Ventricular maximum pressure	142.918	142.951
FLOW		
Heart rate (bpm)	70.000	70.000
Pump stroke volume (ml)	90.278	90.297
Systolic time	0.292	0.299
Systolic percent of cycle	34.116	34.922
Aortic forward flow time	0.276	0.278
Aortic cardiac output	4.071	3.985
Aortic forward volume	61.185	60.022
Aortic closing volume	-0.984	-0.804
Aortic leakage volume	-2.046	-2.246
Aortic mean flow [P]	229.06	237.060
Aortic RMS flow [P]	268.73	274.076
Aortic peak flow [P]	474.662	475.412
Aortic regurge fraction (%)	4.953	5.086
AREA		
Aortic orifice area [P] (cm2)	1.618	1.652

Table 3.1 Comparison between ViVitest and HeR pulse duplicator post-processing tool outputs on global flow parameters.

In conclusion, the developed post-processing tool seems work with a very good accuracy, allowing a direct comparison between the two workbenches. In this sense *in vitro* tests similarity evaluation of valve prosthesis performance became very fast, with the certainty that the confronted parameters are computed in the same way and in accordance with international regulations, as it will explain in the next chapter.

3.4 Study abstract

The cardiovascular laboratory of ICEA dept. started with this project as the first step into bio-fluid experimental research field, to assess hydrodynamic performances of prosthetic devices. In this chapter a detailed description of the pulse duplicator was provided. The mechanical construction and software development were illustrated, pointing the attention on the different design choice and innovations against others workbenches. The hydraulic circuit is composed by chambers connected by conduits with an electromagnetic motor and a bellow that permit the fluid motion. It exhibits a horizontal distribution, in which is possible to simulate physiological conditions in terms of pressure and flow curves, changing the working conditions in a wide range of values. For example, the stroke volume could vary up to 200 ml/beat with a heart rate from 25 to 120 b/min. In this context, the haemodynamic performances of prosthetic valves could be analysed via the implemented LabView and MatLab tools.

As last, to product silicone components able to simulate vascular derivations, a dedicated technique was developed. Mechanic behaviour and chemical properties of biological and polymeric materials were studied to obtain an aortic arch prototype that is now in test on the pulse duplicator. In conclusion, from this first analysis seems that the pulse duplicator gives the possibility to expresses several fluid dynamic conditions, holding the pressure and flow requirements request by the international guidance with high accuracy.

Seems important to remark how this work was carried out with a low economic investment, less than 1/3 if compared with the commercial ViVitro workbench.

3.5 Chapter Bibliography

[1]. AA.VV. Heart valve hydrodynamic test apparatus. Service instruction manual, Dept. of Medical Physics and Clinical Engineering, Royal Halmshire Hospital, Sheffield, 1989.

[2]. Bazan O., Ortiz J.P., Design and construction of a new pulse duplicator system for in vitro evaluation of prosthetic heart valves – conception of an experimental setup on mitral position. 21st Brazilian Congress of Mechanical Engineering. October 24-28, 2011, Natal, RN, Brazil.

[3]. Barbaro V., Daniele C., Grigioni M., Descrizione di un sistema a flusso pulsatile per la valutazione delle protesi cardiache valvolari. ISTISAN 91/7 (ISSN-0391-1675), Roma, 1991.

[4]. Biglino G, Giardini A, Baker C, Figliola RS, Hsia T-Y, Taylor AM, Schievano S. In-vitro study of the Norwood palliation: a patient-specific mock circulatory system. ASAIO J 2012; 58(1):25–31.

[5]. Biglino G., Verschueren P., Zegels R., Taylor A.M., and Schievano S., Rapid prototyping compliant arterial phantoms for in-vitro studies and device testing. Journal of Cardiovascular Magnetic Resonance 2013, 15:2 http://www.jcmr-online.com/content/15/1/2

[6]. Canstein C, Cachot P, Faust A, Stalder AF, Bock J, Frydrychowicz A, Kuffer J, Hennig J, Markl M. 3D MR flow analysis in realistic rapid-prototyping model systems of the thoracic aorta: comparison with in vivo data and computational fluid dynamics in identical vessel geometries. Magn Reson Med 2008; 59(3):535–46.

[7]. Cloonan A.J., 3D-Printed tissue mimicking phantoms for medical imaging and computational validation applications. Mary Ann. Liebert, Inc., Vol.1,n°1, 2014.

[8]. Dal Borgo V., Studio fisico dell'aorta normale e patologico. Pontificia Academia Scientiarum, 1952.

[9]. Doyle B.J., Morris L.G., Callanan A., Kelly P., Vorp D.A. and McGloughlin T.M., 3D Reconstruction and manufacture of real abdominal aortic aneurysms: from CT scan to silicone model. J. of Biomechanical Engineering. 130, 2008, DOI:10.1115/1.2907765.

[10]. Fortini S., Espa S., Querzoli G., Cenedese A., Turbulence investigation in a laboratory model of the ascending aorta, J. of turbolence, Vol. 16, No. 3, 208–224.

[11]. Gao F., Watanabe M., Matsuzawa, Stress analysis in a layered aortic arch model under pulsatile blood flow. BioMedical Engineering OnLine 2006, 5:25 doi:10.1186/1475-925X-5-25.

[12]. Grigioni M., Daniele C., Romanelli C., Barbaro V., Mock circulatory system for the characterisation of mechanical cardiac system support. ISSN 1123-3117 Rapporti ISTISAN 03/21, Roma, 2003, (in italian).

[13]. C.M. García Herrera, J.M. Atienza, F.J. Rojo, E. Claes, G.V. Guinea, D.J. Celentano, C. García Montero, R.L. Burgos, Mechanical Behaviour and rupture of normal and pathologic human ascending aortic wall, Medical & Biological Engineering, 03/2012; 50(6):559-66. DOI: 10.1007/s11517-012-0876-x.

[14]. Insnard R.N., Pannier B.M., Laurent S.L., London G.M., Diebold B., Safar M.E., Pulsatile diameter and elastic modulus of the aortic arch in essential hypertension: a non-invasive study. JACC Vol. 13. No. 2 February 1989:399405.

[15]. Kazakidi A., Computational studies of blood flow at arterial branches in relation to the localization of atherosclerosis. Department of Aeronautics Imperial College London, London SW7 2AZ, master thesis.

[16]. Lumsden A., Bismuth J., What exactly is radial fit? Adaptable technology is crucial in accommodating a variety of patient needs. Supplement to endovascular today; advancing thoracic care. September 2012.

[17]. Markl M, Schumacher R, Kuffer J, Bley TA, Hennig J. Rapid vessel prototyping: vascular modeling using 3t magnetic resonance angiography and rapid prototyping technology. MAGMA 2005; 18(6):288–92

[18]. Querzoli G., Fortini S., Espa S., Costantini M., Sorgini S., Fluid dynamics of aortic root dilation in Marfan syndrome. J. of Biomechanics, 3120-3128, 47.

[19]. Reul H., Tesch B., Schoenmackers J., Effert S., Hydromechanical simulation of systemic circulation, Medical and Biological Engineering, July 1974, 431-436.

[20]. Sulaiman A., Boussel L., Taconnet F., Serfaty J.M., Alsaid H., Attia C., Huet L., Douek P., In vitro non-rigid life-size model of aortic arch aneurysm for endovascular prosthesis assessment. European Journal of Cardio-thoracic Surgery 33 (2008) 53—57.

[21]. Yokoyama Y., et al., A new pulse duplicator with a passive fill ventricle for analysis of cardiac dynamics. J Artif Organs (2010) 13:189–196, DOI 10.1007/s10047-010-0518-8.

Chapter 4

HeR Pulse Duplicator in vitro performances

4.1 Qualitative comparison against physiology

This section focuses on a preliminary induction of the workbench ability to mimic the physiologic behaviour. A qualitative comparison between theoretical optimal trends and *in vitro* results is provided, to better understand which pressure and flow curves characteristics are fundamental to replicate.

4.1.1 Mechanical valve

In this test an aortic mechanical bileaflet OnX valve, 25 mm size, was used. The flow conditions were: CO = 4 l/min, HR = 70 bpm, SV about 64 ml, mean aortic pressure about 100 mmHg. The working fluid was physiological saline solution, at a temperature about 37°C. In *fig.4.1* are shown the obtained pressure curves (mean of 10 cycle), instead below (*fig.4.2*) is illustrated a typical reference behaviour by Gayton (Gayton & Hall, 2005). The highlighted points referred to important phases of the cycle. From a first look, experimental curves and theoretical reference are correlated in terms of distribution of the phases length along the cycle: same duration of systole and diastole, same instant of opening and closing for the valve, about the same time to reach the maximum ventricular pressure. The mutual behaviour of the pressures is also significant: from valve opens to the pressure peak the ventricular pressure is always above aortic. Instead, during closing, the aortic start progressively to diverge from the ventricular since the complete closure, identified by the vertical fall of the upstream pressure. In diastole, the aortic pressure decreases progressively since its minimum, instead the ventricular remains constant to zero.

In particular, referring to Gayton, the aortic valve opens normally about 75 – 80 mmHg and closes in a range between 90 – 105 mmHg. *Fig.4.1* presents the opening at P_1 = 77.8 mmHg, and closure at P_3 = 105.4 mmHg, strongly close to the physiological reference. Also the peak values are similar (P_2 = 125.9 mmHg) demonstrating the pulse duplicator ability to reproduce the physiology. The end of cycle aortic pressure value (P_5) is also correct, strengthens the

goodness of compliant behaviour. An important effect was also reconstructed: the dicrotic notch. This event appears just after the closure and represents a hummer effect created by a pressure waves that travel in the opposite direction of the flow, produced by the arteries compliant phenomenon. The physiological range of this pressure jump is normally no more than 5 – 10 mmHg. *In vitro* test shows a pressure anomalous peak, P_4, about 160 mmHg, instead a normal dicrotic notch. A realistic idea is that the dicrotic notch adds up to a bump effect, caused by the hurt of valve leaflets on the metallic annulus that is transferred to the rigid conduit and to the pressure sensor.

This idea is reinforced by the evidence of a pressure peak on ventricular curve, just few instants late. That phenomenon seems directly correlated with the pressure bump suffered by the aortic pressure. The aortic-ventricular peak difference is about 8 mmHg, that could justify the additional presence of the dicrotic notch in the aortic pressure, instead of the ventricular.

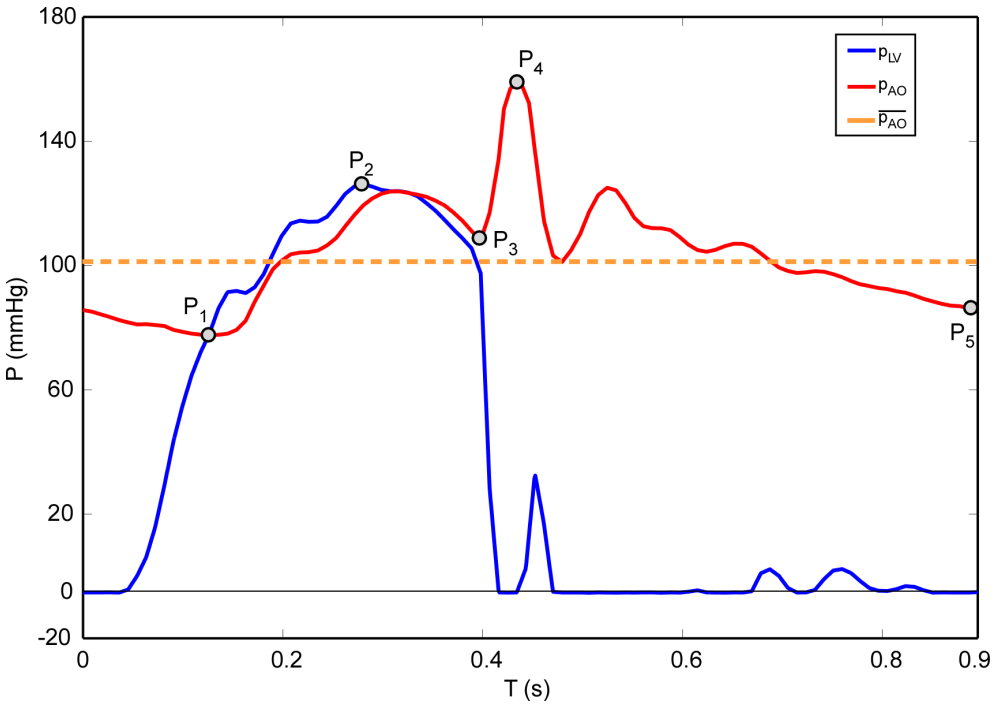

Fig.4.1 Ventricular, aortic pressure trends (mean of 10 cycles) and mean aortic pressure value are reported for a typical test with OnX aortic mechanical valve. Grey dots highlight the principal curve points.

For the same experiment the flow curve is expressed in *fig.4.3*, upstream aortic literature behaviour is visible for comparison in *fig.4.4*. As for the pressure trends, the phase of the cycle are respected and close to the physiological reference given by Caro (Caro et al., 2012). Looking at *in vitro* result some points has been highlighted to facilitate the contrast. F_1

corresponds with the aortic valve opens and for both the curves is followed by a rapid increase of the flow. The peak, F_2, is reached about 0.25 – 0.3 s for both and its value depends on test stroke volume. The valve closure seems faster in the *in vitro* model compared to the reference, indeed the maximum regurgitation, F_3, is moved up by 0.08 s. Except for this difference, the typical behaviour for closing, leakage and aortic valve closes flow jump (F_4) is perfectly repeated in the experiment.

In conclusion, from this curves analysis seems acceptable to say that the pulse duplicator is able to provide pressure and flow trends that from a semi quantitative point of view, and in terms of respecting of the main cardiac phases, mimic very well the physiological references.

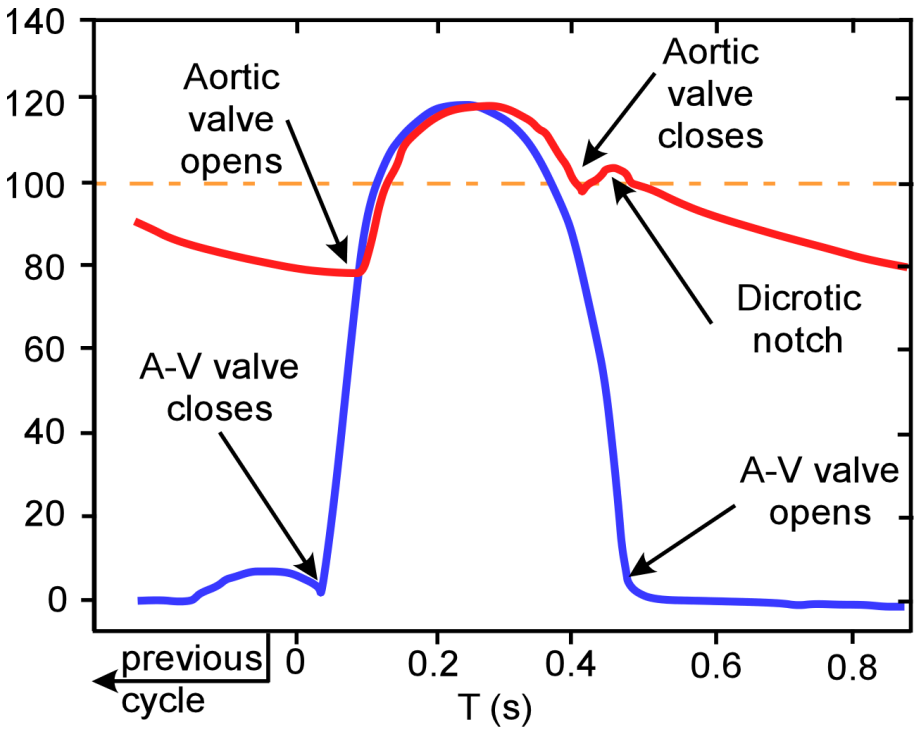

Fig.4.2 Physiological reference curves from Guyton, the same curve colours of *fig.4.1* has been used, for a faster comparison. Labels highlight the principal cardiac cycle phases.

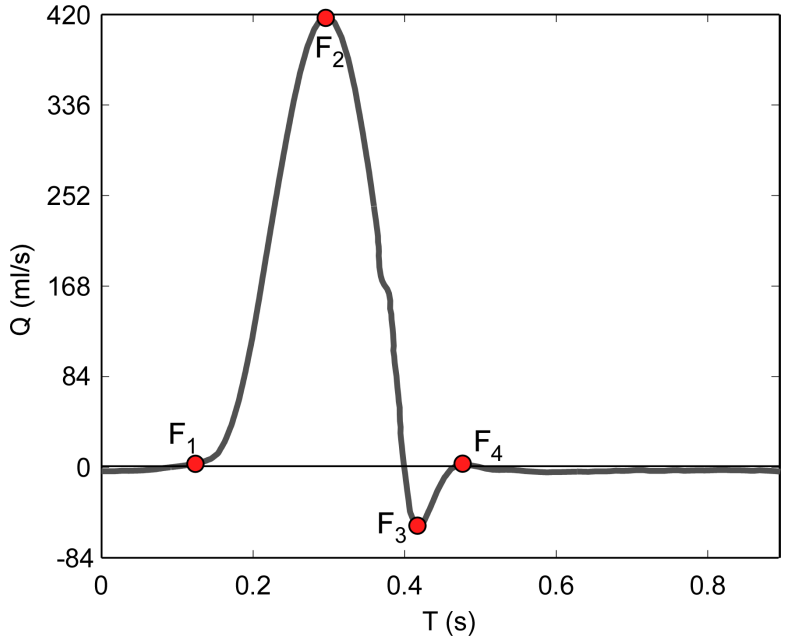

Fig.4.3 Upstream aortic valve flow trend (mean of 10 cycles), for a typical OnX aortic mechanical valve test. Red dots highlight the principal curve points.

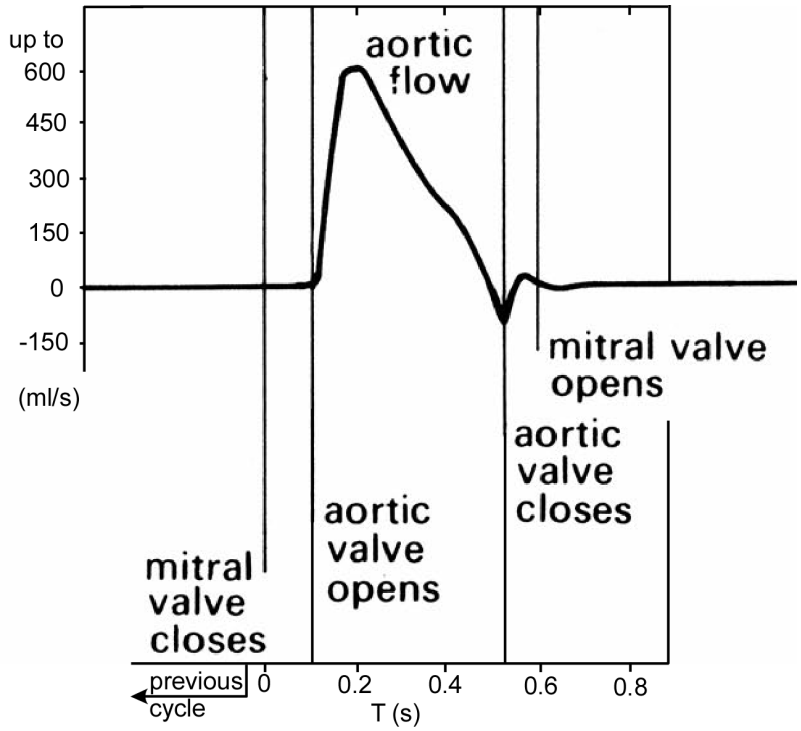

Fig.4.4 Physiological reference curve shape of flow upstream an aortic valve, from Caro. Labels highlight the principal cardiac cycle phases.

4.1.2 Bioprosthesis porcine valve

A second preliminary test was carried out using an aortic porcine St.Jude Epic valve 25 mm size at the annulus. The aim was to investigate the presence of a hummer effect high as the one saw for the mechanical valve. Flow conditions were: CO = 4.1 l/min, HR = 70 bpm, SV about 62 ml, mean aortic pressure equal to 100 mmHg. The working fluid was physiological saline solution, at a temperature about 37°C.

From a first look at obtained pressure curves (*fig.4.5*, mean of 10 cycle), experimental curves Guyton's reference and the mechanical valve curves are strongly correlated in terms of distribution of the phase duration along the cycle. Pressures behaviour is also coherent across the tests, with physiological values and correct timing of opening and closing, as well as curves slope. In particular, in this case the aortic valve open at at P_1 = 72 mmHg, and close at P_3 = 120 mmHg. Peak value is P_2 = 137 mmHg, and dicrotic notch stops about 138 mmHg (P_4). The end of diastole pressure is P_5 = 78 mmHg.

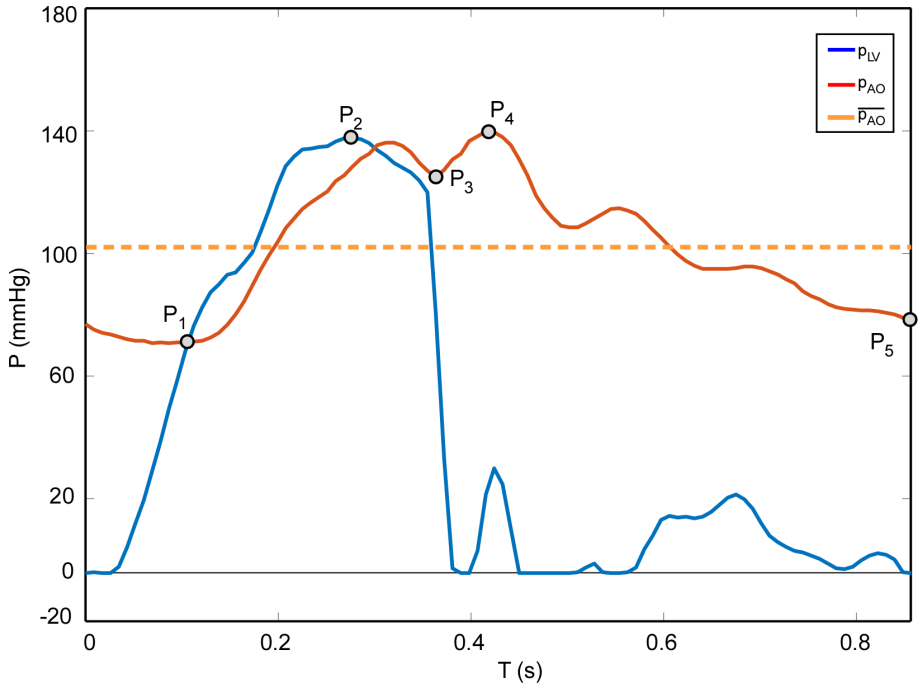

Fig.4.5 Ventricular, aortic pressure, and mean aortic pressure curves for a test with St.Jude Epic aortic porcine valve. Grey dots highlight the principal curve points.

The obtained values remark the pulse duplicator ability to obtain curves closed to physiological references, and strengthen the hypothesis of a bump effect caused by the metallic structure, here mitigated by the presence of a more elastic tissue and Teflon valve annulus (the housing system was the same, also in hole dimension).

4.1.3 Comparison against ViVitro

As third and last semi-quantitative comparison, the pressure and flow trends obtained with HeR pulse duplicator and ViVitro were compared. In these tests the same mechanical and biological valves were adopted (On-X 25mm at annulus), also equal flow conditions were imposed (see *4.1.1*). Moreover, the aortic root in the same setup was a straight root without sinuses, to be close to HeR configuration.

In *fig.4.6* and *fig.4.7* are reported ViVitro mean curves for 10 cycles, for mechanical and bioprostesis, respectively. These trends have to be compared to *fig.4.1* and *fig.4.5*. In particular, referring to *fig.4.1* (mechanical valve), the opening and closing pressures (P_1 = 77.8 mmHg and P_3 = 105.4 mmHg) are slightly different between the experiments, where the ViVitro normally shows similar opening but higher closing pressure (about 130 mmHg). Instead, the ventricular systolic peak value is analogous. In terms of global timing of the cardiac cycle the main phases are conserved and similar in the two experiments, with same percentage of systole, same point of aperture, closure and maximum closing volume.

Fig.4.6 Mean pressures (p_v, yellow line; p_{ao}, red line) and flow (upstream aortic valve, blue line) trends for Sorin Bi-Carbon 25 mm obtained with ViVitro superpump.

The flow peak is a bit higher in the ViVitro (similar aortic forward volume in one cycle, 70 ml), but the curve shape is very close between the experiments. Considering the ViVitro pump as a gold standard, the absence of a so wide peak as the saw for the HeR curves could be explained looking at the amount of working fluid. The *4 l* necessary to perform ViVitro tests reduces significantly the inertia, moreover, a less rigid system and shorter upstream and downstream tubes less affect pressure reflection phenomena that affect the

dicrotic notch. Starting from these consideration a revision of the HeR aortic section is in progress.

Table 4.1 expresses a brief comparison between the two workbenches (referred graph are *fig.4.1* and *fig.4.6*), in which the differences are highlighted in light orange. Seems clear how a more homogenous positive pressure drop, seen in HeR curves, produces a higher transaortic drop, that reflects in a smaller EOA. That difference could be ascribed at the different compliance of the aortic area between the experiments. Despite the already discussed aortic peak value, the other parameters are aligned between the two tests, except for the regurgitant fraction (and the relate volumes). This is probably due to the different valve housing, is opinion of the author that the original ViVitro housing due to its rigidity could sometimes improve fictitiously the regurgitant quantities.

Data Description	ViVitro	HeR
TransAortic press drop (mmHg)	4,57	11,08
TransAortic max pressure (mmHg)	21,13	28,20
Aortic mean pressure (mmHg)	98,62	100,82
Aortic minimum pressure (mmHg)	70,75	70,81
Aortic maximum pressure (mmHg)	129,44	168,67
Ventricular max pressure (mmHg)	127,01	133,54
Pumped stroke volume (ml)	105,78	104,20
Aortic forward volume (ml)	84,17	75,43
Aortic cardiac output (l/min)	5,01	5,01
Aortic closing volume (ml)	-4,46	-3,43
Aortic leakage volume (ml)	-8,18	-0,64
Aortic peak flow [P]	576,04	530,45
Aortic regurge fraction (%)	15,02	5,61
Aortic orifice area (cm^2)	3,21	2,49

Table 4.1 Global hydrodynamic parameters comparison between Vivitro and HeR pulse duplicator for an On-X 25mm aortic valve.

For porcine valve test the comparison gave very good results. Both in terms of pressure curves shape and also from a quantitative point of view for opening ($P_1 \approx 70$ mmHg), closing ($P_3 \approx 130$ mmHg), ventricular systolic peak ($P_2 \approx 145$ mmHg) and aortic dicrotic notch values (*fig.4.7* and *fig.4.5*). The main phases of cardiac cycle are analogous in the two experiments, with same percentage of systole, same instant of aperture, closure and maximum closing volume. Moreover, pressure and flow values are similar to physiological references, reinforcing the goodness of the experimental model.

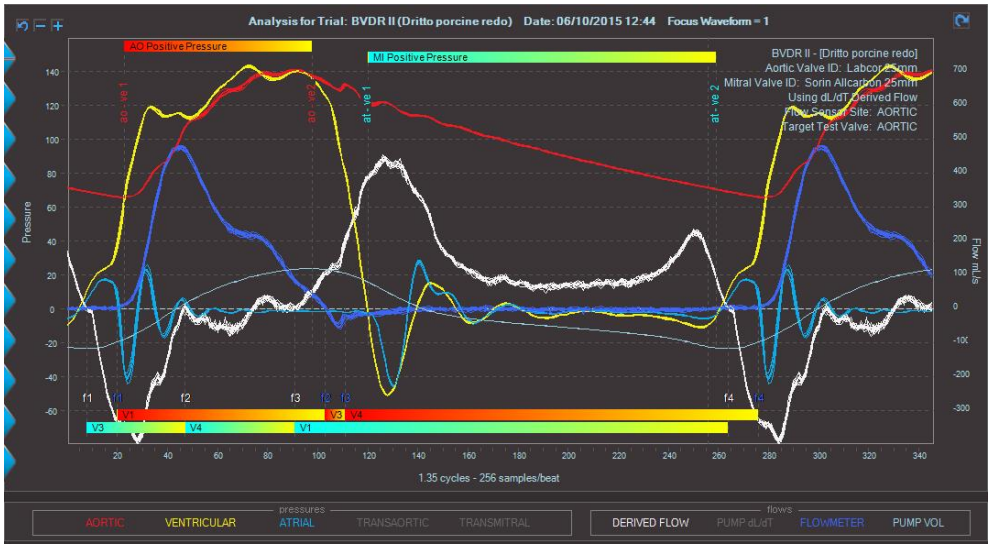

Fig.4.7 Mean pressures (p_v, yellow line; p_{ao}, red line) and flow (upstream aortic valve, blue line) trends for Labcor porcine 25 mm, obtained with ViVitro superpump.

4.2 First results for flow variation

To investigate the performance range of the mock loop, and its ability to provide coherent results for different parameters, a test campaign was developed. The boundary flow conditions were varied inside a physiological range, and a comparison of the hydrodynamic performances was carried out. Two flow parameters were varied: stroke volume and period of the cardiac cycle, maintaining the same ratio between systole and diastole phases.

For all the exams, an aortic mechanical bileaflet On-X valve (25 mm) and a mitral mechanical bileaflet Sorin Allcarbon valve (27 mm) were used. The fluid was saline solution at environment temperature. Each described test (and referred hydrodynamic parameters) will be presented as a mean of 10 non-consecutive cycles.

4.2.1 Stroke volume changes

The one cycle aortic forward volume was varied from 55 ml to 95 ml, maintaining the heart rate equal to 70 bpm. Four levels were studied (Q_1 = 55 ml, Q_2 = 75 ml, Q_3 = 85 ml, and Q_4 = 95 m), taking Q_1 as rest reference condition. This stroke range produces a cardiac output from 3.9 l/min to 6.5 l/min. The waveforms were saved when mean aortic pressure reached 100 mmHg. To obtain a more concise analysis, the differences between these conditions are condensate in *fig.4.8* and *fig.4.9*, for pressure and flow variations, and in *table 4.1* for what concerns with the hydrodynamic parameters.

Fig.4.8 shows the 4 coupled pressure curves, with a specific colour legend, maintained for the flow curves too. Ventricular trends are similar in shape and timing, with the exception of the 75 ml (yellow) that seems a bit shifted forward. The aperture of the valve is anticipated (in pressure) for higher stroke volume (from 70 to 47 mmHg, increasing the stroke), as the peak value, that increases for the different flow conditions (from Q_1 = 135 to Q_4 = 165 mmHg). The closing phase is extremely fast for all configurations, and hummer effect in aortic pressure increases proportionally to the ventricular peak.

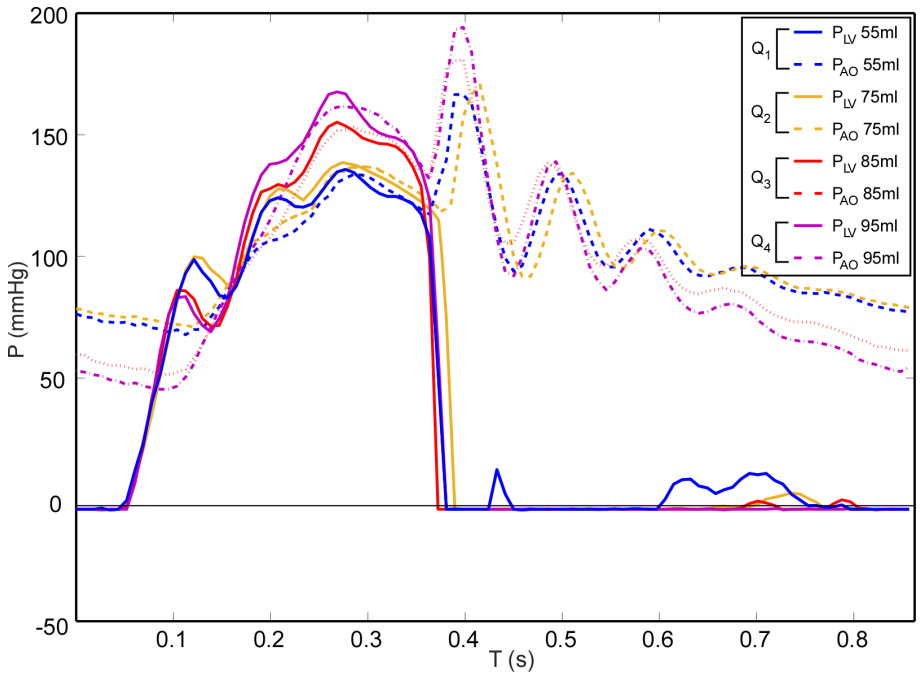

Fig.4.8 Measured pressures across the aortic valve for different flow conditions. Four ejected volumes are shown: Q_1 = 55 ml, Q_2 = 75 ml, Q_3 = 85 ml, and Q_4 = 95 ml.

Fig.4.9 expresses flow behaviour just upstream the aortic valve. Here the differences between the experiments are clearly evident in a proportional increasing of the flow peak and a semi-perfect scaling of the curves (from 437 ml/s, 532 ml/s, 600 ml/s, up to 700 ml/s for Q_4). Seems interesting to notice how the shift in the initial phase becomes close to zero during flow decreasing. A different closing volume is also observable: for 55, 75 and 85 ml they are very similar, instead for Q_4 (95 ml forward volume) it increases a lot. That effect has been confirmed also by hydrodynamic parameter values.

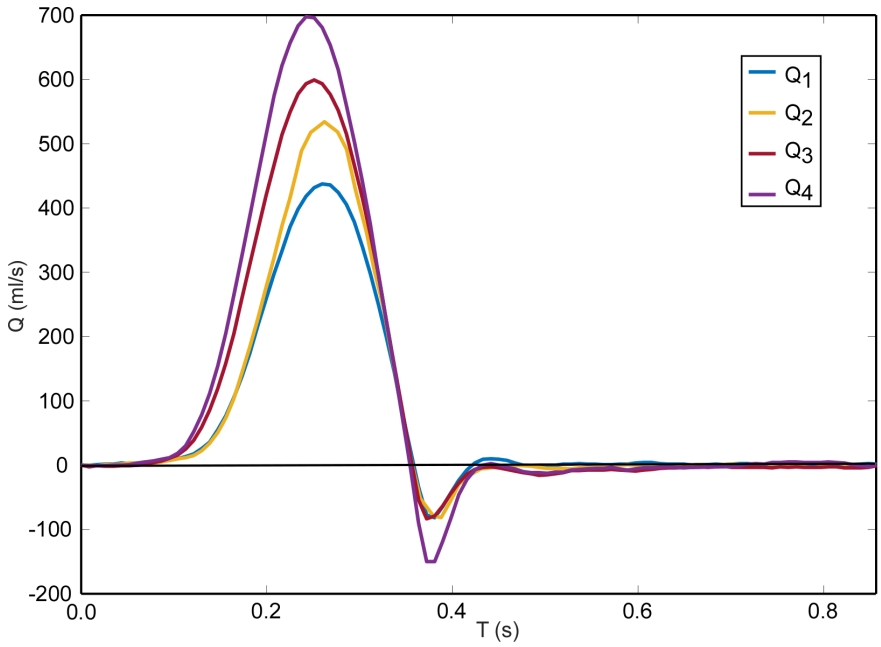

Fig.4.9 Measured flows upstream the aortic valve for the described four conditions.

Table 4.1 summarizes the hydrodynamic parameters (computed following ISO 5840:2009) for these experiments, carried out using the MatLab post-processing developed program. Looking at highlighted green values seems acceptable to assert that the increasing of forward volume is well replicated in the variation of hydrodynamic quantities. This helps to affirm that the pulse duplicator is able to simulate with a good precision different flow conditions. In yellow are highlighted the closing volumes: for Q_4 it is higher than the previous, as was seen in *fig.4.9*. That unusual variability will check with a larger measurements campaign. The well-know hummer problem has been highlighted in red: the non-proper physiological values underline the necessity to develop a more elastic housing especially for high cardiac output experiments that will be performed.

Data Description	Q1	Q2	Q3	Q4
TransAortic press drop (mmHg)	9,94	11,08	12,06	13,80
TransAortic max pressure (mmHg)	29,31	28,20	31,99	35,48
Aortic mean pressure (mmHg)	101,36	100,82	99,13	99,31
Aortic minimum pressure (mmHg)	69,34	70,81	54,20	47,35
Aortic maximum pressure (mmHg)	158,62	168,67	179,72	190,60
Ventricular min pressure (mmHg)	-4,12	-3,98	-4,04	-4,01
Ventricular max pressure (mmHg)	136,42	133,54	155,39	165,88

Pumped stroke volume (ml)	86,41	104,20	119,17	131,74
Aortic forward volume (ml)	60,86	75,43	83,95	96,28
Aortic cardiac output (l/min)	3,99	5,01	5,56	6,42
Aortic closing volume (ml)	-3,12	-3,43	-3,35	-5,10
Aortic leakage volume (ml)	-0,08	-0,64	-1,67	-1,12
Aortic peak flow [P]	440,42	530,45	604,83	689,67
Aortic regurge fraction (%)	5,12	5,61	5,99	4,79
Aortic orifice area (cm^2)	2,05	2,49	2,76	2,96

Table 4.2 Global hydrodynamic parameters comparison for the stroke volume changes.

4.2.2 Period changes

In this second investigation the period was varied from 70 bpm to 100 bpm, maintaining the aortic forward volume about 75 ml. Three intensities were studied: T_1 = 70 bpm, T_2 = 85 bpm and T_3 = 100 bpm, producing a CO = 5.0, 6.2 and 7 l/min. T_1 was kept as reference physiological rest condition. Also for this campaign, the difference pressure and flow variations were measured and are shown in *fig.4.10* and *fig.4.11*, respectively. The results are shown using a percentage scaling, to better enhance the differences across the experiments.

Looking at the pressure trends, the opening and closing values are in general correct. Rising the heart rate, the mock loop answer is not dissimilar across the tests in terms of minimum and maximum pressures. Instead, a re-scaling of the x-axis values has enhanced a shift of the pressure curves, which tend to move forward in the cycle for high heart rate. This effects is easily observable at the closure, where the closing point move to the right (a difference of t/T=10% between T_1 and T_3 was measured) with a strong decrease of the aortic pressure, that follows the ventricular fall after the initial closing. A shift appears also in the flow trends, with the same gap observed for the pressures. This difference seems strongly connected to oscillatory phenomenon that characterized the high heart rate experiments.

A flow mass oscillation seems clearly affected the pressure trends, with a frequency that doesn't change across the tests but, probably due to the intensification of the repetitions, affects more the curves. Is still not completely clear which physical effect exists behind. A reasonable hypothesis could be the presence of a pressure vibration produced by the rigid housing system. This contribution appears only at valve open in ventricular and aortic trends and after lingers in the aortic curve, underlining its origin downstream the aortic valve. However, a so significant oscillatory behaviour couldn't be explained only in terms of discharge. This comportment, visible in *fig.4.10*, doesn't affect the flow upstream the valve (*fig.4.11*), so it could be also read as a pressure phenomena without a direct influence on the flow discharge. For increased heart rate, flows tend to become higher in terms of peak value, although the pumped stroke volume remains constant about 102 ml/beat.

An important practical consequence of the described oscillations is represents by the impossibility to achieve the correct hydrodynamic performance with high accurancy. In particular, pressure drop and effective orifice area, are strongly affected by this phenomena and seems now not suitable for a quantitative comparison with the other literature results.

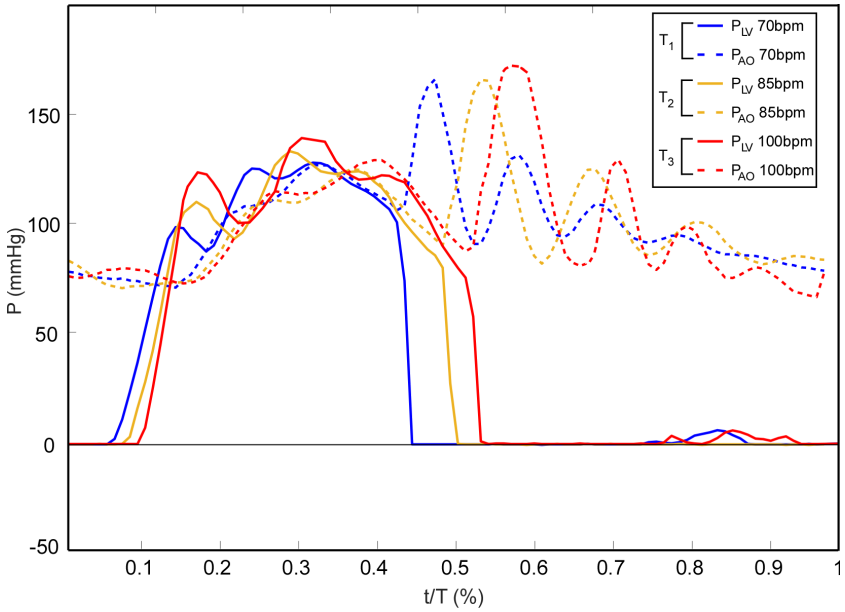

Fig.4.10 Ventricular and aortic pressure curves for period changes. The trends are expressed on x-axes in percentage, for a faster comparison.

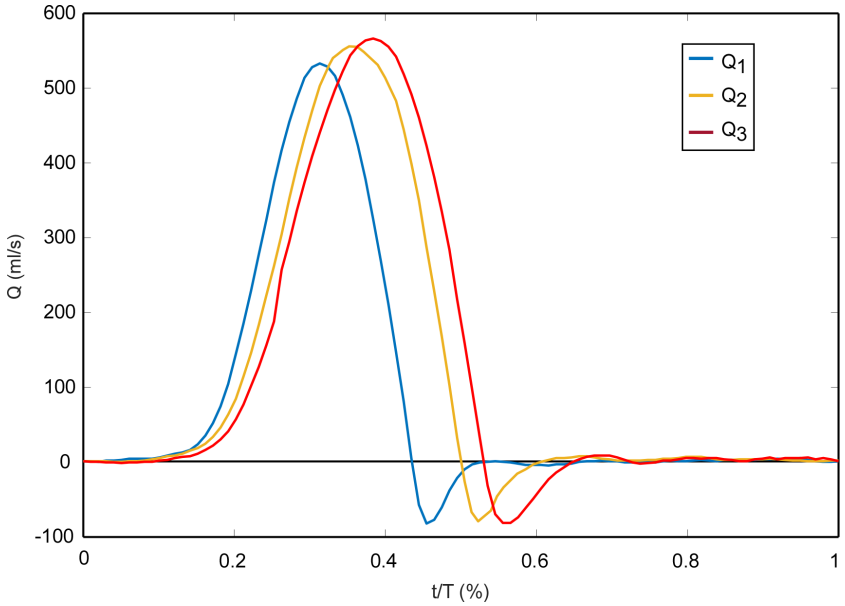

Fig.4.11 Flow curves upstream the aortic valve for period changes. The trends are expressed on x-axes in percentage, for a faster comparison.

To better understand the origin of this disturb, a basic signal analysis has been developed. Interesting results come out: across the experiments a constant frequency of the oscillations was found. In particular, *fig.4.12* illustrates 75 and 100 bmp ventricular and aortic pressure waves filtered with a digital filter that cuts precisely only a span of frequencies between 10 and 20 Hz. The comparison between the "raw" curves is immediately, with a strong decrease of the main oscillation path. Despite a digital post-processing of the waves seems not a scientific doable way, could help to find the physical origin of the problem.

In order to better understand this, a larger comparison campaign with a porcine valve, is in develop. Moreover, a new elastic housing system is in production. That solution will surely modify the answer of the system in proximity of the aortic valve, where the pressure taps are inserted.

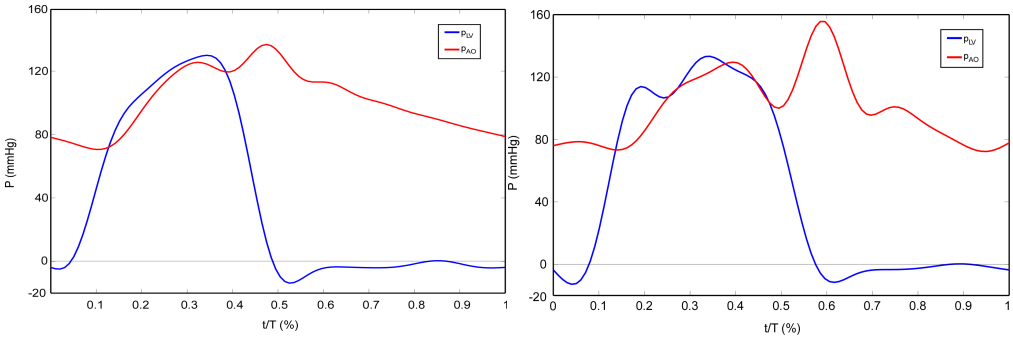

Fig.4.12 Left: filtered pressure curves with a selective bandpass filter for the T_1 test. Right: same filtering for T_3.

4.3 HeR pro and cons

After this first induction, seems that the mock loop expresses a good ability to simulate a physiological behaviour in terms of pressure curves and flow trends. In comparison with physiological literature curves, the pulse duplicator provides a correct distribution of cardiac cycle phases timing and values for remarkable pressure and flow points. The possibility of a wide range variation in terms of cardiac output is clearly an advantage in an experimental view, already possible in the actual configuration. Although little problems for high (about 100 bmp) heart rate, founded after a first experiment campaign, several improvements are in development. Despite that, the ability to reach considerable cardiac output is important and satisfied with suitable capacity. Another important skill is represents by the high modulability of the pulse duplicator, which could be modified or extended in function of the particular research topic (as for example the insertion of a compliant phantoms to mimic a vessel region).

Of course, a step-by-step improvement needs a longer time compared to a closed commercial solution, but allows a better understanding of the design complexity and of the physical mechanisms that stay behind the realization. However, at the end of this PhD careers seems possible to affirm that the pulse duplicator expresses good hydrodynamic performance.

Moreover, a custom development without private companies influence, except for the linear motor and the measurement instrumentations, allowed a strong decrease of the cost in comparison with commercial solution. An example comes from the ViVitro cost, that is about 100 thousand Euros, instead of a HeR Pulse Duplicator that is 28 thousand Euros, at this time.

Also weaknesses are present in the workbench, as the considerable encumber of the system, the high amount of fluid solution that has to be used, and the high rigidity of some parts (as the valve housing). In this way, the new silicon aortic arch will give a benefit in terms of pressure fields and workbench elasticity. As last, the signal processing and post-processing tools are good but still not “perfect”, as the ViVitro software analysis. Despite that the main fluid dynamic parameters requested by the international regulation could be computed and the pulse duplicator can be steers in live-view mode.

4.4 Chapter bibliography

[1]. Caro C., Pedley T., Schroter R., Seed W., The mechanics of the circulation. Cambridge University Press (2ed., CUP, 2012), ISBN 9780521151771.

[2]. Guyton A.C., Hall J.E., Textbook of Medical Physiology. Elseviers Saunders, Eleven Edition. ISBN 0-7216-0240-1.

[3]. FDA Draft Guidance for Industry and FDA Staff Heart Valves – Investigational Device Exemption (IDE) and Premarket Approval (PMA) Applications, last update in 2010.

[4]. European Standard EN ISO 5840:2009, Cardiovascular Implants – Cardiac valve prosthesis – revision of 2005 version. Fourth Edition 2005-03-01. EUROPEAN COMMTEE FOR STANDARDIZATION.

Chapter 5

In vitro analysis of CardioWest™ TAH-t hydrodynamic performance: Freedom® portable driver behaviour

5.1 Introduction to heart transplant and Total Artificial Heart prosthesis, overview and statistic data

The present chapter, and the described research, is focused on the determination of *in vitro* fluid dynamic response of a temporary total artificial heart substitute, the CardioWest™ (CW), using physiological parameters values for pressure range and Cardiac Output (CO). The role of artificial heart devices become relevant in clinical field about 15 years ago, due to a constant grow of heart failure and serious heart pathologies. As extreme but not rare chance, the substitution of an ill heart imposed the insertion of a mechanical double-pump, one for each ventricle, which normally is powered by an external drive. This solution is normally temporary and installed as a bridge to transplantation device. Of course if the location of the power console is outside the body -as for CW-, from one side allows limiting the weight inside the body, but from the other creates problem of a direct-wired connection from inside to outside of the patient. The deducible complexity in the design and realization of a TAH-t figure out how the market's solutions are restricted to two: the AbioCor™ and CardioWest™ total artificial hearts (Cohn et al., 2015). Devices like the CW are necessary in case of acute heart failure (HF), underling the importance of a constant development and performance assessment of more and more reliable devices that could be implanted in easy way and that have to operate in a such complex environment.

The characteristics of the CW coupled with a portable drive unit, the Freedom® driver (FD), was analysed in this experimental work. The principal aim was to determine if the CW simulator is a reliable workbench to test the coupled system, able to enhance the best and diminish the weak points of the driver, in order to give some suggestions to the clinicians and the device designer. The investigation was performed using a parallel approach. Several

in vitro tests, to estimate the performance of the FD using a specific mock loop as patient simulator, were performed, and *in vivo* tracking of a very long-term implantation was done.

The experimental investigation presented in this chapter was promoted by a clinical need, referred on a specific case, registered in the Centro V. Gallucci, within the Cardiovascular Surgery Operative Unit, Central State Hospital of Padova (Tarzia et al., 2015). In particular, the patient was subjected to implantation of CardioWest™ in December 2007 (first Italian CW implant). The heart transplant was performed after 1374 days, so the patient was linked to the TAH-t for longer than anyone had been previously in the world. During that period, different external consoles were adopted (BigBlue, Companion®, and then portable Berlin-heart Excor®) and several CPET baseline tests were performed. In December 2010 the patient was moved to the Freedom® portable driver, and other CPET exams were carried out at a fixed time gap, to monitor the patient's condition. A couple of months after the last driver change, the patient showed a dyspnea with pulmonary edema: these symptoms had not been previously expressed. In particular, due to an observed reduction in maximum power output and a lower peak of VO_2 in Freedom CPET (10.1 mL/Kg/min, 34% predicted) compared to the Baseline, the patient was listed for an urgent heart transplant. These evidences stimulated the surgeons to investigate the problem from a bioengineering point of view, bringing the clinical need to our attention.

To better understand the technical purpose of this work, and the thought at the base, seems essential a fast introduction focused on the prosthetic solution, for patient waiting for heart transplant, based on the most relevant literature data.

5.1.1 The scarcity of donors and increment of heart failure

Recently, the National Health and Nutrition Examination Survey (NHANES) indicates that more than 23 million people in the world are affected by diseases related to HF. Of these, 7 million are located in Europe, and 7.5 million in North America (about 5 million people in USA ≥20 years of age) (Westaby, 2013; Go et al., 2013). This review-data put the HF at the top of the medical issues impact ranking, in terms of human and economic resources. It is evaluated that, for the US, the direct and indirect costs for adult treatment were greater than $34 billion in 2008, and predicted to be $44.9 billion in 2015, rising to $70 billion in 2030 (Guruprasad et al., 2012). It is also estimated that heart disease has high incidence in the population over 65 years of age, and the occurrence of HF is about 10 per 1000 people (Go et al., 2013). Patients affected by HF are split into four increasing severity classes, in accordance with the common classification method released by the New York Heart Association (NYHA) (McMurrey et al., 2012). From the National Heart Lung and Blood Institute (NHLBI) data, around 35% of the patients fall into Class I, the same proportion into Class II, 25% into Class III, and the remaining 5% into Class IV. The main

treatments for HF are: medical drugs, heart resynchronization (CRT), heart transplant (HT), or, in specific cases, the uses of mechanical prosthetic assistance circulation devices, like Total Artificial Heart (TAH) or Ventricular Assist Device (VAD) (Guruprasad et al., 2012). From the latest studies, only 8% of the treated patients were alive at a two year follow-up. Furthermore, the patients treated with drug therapy or CRT, displayed a one year mortality equal to 15% and 28%, for Classes III and IV respectively (Westaby, 2013; Guruprasad et al. 2012; Kemp, 2012). In this introduction, and for the discussed study, we will focus on the highest risk class, i.e. on the patients who are unable to perform any physical activity without pain. For this case, the mostly common treatment is replacing the heart (Westaby, 2013). From the Organ Procurement and Transplantation Network (OPTN) data, there are about 3555 people waiting for HT, updated on 6 September 2013, considerably greater than the number of donors in 2012, which was 24516 (ref. OPTN). This gap, and the steady increase of people affected by HF, emphasizes the key role of prosthetic devices, like TAH, to provide cardiovascular functionality for people waiting for HT.

5.1.2 The prosthetic solutions: AbioCor™ and CardioWest™

These prosthetic devices express a high mechanical complexity, but at the same time they must guarantee a high reliability and a long-life at fatigue for all the components. The AbioCor™ is designed to sustain the body's circulatory system and to extend the lives of patients who would otherwise die of heart failure. Its unique design allows it to be totally implanted within the body. The patients are not tethered to air-pumping console nor do they have wires or tubes piercing their skin. As the CardioWest™, it is intended for use in end-stage heart failure patients whose hearts have irreversible left and right ventricular failure and for whom surgery or medical therapy is inadequate.

The thoracic unit consists of the artificial ventricles, which contain their corresponding valves, and a motor-driven hydraulic pumping system. The hydraulic pumping system uses pressure to shuttle blood from side to side—in this case, from the artificial right ventricle to the lungs or from the artificial left ventricle to the rest of the body. To create this pressure, the pump's motor rotates at 4000 to 8000 revolutions per minute. An internal emergency rechargeable battery is continually charged by the external power source. The internal battery can provide up to 20 minutes of operation while disconnected from the main battery pack. The AbioCor is normally powered by an external console or battery packs. The internal battery will power the pump only when the external power supply is disconnected. Power to the AbioCor is achieved with an energy-transfer device called a transcutaneous energy transmission (TET) system. The TET system consists of internal and external coils that are used to transmit power across the skin. Because tubes or wires do not pierce the skin, the chances of developing an infection are decreased. External battery packs can power the AbioCor for 4 hours.

The AbioCor competitor, and the most used TAH-t in the world, is the CardioWest TAH-t. The technical characteristics of the CW will be discussed in detail in the next section, here the attention is focused on a fast literature review about the implanted outcome and the international certifications obtained by SynCardia.

In 2004, the SynCardia Systems, Inc. received FDA endorsement for the commercialization of the CardioWest™ temporary Total Artificial Heart (CW), and the approval from Centers for Medicare & Medicaid Service reimbursement, in 2008 (PMA FDA). This device is specified as a temporary total artificial heart and the clinical designation is a Bridge To Transplantation (BTT) device in patients with imminent risk of death (Class IV). These patients normally suffer from total aortic dysfunction and multi-organ failure, so the TAH-t could be the best solution, as it allows an organ to recover from a previously imposed high cardiac output. In particular, the CardioWest™ is the first TAH approved by FDA for use as a BTT device and, since 2004, has had more than 1200 installations (over 335 patients per year) (Slepian et al., 2013; Torregrossa et al., 2013). In 2012, the TAH received the FDA designation as a Humanitarian Use Device (HUD) for use in U.S. patients with critical condition who are not eligible for heart transplant. This is a step towards clinical use, as an alternative to HT, i.e. for ‘‘destination therapy” (FDA HUD). This topic is still in full development and will become increasingly followed (Torregrossa et al., 2013). It is quite easy to find clinical case studies for the BTT CW in the literature, due to a large data set collected over 20 years of use by US and Europe principal medical centres (Copeland et al., 2004-2; Copeland et al., 2004; Copeland et al., 2012; El-Banayosy et al., 2005; Leprince et al., 2002). All these studies show the great difficulties to point out the real performances of the CW in repeatable and non patient specific conditions. In particular, it becomes clear that it is necessary to carry out several in vitro tests, to explain the performance of the “stand-alone” device, in reliable physiological conditions. Specifically in this context, *in vitro* experiments are preferred to *in vivo* analysis because they allow the free control and fine adjustment of all the physiological parameters of the system (e.g. pressure range, cardiac output, etc.). In this study we show how this goal can be reached using a customized mock loop developed for *in vitro* tests for the CW TAH-t: the CardioWest Simulator (CWS). Only one scientific study was performed using the CWS (Spurlock et al., 2012), to test the performance of a new design of pump for a temporary extra-corporeal device. In literature, few *in vitro* works try to point out the performance of continuous flow TAH (Fukamachi et al., 2010), or pulsatile bioprostetic TAH (Jansen et al., 2012), or, even, to evaluate the *in vitro* response to preload and afterload of the MagScrew TAH (Weber et al., 2002), using other pulse duplicator systems. Another work tried to estimate, via a non-invasive method, the mean parameters in the Jarvik-7, using the Donovan mock loop. (Vonesh et al., 1991). Other mock loops were developed to estimate the in vitro performance of electrical TAH (Zapanta et al., 2005), or

the CFTAH performance used as pulsatile devices (Khalil et al., 2010). All these *in vitro* studies underline the importance of an experimental methodology applied to the cardiovascular device, in order to improve understanding of their behavior.

In the present study, the CW behavior was tested in a simulation of post-hospitalization therapy, using the only portable drive unit developed by SynCardia: the Freedom® one (Jaroszewski et al., 2011; Friedline & Hassinger, 2012). The *in vitro* tests performed provide the hydrodynamic characterization of the system, and a first estimation of the drive behavior. The controlled change of the main physiological parameters (cardiac output and pressures), for different levels of blood circuit resistance, allowed the understanding of the stand-alone behavior of the drive, giving possible suggestions for a specific clinical case.

5.2 CardioWest TAH-t, drive systems and patient simulator mock loop

In this section are described the most relevant instruments used to perform the *in vitro* tests; starting from a functional description of the TAH-t, then moving to the workbench specifically designed to housing the prosthetic artificial heart, and finally focusing on the different external pumps used to provide the correct power to the system. The last section describes the direct measured quantities during the tests and the estimated physiological parameters.

5.2.1 CardioWest TAH-t

The SynCardia CardioWest™ (CW) TAH evolved from the early design of Kolff, Olsen and Jarviks during the '70s. The actual CW is made of two independent ventricles, which are implanted intra-thoracically in the orthotopic position, (*fig.5.1a*). The implantable ventricles are connected to an external driver system, a pneumatic compressor, allowing co-ordinated ventricle activation with independent parameters for each ventricle, through two percutaneous drivelines (*fig.5.1b*). The two artificial ventricles are subdivided, via a movable diaphragm, into a blood chamber and a gas section. Each chamber is housed in an external case fabricated with polyurethane solution (SPUS), over laid with a DacronTM mesh, to which are connected a PVC driveline, and a superior part that contains both the inflow and outflow zone made with SPUS graft and isoPlastTM (thermo plastic polyurethane) connections. Two mechanical monoleafleat Medtronic-Hall™ heart valves (25 and 27 mm, for outflow and inflow) are here placed. The diaphragm is comprised of a multilayer SPUS matrix, with the four layers providing resilience and toughness to the membrane, which must undergo more than 5107 cycles/year. CW is usually implanted in orthotopic position after the complete

replacement of patient's native ventricles. It is designed to provide conditions closest to the physiological range, i.e. 50 ml for stroke volume (SV) and 6 l/min for the cardiac output (Shah et al., 2011; Slepian et al., 2013). However, the SynCardia™ Inc. ensures proper functioning up to 70 ml and 9.5 l/min respectively (SynCardia Systems, Inc., Summary of Safety and Effectiveness, CardioWest TAH-t FDA Premarket Approval Application). Indeed, the designed work conditions include a partial filling and total emptying of the ventricles; in this way, the device provides a CO reserve (10-20 ml) for an increased requirement of oxygenated blood during physical activities, or allows an increment in the venous return.

Understood the design complexity of the prosthesis, is important to remind that also the usual work conditions are quite hard. Indeed, most of the parts are in continuative contact with blood and physiological fluids. This topic opens the important issue of the biocompatibility of the adopted materials, which involved lots of limitations and additional attention. In these studies we completely don't take in account biocompatibility problems, using desalined water as work solution.

5.2.2 External Drivers

The extra-corporeal drivers, named Companion® and Freedom®, are today the most common driving units used for giving the correct power to the TAH-t (*fig.5.1c*). The Companion® is uniquely designed for hospitalized patients; it is quite cumbersome, but provides a great flexibility of use, allowing many variants of working parameters (Slepian et al., 2011; Slepian et al., 2013), see performances in Table 1.

The state-of-the-art Companion 2 (C2) hospital driver supports patients from implant of the SynCardia temporary Total Artificial Heart until their condition becomes stable and they can be switched to the Freedom® portable driver. The C2 driver provides pneumatic pressure for the Total Artificial Heart using one of two air sources. The primary source is hospital air, which provides quieter operation. The secondary source is two internal, redundant compressors to provide increased patient safety and reliability. The C2 also supplies independent vacuum for the left and right ventricles to provide optimum performance for each patient based on their individual needs. For the operating room and initial stages of patient recovery, the C2 driver is docked in the Companion Hospital Cart, which features sturdy support handles and locking casters to provide robust, reliable support. Once the patient is out of bed and ambulatory, the C2 driver can be docked in the Companion Caddy to provide the patient with greater mobility in the hospital. The Caddy supports patient recovery by making it easier for patients to move and exercise, which helps them to rebuild their strength and improve their health. The C2 user interface features a full-color touch screen. This screen displays alarm and power status, and on-screen adjustable parameters including pressure, flow and cardiac output. The C2 can operate in three different modes:

- Operating Room (OR) Mode – a password is required to enter OR Mode, which provides full menu access, including system check and muted alarms.
- Intensive Care Unit (ICU) Mode – a password is required to enter ICU Mode from Ambulatory Mode, and requires double confirmation for any changes.
- Ambulatory Mode – no changes are permitted, and graph and settings data can be minimized.

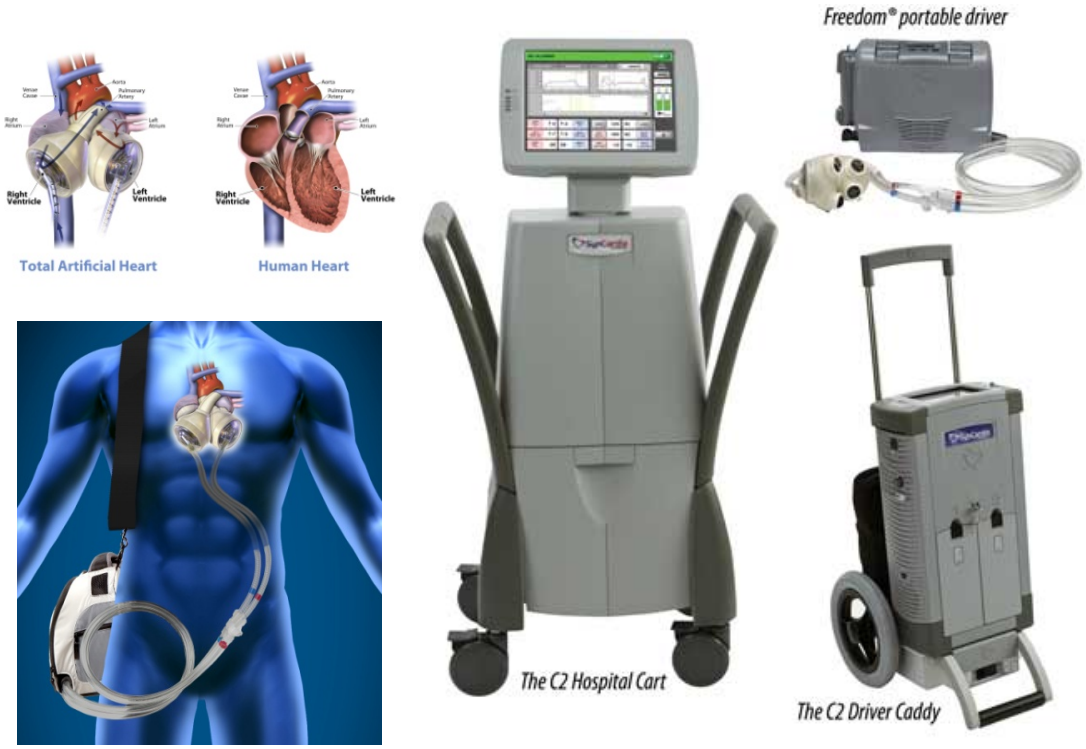

Fig.5.1 The CardioWest TAH-t implanted site and positioning (1a). The device connection to the external drive through two percutaneous cables (1b). The extra-corporeal drivers, Companion® Hospital cart and Freedom® portable driver are the most common driving units used to ensure the correct power to the TAH-t (1c).

When eligible patients become stable, they can be switched from the C2 hospital driver to the Freedom® portable driver, which provides the patient with greater mobility. Patients who meet discharge criteria can then leave the hospital to wait for a matching donor heart at home and in their communities.

The FD, provides a simpler user interface, portability and lightness even outside a hospital environment (7 Kg in a backpack size). The latter is

unquestionably the best solution for non-hospitalized patients. Because of its lightness and functionality, this device improves the quality of life to unthinkable standards only a few years ago. The pump is powered by two lithium-ion batteries that are re-charged using a standard electrical outlet or the cigarette lighter adaptor in a car. This allows patients to recharge their batteries while traveling and at night while they are sleeping. The Freedom drive is strictly embedded, with the regulation of only one parameter possible: the change of the work frequency (125±15 bpm), alterable only by qualified staff during hospital visits (SynCardia Systems, Inc., driver Freedom® user guide), see Table 1 for details.

5.2.3 Patient Simulator

The CardioWest Simulator (CWS) (*fig.5.2*) is the patient simulator used in the *in vitro* tests described in this chapter. Its developed and authorized by SynCardia Inc. for staff training or pre-implantation tests of the CW (SynCardia Systems, Inc.,Temporary Total Artificial Heart – Patient Simulator and Training Center - MOCK CIRCULATION TANK user's manual). Basically, it is a hydraulic system for cardiovascular device performance estimation, and it is a modified version of the most common Donovan mock loop (Donovan, 1975). It is capable of simulating the cardiovascular system and it reproduces typical human resistance, compliance and pressure range. The normal use of this device is for trial and clinical application. It reduces high costs and the risk of *in vivo* trials during the clinical investigation, and it is also used in the test protocol to verify the CW performance, just before surgical implantation into the patient. Let's have a fast look at the CWS construction, helped by *fig.5.2*. It is made of a plexiglass structure with a total size of around 23 l; the external dimensions are h=40.7, l=64.0 and d=20.4 cm. It is divided into four main chambers, to reproduce the four physiological pressures of the cardiovascular system: Aortic artery chamber (AoP), Pulmonary Artery chamber (PAP), Left Atrial chamber (LAP) and Right Atrial chamber (RAP). A toggle valve is placed at the top of each block, which allows for the adjustment of individual compliance levels, according to the proportional behaviour, $P \cdot V = k$ (P=pressure, V=volume, k=constant), i.e. air volume increases results in increased compliance (Hicks, 1990).

The TAH-t is normally connected to the mock loop using two suitable elastic pipes. The right ventricle of the TAH is connected to the RAP chamber, through the right inflow tube, and to the PAP chamber using the right outflow tube. In a similar way for the left ventricle, even if here LAP is the inflow chamber and AoP is the outflow chamber. The CWS is also able to simulate the human vascular resistance: a gate valve placed at the connection between the AoP and RAP chambers allows for regulation of the systemic vascular resistance (SVR). Similarly, the tract between PAP and LAP represents the pulmonary circulation, where the gate acts as a pulmonary vascular resistance (PVR). The AoP (and similarly PAP) chamber contains a bellow filled with

water, connected to the valve gate and to a height adjustable reservoir. As the reservoir is raised, the static pressure into the bellow increases, causing the bellow to expand. The result is an increase of the flow resistance, SVR (PVR), from one chamber to the other one.

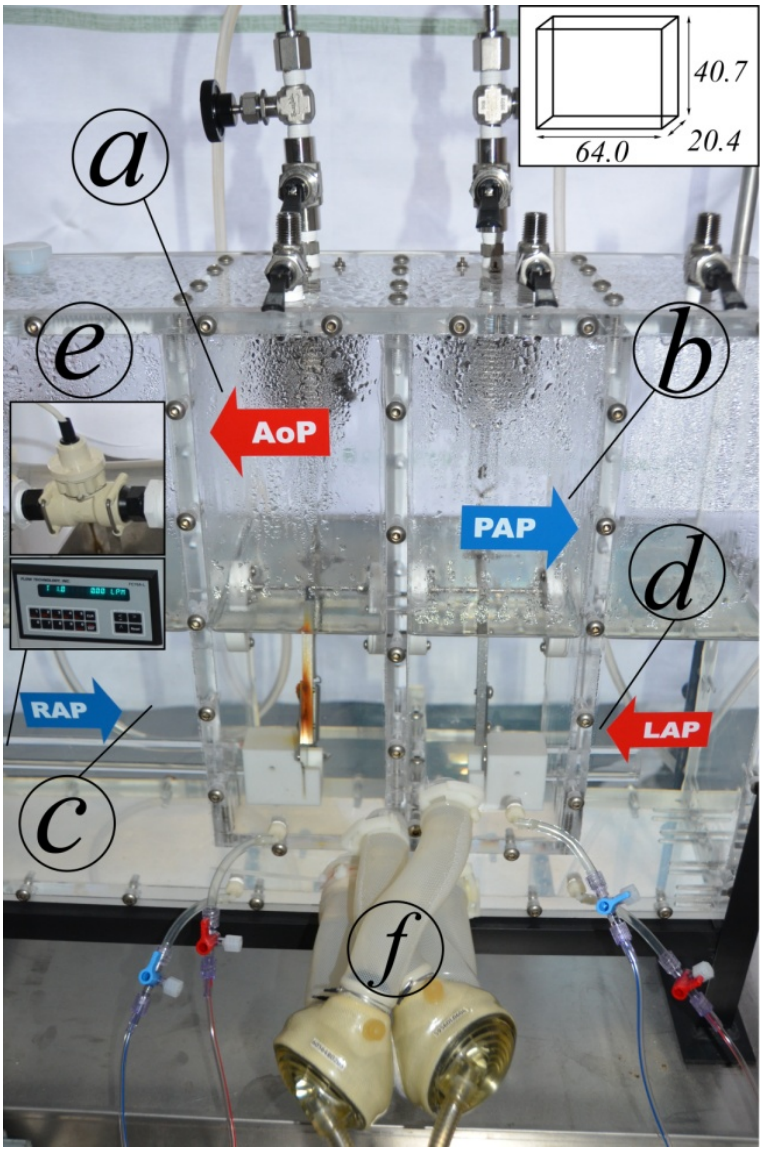

Fig.5.2 The CardioWest patient simulator in a front view, where are visible the different parts: a) aortic chamber, b) pulmonary artery chamber, c) right atrial chamber, d) left atrial chamber and f) is the tested CardioWest TAH-t. In the right up angle the CWS dimension are showed, in cm. e) Shows the ultrasound flowmeter placed at the outflow tract from the aortic chamber.

All the tests performed were related to a specific setting of the vascular resistance (seven levels) and fluid dynamics condition for the patient simulator. In this way, a linear increment of the human vascular resistance was simulated, within a physiological range. Specifically, level 1 corresponds to the minimum vascular resistance, and level 7 to the maximum. This setup allows for 49 combinations of SVR and PVR. For each test, the level of resistance, the Freedom® work parameters, and the fluid-gas volumes ratio in the chambers were set (see Table 1). The work fluid used in the study was desalinized water at 20°C, with a viscosity of 1.001 cP, and a kinematic viscosity of 834.17·10-6m^2/s.

5.2.4 Measured quantities in *in vitro* tests

The measurements performed in the study are: the Left Atrial Pressure (PLA), the pressure range in the Aortic root (PAO), the Right Atrial Pressure (PRA) and the Pulmonary Artery Pressure (PAP). The cardiac output from the left ventricle (COL) and the left Ventricular Fill (VFL) were detected from Freedom's LCD display. Moreover, a posteriori pulmonary and systemic resistances (Rp and Rs) were calculated, and compared to the set on the CW patient simulator. The pressure in the different districts with measured using analog piezometers. The sites for measuring the pressure of PAO and PAP were located immediately downstream of the ventricles, while the PLA and PRA pressure sites are placed just upstream of the left and right ventricles. The *fig.5.3* shows a static calibration example of the PAO piezometer following the SynCardia reference static pressure value (0.835 mH2O), with the reported setup configuration. Starting from the reference value (AoP labeled arrow), the work solution was added and the chamber fluid height (pcalc = δ*10/13.56) was compared to the measured value by the piezometer (pmeas). The correlation value between them is quite high ($r^2 \approx 1$), and confirms the reliability of the obtained measures. The piezometers are designed to only provide the mean value of the pressure in the cycle; moreover five different tests have been performed for each configuration, to provide reliability for the obtained values.

Each set of measurements is composed of the four pressures, the CO and the VF. From the direct measurement of pressures, the pulmonary and systemic pressure drops in the pulmonary circulation derived:

$\Delta P_L = P_{AO} - P_{RA}$, $\Delta P_R = P_{AP} - P_{LA}$.

Knowing the previous parameters, the pulmonary and systemic resistances were computed, as: $R_p = \frac{\Delta P_R}{CO_R}$, $R_s = \frac{\Delta P_L}{CO_L}$, where $CO_R = CO_L - (CO_L \cdot 0.05)$

The cardiac output from the right ventricle (COR), not shown on the display, was calculated via the guidelines of SynCardia Inc., as CO_R = HR VF_r. These quantities help us to better understand the reliability of the system in simulating the human circulation, and to confirm that the physiological output parameters are acceptable.

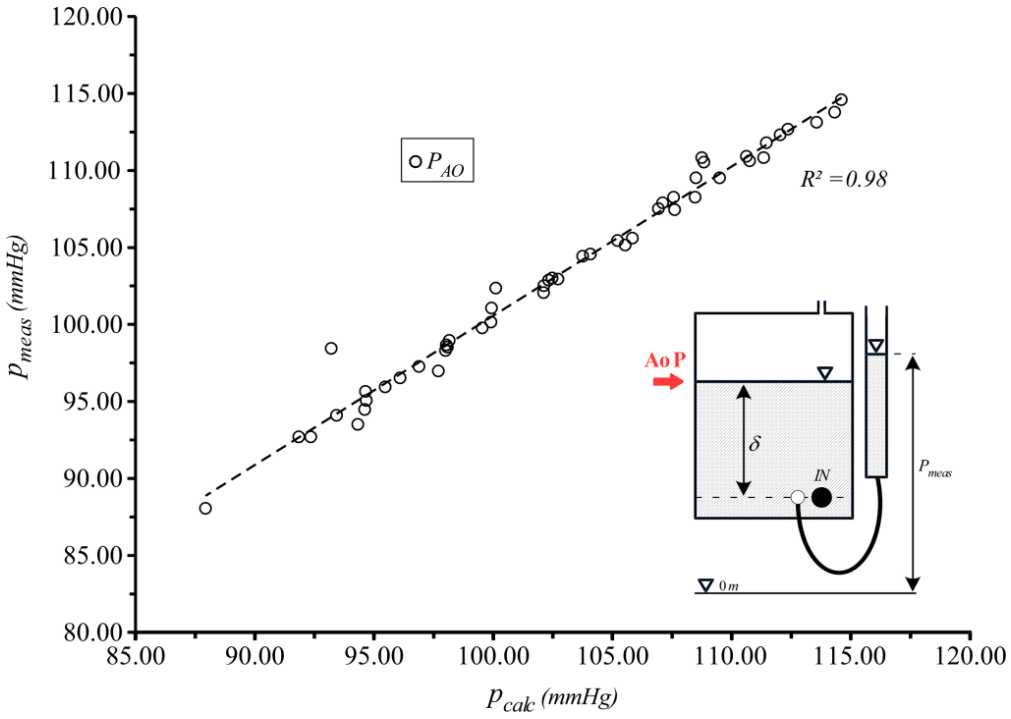

Fig.5.3 A static calibration example for the PAO piezometer, where: IN is the outflow tract downstream the CardioWest left ventricle, at the same high of the measuring site (white dot), d is the distance between the probe site and the free surface (in m of water, or pcalc in mmHg), pmeas the piezometer pressure measured values.

5.3 Hydrodynamic performances of CW and Freedom drive

The performed *in vitro* tests with the CWS and FD, allow the collection of hydro-dynamic data to assess the performance of the coupled system (Table 2).

5.3.1 Workbench sensitivity test

As first examination, a sensitivity analysis was performed in order to verify the correct behaviour of the workbench. In *fig.5.4*, the incremental trend of left atrial pressure (PLA) versus the systemic and pulmonary resistance (SVR and PVR) is shown. The relationship between PLA and PVR is linear, with a regression coefficient equal to k=-0.48, and PLA decreasing by 1 mmHg at each increment of pulmonary resistance. Moreover, the PLA remains constant for different steps of SVR. As can be seen in the inset of *fig.5.4*, the aortic

pressure was stable, as expected, around a constant value (102+-2.5 mmHg), for all the different steps of PVR. The waveforms behavior confirm that the coupled system CWS-FD reproduces physiological behavior with good likeness.

To improve the accuracy of the experimental model, and to verify the correspondence between the stepping workbench resistance and the computed pulmonary resistance (Rp, in Wood units), a posteriori investigation was performed. The results are summarized in *fig.5.5*, where the trend between Rp and steps of PVR is expressed, for 5 repeated experiments. For each pulmonary resistance step (PVR), the systemic resistance was altered, and 7 different measurements were obtained and plotted on a graph (Rs1 – Rs7). The CWS reproduces both a marked hypo-physiological pulmonary resistance (0-1 WU), and a full physiological range of pulmonary resistance (<3 WU), in particular from 1.0 to 2.7 WU. After an initial linear trend, the Rp tends to a plateau, and the curve shapes deviates markedly from the previous semi-linear increment, a sign of an upper limit on the expressible CWS performance. The curve of best fit (black line in *fig.5.5*), expresses how from the fourth to the seventh step of pulmonary resistance, the Rp falls into the physiological range. However, from the first to third step of PVR, the Rp reflects a resistance behaviour that is hypo-physiological. This behaviour underlines the need to test the TAH-t in a wide range of conditions, both physiological and non-physiological.

5.3.2 Freedom Drive performance

One of the most important results of the study is the proven ability to test the FD in physiological conditions, to measure the PAO and PAP pressure range and the SVR and PVR resistances, using an *in vitro* workbench normally designed only for simple device calibration. It is out of doubt that the CW device, in couple with the FD, provides the best actual choice for class IV (or over) patients waiting donors for HT surgery. After adequate training, the hospitalized patient can be transferred to a home recovery, greatly improving life quality. Moreover, the idea for the implanted CW is now shifting from a temporary BTT device to a destination therapy device. In this perspective, the portability and lightness of the device become key in supporting an extra-hospital environment, increasing patient mobility, and their ability of a faster cardiopulmonary rehabilitation. Last but not least, this solution helps to strongly decrease hospital costs.

Looking at the disadvantages of the Freedom Drive, it is not easy to find good statistical or engineering data in literature. In particular, some clinical problems could be related to use of a CW in couple with the Freedom® portable device (Shah et al., 2013; Jaroszewski et al., 2011). Other tests were performed to study the relationship between in vitro measured pulmonary artery pressure and estimated Rp in greater detail.

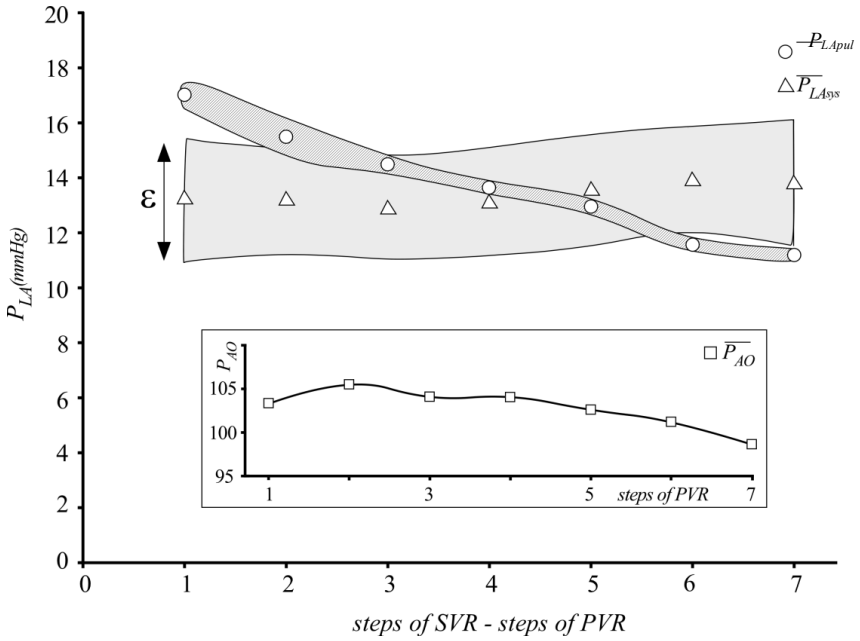

Fig.5.4 Behavior of the left atrial pressure (PLA) versus the systemic and pulmonary resistance (SVR and PVR) changing by steps. The PLApul express a strong decreases instead the PLAsys stays quite constant for every resistance steps. In the inset is present the observed semi-constant PAO trend in changing of PVR by steps.

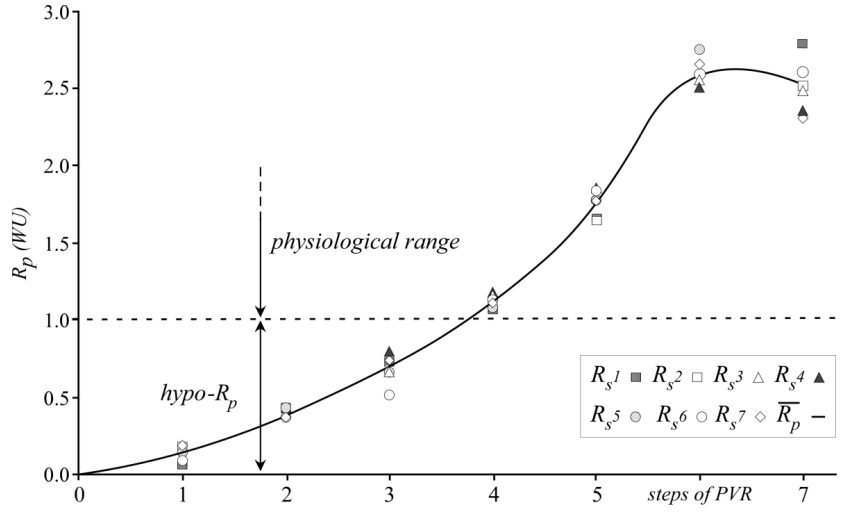

Fig.5.5 A-posteriori calculated pulmonary resistance (Rp) versus steps of pulmonary vascular resistance (PVR). Each mark corresponds to a specific step of systemic vascular resistance. The black line follows the mean value of Rp through the 7 different systemic resistance increments.

In *fig.5.6*, the results of the relationship between the measured PAP and the a-posteriori obtained Rp are proposed. As illustrated, after an initial slow increase, where the R_p is in a hypo-physiological resistance range, the relationship becomes linear, with k=0.191. This behaviour can be seen when R_p varies from 0.6 to 1.4 WU, which is associated to a physiological pulmonary pressure, ranging from 18.0 to 25.0 mmHg. For Rp>1.4 WU, the PAP grows up and exceeds the clinical warning threshold, which applies to half of the total measuring range. This trend seems to support the idea that, in a normal R_p range and under constant flow rate condition, the Freedom Drive could produce unsafe values of P_{AP}. This could generate a potential dysfunction within the human body. It is also easy to observe from *fig.5.6* how the pulmonary pressure increases from about 25.0 to 33.0 mmHg, and the imposed R_p increases from 1.4 to 2.6. This result seems significant, because – clinically- the pulmonary hypertension is established if the mean P_{AP} is greater than 25 mmHg (Galiè, 2009).

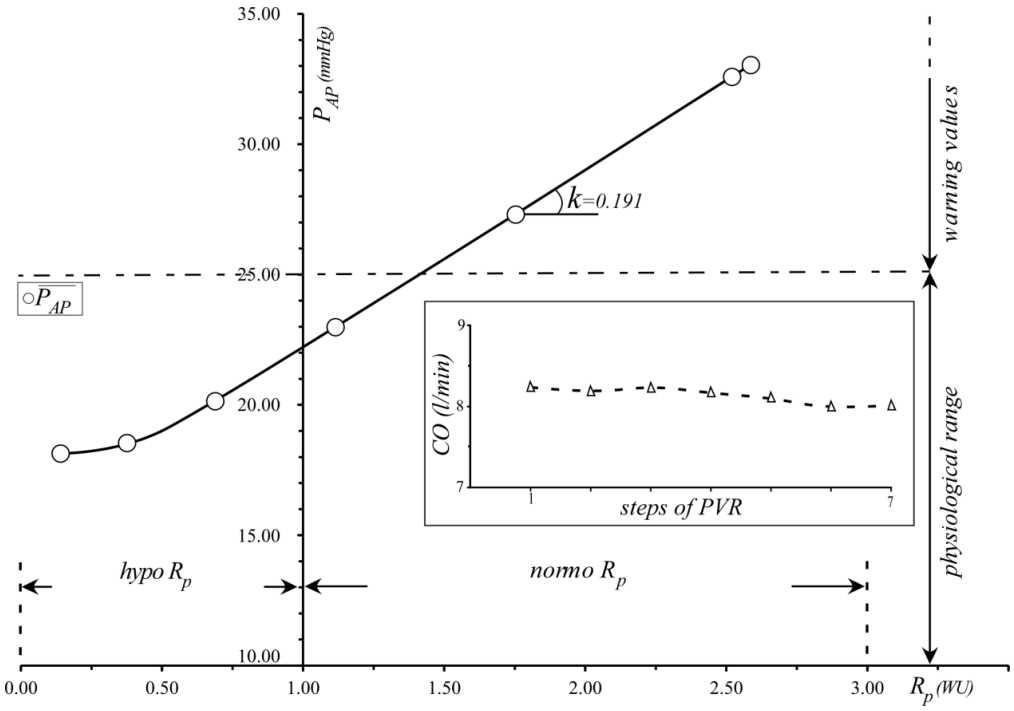

Fig.5.6 Relationship between in-vitro measured pulmonary artery pressure and estimated R_p. The graph is divided in physiological and warning pressure values (>25mmHg), and in hypo or normo pulmonary resistance (threshold at 1 WU). The seven white dots correspond to the seven chosen steps for R_p. In the inset is shows the behavior of the cardiac output during the tests, for all the *PVR* steps.

In conclusion, *fig.5.6* allows for detailed observation of how the FD could operate in specific physiological conditions, inducing a non-adjustable high P_{AP}, which could produce pulmonary edema in a human body. Moreover, seems important to be reminded that the Freedom Drive keeps the CO constant, imposing a high driving pressure, in order to compensate for a potential increase of the R_p, thus increasing the P_{AP} over the warning threshold, including when the increase of the resistance remains within the physiological limit. All of these remarks seem to explain the clinical case discussed by Tarzia (Tarzia et al., 2015).

5.4 A patient reported case

As reported in the Chapter introduction, the research performed in this section was supported and justified by an important reference clinical case. In particular, a clinical research work described in-hospital rehabilitative and evaluative interventions (CPET methodology), from the beginning to the 1215th day of treatment (Tarzia et al., 2015). Next paragraphs are centred on the clinical view –and solution- to the encountered problems, and on the engineer answer that we tried to delineate through this research.

5.4.1 The clinical answer

Looking at the patient's condition according to the result of examinations, the medical equipe identified the cause of deterioration in the patient's clinical state was due to the lower increase of the cardiac output as a result of using the Freedom, compared to the Baseline CPETs. The surgeons supported the idea that the dyspnea (and worsening CO with exercise) could be explained by the sudden increase of pulmonary arterial pressure, due to switching from EXCOR to the Freedom driver, in a patient where pulmonary vascular resistances had likely decreased over time (under EXCOR support) (Tarzia et al., 2015). This scenario seems to be clear despite of the fact that the Freedom® showed a satisfactory flow of 8 l/min, according to output data. In literature, the clinical complication related to use of CW was largely investigated, but only few cases of pulmonary edema were collected (Copeland et al., 2004; Copeland et al., 2012, H.Copeland & J.Copeland, 2012). In all these clinical studies, the utilized driver was the "Big Blue" or the Companion®. Previously, this topic was studied by Vonesh (Vonesh et al., 1991) who underlined the absence of an accurate determination and close regulation of the pressure-flow relationship in the pulmonary vasculature using the TAH, and observed that high incidence of hypertension, edema and respiratory diseases in the pulmonary districts was encountered in TAH recipients (Griffith, 1989; DeVries et al., 1984).

5.4.2 The engineer point of view

From the engineering perspective, some information on that issue can now be added. In particular, the FD is designed to provide a constant flow rate (CO=7-8 l/min), regardless of the boundary body conditions. *In vitro* literature experiments, performed using a CardioWest™ simulator and a portable Freedom® drive unit under several fluid dynamics conditions, showed a noticeable increase of pulmonary arterial pressure although the pulmonary resistance remains in the physiological range (<3 WU) (Galiè, 2009; Chen, 1997).

In the present *in vitro* study a mean pulmonary artery pressure of about 27.5 mmHg, for pulmonary resistance between 1 and 2.6 WU, was observed. In that condition, no output warning was provided by the FD. The high medium pulmonary pressure could be a consequence of the high Freedom's left and right constant drive pressures (205 mmHg and 110 mmHg, respectively). These evidences could open a parenthesis on Freedom's alarm system, and in general on the difficult task of a private company to provide, to unspecialized individuals, a medical device adequately to the high reliability/performance requested and, at the same time, that guarantees the complete safety for the patient. In this context the FD, compared to the Companion drive, seems to be a great step forward in terms of portability and patient quality life, but at the other hand the strong embedded functionalities don't allow a modification that could improve, in certain conditions, the patient outcome.

As an operative example, the obtained P_{AP} values during the tests suggests that it could be useful to provide a controlled access of the drive settings in a home environment to make fine proper adjustments. Moreover, implementing a more sophisticated electronic closed loop control system on the machine, by reasonably lowering the pressure of the right actuator, or the CO. Furthermore, the idea of keeping the CO and the right drive pressure unchangeable to facilitate a long term organ recovery, but also maintaining high vascular resistance, seems to be in contrast with the obtained *in vitro* and *in vivo* results, that show high P_{AP} in the case of patient physiological R_P.

Table 1

Parameter	*Freedom*	*Companion*
Left drive pressure - LDP	*205 mmHg*	*120 -280 mmHg*
Right drive pressure – RDP	*110 mmHg*	*40 – 150 mmHg*
left vacuum – LV	*-10 mmHg*	*0 – -30 mmHg*
Right vacuum – RV	*-10 mmHg*	*0 – -30 mmHg*
% Systole	*50%*	*40 – 60 %*
Heart rate – HR	*125±15 bpm*	*40 – 150 bpm*

Table 2

Parameter	$\overline{Hi\ LAP}$ (mm Hg)	σ Hi LAP (mm Hg)	$\overline{Hi\ AoP}$ (mm Hg)	σ Hi AoP (mm Hg)	$\overline{Hi\ PAP}$ (mm Hg)	σ Hi PAP (mm Hg)	$\overline{CO_{sx}}$ (l/min)	σ CO_{sx} (mm Hg)	$\overline{R_{polm}}$ (mmHg/min/l)	σ R_{polm} (mmHg/min/l)
s_1	17.06	0.76	103.34	5.59	18.13	0.60	7.66	0.23	0.14	0.05
s_2	15.54	0.58	105.50	6.58	18.54	0.48	7.97	0.29	0.38	0.02
s_3	14.54	1.29	104.09	8.13	20.14	0.61	8.10	0.36	0.69	0.10
s_4	13.69	0.33	104.04	6.95	22.98	0.19	8.33	0.05	1.12	0.03
s_5	13.02	0.42	102.59	6.09	27.30	0.31	8.14	0.08	1.75	0.08
s_6	11.60	0.14	101.19	7.96	33.04	0.55	8.29	0.07	2.59	0.09
s_7	11.24	0.32	98.66	7.76	32.58	1.05	8.47	0.13	2.52	0.17
1_p	13.65	2.06	93.67	2.96	24.66	6.93	8.24	0.19		
2_p	13.62	1.83	96.51	2.67	24.31	6.36	8.19	0.33		
3_p	13.29	1.79	98.29	3.23	24.25	6.17	8.23	0.28		
4_p	13.62	1.99	102.73	2.38	24.48	6.33	8.17	0.23		
5_p	13.98	2.22	106.66	2.47	25.06	6.61	8.11	0.25		
6_p	14.31	2.69	109.32	2.08	25.02	6.34	8.00	0.41		
7_p	14.21	2.38	112.22	2.13	24.96	5.92	8.01	0.48		

5.5 Study abstract

The gold standard therapy for people affected by advanced heart failure is heart transplant. The gap between donors and patients in waiting lists has promoted the development of circulatory support devices, such as Total Artificial Heart (TAH). This study was focused on the *in vitro* performance of a specific device: the temporary CardioWest™TAH, driven by the SynCardia Freedom® portable pump. The aim was to evaluate the ability of drive to adapt to changes of physiological parameters, using an ad-hoc developed hydraulic circuit as a patient simulator, and to provide possible interpretation for specific clinical cases. *In vitro* tests were performed using an hydraulic closed loop acting as patient simulator, developed by SynCardia Company. Several hydrodynamic parameters were obtained, as: cardiac output, the filling of the ventricles, pressures in the atria, and ventricles. The aorta and pulmonary artery pressures were measured at different values of vascular resistance, that were simulated in the range of systemic (*SVR*) and pulmonary physiological resistances (*PVR*).

The realized measuring campaign, and the measured quantities, highlights the ability of the coupled system to provide behaviour close to the physiological. This answer allows the thought that the used mock loop could provide interesting non-patient biased results in terms of haemodynamic performances of artificial heart devices and drive pumps.

Despite good results in terms of physiological quantities simulation, the Freedom drive expressed also some weak points. In particular, the mean pulmonary artery pressure (PAP) increases above 30 mmHg, also in the range of physiological *PVR* (2.6 WU), with a CO of 8.29 l/min. This appened although, after increasing the *PVR*, the left atrial pressure decreases, according to the expected physiological trend, whilst aortic pressure remains almost stable. A large increase of P_{AP} is probably associated with the preset settings of the FD. This could correlate with the clinical course of a patient who was supported by the CardioWest™TAH and experienced complications after being switched to the new FD, highlighted by the occurrence of dyspnea and pulmonary edema despite a high cardiac index.

In conclusion, this study provides a new way to perform a sensitivity analysis of the performance of CardioWest patient Simulator and the CardioWest™ TAH-t coupling system, powered by the Freedom Drive. To improve understanding of the behavior of the drive, including in clinical cases, the system was analysed in terms of fluid dynamics and primary cardiovascular parameters. In particular, the CardioWest workbench was used as a real patient simulator, not delimiting its operative field as a pre-operation test device, showing its suitability for being used in *in vitro* investigations over a wide range of physiological conditions.

The results of the tests suggest that the Freedom drive is an extremely useful device, which could increase the quality of life of the patient, and help in the

way of a long-term implantation device. On the other hand, its rigid work dynamic behavior could not induce the correct response of the organ under certain specific conditions. The results obtained can also help to justify, with good accuracy, detection of some symptoms in clinical cases, and to entail a prospective design for the device.

5.6 Chapter bibliography

[1]. Bellotto F, Compostella L, Agostoni P, et al. Peripheral Adaptation Mechanisms in Physical Training and Cardiac Rehabilitation: The Case of a Patient Supported by a Cardiowest Total Artificial Heart. J Card Fail 2011;17:670-675.

[2]. Chen JM, Levin HR, Michler RE, et al. Reevaluating the significance of pulmonary hypertension before cardiac transplantation: determination of optimal thresholds and quantification of the effect of reversibility on perioperative mortality. J Thorac Cardiovasc Surg 1997;114:627-634.

[3]. Cohn W.E., Timms D.L., and Frazier O.H., Total artificial hearts: past, present, and future. Nat. Rev. Cardiol. advance online publication 2 June 2015; doi:10.1038/nrcardio.2015.79

[4]. Copeland H, Copeland J. Experience with Total Artificial Heart Bridge to Transplantation in 15 Women. J Heart Lung Transplant 2012;31:S269.

[5]. Copeland JG, Smith RG, Arabia FA, et al. Total Artificial Heart Bridge to Transplantation: A 9-Year Experience With 62 Patients. J Heart Lung Transplant 2004;23:823-831.

[6]. Copeland JG, Smith RG, Arabia FA, et al. Cardiac replacement with a Total Artificial Heart as a Bridge to Transplantation. N Engl J Med 2004;351:859-868.

[7]. Copeland JG, Copeland H, Gustafson M, et al. Experience with more than 100 total artificial heart implants. J Thorac Cardiovasc Surg 2012;143:727-734.

[8]. DeVries WC, Anderson JL, Joyce LD, et al. Clinical use of the total artificial heart. N Engl J Med 1984;310:273-278.

[9]. Donovan FM. Design of a Hydraulic Analog of the Circulatory System for Evaluating Artificial Hearts. ABB 1975;3:439-449.

[10]. El-Banayosy A, Arusoglu L, Morshuis M, et al. CardioWest Total Artificial Heart: Bad Oeynhausen Experience. Ann Thorac Surg 2005;80:548-552.

[11]. Friedline K, Hassinger P. Total Artificial Heart Freedom Driver in a Patient With End-Stage Biventricular Heart Failure. AANA Journal 2012;80:105-112.

[12]. Fukamachi K, Horvath DJ, Massiello AL, et al. An innovative, sensorless, pulsatile, continuous-flow total artificial heart: Device design and initial in vitro study. J Heart Lung Transplant 2010;29:13-20.

[13]. Galiè N, Hoeper MM, Humbert M, et al. Guidelines for the diagnosis and treatment of pulmonary hypertension. Eur Heart J 2009;30:2493–2537.

[14]. Go AS, Mozaffarian D, Roger VL, et al. Heart Disease and Stroke Statistics - 2013 Update A Report From the American Heart Association. Circulation. 2013;127:e6-e245.

[15]. Griffith BP. Interim use of the Jarvik-7 artificial heart: Lessons learned at Presbyterian-University Hospital of Pittsburgh. Ann Thorac Surg 1989;47:158-166.

[16]. Guruprasad A, Giridharan, JL Thomas, et al. Miniaturization of Mechanical Circulatory Support Systems. Artif Organs 2012;36:731-758.

[17]. Hicks A. R., EVALUATION OF A MOCK CIRCULATION MODEL THROUGH TIME-SERIES ANALYSIS. A thesis submitted to the School of Graduate Studies and Research in partial fulfilment of the requirement for the degree of Master of Applied Science in the Departrnent of Chemical Engineering University of Ottawa, Ottawa, Canada, 1990.

[18]. Jansen P, van Oeveren W, Capel A, Carpentier A. In vitro haemocompatibility of a novel bioprosthetic total artificial heart. Eur J Cardiothorac Surg. 2012;41:e166-e172.

[19]. Jaroszewski DE, Anderson EM, Pierce CN, Arabia FA. The SynCardia freedom driver: A portable driver for discharge home with the total artificial heart. J Heart Lung Transplant 2011;3:844-845.

[20]. Kasirajan V., Arabia F., Tang D. et al., Artificial Heart Patients Discharged Home with a Portable Pneumatic Driver – The Pivotal US Clinical Trial Experience, J of Heart and Lung Trans. (2013), 32(4), Supplement 149.

[21]. Kemp CD, Conte JV. The pathophysiology of heart failure. Cardiovascular Pathology 2012;21:365–371.

[22]. Khalil HA, Cohn WE, Kerr DT, Frazier OH, Schusterman II MA, Radovancevic B. Induced pulsation of a continuous-flow total artificial heart in a mock circulatory system. J Heart Lung Transplant 2010;29:568-573.

[23]. Kiyotaka Fukamachi, Current Status of Artificial Heart (Assist/Replacement) Development in the United States, Artificial Organs (2013), 37(8), 675–676.

[24]. Leprince P, Bonnet N, Rama A, et al. Bridge to Transplantation With the Jarvik-7 (CardioWest) Total Artificial Heart: A Single-center 15-Year Experience. J Heart Lung Transplant 2003;22:1296-1303.

[25]. McMurray JJV, Anker SD, Auricchio A, et al. ESC Guidelines for the diagnosis and treatment of acute and chronic heart failure 2012. Eur Heart J 2012;33:1787-1847.

[26]. Organ Transplant and Procurement Network. <http://optn.transplant.hrsa.gov/data>. Accessed September 6, 2013.

[27]. Shah KB, Volman RA, Harton S, Tang DG, Kasirajan V. Fracture of the total artificial heart pneumatic driveline after transition to the portable driver. J Heart Lung Transplant 2013;32:1041-1043.

[28]. Shah KB, Tang DG, Cooke RH, et al. Implantable Mechanical Circulatory Support: Demystifying Patients With Ventricular Assist Devices and Artificial Hearts. Clin Cardiol 2011;34:147-152.

[29]. SynCardia Systems, Inc., CardioWest temporary Total Artificial Heart (TAH-t) - PATIENT SIMULATOR and TRAINING CENTER (MOCK CIRCULATION TANK) user's manual, SynCardia Systems, Inc. (1992) E. Silverlake Road Tucson, Arizona 85713.

[30]. SynCardia Inc., SynCardia con Sistema driver Freedom - Cuore artificiale completo provvisorio (TAH-t) SynCardia con sistema driver Freedom™ Guida per il paziente e l'assistente domiciliare. Emergo, Europe, Molenstraat 15 2513 BH, The Hague, The Netherlands.

[31]. SynCardia's Total Artificial Heart Receives HUD Designation for Destination Therapy from FDA. <http://www.syncardia.com/2012-Press-Releases/syncardias-total-artificial-heart-receives-hud-designation-for-destination-therapy-from-fda.html>

[32]. SynCardia Systems, Inc.. Summary of Safety and Effectiveness, CardioWest temporary Total Artificial Heart (TAH-t) - Premarket Approval (PMA) Application PO3001 1. SynCardia Systems, Inc. (1992) E. Silverlake Road Tucson, Arizona 85713.

[33]. Slepian Marvin J, The SynCardia Temporary Total Artificial Heart-Evolving Clinical Role and Future Status, US Cardiology, 2011, 8(1):39–46.

[34]. Slepian MJ, Alemu Y, Soares JS, Smith RG, Einav S, Bluestein D. The Syncardia™ total artificial heart: in vivo, in vitro, and computational modeling studies. J Biomech 2013;46:266-275.

[35]. Spurlock DJ, Ranney DN, Fracz EM, Mazur DE, Bartlett RH, Haft JW. In Vitro Testing of a Novel Blood Pump Designed for Temporary Extracorporeal Support. ASAIO 2012;58:109-114.

[36]. Tarzia V., Braccioni F., Bertolussi G., et al., Cardiopulmonary Exercise Testing Responses to different External Portable Drivers in a patient with a CardioWest Total Artificial Heart, *submitted and accepted at Artificial Organs.*

[37]. Torregrossa G, Gerosa G, Tarzia V et al. Long Term Results with Total Artificial Heart: Is It Prime Time for Destination Therapy?. J Heart Lung Transplant 2013;32:S118.

[38]. Vonesh MJ, Cork RC, Mylrea KC. A noninvasive method of estimating mean pulmonary artery pressure in the pneumatic total artificial heart. J Clin Monit 1991;7:294-303.

[39]. Weber S, Kazuyoshi D, Massiello AL, et al. In Vitro Controllability of the MagScrew Total Artificial Heart System. ASAIO 2002;48:606-611.

[40]. Westaby S. Cardiac transplant or rotary blood pump: Contemporary evidence. J Thoracic Cardiovasc Surg 2013;145:24-31.

[41]. Zapanta CM, Snyder AJ, Weiss WJ, et al. Durability Testing of a Completely Implantable Electric Total Artificial Heart. ASAIO 2005;51:214-223.

Chapter 6

Physiological vortices in the Valsalva sinuses: an in vitro answer for bio-prosthetic valves

6.1 Introduction: haemodynamic performances of aortic valves

The principal aim of this study was to try to give an answer at the different flow patterns founded in literature, describing the vertical structure downstream an aortic prosthetic heart valve. In this context, the present chapter and the described research adopted an *in vitro* strategy, to determine the hemodynamic performances expressed by different aortic valve plus root coupled system. In particular, the estimation of the vortices in the Valsalva sinuses, for bioprosthetic heart valves, was performed designing different silicone mock roots and testing them in a pulse duplicator through a particle image velocimetry technique. The measurement of the global parameters of the flow (ΔP, EOA, energy loss) and local parameters of the flow (velocity maps, streamlines), allowed to better understanding how a valve and root coupled system form a unique environment.

Before going in deep on the workbench and instruments description, and on the experimental campaign results, the next session is depicted to a short introduction to the well-known literature issue of the vorticity structure in the Valsalva sinuses.

6.1.1 Vortices in the Valsalva sinuses

The presence of vortices within the Valsalva sinuses has been a known phenomenon since the 1960s, stimulated by the development of the first heart valve replacement. Although accepted by the scientific community, other studies gave conflicting views of the role of the sinuses on the valve leaflet dynamics (Keele, 1952; Bellhouse & Reid, 1969; Bellhouse & Bellhouse, 1968; Van Steenhoven & Van Dongen, 1979). It now seems to be well accepted that the sinuses of Valsalva not only improve the dynamic behaviour of the valve in the leaflet dynamics, but also play an important role in the washing out of the sinuses, and blood supply of the coronaries (Van Steenhoven & Van Dongen,

1979; Peskin, 1982; Peacock, 1990; Rubenstein et al., 2012; Caro et al., 2012; Ducci et al., 2013). However, the specific contributions of the sinus architecture upon the hemodynamic are still unclear, and often contradictory. Defining a positive vortex as in the description in *fig.6.1*, the mechanism proposed by Bellhouse, suggests the formation of an entrapped positive vortex (ω) in the sinus (Bellhouse & Bellhouse, 1968). This vortex is generated at the exit of the leaflets during early systole, and expands into the sinus, where it remains trapped. This vortex persists into early diastole, promoting leaflet closure (Ming et al., 1986; Swanson & Clark 1973; De Hart, 1997; De Hart et al., 1997; De Hart et al., 2003; Korakianitis et al., 2006; Katayama et al., 2008).

Later studies report an alternative mechanism, where the initial eddie produced during early systole at the leaflets edge, does not expand into the Valsalva sinus, but migrates far from the valve along the root, generating a slower negative vortex in the sinus. This negative vortex is a counter vortex in the sinus, working in an opposite direction to that of the sinus vortex in the previous studies. This vortex seems to help the closure of the leaflets, whilst the original positive vortex is located in an area that is the ideal continuation of the leaflet profile into the flow. In particular, observing this issue from an experimental *in vitro* point of view, it is possible to follow this mindset in several works (Ducci et al., 2013; Leo et al., 2005; Leo et al., 2006; Dasi et al., 2009; Saikrishnan et al., 2012).

Alternative mechanisms for the vortices in the root were obtained by numerical studies, tending towards the positive vortex mode, although some conclude the presence of multiple vortices within the sinus (Fukui et al., 2013). Recently, newly available high intensity MRI images with a specific tracer in the blood have allowed in vivo flow visualisation (Yang et al., 1998; Markl et al., 2005; Escobar et al., 2004; Ranga et al., 2006; Markl et al., 2011). These studies tend to suggest the presence of a positive vortex, stable within the sinus. However, due to the difficulty of differentiating fast and slow vortical structures within the main jet using this technique, the potential error in the computed particle tracking is significant. Therefore, current *in vivo* studies mainly provide a global indication of the flow behaviour in the aorta, and are not sufficient to provide a conclusive answer on the local fluid motion inside the sinuses.

This study aims to provide a clearer and more generalised view of the flows in the aortic root, with specific attention on an idealised healthy situation. A number of *in vitro* experiments were performed, using a pulse duplicator to mimic the physiological pressure curves, and a 2D particle image velocimetry (PIV) system to measure the local flow field parameters. Various aortic root geometries were combined with prosthetic valves of different sizes. Particular attention was placed on how the size of the sinuses of Valsalva affects their function and the downstream flow of the aortic valve. Healthy and idealised operating conditions were considered, whilst the geometric ratios of the inflow,

outflow, and sino-tubular junction diameters are preserved across the various roots, mimicking the different literature valve housing set-up.

In a short summary this study tends to provide a new insight in the physiological function of Valsalva sinuses, and on the effect of anatomical variations upon the function of the native and prosthetic valves.

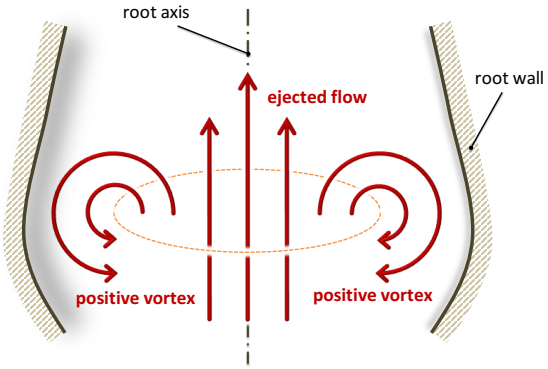

Fig.6.1 Definition of a positive vortex ω. Y is the main jet flow direction, x is the span-wise direction. In the experimental set-up the positive vortex could be seen as an un-counter vortex in the left sinus.

6.2 Set-up for the experimental campaign

In this paragraph are described the different instruments utilized in the experiments, starting from the workbench and the laser-PIV instrumentation, moving to the silicone mock roots design and then describing the global and local measured quantities, that will be show in the result section.

6.2.1 Testing workbench: ViVitro Superpump

All the experiments were carried out using a hydro-mechanical commercial pulse duplicator system (Vivitro Superpump System SP3891, ViVitro Labs Inc., Canada). The system simulates the heart function by generating a pulsatile flow through mock heart chambers, with variable systemic resistance, and variable aortic, systemic and ventricular compliances (*fig.6.2a*). Millar Mikro-Tip® high resolution pressure catheters were used to collect the pressure fields upstream and downstream of the aortic valve. An electromagnetic flowmeter (Carolina Medical Model FM501) with a 28 mm flow probe (Model EP688) was used, located just upstream of the aortic valve, allowing quantification of the forward, closing and leakage flows through the aortic valve. All these global flow fields were collected using the ViViTest software control system. All the tests were performed according to the requirements of the standard ISO 5840:2009, using a physiological flow rate of 4 l/min, a heart rate of 70 bpm, and a mean aortic pressure of 100 mmHg.

6.2.2 Particle Image Velocimetry technique

The local fluid dynamic fields were determined using 2D PIV (TSI Inc.). This non-intrusive optical technique provides the measurements of the instantaneous velocity vector field of an investigated area, by seeding the analysed volume with reflective particles, which become illuminated when a laser sheet is passed over them. The images from two controllably spaced laser pulses are recorded via a high speed camera, and computer software calculates which particles in the first image correlate in the second image, and produces a velocity map from the resultant displacement. In this study the region of interest was the aortic root cross section (sagittal plane) downstream the aortic valve. The neutrally buoyant, low lag, and passive tracer particles used for all these tests were hollow glass particles (Dantec Dynamics HGS-10, nominal diameter 10 μm). A high-powered laser light sheet (YAG PIV laser with dual cavities, 70mJ (x2) at 15 Hz, 532 nm, 1.5 mm maximum laser thickness) was used to selectively illuminate the seeded solution. The PIV system was synchronised with the ViVitro pulse duplicator through a timing box, to trigger the camera at the desired time instant of the cardiac cycle (see *fig.6.2,b*) and collect a pair of images. A photo and equivalent diagram of the experiment are shown in *fig.6.2,a*, alongside the 5 valve and root setups.

6.2.3 Adopted work solution

Due to the number of experiments required in this investigation, and concerned with the effect of glycerine upon tissue leaflets, was preferred to use a non-glycerine solution, within international regulations (Fisher et al., 1988). The work solution was a mix of deionised water and potassium iodide (KI), with a hydro-dynamically insignificant quantity of sodium thiophosphate, to remove colour from the liquid. The resultant clear colourless solution has the same dynamic viscosity of saline water at 37 °C (η=1·10-3 Pa·s) and minimum refractive index mismatch with the mock aortic roots and valve leaflets (n = 1.40) was used. Refractive index (RI) matching was verified by analysing the distortion of a grid produced when viewed through a silicone root in the testing solution (*fig.6.2c*).

6.2.4 Aortic valves and mock roots

Porcine valves were preferred due to their similarity with healthy human aortic valves in terms of shape, thickness and material (Thubrikar, 1990). The valves used for the tests were two stented aortic Labcore TLPB supra-annular porcine surgical prostheses, with diameters of 25 and 29 mm. The 29 mm valve was selected because its inner diameter (i.e. the leaflets diameter) is about 25 mm and therefore, when coupled with a 25 mm mock root, better describes the healthy physiological geometry of a 25 mm root. The valves were placed in the optimal surgical supra annular position unless specified

differently, to mimic the physiological ratio between leaflet and sinus. The valves were inserted into a series of mock roots of different design: a straight root of 25 mm diameter with no sinuses; two physiological roots, with a 25 and 29 mm diameter at the annulus and at the sinotubular junction, with three equal sinuses; and a 25 mm diameter aortic root identical to the one previously described but designed to host the stent of the 29 mm valve, mimicking a stentless-like configuration with physiological leaflets. Sinuses were based on the geometric proportions described by Swanson & Clark (Swanson & Clark, 1973), the epitrocoidal top view profile defined by Reul (Reul, 1990), the angles of attachment of the leaflets from Thubrikar (Thubrikar et al., 1981), and the saggital plane sinus profile from Grigioni (Grigioni et al., 2005). The chosen designs reflect the idea of the hugest span of possibilities, going from the total absence of sinuses (similar to a Dacron aortic root replacement), to a expanded aderly-root, to a physiological healthy root configuration. All roots were made of optically clear, solvent free, low viscosity silicone elastomer (MED-6015, NuSil Technology, Carpinteria, CA, USA, refractive index n = 1.4). The tested roots had negligible compliance.

6.2.5 Global and local measurement fields

The global hydrodynamic performances of the valves were determined by measuring the transvalvular pressure drop (Δp), and flow (Q), of the cardiac cycle, over 20 cycles with an acquisition frequency (fc) of 300 Hz (256 samples per cycle). The effective orifice area (EOA), and the total energy loss (Eloss) were based on Gorlin's formula (ISO 5840:2009). The local flow field studied through image velocimetry gave 2D images of selected instant in the cardiac cycle. The instants for imaging (in the results section) were selected to best characterise the flow features during the cardiac cycle (see *fig.6.2b*).

These five instants are: maximum increase of flow (1), maximum flow (2), the maximum decrease of flow (3), the first plateau of decreasing flow (4), and the flowrate equal to zero (5). For each instant, two consecutive laser pulse beams were triggered, with an adjustable Δt rising from 50 to 400 μs, to capture the hydrodynamic behaviour in both the relatively fast and slow regions of the flow field. The images were processed using Insight4G (TSI Inc.), with a spatial calibration ranging from 20 - 25 μm/pixel. The vector velocity maps generated were averaged in Tecplot, which also computed and plotted the streamlines. For each test the refractive index matching and the dynamic viscosity of the solution were monitored and kept constant. Finally, the local flow fields were computed from 200 phase resolved images for each instant; this quantity of images was found from preliminary investigations to be the start of a quality plateau.

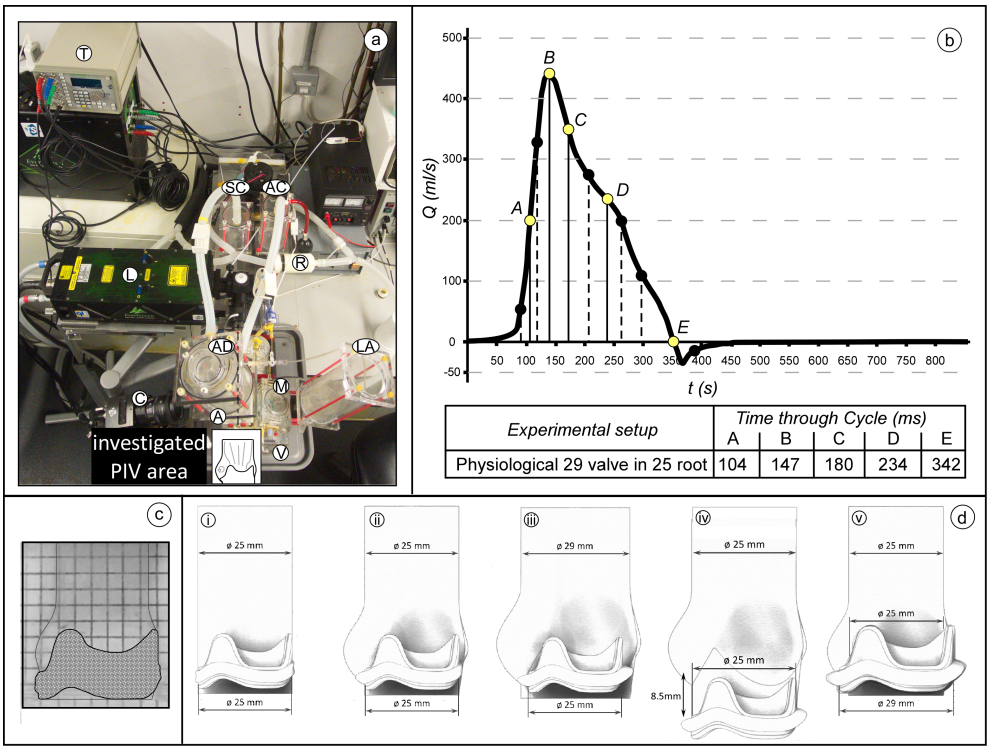

Experimental setup	Time through Cycle (ms)				
	A	B	C	D	E
Physiological 29 valve in 25 root	104	147	180	234	342

Fig.6.2 *a)* Picture of the typical experiment set-up: LA = left atrium, M = mitral valve, A = aortic valve, AD = aortic district, SC = systemic compliance, AC = aortic compliance, R = resistance, C = high speed camera, L = laser, T = trigger. *b)* Typical flow behaviour upstream the aortic valve and the chosen time instants through the cycle. *c)* Refractive index matching for the stentless root, using a reference grid. *d)* Illustration of the different mock roots.

6.3 Results: velocity vector maps and global performances following the ISO 5840:2009

Contour maps of the average magnitude of velocity and streamlines in the plane are presented. The hydrodynamic performance of the different systems were also assessed in terms of mean systolic transvalvular pressure drop (ΔP); Gorlin's effective orifice area (EOA), regurgitative volumes (forward and closing), and total energy loss components. The leakage volume in each setup is mainly due to the paravalvular leak between the prosthesis and the hosting holders, which would be negligible for surgical bioprostheses correctly implanted in patients, and so has been omitted from this report.

6.3.1 Straight mock root

To identify the main function of the sinuses in the development of vortical structures downstream of the valve, an extreme reference case was studied by removing the Valsalva chambers. The 25 mm external diameter porcine valve was placed and tested in a straight tube of 25 mm diameter. The most descriptive images from the PIV study are represented in *fig6.3*. During systole,

positive vortex rings are generated at the exit of the opening leaflet, in close proximity to the aortic wall (*fig.6.3,a*) and, finding no physical space within which to be constrained, escape quickly away from the valve, driven by the ejected flow (*fig.6.3,a-b*). This mechanism, evident during maximum forward flow (*fig.6.3,b*), narrows the cross-section of the main jet. The vortex escape phenomenon repeats several times during the ejection phase so that, later in systole, a series of positive vortices interfere with the shape of the main jet, and is still significant in late systole, with the deceleration of the flow (*fig.6.3, c-d*), and disappears only after the valve is fully closed (flowrate equal to 0 l/min, *fig.6.3,e*). Another positive vortex is detected above the commissure, on the right side in *fig.6.3,a*; which remains in this region during the whole systolic phase. For this configuration, the maximum velocity, detected as the fastest particle flowing in the investigated region, is 3.0 m/s. From the PIV images at the maximum averaged velocity, the fast forward jet width results equal to 1.4 cm. In terms of hydrodynamic performances, the valve produces a ΔP of 10.98 mmHg, alongside a computed *EOA* of 1.57 cm^2. This corresponds to 32% of the root cross section, and about 45% of the internal stent diameter. The energy loss was equal to 137.27 mJ, and the closing volume regurgitation is 0.7 ml (*Table 1* and *fig.9*).

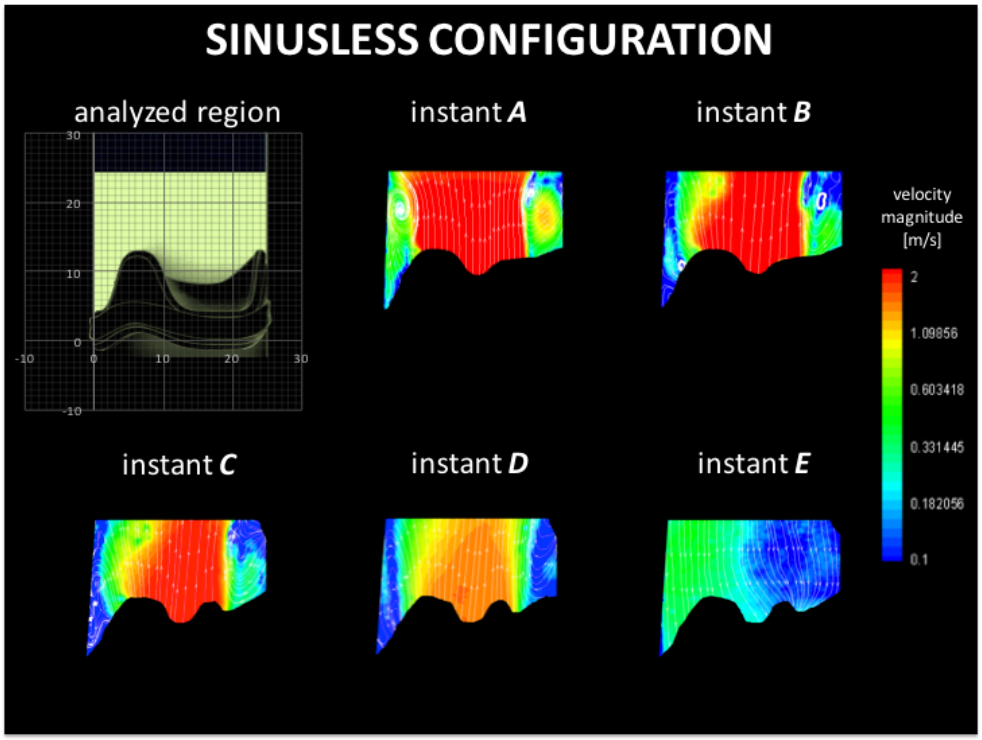

Fig.6.3 Velocity maps and streamlines for sinusless configuration.

6.3.2 Physiological 25mm mock root

In a second experiment, the same valve was tested on an idealized physiological aortic root including Valsalva sinuses, having an identical diameter (25 mm) at the sino-tubular junction as the previous straight root, and using the same 25mm porcine valve. The velocity maps in *fig.6.4* describe the

behaviour of the flow across a sagittally symmetrical plane for this analysis. A positive vortex develops at the leaflet exit at the beginning of systole, but this time remains entrapped into the sinus (*fig.6.4, a-b*). The vortex remains confined in the Valsalva sinuses whilst fully developing, from the instant of flow peak, (*fig.6.4, b*) until the end of the closing phase (*fig.6.4, c-d*), as founded in previous research. The forward main jet has a conical spreading shape on the right side, but is impinged by a vortical ring that develops on top of the stent. This forms at the beginning of the systolic phase, and expands towards the centre of the root during late systole (*fig.6.4, a-b-c-d*). In *fig.6.4, e*; the vortex in the sinus loses some energy, leaving a weak recirculation with predominant backflow from the sinus to the commissure. Velocity analysis indicates a maximum jet velocity around 2.9 m/s, and a fast forward jet width of 1.7 cm. In terms of hydrodynamic performances, the valve produces a ΔP = 8.63 mmHg, whilst the computed EOA is equal to 1.65 cm^2, corresponding to 38% of the root cross section, and about 48% of the internal stent diameter. The total energy loss is equal to 79.66 mJ, and the closing regurgitation volume is 0.45 ml.

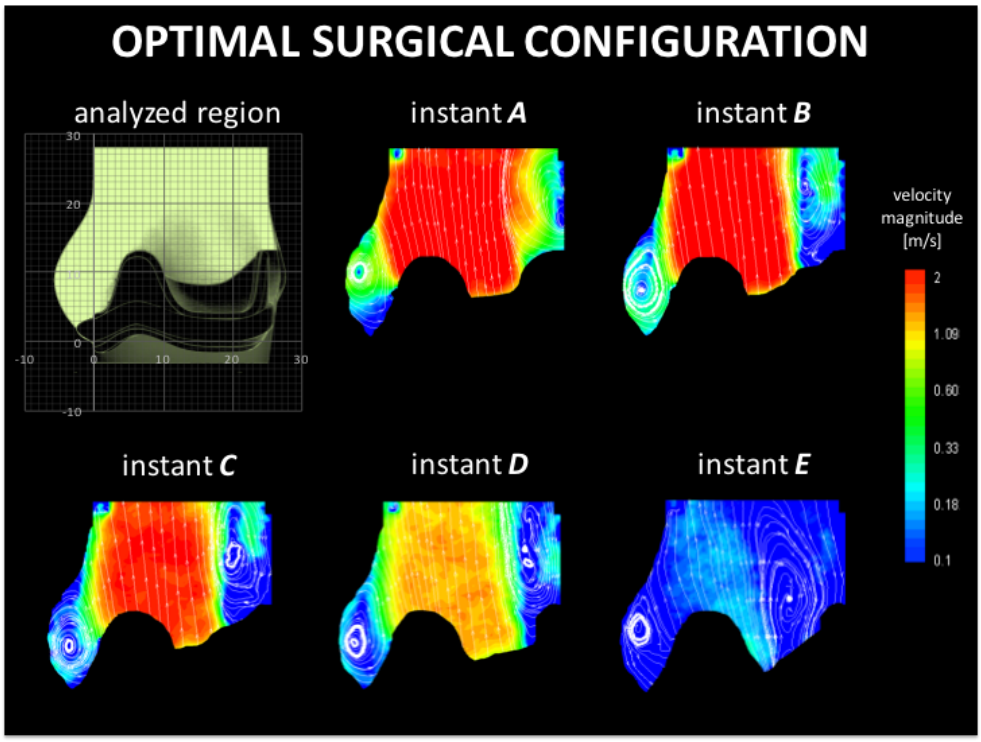

Fig.6.4 Velocity maps and streamlines for ideal-surgical configuration.

6.3.3 Physiological 29mm mock root

The experiment performed in section 6.3.2 was repeated using the same 25 mm porcine valve, but positioned in a scaled up aortic root of identical shape, characterised by a diameter at the sino-tubular junction equal to 29mm. The most descriptive PIV images for this configuration are represented in *fig.6.5*.

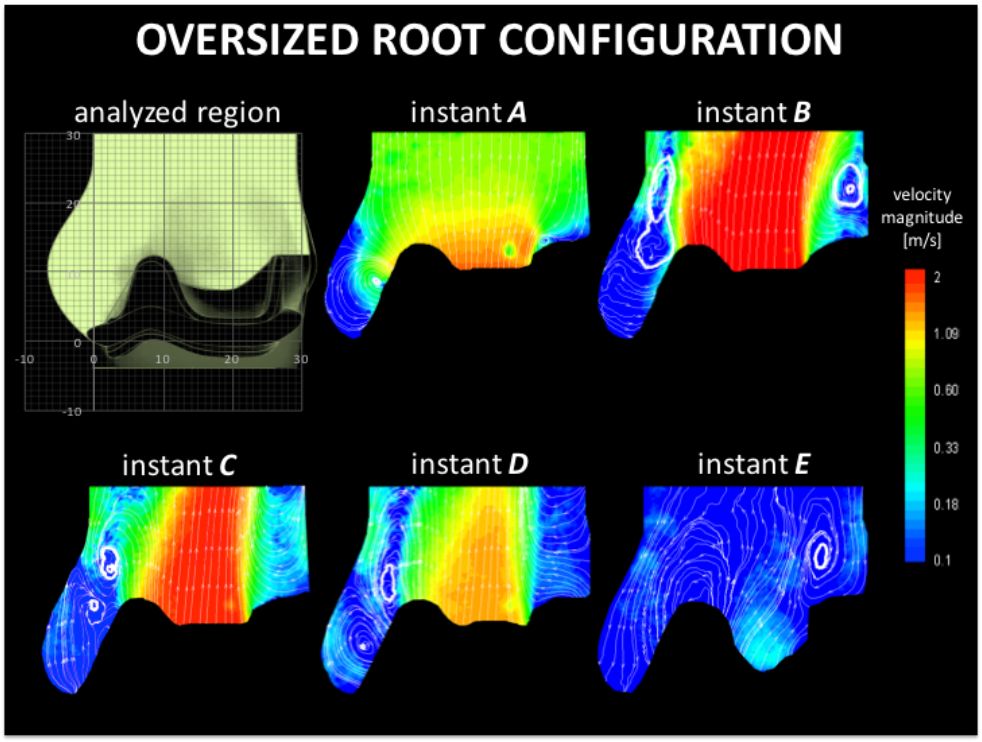

Fig.6.5 Velocity maps and streamlines for valve-mismatch configuration.

In the early phase of systole – maximum increasing flow (*fig.6.5, a*) - a positive vortex forms inside the sinus, and a spread main jet develops just over the leaflets. At maximum ejection, the positive vortex escapes from the sinus, with a similar mechanism as that observed for the straight root. The vortex relocation confines the main jet profile, narrowing the high speed region (*fig.6.5, b-c*). This geometrical mismatch also produced a vortical structures not observed before. In particular, towards the end of the systole a positive vortical ring, recovering energy from the main forward flow, becomes stronger and stable in proximity of the sinotubular junction (*fig.6.5, c-d*). This generates a fully developed lower velocity counter-vortex inside the sinus (*fig.6.5, d*). The *fig.6.5, e*; represents the instant of the inversion of the flow, in which the valve has already begun the closing stage. As in previous cases, a positive vortex forms on top of the commissures (*fig.6.5, a-b-c-d*). This structure moves over during systole, becoming stable with the vortex centre about 2 cm above valve stent at the maximum negative gradient instant. A maximum forward jet velocity of 2.8 m/s (with a width around 1.62 cm) was detected just before the peak of the flow. In terms of hydrodynamic performances, the valve produces a ΔP of 9.29 mmHg, and an *EOA* of 1.53 cm^2, corresponding to 23% of the root

cross section and about 44% of the internal stent diameter. The total energy loss is equal to 118.70 mJ, and the closing regurgitation volume 3.27 ml.

6.3.4 Physiological 25mm mock root, low valve

In order to verify the effect of an inaccurate valve positioning, a 25 mm porcine valve was moved 8.5 mm lower than the usual ideal supra-annular surgical height. This standard geometric valve housing was reported in previous studies, and is the default position for the valve housing in the Vivitro pulse duplicator (33 34 35). The processed PIV images for this configuration are represented in *fig.6.6*.

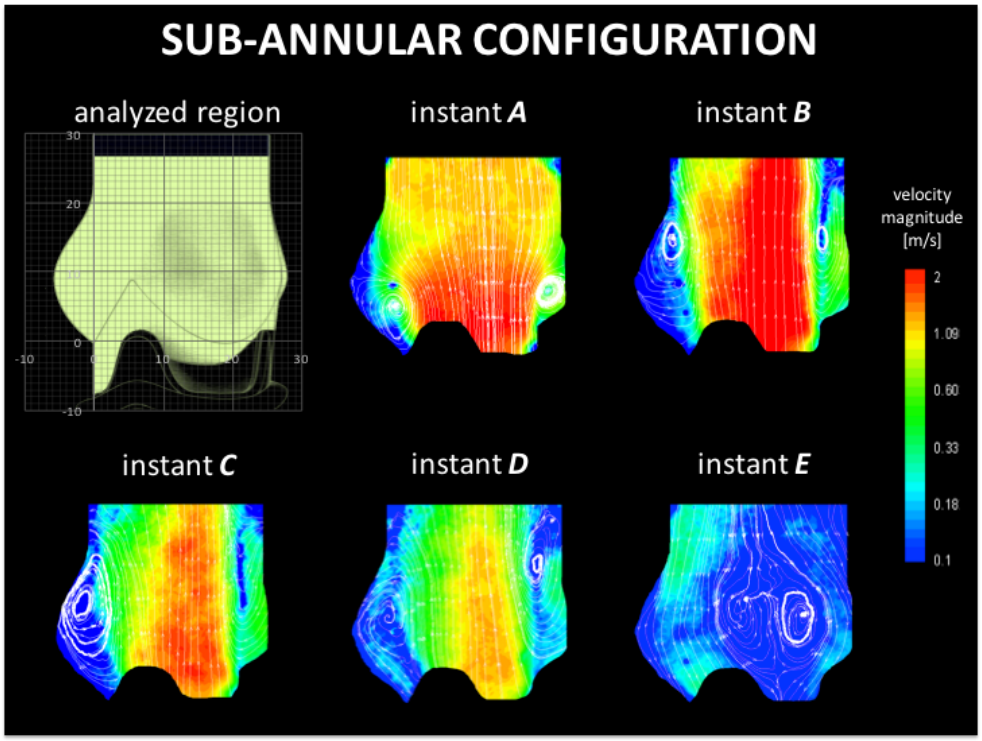

Fig.6.6 Velocity maps and streamlines for low-valve configuration.

A positive vortical ring starts developing at the base of the sinus at the beginning of the systolic phase (*fig.6.6, a*). In the interval between the valve opening and the flow peak through the valve, this positive vortex increases in size, and eventually leaves the sinus. Hence, at the flow peak the vortex moves up in proximity of the sino-tubular junction (*fig.6.6, b*). During the closing phase, a second vortex generates at the sinus base, and develops inside the Valsalva sinus, where it remains (*fig.6.6, c-d*). This expands during the closing phase, moving from the sinus cavity towards the centre of the aortic root and promoting the leaflets' closure (*fig.6.6, e*). A vortex is also generated above the stent-commissure, which moves far from the valve during the late closing phase (*fig.6.6*).

The measured maximum velocity is around 2.9 m/s, and the fast forward jet width results equal to 1.1 cm. In terms of hydrodynamic performances, the

valve produces a Δ*P* of 10.91 mmHg and an EOA of 1.41 cm^2, corresponding to 29% of the root cross section and about 41% of the internal stent diameter. The total energy loss is equal to 87.24 mJ, with a regurgitated closing volume of 0.16 ml.

6.3.5 Stentless 25mm mock root (native configuration)

All described tests are related to configurations achievable with bioprosthetic stented valves, rather than an idealised physiological configuration. In fact, the stent thickness necessitates the use of leaflets of smaller size than the native ones, which occupy a smaller portion of the sinuses during opening. Moreover, the stent thickness is likely to enhance the swirling structures observed in all tests above the stent (and along the wall) (section 6.3.1 to 6.3.4). In order to reduce the influence of the valve stent, a final test was performed using an aortic root identical to the one used in sections 6.3.2 (25 mm at the sino-tubular junction), with the exception of an encasing designed to host the stent thickness of an identical valve of larger size (29 mm), characterised by an inner stent size similar to the root size at the sino-tubular junction (25 mm). This configuration provides physiological leaflet matching.

The velocity maps and streamlines for the stentless-like configuration are represented in *fig.6.7*. At the maximum gradient of flow, the map shows a divergent main vertical jet, with a positive vortex inside the sinus (*fig.6.7, a*). In the fully open state, at the peak of the flow, the valve leaflets, now larger than the previous ones, expand closer to the sinus wall, demonstrating a more physiological geometric ratio (*fig.6.7, b*). The main forward jet develops in all the acceleration phase without any lateral obstruction (maximum velocity around 1.7 m/s, width of 1.92 cm), and is still uniform and wide after the flow peak, with minor vortical effects visible at the root wall (*fig.6.7, a-b-c*). Before the velocity peak, a positive vortex forms in the Valsalva sinus, and during the maximum negative gradient this is clearly developed inside the sinus (*fig.6.7, b-c*). The positive vortex is still visible in the sinus and at the leaflet edge at 234 ms (*fig.6.7, d*), when another vortical structure forms at the right side, above the commissure, which is reduced in profile but still partially evident. Closure is characterised by the permanence of the positive vortex inside the sinus, and a slow flow velocity region close to the leaflet edges (*fig.6.7, e*).

In terms of hydrodynamic performances, the valve produces a Δ*P* of 3.29 mmHg and a computed *EOA* of 2.99 cm^2, equating to 61% of the root cross section. The closing regurgitant volume is much higher than in previous cases (3.20 ml), due to the larger leaflets, but the associated energy losses are significantly smaller (29.62 mJ) than the gain in terms of systolic performance.

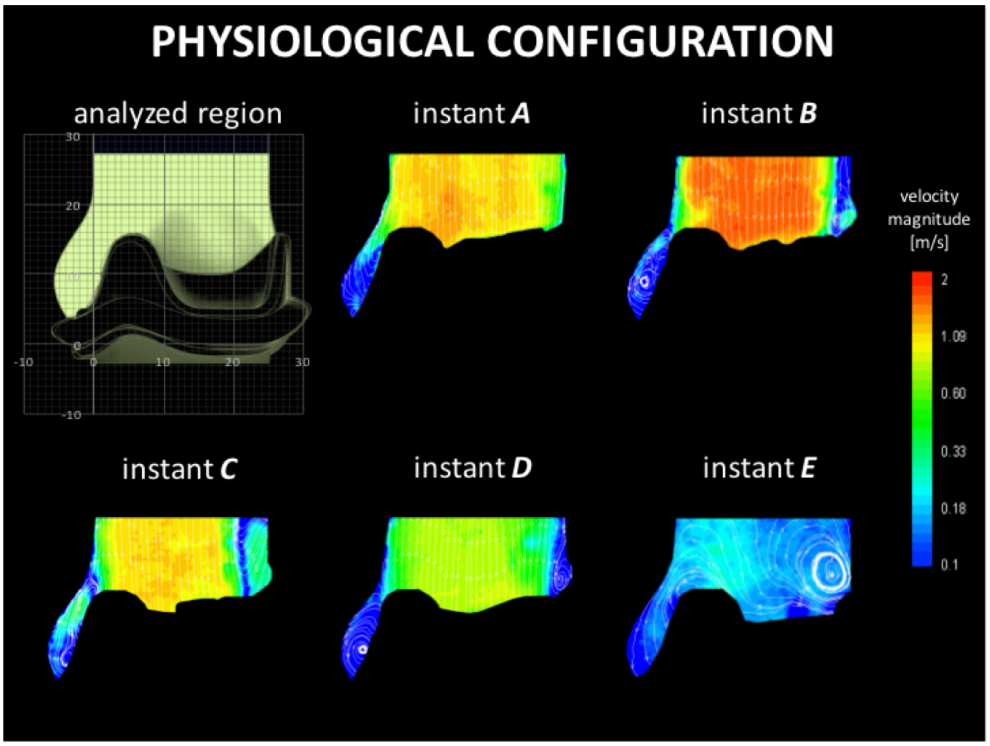

Fig.6.7 Velocity maps and streamlines for stentless configuration.

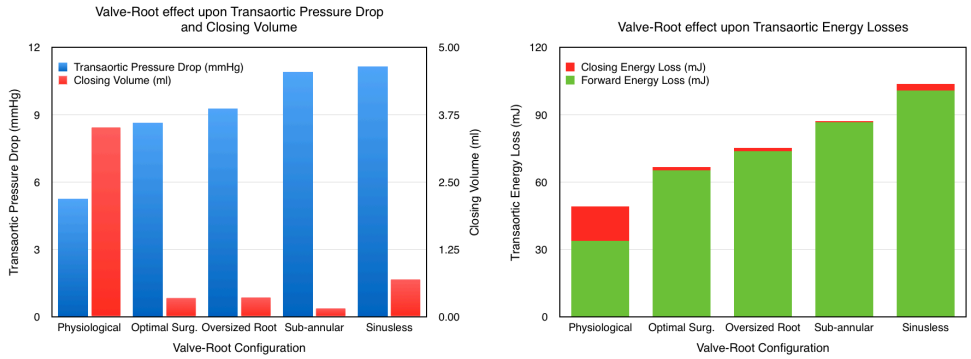

Fig.6.8 *a)* plot of EOA and transaortic pressure drop for each configuration; *b)* plots of transaortic enegry losses and valve regurgitation for each configuration.

Experimental Valve/Root Setup	Effective Orifice Area (cm^2)	Transaortic Pressure Drop (mmHg)	Transaortic Energy Losses (mJ)					Regurgitant Properties		
			Forward	*Closing*	*Forward + Closing*	*Leaking*	*Total*	*Closing Volume (ml)*	*Leakage Volume (ml)*	*Regurgitive Fraction (%)*
Physiological, 29V-25R	2,998	3,289	13,881	14,587	28,468	1,155	29,623	-3,196	-3,187	9,616
Ideal surgical 25V-25R	1,653	8,630	65,352	1,280	66,632	13,028	79,660	-0,450	-1,169	2,366
Valve Mismatch, 25V-29R	1,532	9,285	73,675	1,569	75,244	43,459	118,703	-3,267	-6,336	5,962
Straight Tube, 25V-25R	1,572	10,982	100,884	2,740	103,624	33,653	137,277	-0,702	-2,646	5,311
Low Position, 25V-25R	1,410	10,906	86,593	0,504	87,097	0,147	87,244	-0,159	0,000	0,272

Table1. Hydrodynamic data for all configurations.

6.4 Discussion about the flow dynamic patters in integrated valve-root aortic system

One of the most interesting ongoing issues with the flow dynamics of prosthetic valves is the recreation of an experimental setup able to closely mimic the physiological flow behaviour. In this context, the local flow behaviour in the human aortic root appears to be still unclear, with reports of different vortical structures within the Valsalva. This study focused on different experimental combinations of mock aortic roots and porcine valves, in order to identify the closest physiological condition and offer an explanation for the different fluid dynamics observed in the sinuses and reported in literature.

The repeated formation and migration of vortices observed in the sinusless configuration corroborates the hypothesis that the development of the vortices depending upon the root geometry (fig.6.9) (Bellhouse & Bellhouse, 1968; Peskin, 1982; Van Steenhoven et al., 1982; Peacock, 1990). Comparison between the 25 mm physiological root and the 25 mm straight root suggest that the presence of Valsalva sinuses act as chambers, which host the vortical rings formed during systolic ejection, enabling the main jet to reattach to the wall just after the sino-tubular junction (fig.6.9, i-ii). It also suggests that presence of the Valsalva sinuses is sufficient to substantially enhance the hydrodynamic performance of the valve. In both cases a strong stable vortex above the commissure (fig.6.3, a-d; fig.6.4, a-d) was observed. However, as described above, other operative modes have been observed, which are characterised by a mixed behaviour. The alternative dynamics reported in the literature often resulted from investigations where there was geometric mismatch between the valve and the testing root (which is commonly larger than the ideal physiological root, in order to host valves of various dimensions), or the axial position of the valve, which is often housed between the ventricular and the aortic chamber, was below the physiological position. Hence both conditions were simulated, in order to verify how they affect the flow and if they can justify the reported inconsistencies.

The valve mismatch (e.g. due to undersizing), represented here by placing a 25 mm valve into a 29 mm physiological root, results in intermediate flow

patterns: the systolic vortex ring expands into the sinuses but, due to the large cross-section at the sino-tubular junction, it escapes into the ascending aorta, resulting in a narrowing of the high velocity blood stream (fig.6.9, iii). This mechanism increases the transvalvular pressure drop. Interestingly, despite an aortic root cross section 35% larger than in the other tests, the effect of the jet contraction results in a significant reduction in EOA, which is similar to the case study with no sinuses. Closing regurgitant fractions and global energy losses are intermediate between the ideal surgical and the cylindrical configurations. This testing configuration, common in in vitro tests due to the need for universal roots fitting the different valve sizes, also describes the case of under-dimensioned valves or dilated aortic roots, providing an idea of the change in performance associated with geometric changes occurring in pathologic scenarios (Leo et al., 2006; Dasi et al., 2009; Saikrishnan et al., 2012; Moore et al., 2014).

In the low position valve experiment, the vortex-escaping phenomenon was accompanied by a positive entrapped vortex in the Valsalva sinus (*fig.6.9*, iv). As a result, the forward main jet is rapidly confined on one side by the escaped vortical structure, producing a narrower vena contracta. Whilst the formation of a large positive vortex in the Valsalva chamber supports early coaptation of the leaflets, reducing the closing regurgitant volume, the global energy loss performance is diminished. The resulting mixed mechanism (escaping and trapped vortices) appears similar to the one reported in different in vitro studies, and demonstrates how the valve housing design is crucial (Lim et al., 1997; Lim et al., 1998; Lim et al., 2001). This experiment suggests that current supra-annular implantation approach, recently preferred to infra-annular implantation, may result in enhanced performance with both a more favourable geometric orifice area and improved hemodynamics.

The ideal surgical configuration, with matching valve and root sizes, produces hydrodynamic performance superior to all other stented cases (*fig.6.9*, ii). Removing the sinuses, which describes the case of a valve implanted into a tubular aortic graft, results in the vortices that form during systole to cause repeated contractions of the jet. This results in an increase of the transvalvular pressure drop greater than 25%, and a 5% reduction in the EOA, as well as a reduction in closing efficiency, characterised by a regurgitant volume more than twice that of the ideal surgical configuration. This may be due to the absence of radial flows, which can develop in the sinuses and promote coaptation of the leaflets. Globally, the energy losses due to the absence of sinuses are estimated to be more than 50% higher than for the physiological root. Our results confirm the finding from Pisani (Pisani et al., 2013), and the hypothesis developed from in vivo study (Schoenhoff et al., 2013), providing a justification via fluid dynamics for the reduction in EOA.

The most efficient valve configuration, as expected, is the stentless-like arrangement (or native configuration), which has the largest annulus orifice area and more closely replicates physiological conditions, due to leaflet matching and an embedded valve stent (*fig.6.9*, v). This is associated with a transvalvular pressure drop 62% lower than that of the stent-matching surgical idealised set up, and 70% lower than with the worst performing configuration (straight root). This stentless configuration is characterised by a positive entrapped vortex present during almost all the cycle in the Valsalva sinus, and for the restricted presence of the recirculation region above the commissure.

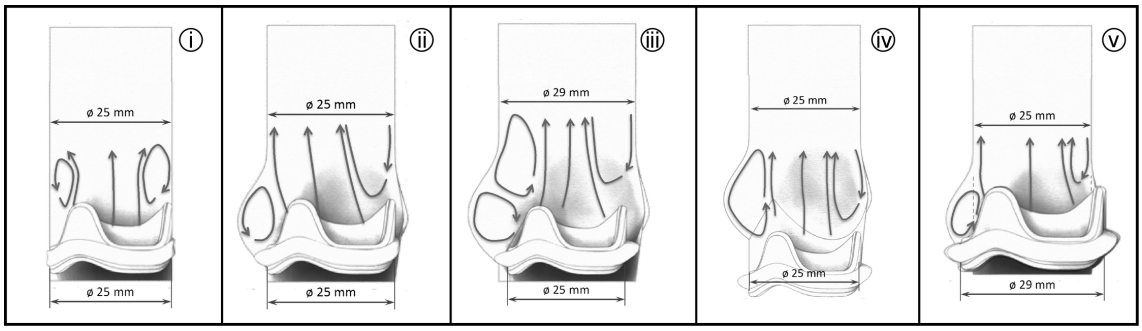

Fig.6.9 Sketch characterisation of flow patterns in all configurations.

6.5 Study abstract

The *in vitro* behaviour of the local flow downstream of a prosthetic heart valve is a widely discussed topic, since the '60s. The physiological flow dynamics in the Valsalva sinuses, in terms of global and local parameters, is still controversial. This study attempts to identify the physiological conditions as closely as possible, and give an explanation of the different and contradictory results in literature. To better understand in details the flow patterns inside the aortic district an *in vitro* approach to test different mock aortic roots, coupled with two different surgical porcine bio-prosthetic valves (stent matching and leaflets matching), were developed. The global and local flow performances were carried out *in vitro*, on a pulse duplicator, using a 2D particle image velocimetry technique. All tests were performed under physiological pressure and flow condition, following the ISO 5840:2009.

The obtained results show how the stentless-like aortic root provided the physiological reference system, and characterised by the best hemodynamic performance. Tests on other root-valve configurations also evidence that the shape and the dimension of the root play an essential role in assessing the hydrodynamic performance of the valve. In particular, these outcomes show how a stent mismatch, leaflet mismatch, or different positioning of the valve could produce significantly different flow patterns and velocity fields in the Valvsalva sinuses, as well as the importance of the sinuses in leaflet closure. It is opinion of the authors that these tests give an explanation for the different vortical structures found in literature, but also raises new considerations, reinforcing how difficult could be to accurately describe and assess the performance of a prosthetic heart valve, even if only considering the ΔP and EOA parameters.

In conclusion, this study should provide a new answer for the vortical structures normally seen downstream of flexible leaflet heart valves. Different combinations of flows reported in the literature have been reproduced, identifying the optimum physiological fluid dynamics and the perturbations introduced by geometric mismatches. This works shows that the valve and aortic root act as a system, greatly affecting valve dynamics and hemodynamic performance, and therefore must be considered relative to each other in order to assess performance. It is therefore suggested that an objective assessment

of the device should be carried out on specifically designed aortic root systems. These observations strengthen the importance of a new global definition for “valve” performances.

As last, this experimental induction technique could provide an interesting base to design and develop new higher performance bioprosthesis.

6.6 Chapter bibliography

[1]. Baumgartner, H. et al. Echocardiographic assessment of valve stenosis : EAE / ASE recommendations for clinical practice. Eur. J. Echocardiogr. 1–25 (2008). doi:10.1093/ejechocard/jen303

[2]. Bellhouse, B. J. & Reid, K. G. Fluid mechanics of the aortic valve. J. Fluid Mech. **35,** 721–735 (1969).

[3]. Bellhouse, B. J. & Bellhouse, F. H. Mechanismn of Closure of the Aortic Valve. Nature **217,** 86–87 (1968).

[4]. Caro, C. G., Pedley, T. J., Schroter, R. C. & Seed, W. A. The Mechanics of Circulation. (Cambridge, 2012).

[5]. Dasi, L. P., Simon, H. a., Sucosky, P. & Yoganathan, A. P. Fluid mechanics of artificial heart valves. Clin. Exp. Pharmacol. Physiol. **36,** 225–237 (2009).

[6]. De Hart, J. Numerical Analysis of a Three-Leaflet Aortic Valve Prosthesis Numerical Analysis of a Three-Leaflet Aortic Valve Prosthesis. (Eindhoven University of Technology, The Netherlands, 1997).

[7]. De Hart, J., Peters, G. W. M., Schreurs, P. J. G. & Baaijens, F. P. T. A three-dimensional computational analysis of fluid-structure interaction in the aortic valve. J. Biomech. **36,** 103–112 (2003).

[8]. Ducci, A., Tzamtzis, S., Mullen, M. J. & Burriesci, G. Hemodynamics in the Valsalva sinuses after transcatheter aortic valve implantation (TAVI). J. Heart Valve Dis. **22,** 688–696 (2013).

[9]. Escobar Kvitting, J. P. et al. Flow patterns in the aortic root and the aorta studied with time-resolved, 3-dimensional, phase-contrast magnetic resonance imaging: Implications for aortic valve-sparing surgery. J. Thorac. Cardiovasc. Surg. **127,** 1602–1607 (2004).

[10]. Fisher, J. & Wheatley, D. J. Hydrodynamic function of ten prosthetic heart valves in the aortic position. Clin. Phys. Physiol. Meas. **9,** 307–317 (1988).

[11]. Fukui, T. & Orinishi, K. Influence of Vortices in the Sinus of Valsalva on Local Wall Shear Stress Distribution. Int. J. Life Sci. Med. Res. **3,** 94–102 (2013).

[12]. Grigioni, M. et al. Three-Dimensional Numeric Simulation of Flow Through an Aortic Bileaflet Valve in a Realistic Model of Aortic Root. Am. Soc. Artif. Intern. Organs **51,** 176–183 (2005).

[13]. Keele, K. D. Leonardo da Vinci as Physiologist. Postgrad. Med. J. 521–528 (1952).

[14]. Korakianitis, T. & Shi, Y. Numerical simulation of cardiovascular dynamics with healthy and diseased heart valves. J. Biomech. **39,** 1964–1982 (2006).

[15]. Katayama, S., Umetani, N., Sugiura, S. & Hisada, T. The sinus of Valsalva relieves abnormal stress on aortic valve leaflets by facilitating smooth closure. J. Thorac. Cardiovasc. Surg. **136,** 1528–1535.e1 (2008).

[16]. Leo, H. L., Simon, H., Carberry, J., Lee, S. C. & Yoganathan, A. P. A comparison of flow field structures of two tri-leaflet polymeric heart valves. Ann. Biomed. Eng. **33,** 429–443 (2005).

[17]. Leo, H. L., Dasi, L. P., Carberry, J., Simon, H. a. & Yoganathan, A. P. Fluid dynamic assessment of three polymeric heart valves using particle image velocimetry. Ann. Biomed. Eng. **34,** 936–952 (2006).

[18]. Lim, W. L., Chew, Y. T., Chew, T. C. & Low, H. T. Steady flow velocity field and turbulent stress mappings downstream of a porcine bioprosthetic aortic valve in vitro. Ann. Biomed. Eng. **25,** 86–95 (1997).

[19]. Lim, W. L., Chew, Y. T., Chew, T. C. & Low, H. T. Steady flow dynamics of prosthetic aortic heart valves. J. Biomech. **31,** 411–421 (1998).

[20]. Lim, W. L., Chew, Y. T., Chew, T. C. & Low, H. T. Pulsatile flow studies of a porcine bioprosthetic aortic valve in vitro: PIV measurements and shear-induced blood damage. J. Biomech. **34,** 1417–1427 (2001).

[21]. Markl, M. et al. Time-resolved three-dimensional magnetic resonance velocity mapping of aortic flow in healthy volunteers and patients after valve-sparing aortic root replacement. J. Thorac. Cardiovasc. Surg. **130,**

456–463 (2005).

[22]. Markl, M., Kilner, P. J. & Ebbers, T. Comprehensive 4D velocity mapping of the heart and great vessels by cardiovascular magnetic resonance. J. Cardiovasc. Magn. Reson. **13,** 7 (2011).

[23]. Moore, B. & Dasi, L. P. Spatiotemporal complexity of the aortic sinus vortex. Exp. Fluids **55,** (2014).

[24]. Ming, L. & Zhen-huang, K. Study of the Closing Mechanism of Natural Heart Valves. Appl. Math. Mech. **7,** 955–964 (1986).

[25]. Peskin, C. S. the Fluid Dynamics of Computational Methods. Ann Rev Fluid Mech **14,** 235–259 (1982).

[26]. Peacock, J. a. An in vitro study of the onset of turbulence in the sinus of Valsalva. Circ. Res. **67,** 448–460 (1990).

[27]. Pisani, G. et al. Role of the sinuses of Valsalva on the opening of the aortic valve. J. Thorac. Cardiovasc. Surg. **145,** 999–1003 (2013).

[28]. Otto, C. M. & Pearlman, A. S. Doppler Echocardiography in Adults With Symptomatic Aortic Stenosis: Diagnostic Utility and Cost-effectiveness. Arch Intern Med **148,** 2553 – 2560 (1988).

[29]. Ranga, A., Bouchot, O., Mongrain, R., Ugolini, P. & Cartier, R. Computational simulations of the aortic valve validated by imaging data: evaluation of valve-sparing techniques. Interact. Cardiovasc. Thorac. Surg. **5,** 373–378 (2006).

[30]. Reul, H. et al. The Geometry of the Aortic Root in Health , at Valve Disease and after Valve Replacement. J. Biomech. **23,** 181–191 (1990).

[31]. Rubenstein, D. A., Yin, W. & Frame, M. D. Biofluid mechanics. (Elsevier, 2012). doi:10.1515/bmte.1998.43.4.94.

[32]. Saikrishnan, N., Yap, C.-H., Milligan, N. C., Vasilyev, N. V. & Yoganathan, A. P. In Vitro Characterization of Bicuspid Aortic Valve Hemodynamics Using Particle Image Velocimetry. Ann. Biomed. Eng. **40,** 1760–1775 (2012).

[33]. Schoenhoff, F. S. et al. The role of the sinuses of Valsalva in aortic root

flow dynamics and aortic root surgery: evaluation by magnetic resonance imaging. J. Heart Valve Dis. **18,** 380–385 (2009).

[34]. Swanson, W. M. & Clark, R. E. Aortic valve leaflet motion during systole. Numerical-graphical determination. Circ. Res. **32,** 42–48 (1973).

[35]. Thubrikar, M. J. The Aortic Valve. (CRC Press, Inc., 1990).

[36]. Thubrikar, M. J., Piepgrass, W. C., Shaner, T. W. & Nolan, S. P. The design of the normal aortic valve. Am. Physiol. Soc. H795 – H801 (1981).

[37]. Van Steenhoven, A. A. & Van Dongen, M. E. H. Model studies of the closing behaviour of the aortic valve. J. Fluid. Mech. **90,** 21–32 (1979).

[38]. van Steenhoven, A. A., Veenstra, P. C. & Reneman, R. S. The Effect of some Hemodynamic Factors on the Behaviour of the Aortic Valve. J. Biomech. **15,** 941–950 (1982).

[39]. Yang, G. Z., Mohiaddin, R. H., Kilner, P. J. & Firmin, D. N. Vortical Flow Feature Recognition : A Topological Study of In Vivo Flow Patterns Using MR Velocity Mapping. J. Comput. Assist. Tomogr. **22,** 577–586 (1998).

Chapter 7

Coupling PIV measurements and numerical modelling of RBCs to predict thrombogenicity of mechanical prosthetic heart valves

7.1 Introduction: haemolysis problem for a mechanical prosthetic aortic valve

The principal aim of this study was to approach the haemolysis problem in a different way respect to the usual non-physical based studies founded in literature (Sutera et al., 1975; Heusen et al., 1980; Paul et al., 2003; Goubergrits et al., 2004). Moreover, this research gives the chance to approach the numerical studies and the mechanical modelling of small bodies, working in couple with a numerical physicist researcher: Giuseppe Fadda, from the Mathematical Dept. of the University of Padua.

In this context, the present chapter and the described research focused on:
1) estimation of the damage supported by a cardiovascular prosthesis, via numerical analysis, starting from velocity fields from *in vitro* data;
2) determination of the *haemolysis index* and the "damage trajectories" for a cloud of red blood cells flowing through a mechanical prosthetic valve (MPV), placed in aortic position.

The valve data were obtained from a previous study (Toninato MSc thesis, 2012), and consist of *in vitro* velocity maps of the aortic region downstream a MPV. Eulerian maps were measured via particle image velocimetry technique (*PIV*), and are here used as a flow velocity reference to direct the red blood cells (*RBCs*) as passive bodies through the measured field. Every single RBC was modelled using a specific 2D shape, adopting a mechanical model for the shell, and then injected upstream the valve and followed during the time needed to leave the region of interest. A haemolysis index (*HI*) law was developed and computed using the obtained data, and compared with others literature work, enhancing the importance of a physical based approach instead of a mathematical heuristic path (Wurzinger et al., 1986).

Before going in deep on the technical description of the cell model,it is useful to give some information using the literature view about the haemolysis problem, the power law used strategies to computed the damage, and the idea of a *in vitro-numerical* merged strategy.

7.1.1 Haemolysis phenomena: overview

Since the first implant of prosthetic valves, around the '60s, surgeons understood the crucial importance of how a good interaction between non-self materials, body fluids and organs could determine the implant success (Wootton et al., 1999; Yoganathan et al., 2003).

This characteristic, which was called biocompatibility, is a multi face concept that plays a fundamental role in the choice of the materials, chemical surface treatments, and design of the prosthetic devices. This study doesn't touch any specific problem about the chemical composition of the prosthetic materials however it should give an idea of how a foreign element can modify the body equilibrium, finding the impact of the prosthetic device on the blood damage. As for cardiovascular implants, it was soon clear that the main complications related to the failure of the treatments with mechanical devices were strongly linked on thrombosis and thromboembolism and anticoagulant-related haemorrhage, even far from the device. Events, these latter, that lashed lots of patients during the years after the implantation (Katircioglu et al., 1999; Yin et al., 2006; Sezai et al., 2009).

The thrombosis is directly correlated to a damage suffered from blood particle and it could be defined as the formation of a blood clot inside a blood vessel, free to scatter in the circulatory system. Even when a blood vessel is not injured, blood clots may form in the body under certain conditions. In particular, if the shear stresses suffered by the RBCs flowing through a heart valve are high enough, they can tear up the cell membrane. This causes the disaggregation of the cell, the beckon of the platelets, and the formation of a mass of biologic material. Thromboembolism is the combination of thrombosis and its main complication, embolism.

Now it is easy to understand why the cardiovascular prosthetic devices (e.g. mechanical valves, TAH-t, VADs) exhibit a non-negligible haemolytic potential. For prosthetic valves, the observations of these phenomena arise from far in time, since the first monoleaflet Bjork-Shiley was developed and commercialized during the '70s. The idea was always to maintain high reliability and improve the hemodynamic performance of these prostheses. So, the technological trend was to convert an industrially derived device (a simple hydraulic pipe valve), into a device more and more alike to the biological native structure. Despite a noticeable improvement in performance, the problem of thrombus growth and red blood cells damage still remains one of the main concerns for mechanical heart valves (MHVs). Their design did not substantially change from the early bileaflet valves in the '90s. The

technological trend is to use more and more biological devices, but a sizeable share of market is still held by MHVs.

Therefore, the problem of blood damage remains quite important from an engineering point of view. During the last two decades there were mainly "variations on the same theme" (*fig.7.1*) for discovering and making the best bileaflet mechanical heart valve (BMHV). The results of this strategy was a large range of devices such as the ones illustrated in Figure 7.1 were the structural materials are almost the same, and the changes are in the leaflets design, hinge position, housing height and shape. From these models two main design criterion have been used for BMHVs: i) reduction of stagnation in the hinge area, to avoid deposition and tissue overgrowth, and ii) lowering the flow shear stresses on the leaflets, to preserve RBCs and platelets (PLs). But, up to now, a correct evaluation of the risk in term of damage on particles has not been done using a mechanical-biological model.

So, the presence of trombogenesis and damage processes, due to an incorrect matching of biological request and prosthetic solutions, in terms of biocompatibility and fluid mechanics, beckons the attention on the need to evaluate a physically based hemolysis index.

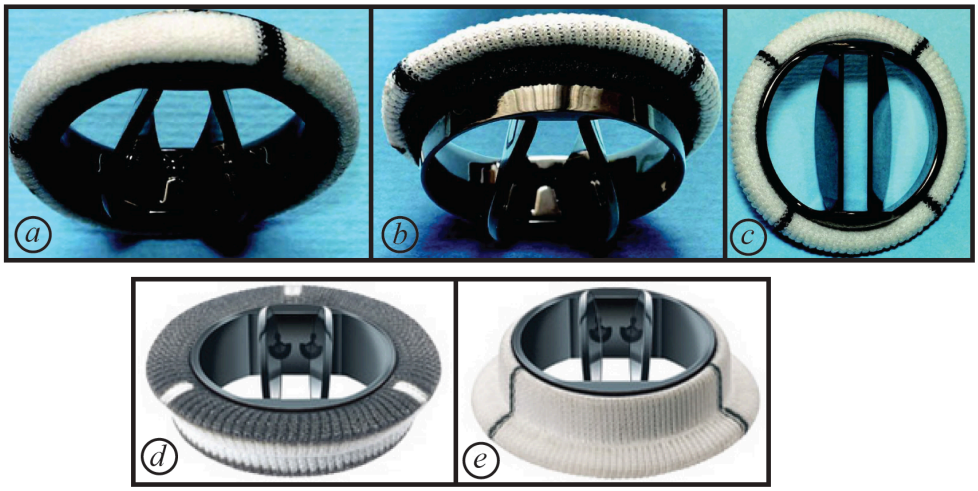

Fig. 7.1: Different BMHVs: a) Sorin Bicabon slimline, b) Sorin Bicarbon overline, c) St. Jude Medical, d) CarboMedics Standard, e) CarboMedics Tophat.

7.1.2 Structure and function of a red blood cell (RBC)

Before talking about the mathematical and mechanical sides of the problem, a brief introduction about the red blood cell biology, structure and function seems useful. This section is intended to be fundamental to better understand the adopted choices in the formulation of the model.

The human erythrocytes (from the greek *erythròs*, «red» e *cytos*, «cell»), or red blood cells, express a fundamental carrier function: they transport the oxygen around the body. They are without nucleus, or other internal organelles, so they have a very simple structure. The cytoplasm is a solution composed by hemoglobin (*Hb*), a red molecule. Each cell contains about $270 \cdot 10^6$ of them, for an internal medium weight of about 26-32 pg. The typical RBC shape is a biconcave profile with a diameter of 6.2-8.2 µm, and a variable thickness: 2-2.5 µm at the edges, 0,8-1 µm in the center (*fig.7.2*). This shape, as it will be clear in the next section, is the best to allow great deformation in shape, without changing the superficial area. The RBCs formation process is called erythropoiesis, and it takes 4-5 days. An averaged population man has about $2\text{-}3 \cdot 10^{13}$ RBCs flowing into the organism, so these cells are the most common in the human body. Because of the absence of a nucleus they totally depends on the production by the red bone marrow. A mature cell lives about 100-120 days, after that it will be erase by the depicted cells. During their life the RBC shell becomes stiff, so the elastic properties drastically change, increasing the probability of a damage and hemolysis.

Characteristic	Value
Disk diameter	6.2-8.2 µm
Maximum thickness	2-2.5 µm
Minimum thickness (at the centre)	0.8-1 µm
Area	140 µm2
Cell medium volume (MCV)	90 fl
Cell medium Hb (MCH)	26-32 pg
Medium life	100-120 days

Table 7.1: Geometric and biological data for red blood cells.

The main function of the RBCs is to carry the oxygen (O_2) from lungs the all the organs and tissues, and bring back the CO_2 to the lungs: this circle is normally completed in 20 seconds. To express their function, the cell cytoplasm of RBCs encloses a specific protein: the hemoglobin (Hb). The hemoglobin is a globular protein with a quaternaries structure. It is composed by 4 sub units (α e β chains) that contain the EME GROUP, which is a protoporfirine molecule linked to an iron ion *(fig.7.3)*. The presence of these ions allows the RBC gas exchange through the membrane.

The hemoglobin is important in this study because the most used strategies to measure or quantify the hemolysis index, and the prosthesis potential dangerousness, are referred to the released *Hb* from the cell lysis.

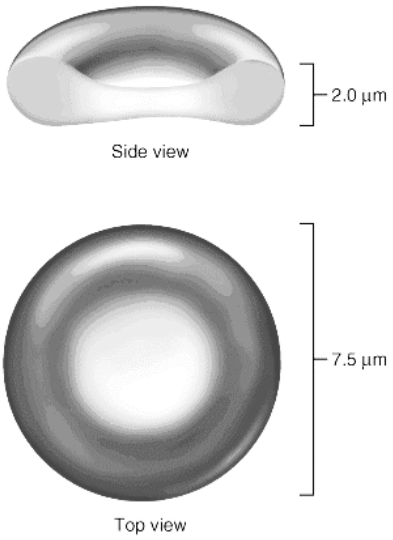

Fig. 7.2: Side and top view of a typical red blood cell.

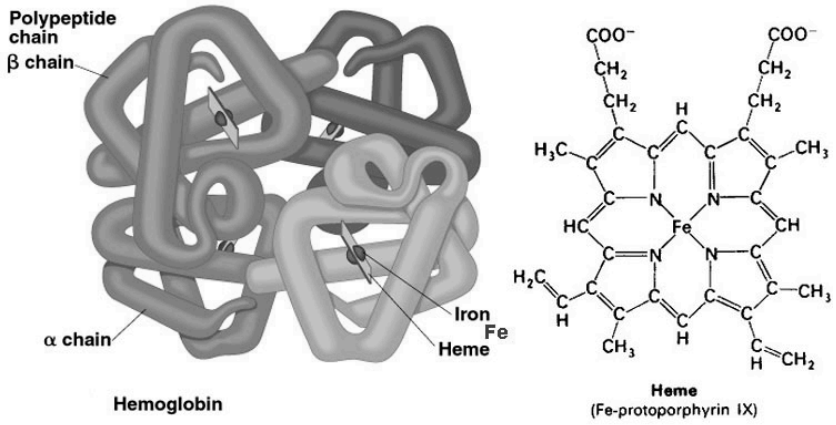

Fig. 7.3: Hemoglobin polypeptide chains and chemical structure of Heme group.

7.1.3 Clinical and engineering views

From a mechanical and fatigue point of view the prosthetic valve devices satisfy the main fluid dynamic needs but, looking locally in the aortic root region (Valsalva sinuses and sinotubular junction) the hematic conditions tend to diverge from the physiological (Yoganathan et al., 1995; Chandran et al., 2006; Dasi et al., 2007; Dasi et al., 2009; Shariari et al., 2012). Consequences of that

are high stresses regions that provide great problems of lysis on the curposcolate part of the blood, and recirculation region with very low velocity, where the clotting of particles is favourite. In the first case the damage is called induced haemolysis and causes the spillage of haemoglobin in the vessel (aorta). Hemolysis is to be avoided for two reasons. First, hemoglobyn molecule can't flow free in the organism, due to its toxicity to the other cells (oxidation processes). Second, the fragments of RBC are normally blocked by platelets and other cells, forming big aggregates, which are potentially very dangerous also far from the aorta (ischemic episodes).

Starting from these considerations, in the last decades different theories were developed to face this task, and this study start from the idea that the literature is still incomplete with respect to the physical interpretation of the problem, and unclear in terms of what really is the haemolysis index and what determines the damage on the cells (Heuser et al., 1980; Wurzinger et al., 1986; Paul et al., 2003; Goubergrits et al., 2004; Arora et al., 2004; Grigioni et al., 2005; Chandran et al. 2006; Zhang et al., 2011; Taskin et al., 2012).

In particular, to better understand the model proposed in the next session, here are reported the main ways adopted in literature to quantify the damage supported by the RBCs. The clinical measurement of the haemolysis comes directly from physiological parameters. The estimation derives from the levels of free haemoglobin in the whole blood (Hb_{free}). The basal value, in absence of damage effects is about 0.02-0.05 mg/L, whereas the warning threshold is set at 0.3-0.6 g/L (Lippi et al., 2009).

In the engineering scenario the haemolysis index is mostly derived from the variation of the free haemoglobin in the blood (ΔHb) after the cells lysis, compared to the whole haemoglobin quantity in the body (Hb_{TOT}).

$$HI(\%) = \frac{\Delta Hb}{Hb_{TOT}}$$

The warning threshold normally adopted is 0.5-1.0% (Lippi et al., 2004).

In literature are collected lots of studies that try to explain the experimental results making use of empiric laws or direct *in vitro* measurements on the cells (Rand, 1964; Blackshear, 1972; Skalak et al., 1973; Evans et al., 1876; Hochmouth et al., 1979; Wurzinger et al., 1986; Bronkhorst et al., 1995; Paul et al., 2003). One of the first evidence in the past was the dependence of the shell damage on the value of the force and of the time interval in which the stress is applied. To better understand the correlation between these two parameters in vitro tests were carried out, where different strain were imposed to a RBC for different times, until the complete lysis of the cell (Sutera et al., 1975). The technological limits, due to the difficulties of testing such small bodies, were overcome in the last 15 years and a well-known and still used important strain threshold is 150-200 Pa (Giersiepen et al., 1990; Paul et al., 2003). Under

these values the stress and the time express the same weight in the computation of the blood damage, over that threshold the time becomes less important to have a lysis of the RBC, (as described in Sutera et al., 1975; Paul et al., 2003; Goubergritz et al., 2004). But this approach seems to be too rough and other strategies were persecuted recently.

To better correlate the shear stress (*t*) to the exposition time (τ),damage laws, called blood damage index (*BDI*) laws, were formulated. They are usually written in the form:

$$HI = f(t, \tau, \alpha, \beta, A)$$

where *t* is the exposition time to the dynamic field, τ is the shear stress on the cell, and *a*, *b* and *A* are experimental derived parameters (from Couette viscosimeter tests) (Heuser et al. 1980; Giersiepen et al., 1990; Paul et al., 2003; Goubergrits et al., 2004; Zhang et al., 2011). From this general form, different specific formulas were derived. The first example is the all-or-none law, defined as:

$$HI = \tau_{CR} t_{CR}$$

Here, the hemolysis is computed using the *critical* values for strain and time variables, over that limits the total lysis is instantaneously (Goubergrits et al., 2004). Other studies have improved that idea developing the “power laws”, where HI is computed as:

$$HI = A\tau^{\alpha} t^{\beta}$$

where stress and time values are weighted through two parameters, *a* and *b*, and also linearly with the scalar *A*. The literature founded values, via empiric strategy, normally follow the differentiation: $\alpha < 1$ e $\beta > 1$, and are summarized in Table 7.3 (Heuser et al., 1980; Wurzinger et al., 1986; Giersiepen et al., 1990; Zhang et al., 2011). Recent comparison studies focused attention on the limitations of these laws, which don’t take in account physical characteristics of the system, where the measured data are collected under particular flow conditions, and are not representative of a set of cells (Taskin et al., 2012).

A numerical alternative to these empiric-derived laws is the “strain-based” approach (Arora et al., 2004; De Tullio et al., 2012). Here the flows, the geometry of the cell, and the stresses, are completely numerically modelled. The RBC is followed during his path into the fluid, and the stresses at its shell are used to compute HI, still using a power law strategy. In particular, De Tullio used a droplet model to simulate a RBC, as a fluid immersed in another liquid with different density.Authors obtained the shear stress from the instantaneously deformation of the drop shape as

$$\varphi_i = \frac{L_i - B_i}{L_i + B_i}$$

where L_i is the longer axis and B_i the shorter of the drop. The shear stress is computed as:

$$\tau = \mu \frac{2\varphi_i f_1}{(1 - \varphi_i^2) f_2}$$

With f_1 = 5.0 s-1 e f_2 = 4.2298*10-4, calibrated parameters of the model to reproduce the mechanical behaviour of a RBC (f_1 depends by the relaxation time of the membrane, and f_2 incorporates the tank trading effect and the ratio between the standard RBC and the area after haemolysis). To finally compute the HI, De Tullio puts the shear stress values into a classic power law equation:

$$\mathrm{HI} = A\tau^{\alpha} t^{\beta}$$

with, α = 0.785, β = 2.416 e A = 3.62. This approach takes in account some aspects related to the physiology and in particular to the geometry of RBCs, but is still a process driven by power law equation, with two non-physically based parameters (f_1 and f_2).

The illustrated models from literature overview don't include the load history experienced by RBCs . The cells are idealized as newborn, and the membrane expresses the same properties for every RBC. These hypothesis are strongly far from a realistic scenario. In attempt to consider the load history into the model, some accumulation models were developed, which give the blood damage index (BDI) as an integral over time of the different HI computed for each instant along a RBC streamline. This is usually done using a rude integration of the power laws equation:

$$\mathrm{d(BDI)} = A\tau^{\alpha} t^{\beta}$$

$$\mathrm{BDI} = \int_{t_0}^{t} A\tau(\phi)^{\alpha} (\mathrm{d}\phi)^{\beta}$$

Or considering, as infinitesimal contribution, the time derivative of the power law:

$$\mathrm{d(BDI)} = \beta A\tau(t)^{\alpha} t^{\beta-1} \mathrm{d}t$$

$$\mathrm{BDI} = \int_{t_0}^{t} \beta A \tau(\phi)^{\alpha} \phi^{\beta-1} d\phi$$

These approaches (Grigioni et al., 2002; Grigioni et al.,2004) are still quite rude. A more sophisticated integration model was proposed still by Grigioni (Grigioni et al., 2005). In this case, starting from the definition of dose, as the contribution of the instantaneous strains on the RBC shell:

$$D = t \cdot \tau^{\frac{\alpha}{\beta}}$$

the BDI is:

$$\mathrm{BDI} = A \cdot D^{\beta}$$

$$\frac{dD}{dt} = \frac{\partial D}{\partial t} + \frac{\partial D}{\partial \tau} \cdot \frac{d\tau}{dt}$$

After some passages, considering $d\tau/dt > 0$ and a constant strain for infinitesimal time steps is possible to obtain

$$dD = \tau^{\frac{\alpha}{\beta}} d\phi$$

$$D(t) - D(t_0) = \int_{t_0}^{t} \tau(\phi)^{\alpha/\beta} \, d\phi$$

that, in an infinitesimal time increment, integrate from t_0 and t gives the BDI at the present time

$$d(\mathrm{BDI}) = d\left(AD^{\beta}\right) = A d\left(D^{\beta}\right) = A\beta D^{\beta-1} dD$$

$$= A\beta \left(\int_{t_0}^{t} \tau(\xi)^{\alpha/\beta} \, d\xi + D(t_0) \right)^{\beta-1} \tau(t)^{\alpha/\beta} dt$$

$$\mathrm{BDI} = \int_{t_0}^{t} A\beta \left[\int_{t_0}^{\phi} \tau(\xi)^{\alpha/\beta} \, d\xi + D(t_0) \right]^{\beta-1} \tau(\phi)^{\alpha/\beta} \, d\phi$$

The term

$$\left[\int_{t_0}^{\phi} \tau(\xi)^{\alpha/\beta} \, d\xi + D(t_0) \right]^{\beta-1}$$

represents the whole mechanical dose that affect a single RBC, obtained as sum of the single doses acting for each time step.

The illustrated literature works are useful to better understand the proposed model in the next session, for some reasons. The first is that these laws seem not able to express the real connection with the physics of the problem; they are simple algebraic forms usually collected in non-physiological flow fields, in terms of geometric, spatial context, velocity and pressure fields (Zhang et al.

2011; Taskin et al., 2012; Kim et al. 2012). Moreover, the idea of an incremental damage is still too poor to justify a real fatigue behavior of the cell, that has to live for more than 100 days in the human body, and experiences more and more passages through a prosthetic device. To overcome these limits a new mechanical physically based model was developed, and tested using experimental data from physiologically *in vitro* flow field.

Model	α	β	A
GW	0.7850	2.4160	$3.620*10^{-5}$
HO	0.7650	1.9910	$1.800*10^{-6}$
ZT	0.6606	1.9918	$1.228*10^{-5}$

Table 7.3: Costant values ued in power model equations (A, α e β). GW: Giersiepen and Wurzinger; HO: Heuser e Opitz; ZT: Zhang e Taskin.

7.2 Rupture model: the ingredients

The mathematical model presented is an approximation of the reality, but it is able to catch a number of aspects of the problem that were not taken in account before. To give an easier overview it will be described in three separate sections; now some general considerations are introduced.

Blood is assumed to behave as a homogeneous, isotropic, and Newtonian fluid with a constant and uniform dynamic viscosity (Rand et al., 1964). Red blood cells are essentially thin (of the order of 1/800 the overall size of the RBC) membranes of phospholipids surrounding the liquid cytoplasm. Because of the porous nature of the membrane, the internal pressure is nearly equal to the external pressure at all times (Rand et al.,1964; Evans, 1983): the inner-outre pressure difference was hence assumed to be equal to zero for simplicity. The action of the fluid on the cell is thus reduced to the viscous part $2\mu D$, where *D* is the strain rate tensor, i.e. the symmetric part of the fluid velocity gradient. Moreover, as bending is generally negligible for small changes of curvature (Evans, 1983; Tan et al., 2010), the membrane theory of thin shells was used. Consider a shell of revolution (axis *Oz*), and a point *M* on its mid-surface; let ξ and η be its principal directions of curvature, and r_ξ, r_η the corresponding radii of curvature (as shown in *fig. 7.4*).

The internal stress (also called traction in the following) can be decomposed into two components T_ξ, T_η along the principal directions of curvature and a shear component *S* (see fig.7.4). In the framework of membrane theory, the equations determining the principal tractions at point *M* are given by (see Flügge, 1973; Ventesel et al., 2001)

$$\begin{cases} \dfrac{1}{r_\xi}\dfrac{\partial(r_c T_\xi)}{\partial\xi} + \dfrac{\partial S}{\partial\eta} - T_\eta\cos\xi = -p_\xi r_c, \\ \dfrac{1}{r_\xi}\dfrac{\partial(r_c S)}{\partial\xi} + \dfrac{\partial T_\eta}{\partial\eta} + S\cos\xi = -p_\eta r_c \\ \dfrac{T_\xi}{r_\xi} + \dfrac{T_\eta}{r_\eta} = p_n \end{cases}$$

where r_c is the principal radius of curvature at point *M* and *p* the external loading; p_n is the component along the outward unit normal $\overrightarrow{e_n}$ to the tangent plane to the shell at point *M*.

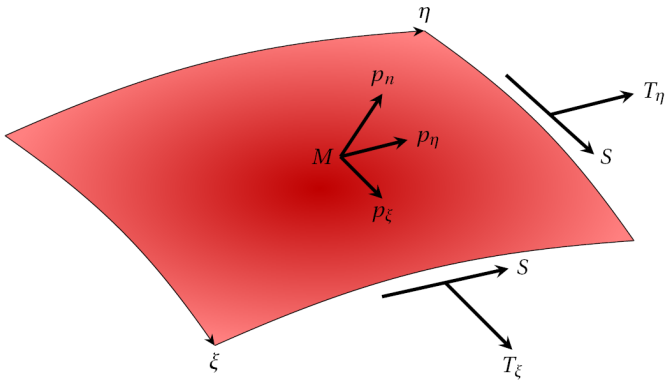

Fig. 7.4: The elements of reduction of the traction on an infinitesimal element of the mid-surface of a shell having ξ and η as principal directions of curvature. The external loading is given by the vector $\vec{p}$.

7.2.1 Geometrical model

Erythrocytes are specialized cells without nucleous, composed of two very different parts: the cytoplasm, which is a liquid, and the membrane, which is essentially a thin layer of phospholipids. In the presented model a single RBC is modelled as an ellipsoid, as can be seen in *fig.7.5*: *a* and *b* are the semi axes on the flow plane (*a* along the flow, *b* transverse to it), and *c* orthogonal to both; the cytoplasm is modelled as incompressible and without motion. The 2D ellipse is placed and held in the streamwise plane. RBCs injected in the flow field are described by different geometrical parameters according to cell age, following *in vitro* experiments (Tran-Son Tay et al, 1987). These characteristics are summarized in Table 7.4.; By symmetry, only 1/4 of the ellipsoid is considered.

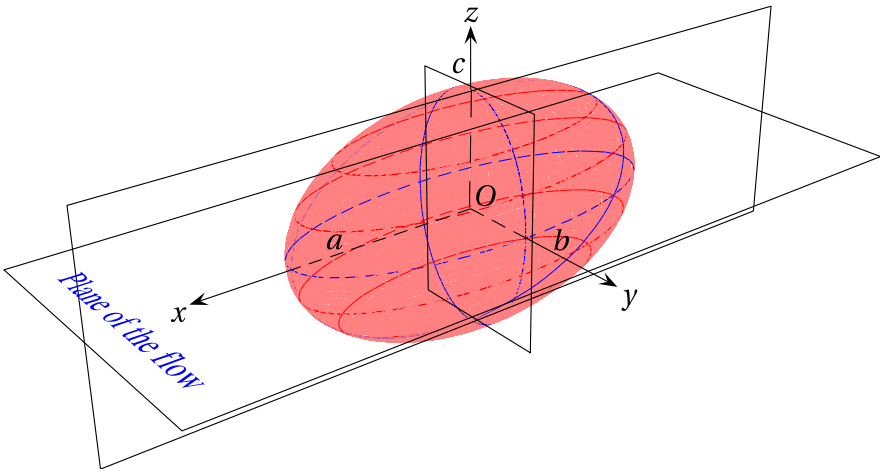

Fig. 7.5: The adopted model for red blood cell geometry: an ellipsoid of semi-axes *a* along *Ox*, *b* along *Oy*, and *c* along *Oz*. The plane of the flow is *Oxy*.

Mean Geometrical Parameters (μm)					
Young			*Old*		
a	b	c	a	b	c
7.410	1.175	2.677	5.822	1.357	2.537

Table 7.4: Geometrical parameters for the RBC in function of the age.

The following analysis is based on the assumption that RBCs do not alter the flow while moving; the load on their surfaces is therefore directly equal to the jump of stress across the membrane.

$$[\sigma] \cdot \overrightarrow{e_n} = (\sigma_{ext} - \sigma_{int}) \cdot \overrightarrow{e_n}$$

Hence, in Cartesian coordinates, the traction exerted by both internal and external fluids on the surface of the RBC (i.e. the load) is given by

$$\overrightarrow{p} = p_i \, \overrightarrow{e_i}$$

$$p_i = ([\sigma] \cdot \overrightarrow{e_n}) \cdot \overrightarrow{e_i}$$

where $\overrightarrow{e_i}$ is the unit vector along direction *i*: here and in the following, the implicit summation over repeated indices is used. For simplicity, the RBC is represented by a triaxial ellipsoid of centre *O* (see *fig.7.5*). Let *M(x, y, z)* be a point at the surface of the ellipsoid; we have the natural parameterization

$$x = asin\alpha\cos\omega\,, \qquad y = bsin\alpha\sin\omega\,, \qquad z = ccos\alpha;$$

α and ω correspond to ξ and η are related to the colatitude θ and the longitude φ through

$$\phi = \arctan\left(\frac{b}{a}tan\omega\right), \quad \theta = \arccos\left(\frac{c}{r}cos\alpha\right)$$

with

$$\mathrm{r} = OM^2 = \sqrt{sin^2\alpha(\alpha^2cos^2\omega + b^2sin^2\omega) + c^2cos^2\alpha}$$

as

$$x = rsin\theta\cos\varphi\,, \qquad y = rsin\theta\sin\varphi\,, \qquad z = ccos\theta.$$

Now only a brief account of the computations is given; for details, see (Novozhilov, 1964; Tran Son Tay et al., 1987; Flügge, 1973). In order to find the principal tractions at the surface of the triaxial ellipsoid (which is not a solid of revolution), we use a linear transformation mapping the ellipsoid into a sphere of radius a. For a sphere of radius a (hence $r_c = r_\xi = r_\eta = a$), the equations that describe the principal tractions simplify into

$$\begin{cases} T'_\alpha = \dfrac{ab}{2c}[\sigma]_{33} + \dfrac{c}{2}\left([\sigma]_{11}\dfrac{b}{a} - [\sigma]_{22}\dfrac{a}{b}\right)\cos 2\omega + c[\sigma]_{12}\sin 2\omega, \\ T'_\omega = \dfrac{ab}{2c}[\sigma]_{33} + \dfrac{c}{2}\sin^2\alpha\left([\sigma]_{11}\dfrac{b}{a} + [\sigma]_{22}\dfrac{a}{b} - 2[\sigma]_{33}\dfrac{ab}{c^2}\right) \\ \quad -\dfrac{c}{2}\cos^2\alpha\left([\sigma]_{11}\dfrac{b}{a} - [\sigma]_{22}\dfrac{a}{b}\right)\cos 2\omega - c\cos^2\alpha[\sigma]_{12}\sin 2\omega, \\ S' = c\cos\alpha\left[[\sigma]_{12}\cos 2\omega - \dfrac{1}{2}\left([\sigma]_{11}\dfrac{b}{a} - [\sigma]_{22}\dfrac{a}{b}\right)\sin 2\omega\right], \end{cases}$$

Starting from here is possible to follow the procedure described in (Flügge, 1973), namely to develop the solutions into Fourier series of the variable ω; as seen in the principal tractions equation, the load has actually only terms of order 0 and 2: consequently, the same holds for the tractions. The following expressions for the tractions on the sphere are then obtained

$$\begin{cases} T_\alpha = T'_\alpha\sqrt{\dfrac{(c_1l_1)^2 + (c_2l_2)^2 + (c_3l_3)^2}{(c_1m_1)^2 + (c_2m_2)^2 + (c_3m_3)^2}} \\ \quad = T'_\alpha\sqrt{\dfrac{[(a\cos\omega)^2 + (b\sin\omega)^2]\cos^2\alpha + (c\sin\alpha)^2}{(a\sin\omega)^2 + (b\cos\omega)^2}}, \\ T_\omega = T'_\omega\sqrt{\dfrac{(c_1m_1)^2 + (c_2m_2)^2 + (c_3m_3)^2}{(c_1l_1)^2 + (c_2l_2)^2 + (c_3l_3)^2}} \\ \quad = T'_\omega\sqrt{\dfrac{(a\sin\omega)^2 + (b\cos\omega)^2}{[(a\cos\omega)^2 + (b\sin\omega)^2]\cos^2\alpha + (c\sin\alpha)^2}}, \\ S = S'. \end{cases}$$

The principal tractions (T1, T2) are then the eigenvalues of the matrix

$$\begin{pmatrix} T_\alpha & S \\ S & T_\omega \end{pmatrix}$$

Using this method is possible to obtain the main tractions on every little area of the RBC shell and then, coupling the rheological model for the cell, compute the deformations.

7.2.2 Mechanical model

The fact that the membrane is thin allows us to use a shell model for the red blood cell; the latter is expected to undergo large deformations before breaking. The hypothesis of small strains cannot thus hold here, implying the necessity of a general constitutive law.

Starting from Jeffery's theory (Jeffery, 1922) the condition of non-perturbation on the flow field was imposed, that is to say the RBC are passive particles. Although the velocity gradient is not uniform, the previous assumption allows a direct solution of membrane equations (provided that a linear transformation is used, i.e. ellipsoid to sphere and back). This strategy enables the computation of the principal tractions on the 2D membrane surface.

To compute the direct deformation on *dA* due to the external flow fields the viscoelastic equivalent of the Skalak model -2D hyper-elastic behaviour- was retained (see Skalak et al., 1973; Evans et al., 1976; Dao et al., 2003), which explicitly includes the resistance to area changes, and is given by:

$$T_1 = \frac{1}{\lambda_1\lambda_2}\left[G\lambda_1^2(\lambda_1^2 - 1) + B(\lambda_1\lambda_2)^2(((\lambda_1\lambda_2)^2 - 1)\right]$$

$$T_2 = \frac{1}{\lambda_1\lambda_2}\left[G\lambda_2^2(\lambda_2^2 - 1) + B(\lambda_1\lambda_2)^2(((\lambda_1\lambda_2)^2 - 1)\right]$$

where (λ_1, λ_2) are the principal stretches, *G* the shear modulus (actually a tension as the membrane is very thin), and *B* the bulk modulus (actually a tension). Viscous behaviour of RBC si taken into account by by adding to the principal tensions the terms:

$$\frac{\mu_M}{\lambda_1}\frac{d\lambda_1}{dt} \quad , \quad \frac{\mu_M}{\lambda_2}\frac{d\lambda_2}{dt}$$

where *M* is the viscoelastic modulus of the membrane (actually a tension multiplied by a characteristic time of relaxation - *T*). The adopted parameters values are shown in Table 7.5-7.6. The implemented rupture criterion is directly linked to global (i.e. for the whole shell) and local (i.e. on each single *dA*) deformation. At this work step, a fragile rupture was assumed: below a specific threshold no damage is done. Once the principal tractions are known, the

differential equations can be integrated and the principal stretches determined for each element depicted in *fig.1*.

	Parameters		
	Shear Modulus – G [N/m]	*Bulk Modulus – B [N/m]*	*Relaxing Time – T [s]*
Literature span (*choosed)	5÷10·10-6 (Rand, Sutera, Skalak, Blackshear)	5·10-3 (Skalak)	0.1÷0.2 (Skalak) (T2=5 s –not implemented)

Table. 7.5: The visco-hyper-elastic model parameter, the red highlighted values are the chosen one.

7.2.3 Haemolysis index

To quantify the haemolysis phenomena, a haemolysis index (HI), directly correlated to the real shear history experienced by the RBC, was computed. This approach does not refer to an analytical formula (e.g. power laws), but actually merges a physical *in vitro* flow field with a direct computation of stress phenomena on the immersed particles by means of a shell model.

Again for simplicity, RBCs are supposed to exhibit fragile rupture: above a certain threshold of one-dimensional elongation (given either by λ_1 or λ_2) or area change (given by the product $\lambda_1 \lambda_2$), the surface element is supposed to break and to release haemoglobin in the blood stream (Hb_{RBC}); the amount released is calculated as the ratio of the ruptured surface over the total surface of the membrane multiplied by the total content of haemoglobin of a single RBC. This enables the computation of the HI directly from the ruptured area for all RBCs present in the blood stream. Thus:

$$HI = \frac{\Delta Hb}{Hb_{tot}} \quad , \qquad where \;\; Hb_{tot} = \frac{Hb_{bas}}{V_{tot}} \cdot V_{ref} + Hb_{RBC} \cdot N$$

$$\Delta Hb = \sum_{i=1}^{M} Hb_{free}^{RBC}(i)$$

where ΔHb is the sum of the Hb_{free}^{RBC} over the M damaged cells. Hb_{tot} is the total haemoglobin contained in the N healthy cells observed during the cycle, plus the Hb related to the blood flowing in the region of interest, with a Hb_{bas} and a volume (total = V_{tot}, and reference = V_{ref}).

Data literatures on the limit values for rupture are lacking: according to (Skalak et al., 1973; Rand, 1964), rupture for isotropic tension occurs at $\lambda \approx 1.08$, whereas the limit is between 1.4 and 1.6 for uniaxial tests. Tran Son Tay (1987) gives values around 2 as being “reasonable”. Area changes, according to Rand (Rand et al., 1964), are of the order of 1.4. Other works consider also the plastic phase in the mechanical cell response (Kuypers et al.,

1998). Values for the mechanical parameters were chosen in order to obtain reasonable values of these critical quantities, comparing our computations with experimental results on Couette flows (see Taskin et al., 2012). In particular the recent work by Zhang (Zhang et al., 2011), and the interpolated power law for the Hemolysis Index

$$\mathrm{HI}(\%) = C\tau^{\alpha}t^{\beta}$$

where C, α, and β are constants, *t* is the exposure time and τ the shear stress in Couette flow. This comparison, plus the obtained results for the *in vitro* flow field data are illustrated in the next session, and gave us the help to better direct the model behaviour.

	Rupture Parameters		
	λ_g $[l_f/l_i]$		λ_l $[l_f/l_i]$
Literature span (*choosed)	1.2÷1.3 Uniaxial (Skalak)	1.04 Isotropic (Rand)	2.0÷2.35÷2.5 (Tran Son Tay)

Table. 7.6: The rupture parameters, the red highlighted values are the adopted in the rupture model.

7.3 Results: power law approach vs. the rupture model; from *in vitro* velocity fields to RBCs damage

7.3.1 *In vitro* PIV results

Phase average velocity field in the transvalvular region was previously obtained by *in vitro* experiments that replicated physiological conditions in both flow and pressure waves for prescribed heart rate and stroke volume (Fortini et al., 2013). Figure 7.6 illustrates the measured 2D velocity field here adopted for HI calculations (SV=64 ml, T=2.4 s; the instant of peak systole is shown). The adopted experimental setup is made up of an aortic deformable root, with three sinuses, and a bileaflet aortic valve. The prosthesis is oriented with one leaflet completely aligned with a sinus (left side of *fig.7.6*), and the camera is perpendicular to the open flat leaflets sides.

It is easy to observe the typical three-jets mid-plane structure for a mechanical prosthetic valve, in which the central jet is wider, compared to the external two. The right one is longer, and develops fast along the side, over the sinotubular junction. This asymmetry of the flow field reflects the geometrical asymmetry of the valve-root coupled system.

In *fig.7.7*, the *2D* viscous shear stresses at the peak of the systole are shown. The maximum stresses are located close to the leaflets, and remain high along the boundary layer.

These data were used as a starting point to compute, first of all, the trajectories of the passive particles (mimicking RBCs injected downstream the valve), then the forces applied on cell surfaces, and finally the relative elongations following the mechanical model implemented for the shell. Before appling the rupture model, another test was performed: using the *in vitro* flow field, the Grigioni dose model was adopted to see how a power law strategy is able to describe the damage phenomena in a realistic semi-physiological scenario.

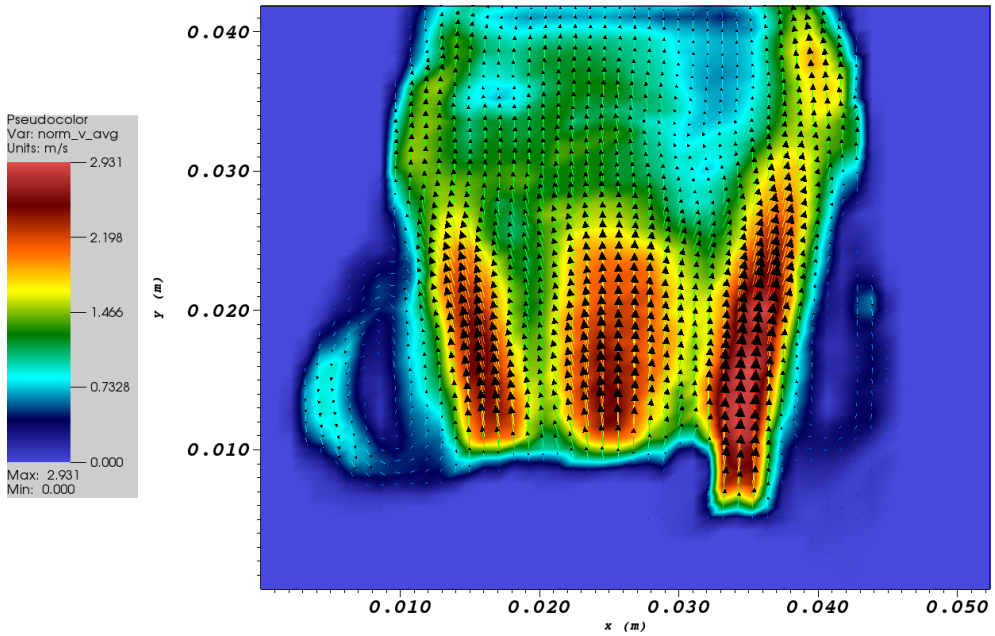

Fig. 7.6: Coloured vector maps of the 2D in vitro velocity flow field at the peak of systole. The valve is positioned following the Grigioni orientation.

Looking at theses maps and following what described before, the haemolysis is a phenomena strongly related to the spatial component (i.e. it depends on the local orientation of the shear forces, and also projects a specific fingerprint of the tested device) and to the environment in which it develops. This aspect is not taken in account in the power laws based literature studies, which decouple the geometry and the damage. This is a clear advantage of the rupture model strategy compared to the conventional heuristic analysis. To better understand if the spatial component is effectively fundamental a comparative test was performed.

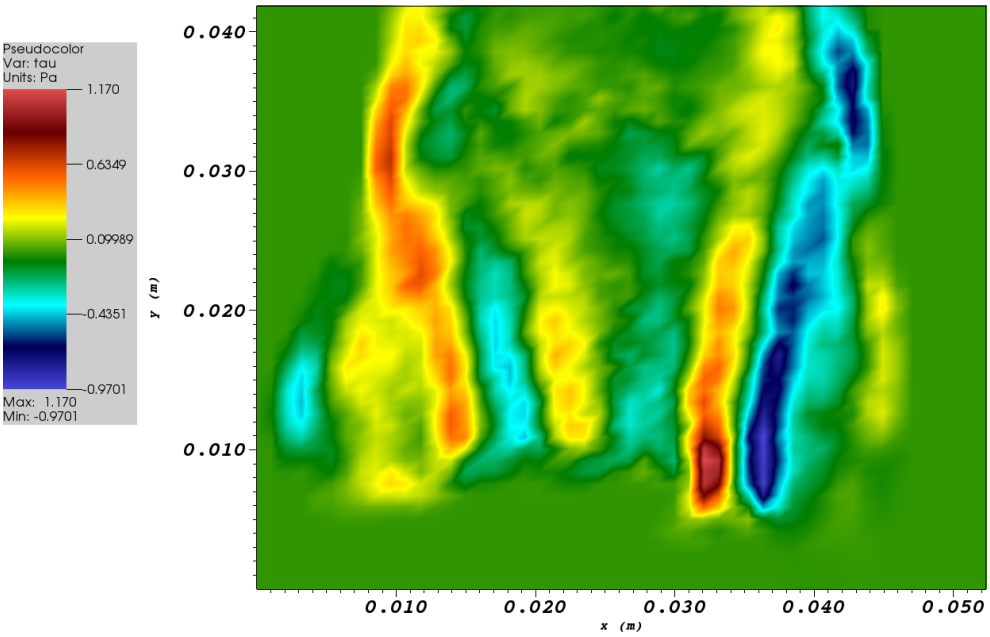

Fig. 7.7: Coloured vector maps of the 2D shear stresses at the peak of systole. The red and blue are enanche the difference in terms of orientation of the stress.

7.3.2 Importance of the spatial information in integrated approach

As first experiment, using the described *in vitro* flow field, *N* particles were injected and an estimation of the *HI* for each particle was determined using a power law equation (so without coupling a mechanical model but thinking at a particle only as a geometric entity that support stresses along a pathway). A multiple passage strategy was adopted. Cumulate damage was quantified using the Grigioni dose model, obtaining a total cumulate damage, at each iteration. For this test were identifies: the trajectories in which the damage is higher in terms of single passage through the valve and 10 damage classes for the trajectories, for cumulate damage after multiple passages through the BMHV.

The results, resumed in *fig.7.8* and *fig.7.9*, allow some considerations:

- The behaviour of the distribution of the number of trajectories in terms of single HI and in function of the belonging class (*fig.7.8*), seems to suggest that the most dangerous trajectories are located in the distribution tails, and are very few (4 orders of magnitude less). This gap remarks as the frequentation of the dangerous trajectories (red areas) could be discouraged by the local flow dynamic, resulting in a containment of the HI. The Index grows principally as integration of little damages along the preferred trajectories (green area).
- Looking at the cumulated HI in function of the HI for single RBC, divided by the pertaining class, it is evident how the damage is almost

totally product (90%) by the passage along the less damaging trajectories (*fig.7.9*).

- The most damaging trajectories produce a haemolysis contribution that is 10 times bigger than the less dangerous. This aspect should have resonance in the design of prosthetic devices, and it can be appreciate only by a spatial investigation.
- The cumulated index in 8 days results about 0.01%, , i.e. much smaller than clinical warning threshold equal to 0.5%. This level is theoretically achieved after a number of passages over the averaged RBC life time.

The above analysis suggests that the power law approach, used in a non-well defined spatial context, could produce a large different span of results. The importance of a correct experimental environment, and an integrated approach, help to better understand how, bounding the power law strategy with more physical contextualized information, is possible to obtain a detailed response.

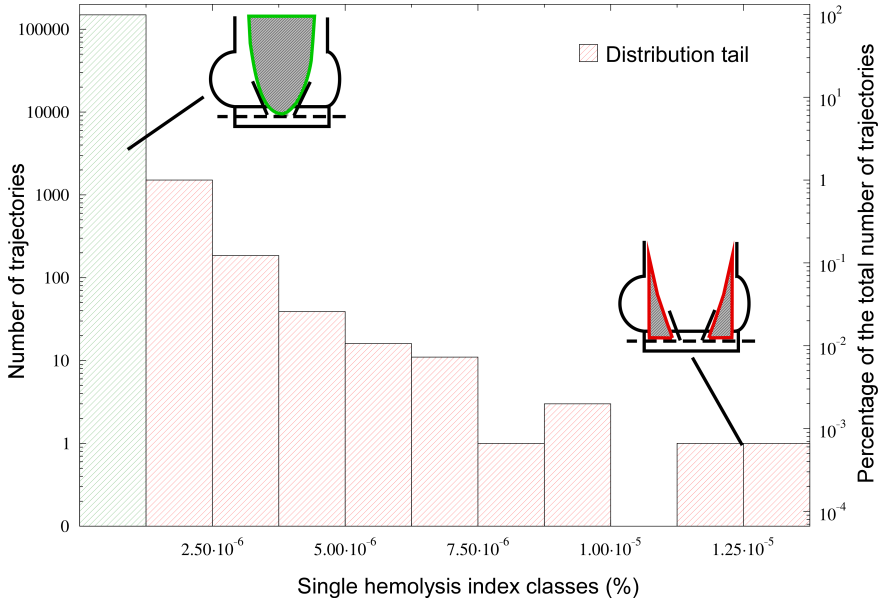

Fig. 7.8: The distribution of the number of trajectories in terms of single HI and in function of the belonging class. The right scale describes the percentage of the total number of trajectories.

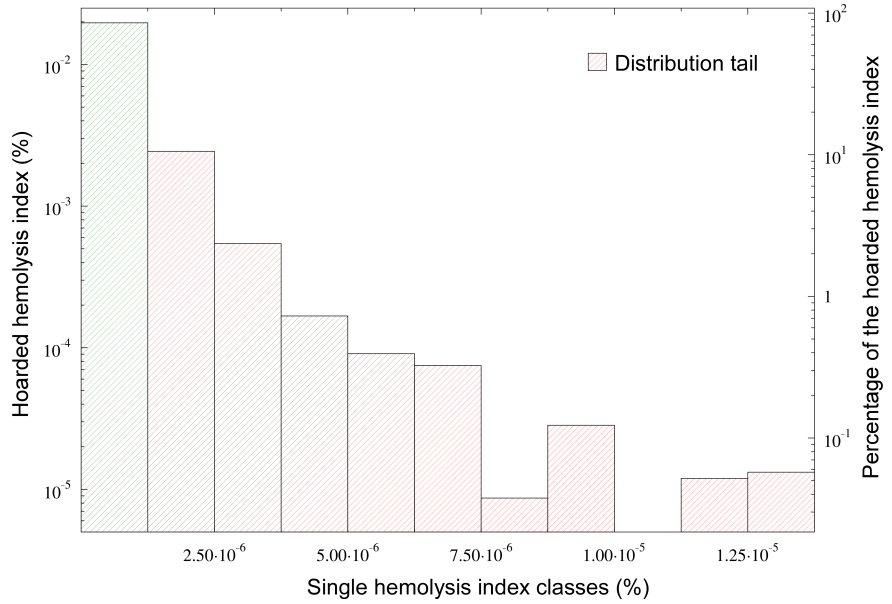

Fig. 7.9: The hoarded HI in function of the HI for single RBC, divided by the belonged class. The right scale shows the percentage of the total hoarded haemolysis index.

7.3.3 The computed trajectories

The second numerical experiment uses the *in vitro* data and the rupture model described in the section 7.2 to study if (and how) the haemolysis is characteristic of specific area inside the investigated flow region. In *fig.7.10* it is possible to observe the calculated trajectories of the RBCs during one single cycle. In particular, *N*=1000 RBCs were examinated. Trajectories of the damaged RBCs (i.e. path lines along which shell damage is occurred) are highlighted in red. It is easy to see how the region of recirculation and vortices formation –in the Valsava sinus-, but in particular the area between the right leaflet and the wall, are the principal areas suspected for the growth of damage. This is due to the relevant shear stresses and to the long resident time for the RBCs ending up in these buckets. Damage also occurs in proximity of the boundary layer between the lateral jets and the two sinuses regions (high velocity gradients).

Full-integrated approach seems able to illustrate using a physical description the damage process suffered by each cell. Moreover, the obtained maps reproduce in detail the main features of the phenomena: the high gradient of the flow, the vorticity regions, and the effect of the boundary layer on the RBCs. Moreover, one of the most important results of the study is the ability of the model to give spatial (and not only temporal) information of the damage process at work. The results show in *fig. 7.10* are robust with respect to changes of the simulation parameters (i.e. the number of RBCs injected, the perturbation of the flow with a ε in the velocity maps, the number of multiple passages). In particular, the areas where damage is accumulated remain the same, reinforcing the reliability of the rupture model.

All these effects couldn't be take in account by a heuristic non-rigorous approaches, as are pre upower law or derivate Grigioni cumulate damage.

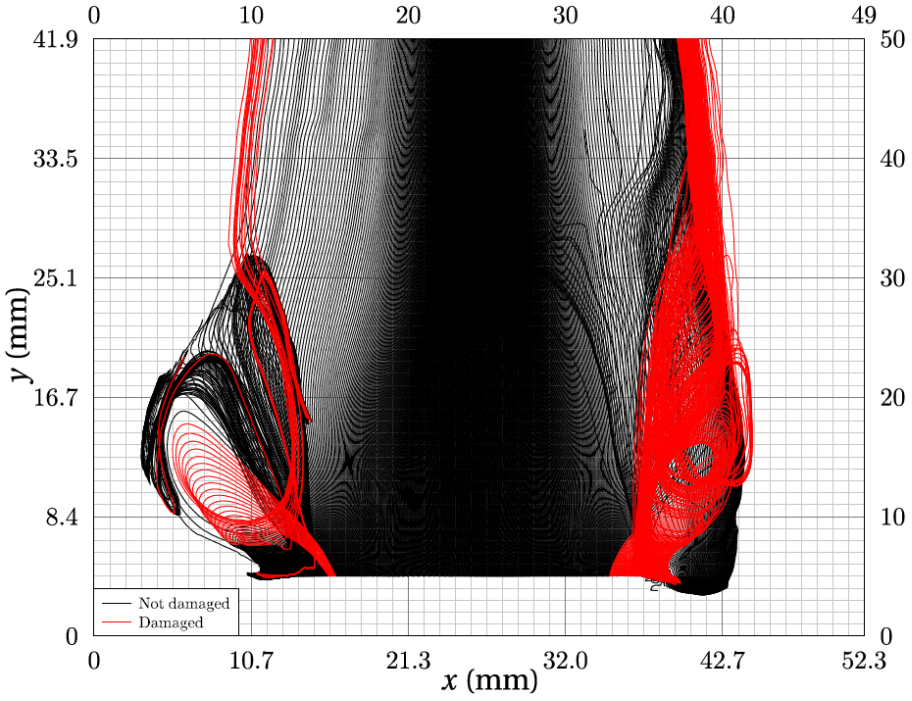

Fig. 7.10: The calculated trajectories of the 1000 RBCs during one single cycle, using the rupture model to describe the damaged and non-injured cells.

7.3.4 The model parameters sensitivity analysis

As last test, a sensitivity analysis of the model parameters was performed. The effect of the variation on the membrane local deformation was first investigated. Then, a comparison with the most recent literature results obtained by Zang (via experimental investigations using a viscometer and real RBCs) was achieved.

The *fig.7.11* shows the change of HI with respect to λ_{loc}. This parameter is the finest to describe the local strength of the membrane, subdivided in the little *dA*s. The adopted value (λ_{loc}=2.35) was proposed by Tran Son Tay. Starting from this, little variations were introduced to understand the weight of this parameter on the solution. In particular, *fig.7.11* illustrates the computed time necessary to reach the clinically relevant threshold of 0.5% (Lippi et al, 2009). Those "damage times" vary exponentially (from 30s to no damage) while related to a linear increment of λ_{loc}. The shape is the same for all the models, and depends strongly on *T*: the time scale of the damage is *T* due to the viscosity of the RBC membrane (and it should not be different, because the viscous term depends only by a single relaxation time in the model). The influence of λ_{loc} is evident, and the relative simplicity of the rupture mechanism

insert into the mechanical model shows here all its limitations. The main problem is to assert and justify the real value of a functional parameter as the local deformation limit, for a such small body as a RBC is, without modifying the mechanical answer of it (for example with micropipette aspiration, Chien et al. 1978; Rand 1964). Probably a much complex mathematical relation has to be used to surpass the gap between the numerical simulation and the reality. This observation is important as the fact that the rupture model in its entirety seems to express a more physically based behaviour if compared with pure mathematical strategies, also in this preliminary version. To improve the model few strategies should be adopted, in particular: insert a second relaxation time in the formulation ($T_2 \approx 5$ s, following Skalak), and introduce a non-fragile rupture mechanism. Both of this additions impose an important additional computational cost, and a reformulation of the model with data (that are still misty in literature), that are not acceptable with the current possibilities.

A confirmation of the goodness of the rupture model is shown in *fig.7.12*. Here are compared *in vitro* results obtained in Couette viscosimeters, and the numerical results of the rupture model. It is clear that for small changes in λ_{loc}, quite different damage times can be obtained. This result wants only to show how the model is robust and able to mimic quoted literature data. A comparison like this can also be useful to retrieve the unknown parameters from the literature, in relation to *in vitro* experiments (as because *in vivo* data are scarce).

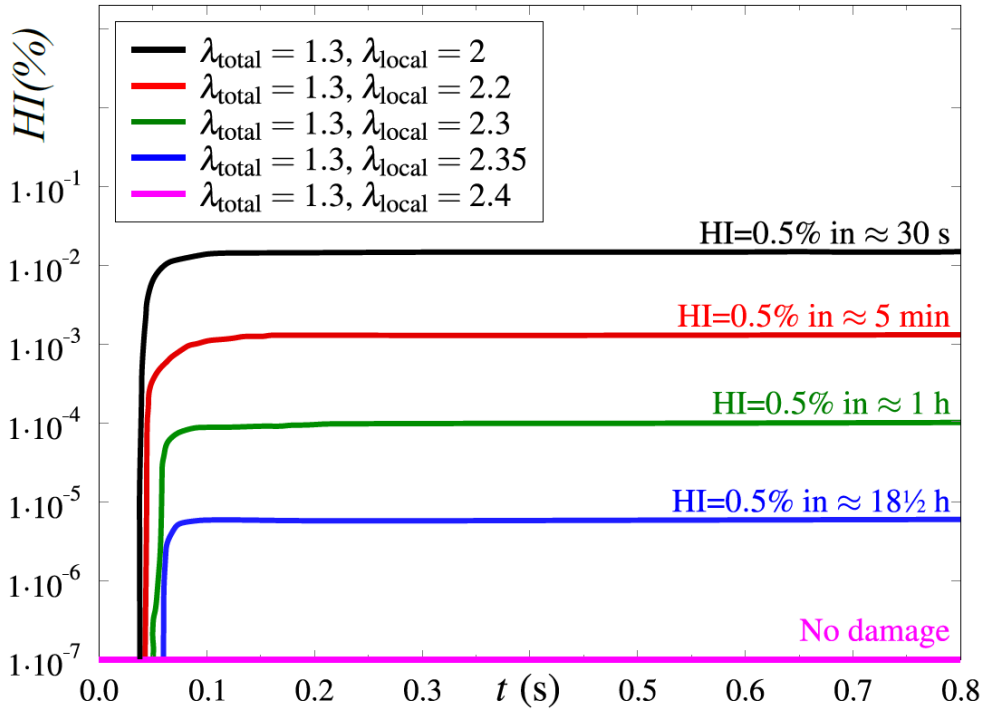

Fig. 7.11: The sensitivity analysis on λ_{loc}, how it changes the rupture model answer fixing the computed haemolysis index at 0.5%. The values of λ_{loc} were varying using a literature span reference.

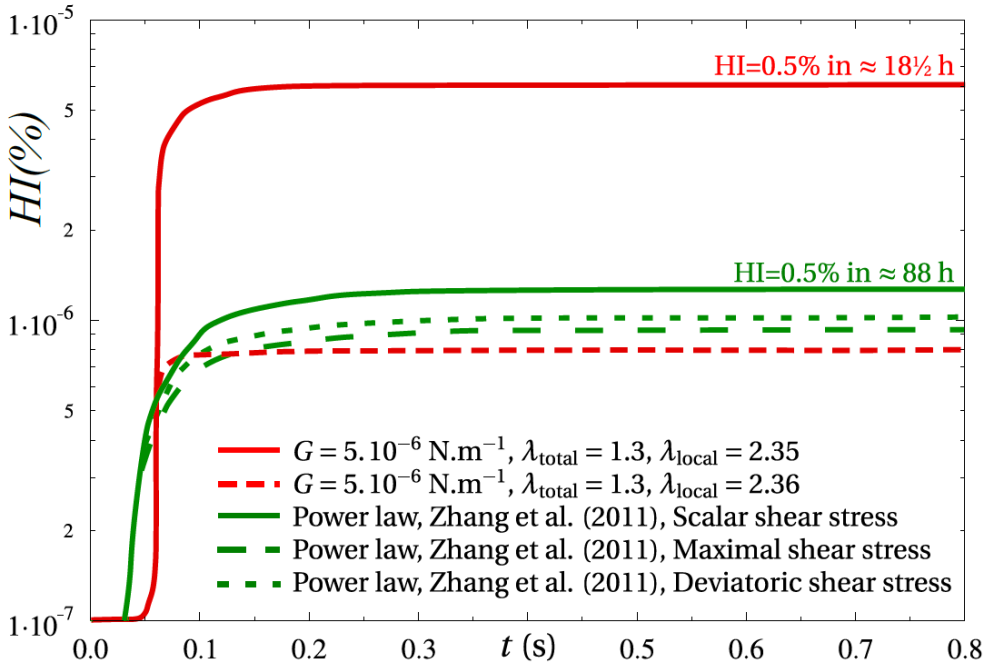

Fig. 7.12: The comparison analysis on *in vitro* results obtained in Couette viscosimeters, and the numerical results of the rupture model, for two different values of λ_{loc}.

In conclusion, the model seems to give a good description of the physiological damage occurring to RBCs, described in a more physical way, with specific spatial information compared to an heuristic approach. Moreover, the integrated approach could be a good strategy to overcame the limit given by the pure numerical or non-physiological experiments, coupling a semi physiologic *in vitro* behaviour for the reference flow field (pressure and stresses) with a mechanical model for the corpuscolate part.

7.4 Study abstract

In this study, the deformation and collapse of RBCs in a physiological flow through a bileaflet MHV, coupling 2D flow velocity fields obtained from previous in vitro experiments, and numerical simulations performed adopting a “passive immerged particle” technique, was investigated developing and running a self-made parallel Fortran code.

First, the RBCs trajectories were computed, highlighting the related fluid patterns. Since experimental velocities are known on a 50x51-node grid, this step was carried out using a bi-cubic interpolation of the known flow field. In turn, the knowledge of particle trajectories allows the reconstruction of the history of shear stresses and pressure experienced by the single RBC while moving in the investigated flow field.

Using the membrane theory, and developing a rheological model with visco-hyper-elastic behaviour, the global RBC deformations were computed. The global information was obtained by the local evaluation of the deformation for small areas *dA* of the cell surface, taking advantage of a specific symmetric geometry (ellipsoid) of the idealized red blood cell.

If the deformation exceeds a specific (a priori fixed) threshold, a quantity of haemoglobin (*Hb*) proportional to *dA* is released from the RBC. The coupling of the mechanical model and fragile damage behaviour is defined as “rupture model”. Then, relating this free *Hb* to the total *Hb* carried by blood, a damage index for RBCs was obtained. This method was simultaneously applied to *N* particles randomly injected just upstream the valve, along a cross-section, orthogonally to the flow.

The results of the tests suggest that an integrated approach is able to carry both the spatial and global haemolysis information about the damaging process suffered by the cells, promoting a new more physical based strategy to investigate the dangerousness of cardiovascular prosthetic device.

Indeed, although the rupture model still is at its first step into this approach, nevertheless it seems a smart way to describe the problem, trying to keep the driving factors and excluding the minor contributions. In conclusion, this study provides a new way to perform a RBCs damage investigation due to the passage through a BMHV, stimulating the literature attention to describe the whole phenomena with more physical details, trying to condensate the more relevant mechanical variables in few global parameters. It’s trivial to observe that the proposed approach can be applied to any othet cardiovascular device, provided that a robust velocity field ‘around the device is given.

7.5 Chapter bibliography

[1]. Arora D., Behr M., Pasquali M., A Tensor-based Measure for Estimating Blood Damage. Artif Organs 2004; 28: 1002-1015.

[2]. Bagchi P., Johnson P.C., Popel A.S., Computational Fluid Dynamic Simulation of Aggregation of Deformable Cells in a Shear Flow. Transactions of the ASME 2005; 127: 1070-1080.

[3]. Blackshear P.L., Mechanical Hemolysis in Flowing Blood. "Biomechanics: Its Foundation and Objectives", Fung YC, Prentice Hall 1972, pp 501-528.

[4]. Bronkhorst P.J.H., Streekstra G.J., Grimbergen J., Nijhof E.J., Sixma J.J., Brakenhoff G.J., A New Method to Study Shape Recovery of Red Blood Cells Using Multiple Optical Trapping. Biophysical J 1995; 69: 1666-1673.

[5]. Chandran K, Rittgers S, Yoganathan A., Biofluid Mechanics: The Human Circulation. CRC Press, Boca Raton 2006.

[6]. Chien S., Sung K.P., Skalak R., Usami S., Tozeren A., Theoretical and Experimental Studies on Viscoelastic Properties of Erythrocyte Membrane. Biophysical J 1978; 24: 463-487.

[7]. Dao M., Lim C. T., and Suresh S., Mechanics of the human red blood cell deformed by optical tweezers. J.Mech. Phys. Solids, 51:2259, 2003.

[8]. Dasi LP, Simon HA, Sucosky P, Yoganathan AP., Fluid Mechanics of Artificial Heart Valves. Clinical and Experimental Pharmacology and Physiology 2009; 36, 225-237.

[9]. Dasi L.P., Ge L., Simon H.A., Sotiropoulos F., Yoganathan A.P., Vorticity Dynamics of a BMHV in an Axisymmetric Aorta. Physics of Fluid 2007; 19(067105): 1-17.

[10]. De Tullio M.D., Namc J., Pascazio G., Balaras E., Verzicco R., Computational Prediction of Mechanical Hemolysis in Aortic Valved Prostheses. European J of Mechanics B/Fluids 2012; 35: 47-53.

[11]. Evans E.A., Hochmuth R.M., Membrane Viscoelasticity. Biophysical J 1976; 16: 1-11.

[12]. Evans Evan A., Membrane derived from buckling instability in micropipet aspiration tests. Biophys. J., 43:27, 1983.

[13]. Fortini S., Espa S., Toninato R., Pacetti L., Querzoli G., Susin M.F., Cenedese A. Analysis of the Flow Field Downstream a Bileaflet Valve inside an Aortic Arch Laboratory Model. 16th Int Symp on Applications of Laser Techniques to Fluid Mechanics. Lisbon Portugal, 9-12 July 2012.

[14]. Flügge Wilhelm, Stresses in shells. Springer-Verlag, Berlin Heidelberg, second edition, 1973.

[15]. Fung Y.C.B., Tong P., Theory of the Sphering of Red Blood Cells. Biophysical J 1968; 8: 175-198.

[16]. Giersiepen M., Wurzinger L.J., Opitz R., Reul H., Estimation of Shear Stress-related Blood Damage in Heart Valve Prostheses—in vitro Comparison of 25 Aortic Valves. Int J Artif Organs 1990; 13: 300-306.

[17]. Goubergrits L., Affeld K., Numerical Estimation of Blood Damage in Artificial Organs. Artif Organs 2004; 28: 499-507.

[18]. Grigioni M., Morbiducci U., D'Avenio G., Di Benedetto G., Del Gaudio C., A Novel Formulation for Blood Trauma Prediction by a Modified Power-law Mathematical Model. Biomech Model Mechanobiol 2005; 4: 249-260.

[19]. Heuser G., Opitz R., A Couette Viscometer for Short Time Shearing of Blood. Biorheology 1980; 17: 17-24.

[20]. Hochmuth R.M., Worthy P.R., Evans E.A., Red Cell Extensional Recovery and the Determination of Membrane Viscosity. Biophysical J 1979; 26: 101-114.

[21]. Jeffery G.B., The Motion of Ellipsoidal Particles Immersed in a Viscous Fluid. Proceeding of the RSL 1922; 102(715): 161-179.

[22]. Katircioglu S.F., Ulus T., Yamak B., Ozsoyler I., Birincioglu L., and Tagdemir O., Acute Mechanical Valve Thrombosis of the St. Jude Medical Prosthesis J Card Surg 1999; 14:164-168.

[23]. Kim Y., Kim K., Park Y., Measurement Techniques for Red Blood Cell Deformability: Recent Advances. "Blood Cell – An Overview of Studies in Hematology", Moschandreou T, InTech 2012, pp 167-194.

[24]. Lippi G., Salvagno G.L., Blanckaert N., Giavarina D., Green S., Kitchen S., Palicka V., Vassault A., Plebani M., Multicenter Evaluation of the Hemolysis Index in Automated Clinical Chemistry Systems. Clin Chem Lab Med 2009; 47: 934-939.

[25]. Paul R., Apel J., Klaus S., Schügner F., Schwindke P., Reul H., Shear Stress Related Blood Damage in Laminar Couette Flow. Artif Organs 2003; 27: 517-529.

[26]. Novozhilov V. V., Thin shell theory. P. Noordhoff, Groningen, 1964.

[27]. Rand R. P., Mechanical properties of the red cell membrane ii. viscoelastic breakdown of the membrane. Biophys. J., 4:303, 1964.

[28]. Rand R. P. and Burton A. C., Mechanical properties of the red cell membrane: I. membrane stiffness and intracellular pressure. Biophys. J., 4:115, 1964.

[29]. Sezai A., Hata M., Niino T., Yoshitake I., Kasamaki Y., Hirayama A., Minami K., Fifteen years of experience with ATS mechanical heart valve prostheses J Thorac Cardiovasc Surg 2010;139:1494-500.

[30]. Shahriari S., Maleki H., Hassan I., Kadem L., Evaluation of Shear Stress Accumulation on Blood Components in Normal and Dysfunctional Bileaflet Mechanical Heart Valves Using Smoothed Particle Hydrodynamics. J of Biomech 2012; 45: 2637-2644.

[31]. Skalak R., Tozeren A., Zarda R.P., Chien S., Strain Energy Function of Red Blood Cell Membranes. Biophysical J 1973; 13: 245-264.

[32]. Sutera S.P., Mehrjardi M.H., Deformation and Fragmentation of Human Red Blood Cells in Turbolent Shear Flow. Biophysical J 1975; 15: 1-10.

[33]. Susin F.M., Toninato R., Espa S., Fortini S., Querzoli G., Fadda G., La Tendenza al Danno Emolitico in una Protesi Valvolare Bileaflet. XXXIV Convegno Nazionale di Idraulica e Costruzioni Idrauliche - IDRA14. Bari Italy, 8-10 September 2014.

[34]. Tan Youhua, Sun Dong, and Juang Wenhao, Mechanical modeling of red blood cells during optical stretching. J. Biomech. Eng. T. ASME, 132:044504, 2010.

[35]. Taskin M. Ertan, Fraser Katharine H., Zhang Tao, Wu Changfu, Griffith Bartley P., and Wu Zhongjun J., Evaluation of eulerian and lagrangian models for hemolysis estimation. ASAIO J., 58:363, 2012.

[36]. Tran-Son Tay R., Sutera S.P., Zahalak G.I., Rao P.R., Membrane Stress and Internal Pressure in a Red Blood Cell Freely Suspended in a Shear Flow. Biophysical J 1987; 51: 915-924.

[37]. Ventsel Eduard and Krauthammer Theodor, Thin plates and shells: theory, analysis, and applications. Marcel Dekker, New York, 2001.

[38]. Waugh R.E., Evans E.A., Thermoelasticity of Red Blood Cell Membrane. Biophysical J 1979; 26: 115-132.

[39]. Waugh R.E., Hochmuth R.M., Mechanics and Deformability of Hematocytes. “The Biomedical Engineering Fundamentals” 3rd ed, Bronzino JD, CRC Press 1995, pp 60-63.

[40]. Wei Y., KRUKENKAMP I.B., SALTMAN A.E., GAUDETTE G., SURESH K., BERNAL O., JESTY J., BLUESTEIN D., Thrombogenic Performance of a St. Jude Bileaflet Mechanical Heart Valve in a Sheep Model ASAIO Journal 2006; 52:28–33.

[41]. Wootton D.M., and Ku D.N., Fluid Mechanics of Vascular Systems, Diseases, and Thrombosis Annu. Rev. Biomed. Eng. 1999. 01:299–329.

[42]. Wurzinger L.J., Opitz R., Eckstein H., Mechanical Bloodtrauma. An Overview. Angeiologie 1986; 38: 81-97.

[43]. Yoganathan A.P., He Z., and Casey S.J., Fluidmechanics of Heart Valves. Annu. Rev. Biomed. Eng. 2004. 6:331–62.

[44]. Zhang Tao, Taskin M. Ertan, Fang Hong-Bin, Pampori Adam, Jarvik Robert, Griffith Bartley P., and Wu Zhongjun J., Study of flow-induced hemolysis using novel 4 couette-type blood-shearing devices. Artif. Organs, 35:1180, 2011.

[45]. Zhang J., Johnson P.C., Popel A.S., Red Blood Cell Aggregation and Dissociation in Shear Flows Simulated by Lattice Boltzmann Method. J of Biomech 2008; 41: 47-55.

[46]. Zhang J., Johnson P.C., Popel A.S., Effects of Erythrocyte Deformability and Aggregation on the Cell Free Layer and Apparent Viscosity of Microscopic Blood Flows. Microvascular Research 2009; 77: 265-272.

Chapter 8

Conclusions & developments

8.1 Overview of the present research

During this PhD numerous studies were carried out, ranging from pure experimental to numerical investigation. All the conducted researches have a common theme that is the assessment of haemodynamic performances for cardiovascular prosthetic devices. This central path was covered from numerous sides, as seen along the different chapters.

From an experimental point of view the principal goal has been the complete realization of a pulse duplicator, able to simulate the systemic circulation. This, from a mechanical design and realization, motion software implementation, and data analysis points of view. After a sensitivity analysis, the workbench demonstrates an excellent ability to mimic the physiological pressure and flow trends. A comparison against a common commercial alternative shows a good capability to assess fluid dynamic performance of aortic valves. A deformable silicone prototype aortic arch technique was described, representing an innovative strategy to product specific copy of vascular parts.

Other experimental activities were conduit with the specific interest of study local flow configurations inside the aortic root. In particular, particle image velocimetry was adopted to study the flow characteristics in terms of local velocity, streamlines and vorticity downstream aortic bio-prosthetic valves, in London. Different valve-root setups were varied to inspect the relation between the root geometry, for sinuses shape and dimension, and sinotubular junction diameter variation. A theory of integrated system able to justify the observed flow patterns was developed.

The aortic root local flow was also investigated from a numerical point of view. Using *in vitro* data of velocity fields for a mechanical bileaflet valve, and developing a mechanical model for red blood cells, the haemolysis index was studied. The adoption of a physically based approach that take in account the visco-iperelastic characteristics of the cell membrane -based on experimental analysis- allowed the development of a rupture model. The application to a real flow field consents spatial information extraction, as the damaging trajectories,

and the computation of a cumulate damage index parameter. This is a new way respect to the usual literature perspective based on power laws equations.

In conclusion, after three years seems acceptable to say that the HeR Lab is on a good way for provide profitable international research results and prototypes development. From a personal point of view, during this PhD experience has been expounded transversal skills, which starts from the design of mechanic-hydraulic circuit and ability to provide *in vitro* reliable results of devices performance, passing through the purchase and organization of the lab materials and instrumentations, and reach aspects as the team activities planning and logistic issues solving. Part of the time was also depicted to public and private founding survey. A relevant result has been the ability of realize a self-founding event with a sailing race and a gala dinner in Venice, that saw the participation of two hundreds of clinicians and engineers.

8.2 Further directions for the HeR Lab

As described before, the HeR Lab is a new born reality in the University of Padua context. It grown quite fast in terms of employed people and research projects, collecting numerous good feedbacks from national and international research groups, and also by some companies. These interesting gave the possibility to start fruitful collaboration and open an exchange path for young researchers.

To fill the workbench disadvantages mentioned along the thesis (*Chapter 3-4*), little mechanical improvements are in development. In particular: a new deformable rubber-silicone valve housing system is in construction, which will provide higher energy dissipation at valve closure, to avoiding bumps effects on sensors measurement. Moreover, a reduction of the fluid mass -redesigning the atrial tank and ventricle chamber- plus a new phantom silicone “ventricle” will also help to limit the system inertia, avoid energy loss, and limit spike pressure waves and backflow from the aortic chamber to the ventricular, in particular during the initial phase of diastole. The “ventricle” silicone mold will be inserted between the inflow and outflow tracts (mitral to aortic derivations), with the aim of reduce the inertia forces to pump the fluid in the aortic branch and the rigidity of the actual system. The silicone part will be obtained by repetitive dipping of an ABS mold, obtained via fast prototype technique. Even though these are important but quite immediate mechanical changes, seems important to give a more wide scenario on the future possibly ways for the experimental research.

The developed pulse duplicator is now an efficient and reliable workbench for *in vitro* tests, and the next works will focus on the performance characterization of bio-prosthetic, mechanical valves and the flow investigation

inside the silicone aortic arch. Indeed, after the publication of the adopted casting technique for vessels prototypes production, the idea is to start a study campaign to examine and describe the flow inside a healthy and pathologic aortic root. This will involve fluid velocimetry techniques and the study of local characteristics of the flow field. A local induction is a not cheap way, normally conducted with particle image velocimetry and laser instrumentation, or via eco-color Doppler machine. Already now is in development a preliminary mixed experimental-numerical research that tries to understand which are the replicable main characteristics of the flow when a endovascular stented prosthesis is inserted in an aneurismatic aortic arch. In particular, a pattern recognition and tracking technique is in progress, with the aim of obtain a LabView tool for the fine motion characterization of the stent migration, under specific flow conditions. In a realistic view, under the right economic support, this could be the experimental Lab prospective for the next years.

The long term idea is to be able to make and test different vessel parts, healthy as pathologic, with the aim of a fluid dynamic characterisation in presence of external devices or to develop new prosthetic solutions.

The necessary investment to cover the described instrumentations for local induction (TSI Inc. 2D PIV System, 90 KEuro, or EcoColor Doppler System, 70 KEuro) and 2D pattern tracking analysis (LabView Visual, 10 KEuro), plus new catheter pressure transducers (Millar MicroTip, 3 KEuro) and a second flowmeter and probe (Transonic, 12 KEuro), an industrial hoven (500 Euro), two fast prototype printers (ABS and resin materials, Formlabs, 10 KEuro), a vacuum chamber, a fridge, new ABS moulds and silicone prototypes (7 KEuro), is about 110.000 Euro. Public and private founding strategies are now sifting through to fill this gap.

Acknowledgements

It is difficult for me to make an acknowledgements wall, because a value of someone is not expressed by its position in a list.

I want to start with Francesca, my professor of cardio vascular fluid dynamics, MS thesis supervisor, and finally PhD supervisor. Thanks for your constant attention on my research needs, for your unshakable faith in the neighbour, and for teach me that there are not bad results when we do the best of us. P&L.

Thanks to Gaetano and Andrea, to teach, improve and strengthen me during the fantastic period at UCL (and also for the beers together). I am in debt with you.

In particular, thanks to Luigi, Roberto and Giorgio, for help me since the beginning of the pulse duplicator realization, and to support me every day in the lab. Thanks also to Andrea B., for your support in the biomaterials field.

I have to mention my favourite sail-man and enthusiastic physician Stefano. He spent itself in the Lab growth and support with very concrete actions our ideas.

Thanks for the amazing friends, colleagues, and people that I met from all parts of the world during the doctorate. In particular, Luigi, Mattia, Lorenzo, Silvia, Matteo, Paolo P. & Paolo B., Federico, Pietro, Stefano. Guys in London: my “brother” Jacob, Ben, Selim, Wembo, Peter and Lee. You gave me more than I expected, it has been a great period.

Last but not least, thanks to my family, you are my backbone; and thanks to my best friends Francesco, Marco, Diego, Davide, Nicola, Enrico. Thanks Marta, you have been close to me for an important part of my life, although now we have taken different ways.
